

UNIVERSITY OF SHEFFIELD



University of
Sheffield

**The search for singlet fission:
non-radiative loss pathways in organic
semiconductors**

by

Daniel Hook

A thesis submitted in partial fulfillment for the
degree of Doctor of Philosophy

in the
Faculty of Science
Department of Physics and Astronomy

April 2024

Declaration of Authorship

I, DANIEL HOOK, declare that this thesis titled, ‘The search for singlet fission: non-radiative loss pathways in organic semiconductors’ and the work presented in it are my own. I confirm that:

- This work was done wholly or mainly while in candidature for a research degree at this University.
- Where any part of this thesis has previously been submitted for a degree or any other qualification at this University or any other institution, this has been clearly stated.
- Where I have consulted the published work of others, this is always clearly attributed.
- Where I have quoted from the work of others, the source is always given. With the exception of such quotations, this thesis is entirely my own work.
- I have acknowledged all main sources of help.
- Where the thesis is based on work done by myself jointly with others, I have made clear exactly what was done by others and what I have contributed myself.

Signed:

Date:

“Well, I mean, yes idealism, yes the dignity of pure research, yes the pursuit of truth in all its forms, but there comes a point I’m afraid where you begin to suspect that the entire multidimensional infinity of the Universe is almost certainly being run by a bunch of maniacs.”

-Douglas Adams, The Hitch-Hiker’s Guide to the Galaxy

UNIVERSITY OF SHEFFIELD



University of
Sheffield

Abstract

In this thesis, we present in-depth investigations into three materials which have been predicted to undergo singlet fission via density functional theory calculations. The first is Pigment Red 254, presented by Padula et al. [1], a diketopyrrolopyrrole derivative which shows great stability in the solid state and is also very cheap to produce, both of which are useful for device fabrication. The second and third are BoDiPy 6 and 7, derivatives of boron dipyrromethane[2].

Singlet fission is a phenomenon which occurs in a small number of organic semiconductor materials that permits the generation of two triplet excitons from one singlet exciton, which promises to greatly increase the efficiency of solar cell devices. In the search for more singlet fission materials, being able to predict the occurrence of singlet fission computationally rather than relying on high-cost, time consuming experimental procedures, it would greatly expedite the process of improving the efficiency of photovoltaics.

However, in this work we demonstrate that none of these materials unequivocally show singlet fission, finding in the case of Pigment Red 254 evidence for rapid non-radiative decay to the ground state which out-competes this process. We perform in-depth infrared investigations of this material, and demonstrate that this decay takes place via a hydrogen bond mediated proton transfer process, resulting in its non-radiative loss mechanism. In the case of the BoDiPy dyes, we show that intersystem crossing takes place preferentially to singlet fission, taking place in the solution phase and showing a strong dependence on the heavy atom substituents in the BoDiPy dyes.

We highlight here the need to account for well known structural markers of singlet fission loss mechanisms when attempting to predict efficient singlet fission materials, including hydrogen bonding and the heavy atom effect.

Acknowledgements

I would like to thank and give credit to the people without whose help this body of work would have been impossible.

Primarily I would like to thank Dr. Jenny Clark, my supervisor, for giving me the resources needed to conduct, contextualise, and rationalise the results of the research I have performed and have described in this paper. Without her advice, not to mention stalwart encouragement and boundless infectious enthusiasm for scientific rigour and the pursuit of exciting research, I would not have been able to successfully complete this document.

I would also like to thank James, my coworker, who has been a fountain of being willing to listen to me ramble.

I would like to thank Ravi, James, David, Sayantan, Rahul, Samara, Shuanqing, Martin, Alex, Eman, Robbie, and Rob, all for their assistance in teaching me the use of setups, techniques, and equipment across the departments. I would like to especially thank Julia, Martin, and Rory, as well as Igor, for their assistance in acquiring time-resolved infra-red spectroscopy measurements.

I would like to thank Samara, Rachel, Daniel T. and Daniel G. for assisting me by helping me gather data for this work.

I would like to thank both the group of Dr. Alessandro Troisi of the University of Liverpool, as well as Marco Cavazzini, of the Istituto di Scienze e Tecnologie Molecolari (ISTM), for providing the predictions for the molecules studied in this work, as well as in the latter case the BoDiPy molecules themselves.

I would like to thank my loving, supportive, and amazing partner, Franny, for being my strength and support every step of the way. Their kindness, gentle compassion, and care has helped me continue through the most stressful times when I lacked the confidence to push forward.

Contents

Declaration of Authorship	i
Abstract	iii
Acknowledgements	iv
List of Figures	viii
List of Tables	xii
Abbreviations	xiv
Physical Constants	xv
Symbols	xvi
Publications	xvii
1 Introduction	1
1.1 Triplet generation	1
1.2 Nonradiative Decay	2
2 Theory & Background	7
2.1 Orbitals	7
2.1.1 Atomic Orbitals	7
2.1.2 Molecular Orbitals	11
2.1.3 HOMO and LUMO	13
2.2 Molecular excited states	15
2.2.1 Spin-defined excited states - Singlets and Triplets	15
2.2.2 Triplet magnetic field effects	19
2.2.2.1 Zero field splitting	21
2.2.3 Excitons and Excimers - delocalised excitations	22
2.2.3.1 Aggregates and changing transition dipole moments	25
2.3 Molecular dynamics	26
2.3.1 The Adiabatic approximation	27

2.3.2	The adiabatic potential energy surface	28
2.3.3	Conical Intersections and their properties	30
2.3.4	Radiative transitions - Absorption and Emission	31
2.3.4.1	Electronic component of absorption	32
2.3.4.2	Vibrational component - the Franck-Condon factor	34
2.3.4.3	The spin factor - spin-orbit coupling	36
2.3.5	Non-radiative transitions	38
2.3.5.1	The Energy Gap Law	41
2.3.5.2	The strong coupling limit	44
2.3.5.3	Intersystem crossing and the Heavy Atom Effect	45
2.3.6	Singlet fission	47
3	Methods	54
3.1	Sample preparation	54
3.2	Steady-state spectroscopy	55
3.3	Transient Absorption Spectroscopy	56
3.3.1	Femtosecond transient absorption spectroscopy	60
3.3.2	Nanosecond transient absorption spectroscopy	61
3.3.3	Time Resolved Infra-Red Spectroscopy	62
3.4	Temperature dependent absorption	63
3.5	Resonance Raman Scattering	63
3.6	Atomic Force Microscopy (AFM)	64
3.7	Grazing Incidence Wide Angle X-ray Scattering (GIWAXS)	65
3.8	Quantum Chemical Calculations	65
3.9	Fourier Transform Infra-Red Spectroscopy	66
3.10	Time Correlated Single Photon Counting (TCSPC)	67
3.11	Data Processing Algorithms	67
3.11.1	Franck-Condon	67
3.11.2	Multivariate Curve Resolution - Alternating Least Squares global fitting	68
4	Pigment Red 254: a potential candidate for singlet fission	69
4.1	Introduction	69
4.2	Results	72
4.2.1	Steady state characterisation	72
4.2.2	Transient absorption spectroscopy	76
4.2.3	Temperature dependent absorption	80
4.3	Discussion	82
4.4	Conclusion	82
5	Infra-Red investigations of proton transfer in Pigment Red 254	84
5.1	Introduction	84
5.2	Results	89
5.2.1	Density functional theory (DFT) calculations	89
5.2.2	Fourier Transform Infra-Red spectroscopy	90
5.2.3	Time-Resolved Infra-Red spectroscopy	92
5.2.4	Fluence dependent TRIR	97

5.3	Discussion	101
5.4	Conclusion	105
6	Investigating singlet fission predictions in BoDiPy dye derivatives	106
6.1	Introduction	106
6.2	Results	111
6.2.1	Atomic Force Microscopy (AFM)	111
6.2.2	Steady State Absorption	113
6.2.3	Time Correlated Single Photon Counting	118
6.2.4	Transient Absorption Spectroscopy	120
6.2.5	Fluence Dependent Transient Absorption Spectroscopy	135
6.2.6	Pump-Energy Dependent Transient Absorption Spectroscopy	140
6.2.7	Multivariate Curve Resolution - Alternating Least Squares	143
6.3	Discussion	146
6.3.1	Conclusion	149
7	Outlook and Further Work	150
A	Pigment Red 254 UV-Vis Supporting Information	153
A.1	Franck-Condon Fitting Details	153
A.2	Grazing Incidence Wide Angle X-ray Scattering (GIWAXS)	155
A.3	Transient absorption spectra identification	157
A.4	Transient absorption lifetime fitting	158
A.5	Temperature dependent absorption residual plots.	159
B	Pigment Red 254 Infra-Red Supporting Information	161
B.1	Uncorrected TRIR spectra	161
B.2	Fluence dependent TRIR decay lifetimes	165
B.3	Full fluence dependent TRIR spectra and kinetics	166
B.4	Comparisons of TRIR kinetics	169
B.5	Fluence dependent TRIR graphical lifetime comparisons	173
C	BoDiPy 6 and 7 Supporting Information	178
C.1	Beam parameters for BoDiPy Transient Absorption Spectroscopy	178
D	Grant Acknowledgements	180
	Bibliography	181

List of Figures

1.1	Chemical structure of Pigment Red 254	4
1.2	Molecular structures of BoDiPy 6 (top) and BoDiPy 7 (bottom)	5
2.1	Hybrid orbitals of eth- hydrocarbons, from Köhler and Bäessler [3]	12
2.2	Structure of the molecular orbitals formed from one carbon atom in a molecule of ethene.	14
2.3	Ordering of molecular orbitals in ethene, from Köhler and Bäessler [3]	15
2.4	Splitting of the potential energy surface of the excited state due to inter-molecular electronic coupling, from Köhler and Bäessler [3]	24
2.5	General geometry and resultant transition dipole moment of molecular aggregates	26
2.6	Conical intersection between the excited state of an aromatic hydrocarbon molecule with the ground state via a pair of charge transfer conical intersections, from Sobolewski and Domcke [4]	30
2.7	Correspondence of energy level transitions to steady-state spectra under the Franck-Condon model.	36
2.8	The contrast between the weak and strong electronic coupling limits, from Englman and Jortner [5].	45
2.9	Illustration of the increase in entropy in going from a delocalised singlet to a localised triplet pair state, from Kolomeisky et al. [6]	51
2.10	Energy level diagram showing the change in energy of the electronic states involved in singlet fission due to entropy.	53
3.1	Schematic representation of the spatial overlap (top) and temporal overlap (bottom) of the pump and probe beams in pump-probe spectroscopy.	57
3.2	Example simulated transient absorption spectrum.	59
3.3	Ultrafast Systems Helios transient absorption spectrometer used for femtosecond transient absorption measurements.	60
3.4	Schematic of the beampath of the long-time nanosecond scale transient absorption setup used in this work.	62
4.1	Structural data on samples of Red254.	70
4.2	Steady state spectroscopic characterisation of Red254.	74
4.3	Nanosecond scale transient absorption of Red254 in solution of DMSO	76
4.4	Transient absorption spectra of sublimated thin films of Red254	78
4.5	Transient absorption kinetics of sublimated thin films of Red254	79
4.6	Temperature dependent difference spectra of sublimated thin films of Red254	81

5.1	Logarithmic comparison of the energy gap law relationship in diketopyrrolopyrrole derivatives	85
5.2	Proposed structure of intermolecular tautomerisation of Red254 in the solid state.	87
5.3	Spine plot of modes found via density functional theory calculations	89
5.4	Vector plots of vibrational modes of Red254 dimers as found via DFT calculations.	90
5.5	Fourier Transform Infra-Red (FTIR) spectra of thermally sublimated film of Red254 on a calcium fluoride substrate	91
5.6	Time Resolved Infra-Red (TRIR) spectra and kinetics of thin film of Red254 on calcium fluoride window substrate using a pump power of 5 mW	93
5.7	Normalised kinetic decays of the 2000-2100 cm^{-1} kinetic slices of time-resolved infra-red spectra of Red254 evaporated thin film on calcium fluoride substrate	95
5.8	Normalised kinetic decays of the 1451 cm^{-1} kinetic slice of time-resolved infra-red spectrum of Red254 evaporated thin film on calcium fluoride substrate	98
5.9	Normalised kinetic decays of the 1610 cm^{-1} kinetic slice of time-resolved infra-red spectrum of Red254 evaporated thin film on calcium fluoride substrate	99
5.10	Early-time time-resolved infra-red fluence dependent spectra of Red254 thin film on calcium fluoride substrate	100
5.11	Late-time time-resolved infra-red fluence dependent spectra of Red254 thin film on calcium fluoride substrate	101
5.12	Model of the non-radiative decay pathway of Pigment Red 254	102
6.1	Molecular structures of BoDiPy 6 (top) and BoDiPy 7 (bottom)	107
6.2	Atomic force microscopy images of amorphous films of BoDiPy 6 and BoDiPy 7	111
6.3	Atomic force microscopy images of thermally annealed films of BoDiPy 6 and BoDiPy 7	112
6.4	Steady state UV-Vis absorption and emission spectra for solutions, amorphous films, and crystalline films of BoDiPy 6	114
6.5	Steady state UV-Vis absorption and emission spectra for solutions, amorphous films, and crystalline films of BoDiPy 7	116
6.6	Time-correlated single photon counting plots of the emissive decay of BoDiPy 6 and BoDiPy 7	119
6.7	Transient absorption spectra and kinetics of BoDiPy 6 in toluene solution.	121
6.8	Transient absorption spectra and kinetics of BoDiPy 6 amorphous film.	122
6.9	Transient absorption spectra and kinetics of BoDiPy 6 crystalline film.	124
6.10	Comparison of early time (1-2 ps) and late time (3000-5000 ps) normalised spectra of BoDiPy 6 solution, amorphous film and crystalline film	125
6.11	Transient absorption spectra and kinetics of BoDiPy 7 in toluene solution.	128
6.12	Transient absorption spectra and kinetics of BoDiPy 7 amorphous film.	129
6.13	Transient absorption spectra and kinetics of BoDiPy 7 crystalline film.	130
6.14	Comparison of early time (1-2 ps) and late time (3000-5000 ps) normalised spectra of BoDiPy 7 solution, amorphous film and crystalline film.	132

6.15	Fluence dependence of the transient absorption of BoDiPy 6 crystalline thin films at 400 nm (3.1 eV) excitation	135
6.16	Fluence dependence of the transient absorption of BoDiPy 6 crystalline thin films at 530 nm (2.3 eV) excitation	136
6.17	Fluence dependence of the transient absorption of BoDiPy 7 crystalline thin films at 400 nm (3.1 eV) excitation	138
6.18	Fluence dependence of the transient absorption of BoDiPy 7 crystalline thin films at 530 nm (2.3 eV) excitation	139
6.19	Pump energy dependent TA and kinetics of crystalline thin films of BoDiPy 6	141
6.20	Pump energy dependent TA and kinetics of crystalline thin films of BoDiPy 7	142
6.21	Species associated spectra and concentrations of BoDiPy 6 in solution and in amorphous film	144
6.22	Species associated spectra and concentrations of BoDiPy 7 in solution and in amorphous film	145
A.1	Franck-Condon fit to the Red254 in DMSO solution-phase absorption spectrum	153
A.2	Franck-Condon fit to the Red254 in DMSO solution-phase emission spectrum	154
A.3	Out-of-plane Grazing Incidence Wide Angle Scattering (GIWAXS) signal of thermally evaporated thin film of Red254 on silicon substrate in atmosphere	155
A.4	Out-of-plane Grazing Incidence Wide Angle Scattering (GIWAXS) signal of thermally evaporated thin film of Red254 on silicon substrate in vacuum	156
A.5	Transient absorption compared with steady state absorption and emission of thin film of Red254	157
A.6	Transient absorption compared with steady state absorption and emission of dilute solution of Red254 in DMSO	158
A.7	Plot of residuals of a linear fit of the temperature dependent absorption spectra to the long-time TA spectra at various time slices for thin films of Red254 on a quartz substrate and on a sapphire substrate	159
B.1	Uncorrected TRIR spectra of Red254 with a pump power of 5mW	161
B.2	Uncorrected TRIR spectra of Red254 with a pump power of 2.5mW	162
B.3	Uncorrected TRIR spectra of Red254 with a pump power of 1mW	163
B.4	Uncorrected TRIR spectra of Red254 with a pump power of 0.5mW	164
B.5	Time Resolved Infra-Red (TRIR) spectra and kinetics of thin film of Red254 on calcium fluoride window substrate using a pump power of 0.5 mW	166
B.6	Time Resolved Infra-Red (TRIR) spectra and kinetics of thin film of Red254 on calcium fluoride window substrate using a pump power of 1 mW	167
B.7	Time Resolved Infra-Red (TRIR) spectra and kinetics of thin film of Red254 on calcium fluoride window substrate using a pump power of 2.5 mW	168

B.8	Normalised kinetic decays of the 1589 cm^{-1} kinetic slice of time-resolved infra-red spectrum of Red254 evaporated thin film on calcium fluoride substrate	169
B.9	Normalised kinetic decays of the 1627 cm^{-1} kinetic slice of time-resolved infra-red spectrum of Red254 evaporated thin film on calcium fluoride substrate	170
B.10	Normalised kinetic decays of the 1643 cm^{-1} kinetic slice of time-resolved infra-red spectrum of Red254 evaporated thin film on calcium fluoride substrate	171
B.11	Normalised kinetic decays of the 1703 cm^{-1} kinetic slice of time-resolved infra-red spectrum of Red254 evaporated thin film on calcium fluoride substrate	172
B.12	Fluence dependence of fitted exponential lifetimes to the 1451 cm^{-1} kinetic slice of the TRIR spectra of Red254 on calcium fluoride substrate, normalised to the 5 mW kinetic.	173
B.13	Fluence dependence of fitted exponential lifetimes to the 1589 cm^{-1} kinetic slice of the TRIR spectra of Red254 on calcium fluoride substrate, normalised to the 5 mW kinetic.	174
B.14	Fluence dependence of fitted exponential lifetimes to the 1610 cm^{-1} kinetic slice of the TRIR spectra of Red254 on calcium fluoride substrate, normalised to the 5 mW kinetic.	175
B.15	Fluence dependence of fitted exponential lifetimes to the 1627 cm^{-1} kinetic slice of the TRIR spectra of Red254 on calcium fluoride substrate, normalised to the 5 mW kinetic.	175
B.16	Fluence dependence of fitted exponential lifetimes to the 1643 cm^{-1} kinetic slice of the TRIR spectra of Red254 on calcium fluoride substrate, normalised to the 5 mW kinetic.	176
B.17	Fluence dependence of fitted exponential lifetimes to the 1703 cm^{-1} kinetic slice of the TRIR spectra of Red254 on calcium fluoride substrate, normalised to the 5 mW kinetic.	177

List of Tables

4.1	0-0 vertical (absorption) and adiabatic (emission) transition energies of Red254. Calculated singlet energy and triplet energies from Padula <i>et al.</i> [1].	75
4.2	Franck-Condon fitting parameters for Red254 steady-state solution spectra. Values presented with an asterisk (*) in the solution absorption indicate where fitting parameters were allowed to vary freely.	75
4.3	Lifetimes and uncertainties of the decays of sublimated thin film samples of Red254 on quartz and sapphire substrates	80
5.1	Table of different wavenumbers (ν) assigned to vibrational modes in the DFT calculations, FTIR spectrum, and TRIR spectra. C-X refers to a generic, approximate or representative carbon single-bond mode. "s" denotes a stretching mode, while "w" denotes a waving or bending mode.	94
5.2	Lifetimes of excited vibrational decays from Time-Resolved Infra-Red spectroscopy kinetics as shown in Fig. 5.6. The pump power used for these measurements was 5 mW	96
6.1	Franck-Condon fitting parameters, where applicable, for BoDiPy 6 and BoDiPy 7. A (*) sign indicates the parameter was not obtained through Franck-Condon fitting, but from the maximum point of the spectrum, and thus does not correspond to the "true" 0-0 peak	117
6.2	Lifetimes of emissive decays from Time-Correlated Single-Photon Counting decays as shown in Fig. 6.6.	120
6.3	Lifetimes of excited-state decays of BoDiPy 6 from Transient Absorption Spectroscopy decays as shown in Figs. 6.7, 6.8, 6.9, 6.15, 6.16 and 6.19.	126
6.4	Lifetimes of excited-state decays of BoDiPy 7 from Transient Absorption Spectroscopy decays as shown in Figures 6.7 to 6.9, 6.17, 6.18 and 6.20.	134
6.5	Fitting parameters of exponential and bi-exponential fits to the MCR-ALS concentrations in Fig. 6.21 and 6.22. The (*) indicates that this parameter was taken from the S_1 decay, rather than fit from the late-time concentration data itself.	146
A.1	Table of sample temperature as set by water bath heater versus measured temperature of substrate back surface.	160
B.1	Lifetimes of excited vibrational decays from Time-Resolved Infra-Red spectroscopy kinetics as shown in Figs. B.5, B.6 and B.7	165

C.1	Beam parameters and excitation density of pump laser used for picosecond transient absorption spectroscopy of BoDiPy 6 samples. Areal excitation density was calculated using absorption spectroscopy of the samples used in TA at the wavelength of the exciting beam.	178
C.2	Beam parameters and excitation density of pump laser used for picosecond transient absorption spectroscopy of BoDiPy 7 samples. Areal excitation density was calculated using absorption spectroscopy of the samples used in TA at the wavelength of the exciting beam.	179

Abbreviations

TA	Transient Absorption spectroscopy
TRIR	Time Resolved Infra-Red spectroscopy
TCSPC	Time Correlated Single Photon Counting
FTIR	Fourier Transform Infra-Red spectroscopy
BoDiPy	Boron Di-Pyrromethane
DPP	DiketoPyrroloPyrrole
Red254	Pigment Red 254
GSB	Ground State Bleach
ESA	Excited State Absorption
SE	Stimulated Emission
HOMO	Highest Occupied Molecular Orbital
LUMO	Lowest Unoccupied Molecular Orbital

Physical Constants

Speed of Light	c	$=$	$2.997\,924\,58 \times 10^8 \text{ ms}^{-1}$	(exact)
Planck Constant	\hbar	$=$	$1.054\,571\,817 \times 10^{-34} \text{ Js}$	
Electronic Mass	m_e	$=$	$9.109\,383\,701\,5 \times 10^{-31} \text{ kg}$	
Electronic Charge	e	$=$	$-1.602\,176\,634 \times 10^{-19} \text{ C}$	
Boltzmann Constant	k_B	$=$	$1.380\,649 \times 10^{-23} \text{ JK}^{-1}$	
Vacuum permittivity	ϵ_0	$=$	$8.854\,187\,812\,8 \times 10^{-12} \text{ CV}^{-1}\text{m}^{-1}$	

Symbols

m/M	mass	kg
Z	atomic number	
r/R	radial distance (radial wavefunction component)	m
Y	angular wavefunction component	
V	potential energy operator	
l	angular momentum quantum number	
L	orbital angular momentum operator	
J	total angular momentum operator	
H	Hamiltonian	
Q	Molecular normal coordinate	
B	Magnetic field	T ($kg s^{-2} A^{-1}$)
k	Rate constant	s^{-1}
I	Intensity	$W m^{-2}$ ($kg s^{-3}$)
ω	angular frequency	rads^{-1}
θ	polar angle	rads
ϕ	azimuthal angle	rads
ψ, Φ, χ	wavefunctions/wavefunction components	
∇	The laplacian operator	
Λ	The legendrian operator	
μ	dipole moment	Am^2
μ_b	Bohr magneton	Am^2
ρ	reduced mass	kg

Publications

1. F. Bastianini, A. I. C. Hidalgo, D. Z. Hook, J. A. Smith, D. Cumming, and A. Dunbar. Incorporation of Ag Nanoparticles in the Electron Transport Layer of Perovskite Solar Cells: understanding the mechanism that leads to improved efficiency *Pending publication*
2. D. Hook, D. Padula, S. Wang, D. Toolan, R. Kilbride, D. Gillard, R. K. Venktraman, J. Pidgeon, A. Troisi, and J Clark. The importance of accounting for non-radiative decay when screening materials for singlet fission: the case of Pigment Red254. *Pending publication*

For Franny, my love. . .

Chapter 1

Introduction

Fundamental to the field of optoelectronics is energy harvesting from the optically excited electronic state of the material, and is the basis of devices such as photovoltaics[7]. In addition, energy can also be obtained from light-matter interactions by the photothermal effect, by which light incident on a material is converted to heat via internal processes, including nonradiative decay from an electronic excited state.[8].

1.1 Triplet generation

Harvesting energy from the electronic excited states of a material is achieved via the electron-hole pair that is generated by the excitation of a material by light, and the subsequent separation of this pair to produce a net voltage in a closed circuit. This is the basis by which p-n junction solar cells operate[9].

However, in the design of solar cells, the absorption bandgap of the material can only access a small region of the solar energy spectrum, resulting in a large portion of the light that is incident on the cell being lost either through thermalisation of the excess energy or the failure of the incident photon to meet the bandgap of the semiconductor that forms the cell. While the exact efficiency depends on temperature and environmental conditions, the detailed balance limit[10] gives a maximal efficiency for a single junction, p-n type solar cell of 33.7%[11, 12].

This limit may be bypassed and more energy may be harvested by instead using a multi-junction solar cell with a material capable of singlet fission. Singlet fission is a process by which a single, higher energy singlet excitation is able to generate two lower-energy triplet excitations, thus ensuring that more of the higher energy end of the solar spectrum can be efficiently converted to electric current at the back contact of the cell. This is

possible when the energy of the triplet state is significantly reduced via the exchange interaction, meaning that this process is energetically favourable. The low energy end of the solar spectrum can also be accessed more efficiently by triplet up-conversion, by which a low energy singlet can convert via intersystem crossing to a triplet of similar energy, and combine with another triplet to generate a single, high energy singlet via the mechanism of triplet fusion[13–15]. This method, with a two-junction singlet fission sensitised solar cell, can increase the theoretical maximum efficiency limit of the cell to $\sim 44\%$ [11, 16].

Triplet generation is also used in other applications, including in-vivo phototherapeutic applications. Triplets are used in the generation of reactive oxygen species, and can be highly damaging to biological cells. The use of a low-dark-toxicity efficient triplet-generating material can allow targeted destruction of cancerous cells via photo-activated processes[17, 18]. Furthermore, triplet generation can be used in a host of optoelectronic devices, such as in light emitting diodes[19, 20], for generating intense high wavelength light.

1.2 Nonradiative Decay

The energy produced by light incident on a material can also experience non-radiative decay to the ground state through a number of pathways. These decay pathways include non-adiabatic decay, via resonant interaction between electronic states[21], as well as photo-induced chemical processes. These can occur on large scales, in the case of permanent chemical reactions with an energy barrier bypassed by light, as in many unstable chemicals, and used in such devices as photographic plates, or on small scales, such as in the case of Excited State Proton Transfer (ESPT)[4], in which a proton is temporarily or permanently exchanged between adjacent molecules. This latter case often results in efficient nonradiative decay to the ground state, such as in the cases of DNA nucleobases, base pairs, and more complex structures, such as cytosine and cytosine I-motif polymers[22], as well as in solvent-solute interactions from fluorenone derivatives[23–25].

Nonradiative decay processes such as this have many uses, as the energy is dispersed in the form of heat. As such, materials such as this can efficiently generate thermal energy under illumination. This finds use in phototherapy, similarly to triplet generation, for targeted heat-based treatment of cancerous cells[17, 18, 26–28], as well as in filters and photoprotective layers, or indeed for light-induced heating for water desalination and cleaning, a use case which is rapidly becoming more necessary due to droughts and poor water conditions arising from climate change[29].

In choosing materials for these applications, the occurrence of the phenomena of nonradiative decay or triplet generation is not sufficient. In biological applications, photostability and low dark toxicity[30, 31] is vital to prevent unintended harm or degradation into harmful photoproducts that may persist in the body, and in solar cell and water based applications high stability, weathering resistance, and lack of photo- and chemo-degradation is required to ensure long device lifetime. Furthermore, low cost and ease of processibility is desirable to facilitate mass production, as well as environmental resistance for use in harsh conditions. For harvesting of electronic energy, it is also required for the material to have high exciton mobility in order to reach the junction interface rapidly.[32]

In order to find materials which fulfil these requirements for opto-electronic applications, methods for predicting the occurrence of the required molecular processes are desirable. One such method was produced by Padula et al. [1], which uses an algorithm consisting of two increasingly precise DFT energetic calculations to screen the Cambridge Crystallographic Database for materials which fulfil the energy requirements for singlet fission, as shall be discussed in Chapter 2. One positive result of this algorithm is Pigment Red 254, a highly stable diketopyrrolopyrrole molecule which is both cheap and easily processible, being used commercially as Ferrari paint. Furthermore, Marco Cavazzini of the Istituto di Scienze e Tecnologie Molecolari (ISTM), and the Consiglio Nazionale delle Ricerche (CNR), predicted the occurrence of singlet fission via DFT calculations in a pair of BoDiPy molecules[2], 2,6-di-iodo,4-mesityl BoDiPy and 2,6-di-bromo,4-mesityl BoDiPy. Testing the validity and success of these methods, as well as investigating the true decay pathways of these molecules in the case of predictive failure, are part of the goals of this work, in order to discover the structural properties that either enable or disable the singlet fission pathway.

In Chapter 2, we give the theoretical background to the concepts discussed in later chapters, beginning with the fundamental aspects of atomic and molecular states, the adiabatic approximation, excitations and excited state dynamics including radiative and nonradiative decay, as well as in-depth treatment of the different methods of triplet generation. In Chapter 3 we expand on the specifics of the methods used in the paper, including sample preparation, light source and measurement parameters, and algorithms and equations used for modelling. In addition, the concepts behind the key spectroscopic techniques used are discussed: transient absorption and time-resolved infra-red spectroscopy, time-correlated single-photon counting, and Fourier transform infra-red spectroscopy.

In Chapter 4, we introduce Pigment Red 254, a derivative of the diketopyrrolopyrrole base molecule (Fig. 1.1) which is comprised of two pyrrole groups and two phenyl rings

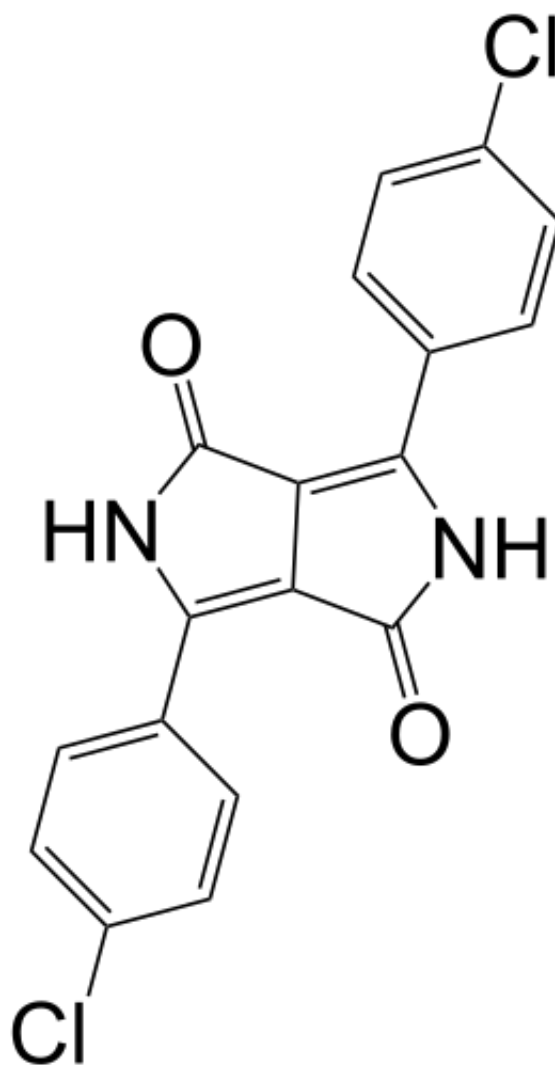


FIGURE 1.1: Chemical structure of Pigment Red 254

substituted with chlorine. This dye was predicted, in a broad DFT analysis of the Cambridge Crystallographic Database by Padula et al. [1], to have favourable energetics for singlet fission. We investigate the photophysical behaviour of this dye in the solid and solution state, using UV-Vis absorption and photoluminescence measurements to characterise the steady state energetics and how they change with sample phase, and find a notable lack of fluorescence in the solid state compared to the solution. We further investigate the dynamics of the excited state of this molecule using ultrafast transient absorption spectroscopy, noting the order-of-magnitude difference in the excited state lifetime between solution and solid states. Using both more highly thermally conductive substrates to conduct transient absorption measurements, as well as performing temperature dependent absorption, we find that instead of the singlet fission predicted by Padula et al. [1], or the radiative decay to the ground state shown in the solution transient absorption kinetics, over a ~ 5 ns timescale, the solid poly-crystalline dye films

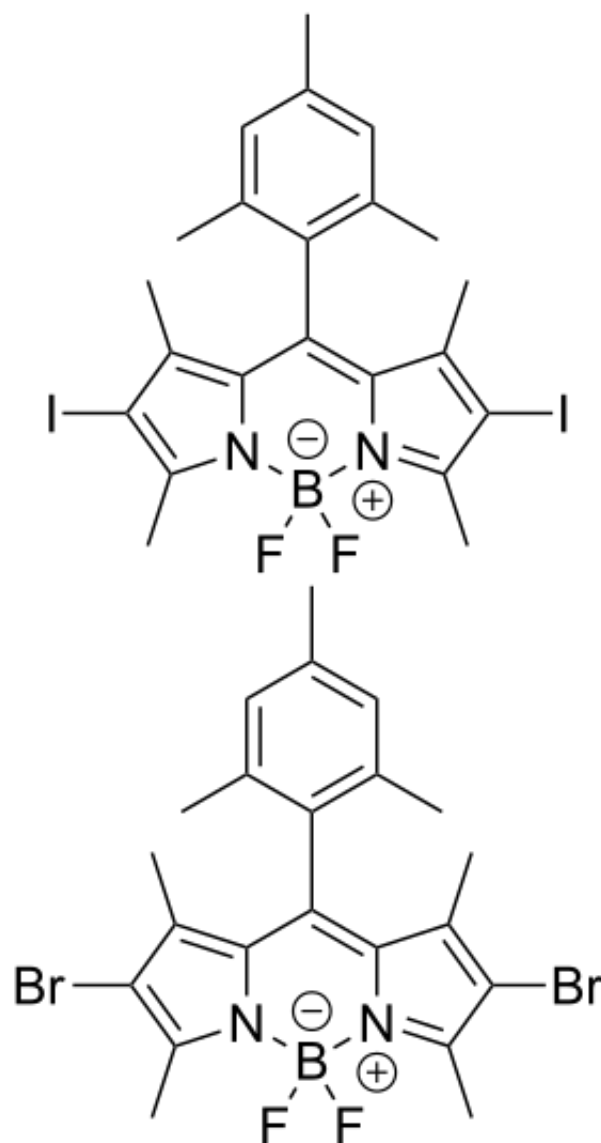


FIGURE 1.2: Molecular structures of BoDiPy 6 (top) and BoDiPy 7 (bottom)

undergo rapid nonradiative decay to the ground state over ~ 5 ps, depositing a great deal of thermal energy into the ground state.

In Chapter 5, we continue the investigation of Pigment Red 254, noting that the non-radiative decay lifetime noted in the Chapter 4 is two orders of magnitude shorter than nonradiative decay lifetimes noted in other diketopyrrolopyrrole derivative molecules. As such, we hypothesise a different mechanism mediates the excited state decay compared to other derivatives, which have their N-H groups substituted with alkyl chains. We propose a conical intersection mechanism enabled by partial proton transfer to the oxygen of the adjacent Pigment Red 254 molecule in the solid state, and investigate the vibrational spectra of the solid films using time-resolved infra-red spectroscopy. We detect the presence of a carbon double-bond bleach feature as well as a new carbon

double bond excited state absorption feature, denoting the formation of the C=N bond and the loss of the C=O feature. We suggest the intermediate state which enables this conical intersection is a dark charge-transfer state resulting from the electron deficient character of the diketopyrrolopyrrole core.

In Chapter 6, we perform a comprehensive transient absorption spectroscopy investigation of two BoDiPy derivatives. In this work we refer to them as BoDiPy 6, which has iodine atoms substituted in the 2 and 6 positions, and BoDiPy 7 (shown in Fig. 1.2), where these iodines are replaced with lighter bromine atoms. We prepare samples of BoDiPy 6 and 7 in toluene for solution phase measurements, as well as preparing amorphous and polycrystalline films via spin-coating from solution and subsequent annealing. We find a high yield of a long-lived species present in the solution phase, with molecules including heavier iodine atoms experiencing a faster rate of triplet formation. This suggests that the triplet generating mechanism is heavy-atom effect mediated intersystem crossing. We find similar triplet generation in the solid state samples, though producing a significantly lower yield, and with the exception of the polycrystalline thin film of BoDiPy 7, in which a low energy trap state instead induces quenching of this triplet pathway. In addition, a delayed fluorescence tail was detected in the time-correlated single photon counting spectrum of polycrystalline BoDiPy 6, indicating some reverse process (such as triplet fusion or reverse-ISC) occurs in this state.

Chapter 2

Theory & Background

2.1 Orbitals

2.1.1 Atomic Orbitals

The understanding of the behaviour of organic semiconductor materials must begin with the description of the hydrogen atom and its orbitals, beginning with the time-independent Schrödinger equation. The Hamiltonian of the hydrogen atom can be written as

$$\hat{H} = -\frac{\hbar^2}{2m_e}\nabla_e^2 - \frac{\hbar^2}{2m_N}\nabla_N^2 - \frac{Ze^2}{4\pi\epsilon_0 r}, \quad (2.1)$$

where m_e, ∇_e represent the mass and Laplacian operator for the electron in the hydrogen atom, and m_N, ∇_N are those of the nucleus[33]. The first term represents the kinetic energy of the electron, the second the kinetic energy of the nucleus, and the third is the Coulomb potential of the nucleus, in which Z represents the atomic number, e , the electronic charge, ϵ_0 the permittivity of a vacuum, and r the radial distance from the nucleus.

This Hamiltonian can, instead of being represented by the energy and mass of the electron and nucleus, be reinterpreted from the frame of reference of the centre of mass of the atom:

$$\hat{H} = -\frac{\hbar^2}{2M}\nabla_{cm}^2 - \frac{\hbar^2}{2\rho}\nabla^2 - \frac{Ze^2}{4\pi\epsilon_0 r}, \quad (2.2)$$

in which $M = m_e + m_N$, the total mass of the system and ρ is the reduced mass of the system, $\frac{1}{\rho} = \frac{1}{m_e} + \frac{1}{m_N}$ [33]. ∇_{cm} is the Laplacian of the atomic centre of mass, and ∇ is that of the components of the atom with respect to that centre of mass. The Coulombic term does not change, as the displacement r does not change with the changed frame of reference. As we are considering the internal energy of the atom, the

first term in ∇_{cm} can be dropped from the Hamiltonian, and we can consider only the internal kinetic energy and the Coulomb potential. We can insert this equation into the time-independent Schrödinger equation:

$$(T - V)\psi = E\psi \quad (2.3)$$

$$-\frac{\hbar^2}{2\rho}\nabla^2\psi - \frac{Ze^2}{4\pi\epsilon_0 r}\psi = E\psi, \quad (2.4)$$

in which T and V are the kinetic and potential energy operators, respectively, and E is the total energy[33]. The ∇ operator can be decomposed into the radial and angular components such that

$$\frac{1}{r^2}\frac{\partial^2}{\partial r^2}r\psi + \left(\frac{1}{r^2}\Lambda^2 + \frac{Ze^2\rho}{2\pi\epsilon_0\hbar^2 r}\right)\psi = -\frac{2\rho E}{\hbar^2}\psi, \quad (2.5)$$

where Λ is the Legendrian operator[33]. This Legendrian operator describes the (non-radial) motion of the particle around the nucleus, and can be examined by comparison with the classical angular momentum of the system. By suggesting a separable form of the wavefunction,

$$\psi(r, \theta, \phi) = R(r)Y(\theta, \phi), \quad (2.6)$$

we can obtain the following form of the equation:

$$\frac{1}{r^2}\frac{\partial^2}{\partial r^2}rRY + \left(-\frac{l(l+1)}{r^2} + \frac{Ze^2\rho}{2\pi\epsilon_0\hbar^2 r}\right)RY = -\frac{2\rho E}{\hbar^2}RY, \quad (2.7)$$

where the $\Lambda^2\psi = -l(l+1)\psi$ substitution is made by considering the spherical harmonics of a particle in an infinite spherical well. As the model of the hydrogen atom only differs from this model in the form of the radial boundary conditions, applying a Coulomb potential instead, the angular solutions should not vary and this result should still be valid[33]. As, by making this substitution, no operator to the wavefunction now depends on the polar or azimuthal angles, θ and ϕ , the angular component of the wavefunction $Y(\theta, \phi)$ can be cancelled, leaving the equation only in $R(r)$. By letting $u = rR$, we obtain an equation of the form:

$$\frac{d^2u}{dr^2} + \left(\frac{Ze^2\rho}{2\pi\epsilon_0 r\hbar^2} - \frac{l(l+1)}{r^2}\right)u = -\frac{2\rho E}{\hbar^2}u. \quad (2.8)$$

We can simplify this equation by making the following substitutions:

$$\begin{aligned}
a &= \left(\frac{2\rho}{\hbar b a r^2} \right) \left(\frac{Z e^2}{4\pi\epsilon_0} \right), \\
b &= l(l+1), \\
\lambda^2 &= \frac{2\rho|E|}{\hbar^2},
\end{aligned} \tag{2.9}$$

with the $|E|$ substitution made in order to account for the necessarily negative energy of an electron in a bound atomic state. These substitutions produce:

$$\frac{d^2 u}{dr^2} + \left(\frac{a}{r} - \frac{b}{r^2} \right) u = \lambda^2 u. \tag{2.10}$$

In the limit of large r , the equation reduces to

$$\frac{d^2 u}{dr^2} = \lambda^2 u, \tag{2.11}$$

which has simple solutions of the form $\exp(\pm\lambda r)$, of which only the negative exponent is finite[33]. We can use this trial solution as a base for the full solution of the form:

$$u = L(r)e^{-\lambda r}, \tag{2.12}$$

where $L(r)$ is a polynomial of the form

$$L(r) = \sum_n c_n r^n. \tag{2.13}$$

The resultant form of the Schrödinger equation is[33]

$$L'' - 2\lambda L' + \left(\frac{a}{r} - \frac{b}{r^2} \right) L = 0, \tag{2.14}$$

where

$$\begin{aligned}
L'(r) &= \sum_n n c_n r^{n-1} \\
L''(r) &= \sum_n n(n-1) c_n r^{n-2}
\end{aligned} \tag{2.15}$$

which, on substitution, gives

$$\sum_n n(n-1)c_n r^{n-2} - 2\lambda \sum_n n c_n r^{n-1} + \left(\frac{a}{r} - \frac{b}{r^2}\right) \sum_n c_n r^n = 0. \quad (2.16)$$

For this equation to be satisfied, each power of r must cancel, which includes contributions from different terms in the sum. This results in a recurrence relation for each sum coefficient c_n :

$$c_{n+1} = \left(\frac{2n\lambda - a}{n(n+1) - b}\right) c_n. \quad (2.17)$$

This allows the hybrid polynomial series solution to be constructed. These polynomials are referred to as *Laguerre functions*[33], and they vary with the choice of n . These functions are known and define the radial component of the wavefunction. The angular component of the wavefunction is determined by the spherical harmonic functions. The energy of the radial state is obtained by the argument that, in order for the wavefunction to be finite, the sequence must terminate at some value of n . Therefore, at some value of n ,

$$2n\lambda = a, \quad (2.18)$$

or, by substituting the values of λ and a ,

$$2n\sqrt{\frac{2\rho|E|}{\hbar^2}} = \frac{2\rho}{\hbar^2} \frac{Ze^2}{4\pi\epsilon_0}. \quad (2.19)$$

By rearranging the equation for $|E|$, we obtain

$$|E| = \frac{Z^2 \rho e^4}{32n^2 \pi^2 \hbar^2 \epsilon_0^2}. \quad (2.20)$$

The two quantum numbers, n and l , determine the energy and angular momentum of the system and uniquely specify the atomic orbital states. These states are specified both by the quantum number n , and a letter corresponding the quantum number l , in the order s, p, d, f , of which there are a total number of 1, 3, 5, and 7 states respectively. [33]

2.1.2 Molecular Orbitals

The model detailed above describes atomic orbitals well in isolation, but when additional atoms are introduced, the interaction between them induces a change in the electronic wavefunctions. The first effect that is observed, as the atoms are brought closer together and begin to interact, is the formation of *hybrid orbitals*. Hybridisation occurs due to inter-atomic interactions causing degeneracy between the energies of the orbitals.

The exact shape of the resultant hybrid orbital depends on which orbitals contribute to its formation. For example, a carbon atom has 6 electrons, 4 of which lie in its valence shell. This means that the carbon atom has access to 4 orbitals: $2s$, $2p_x$, $2p_y$ and $2p_z$. Typically, 2 electrons lie in the $2s$ orbital, while the remaining 2 are distributed amongst the $2p$ orbitals. Depending on how many orbitals are degenerate, different hybrid orbitals can be formed. The notation for hybrid orbitals is of the form $2sp^{x-1}$ where x is the number of orbitals that have mixed. For example, carbon can form hybrid orbitals with 1 $2s$ orbital and 2 $2p$ orbitals, forming a $2sp^2$ orbital. The number of hybrid orbitals that are formed, as well as the number of nodes in the spatial distribution of the hybrid orbitals, is the same as the number of orbitals that go towards their formation; in the case of $2sp^2$, which is formed of 3 atomic orbitals, 3 hybrid orbitals are formed, and it is comprised of 3 nodes[3]. This process of forming hybrid orbitals can be seen in the case of ethane, ethene, and ethyne, which are formed from 2 carbon atoms and 2, 4, or 6 hydrogen atoms depending on what hybrid orbitals are formed. These orbitals are shown in Fig. 2.1, where in ethane, two $2sp^3$ orbitals are formed, in ethene, two $2sp^2$ hybrid orbitals and two unhybridised orbitals are formed, and in ethyne, two $2sp$ hybrid orbitals and four unhybridised orbitals are formed.

When atoms are brought closer still, their electrons can be shared between them, forming interatomic bonds. Once atoms are bound together, the spatial distribution of the electrons can no longer be considered to form the previously determined atomic orbitals; instead, they form the basis of *molecular orbitals*. The wavefunctions of these orbitals, can, to a first approximation, be represented using a linear combination of the atomic orbital wavefunctions.

$$\psi_{\pm} = c_1\Phi_a \pm c_2\Phi_b, \quad (2.21)$$

where Φ_a and Φ_b represent the wavefunctions of isolated atom a and b [3]. The two ways in which these wavefunctions can be formed, (+) and (-), arise from the constructive and destructive interference of the component wavefunctions. The (+) solution is referred to as a *bonding orbital*, in which the electron is located primarily between the two atoms

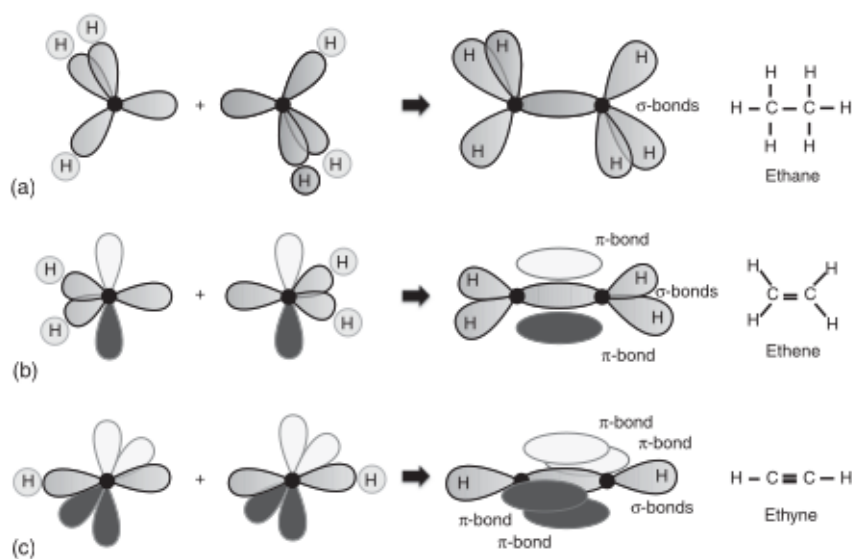


FIGURE 2.1: Schematic of hybrid orbitals formed from ethene, ethane, and ethyne, with the resultant molecular orbitals marked as π or σ orbitals. The hybrid orbital formed in ethene is $2sp^3$, in ethane it is $2sp^2$, and in ethyne it is $2sp$. Reproduced with permission from Köhler and Bässler [3], © 2015 Wiley-VCH Verlag GmbH & Co. KGaA, Boschstr. 12, 69469 Weinheim, Germany.

and is shared between them. The reverse is true of the $(-)$ solution, and it is referred to as an *anti-bonding* orbital. The resultant energy is also split going from the atomic states E_a and E_b to [3]

$$E_{\pm} = \frac{\alpha \pm \beta}{1 \pm S}. \quad (2.22)$$

The three quantities used in the above equation, S , α and β , all arise from interactions between the two atoms in a theoretical diatomic molecule. These quantities are [3]:

1. $S = \int \Phi_a \Phi_b dV$: The *overlap integral* between the two wavefunctions. This physically corresponds to how much the wavefunctions of the hybrid orbitals of each atom overlap with one another, which is determined both by the nature of the orbital as well as the closeness of the atomic nuclei
2. $\alpha = \int \Phi_a H \Phi_a dV$: The *Coulomb integral* of the bond. This is the interaction between an electron on one atom with the nucleus of the other atom.
3. $\beta = \int \Phi_a H \Phi_b dV$: The *resonance* or *exchange integral*. This quantity arises from the interaction between the overlap charge density between the two nuclei with one of the nuclei themselves [33], and it can be demonstrated that this is one of the biggest contributors to the resonance splitting of the mono-atomic energy levels.

The energetic splitting ΔE is determined by

$$\Delta E = E_+ - E_- = \frac{\alpha + \beta}{1 + S} - \frac{\alpha - \beta}{1 - S} = \frac{2\beta - 2\alpha S}{1 - S^2} \approx 2\beta \quad (2.23)$$

for a small overlap integral, and for identical atoms. If each atom has different state energies, and thus different values for α , for small S this energetic splitting instead becomes[3]

$$\Delta E \approx (\alpha_b - \alpha_a) + 2\beta \frac{\beta}{(\alpha_b - \alpha_a)}. \quad (2.24)$$

This demonstrates that in the case where the orbital energies of each atom are not equal to one another, the degree of splitting they experience depends both on the resonance interaction, and on the parameter $\alpha_b - \alpha_a$, that is, the difference in electron-nucleus interaction between the energy levels. Thus, the more different the energy levels, the smaller the splitting.

To move from the concept of molecular orbitals to the concept of molecular states, and thus transitions between those states and their relation to light, we must consider the energetic ordering of these states. [3]

2.1.3 HOMO and LUMO

As an example, we consider ethene, C_2H_4 . Each carbon in this molecule has two $1s$ orbitals, two $2p_z$ orbitals, and 3 hybrid $2sp^2$ orbitals. By considering the shape of these orbitals, and how their shape affects the parameters α , β and S , we can determine their relative energies.

The $1s$ orbitals are the lowest in energy as they have the lowest quantum number n . They lie close to the nucleus, and thus result in low resonance interactions with the other nucleus, and experience low splitting. The molecular orbitals that these atomic orbitals form are called σ -type orbital, and are centred around the inter-atomic axis[3].

The $2p_z$ and $2sp^2$ orbitals are similar to one another in energy, and as such their energetic ordering is determined almost entirely by the degree of their energetic splitting. Similar to the $1s$ orbital, the $2sp^2$ orbital is oriented along the inter-atomic axis. One lobe of this orbital points towards the carbon atom, while the remaining two point towards the hydrogen atoms. As such, this bond is also σ -type. Due to the large overlap between the charge distribution that results from this, there is large resonance integral and thus a high degree of energy splitting[3].

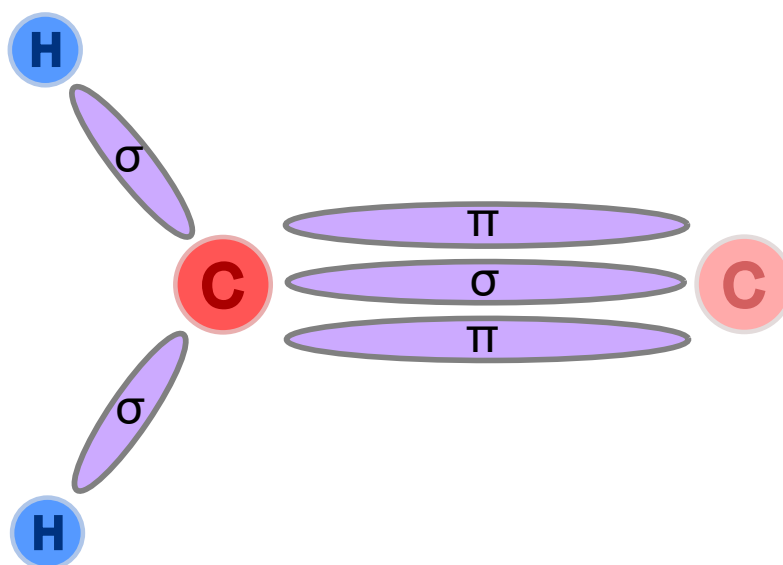


FIGURE 2.2: Structure of the molecular orbitals formed from one carbon atom in a molecule of ethene.

However, in the $2p_z$ orbital's case, the resultant molecular orbital lies apart from the inter-atomic axis, above and below it. As such, the charge overlap is low in these orbitals and thus the splitting is lower than for the $2sp^2$ orbitals. The structure of the hybrid orbitals formed from the orbitals of one of the carbon atoms in an ethene molecule is shown in Fig. 2.2.

Each pair of atomic orbitals is split into a *bonding* and *anti-bonding* molecular orbital. The anti-bonding orbital is relatively higher in energy; all energies in the consideration of electrons bound to a nucleus are by necessity negative relative to unbound electrons. Thus, the higher energy orbital is less bound than the lower energy, bonding orbital. The anti-bonding orbitals are marked with an * (σ_* , π_* etc.)[3]. The ordering of these molecular orbitals are shown in Fig. 2.3.

The electronic population fills these orbitals from the lowest, most bound energy up. There are 8 electrons involved in the bonding of the carbons in ethene - one from each hydrogen, two from the neighbouring carbon, and four from the carbon atom that we are considering. Thus, we have 8 total electrons to consider. Each orbital can sustain two electrons each, due to the Pauli exclusion principle. The 1s orbitals, both bonding and anti-bonding, are filled first, then the bonding π and σ orbitals from the $n = 2$ valence electrons. As such, the $n = 2$ π orbital is the final orbital to be filled. When

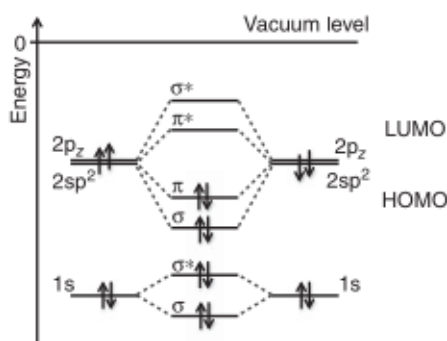


FIGURE 2.3: Ordering of molecular orbitals in ethene, showing the lowest to highest π and σ bonding and anti-bonding orbitals, omitting the orbitals formed with hydrogen. The 2π and $2\pi^*$ orbitals are marked as the Highest Occupied Molecular Orbital (HOMO) and Lowest Unoccupied Molecular Orbital (LUMO). Reproduced with permission from Köhler and Bässler [3], © 2015 Wiley-VCH Verlag GmbH & Co. KGaA, Boschstr. 12, 69469 Weinheim, Germany.

considering processes involving electrons: electron/hole injection, semiconductivity, and photoelectric processes, it is most important to consider both this, the Highest Occupied Molecular Orbital (HOMO), and the next orbital up, the Lowest Unoccupied Molecular Orbital (LUMO). These two orbitals, known as *frontier orbitals*, are important as they represent the smallest possible energy of light the molecule can absorb and the work function of an electrode seeking to donate an electron or hole. [3]

2.2 Molecular excited states

The description of molecular excited states from the perspective of orbitals is incomplete, partially due to molecular orbitals as described here being defined for single electron excited states. They do not take into account inter-electron interactions, in which case the molecular excited states are better approximated by superpositions of electronic configurations, in a manner known as the *configuration interaction*. For example, the first excited state of a molecule can be formed from a weighted sum of configurations defined by filled orbitals up to the HOMO, and an additional pair of electrons in configurations $c_1[HOMO, LUMO] + c_2[HOMO, LUMO + 1] + \dots$. Furthermore, a full description of the states of a molecule must necessarily include a contribution from the electron's spin. [3]

2.2.1 Spin-defined excited states - Singlets and Triplets

Due to the Pauli exclusion principle, which states that no two leptons can occupy the same overall state, each molecular orbital can hold only two electrons, and each must

have opposite spin states. This means that in the case of a filled HOMO, with every orbital below it also filled, the net electronic spin of the molecule is zero. However, once an electron is excited into an unoccupied orbital (LUMO, LUMO+1 etc.), the net spin of the molecule can be non-zero, as the spin of the excited and unexcited electrons need not remain the same. While spin conservation must be maintained, there are processes that can permit the generation of spin-1 excited states, and will be discussed in Sections 2.3.5.3 and 2.3.6. [3]

In considering the spin states of an excited electron (1) and the remaining unpaired un-excited electron (2), under the condition that there is no interaction between the two states, their wavefunctions can be simply stated:

1. $\uparrow_1\uparrow_2$
2. $\uparrow_1\downarrow_2$
3. $\downarrow_1\uparrow_2$
4. $\downarrow_1\downarrow_2$,

where \uparrow and \downarrow are the spin eigenfunctions of the net spin (and \hat{z} component) operators of an uncoupled, individual electron[3]. The net spin of each electrons is of magnitude $1/2$, and their spin magnetic quantum number $m_s = \pm 1/2$. However, these simple spin wavefunctions are only eigenfunctions of the system when the electrons are uninteracting and uncoupled. Many organic molecules have donor and acceptor sites (where the electrons migrate from and to when excited) which are quite close to one another, resulting in coupled electrons in the excited state, and the above states not well describing the system.

We can begin constructing the eigenstates of this system by considering the possible permutations the net spin can take; the total spin can take values of 0, for anti-symmetric spin, or 1, for symmetric spin alignment. In the first case, the magnetic spin quantum number m_S can only equal 0, whereas in the second case, it can take values $m_S = -1, 0, 1$, resulting in 4 total states. Beginning with the extremal cases, we note there is only one way each to construct a state of total spin $S = 1, m_s = \pm 1$ using the states specified above, so we can begin by defining states of $|S, m_s\rangle$ [33]

1. $|1, +1\rangle = \uparrow_1\uparrow_2$
2. $|1, -1\rangle = \downarrow_1\downarrow_2$,

i.e. states 1. and 4. from the uncoupled electron picture. We may find the eigenstate which corresponds to the final spin-1 state, $|1, 0\rangle$, by applying the total spin-down operator to the first term, defined as[33]

$$\hat{S}_{\pm}|S, m_S\rangle = c_{\pm}(S, m_S)\hbar|s, m_s \pm 1\rangle \quad (2.25)$$

with

$$c_{\pm}(S, m_S) = \sqrt{S(S+1) - m_S(m_S \pm 1)}. \quad (2.26)$$

We can apply this operator to the states we've already defined, as[33]

$$S_-|1, 1\rangle = c_-(1, 1)\hbar|1, 0\rangle \quad (2.27)$$

$$= \hbar\sqrt{2}|1, 0\rangle. \quad (2.28)$$

This operation can be equivalently written using the spin operators of the individual electrons, $\hat{s}_{1-}, \hat{s}_{2-}$, which are well defined by the following relations[33]

$$\hat{s}_+|\uparrow\rangle = 0 \quad (2.29)$$

$$\hat{s}_-|\downarrow\rangle = 0 \quad (2.30)$$

$$\hat{s}_+|\downarrow\rangle = \hbar|\uparrow\rangle \quad (2.31)$$

$$\hat{s}_-|\uparrow\rangle = \hbar|\downarrow\rangle. \quad (2.32)$$

Applying these operation to the state $|1, 1\rangle$, we can derive an expression for the state $|1, 0\rangle$ [33].

$$\hat{S}_-|1, 1\rangle = (\hat{s}_{1-} + \hat{s}_{2-})|1, 1\rangle \quad (2.33)$$

$$= (\hat{s}_{1-} + \hat{s}_{2-})|\uparrow_1\rangle|\uparrow_2\rangle \quad (2.34)$$

$$= \hat{s}_{1-}|\uparrow_1\rangle|\uparrow_2\rangle + |\uparrow_1\rangle\hat{s}_{2-}|\uparrow_2\rangle \quad (2.35)$$

$$= \hbar|\downarrow_1\rangle|\uparrow_2\rangle + \hbar|\uparrow_1\rangle|\downarrow_2\rangle \quad (2.36)$$

Therefore, we can compare the two expressions for $\hat{S}_-|1, 1\rangle$ to one another, and obtain an expression for the $|1, 0\rangle$ state in terms of the individual electron spin wavefunctions[33]:

$$|1, 0\rangle = \frac{1}{\sqrt{2}}(|\downarrow_1\rangle|\uparrow_2\rangle + |\uparrow_1\rangle|\downarrow_2\rangle) \quad (2.37)$$

The remaining coupled electron state is one which has a net spin of $S = 0$ and a magnetic spin quantum number of $m_S = 0$. To find the expression for this state, we can exploit two properties of this system. The first is that in order to construct a state of net spin 0, we must necessarily use a combination of $|\uparrow_1\rangle|\downarrow_2\rangle$ and $|\downarrow_1\rangle|\uparrow_2\rangle$, similar to the construction of the $|1, 0\rangle$ state. The second is that as the set of states $|0, 0\rangle, |1, -1\rangle, |1, 0\rangle, |1, 1\rangle$ are a complete set of eigenfunctions (which are real due to the Hermiticity of the \hat{S}^2 operator) of the system of coupled electrons, the $|0, 0\rangle$ state must be orthogonal to the $|1, 0\rangle$ state. Due to this, we can simply infer that[33]

$$|0, 0\rangle = \frac{1}{\sqrt{2}}(|\uparrow_1\rangle|\downarrow_2\rangle - |\downarrow_1\rangle|\uparrow_2\rangle) \quad (2.38)$$

Thus, we have defined the full orthonormal basis set of the coupled electron pair state, in the presence of an external $\hat{\mathbf{z}}$ oriented magnetic field. The states defined by this process are referred to as the *singlet* state, for the spin-0 eigenstate, and *triplet* states, for the spin-1 eigenstates, as there is one state with spin $S = 0$ ($|0, 0\rangle$) and three states with spin $S = 1$ ($|1, -1\rangle, |1, 0\rangle, |1, 1\rangle$).[33]

This set of eigenstates is only valid in the presence of an external magnetic field. Another example of a set of eigenvectors that can describe the electronic excited state is one that is valid without an external applied magnetic field[3, 34]:

$$\Psi_{Tx} = \frac{1}{\sqrt{2}}(|\downarrow_1\rangle|\downarrow_2\rangle + |\uparrow_1\rangle|\uparrow_2\rangle) \quad (2.39)$$

$$\Psi_{Tz} = \frac{1}{\sqrt{2}}(|\uparrow_1\rangle|\downarrow_2\rangle + |\downarrow_1\rangle|\uparrow_2\rangle) \quad (2.40)$$

$$\Psi_{Ty} = \frac{i}{\sqrt{2}}(|\downarrow_1\rangle|\downarrow_2\rangle + |\uparrow_1\rangle|\uparrow_2\rangle) \quad (2.41)$$

$$\Psi_S = \frac{1}{\sqrt{2}}(|\uparrow_1\rangle|\downarrow_2\rangle - |\downarrow_1\rangle|\uparrow_2\rangle) \quad (2.42)$$

It is worthy of note that the S and T_z eigenvectors are the same as the $|00\rangle$ and $|1, 0\rangle$ eigenvectors from the model with an applied magnetic field.

In terms of the energies of the triplets and singlets, triplets are reduced in energy compared to their singlet counterpart by the *exchange energy* due to the inter-electron spin interaction. This energy is equal to twice the value of the exchange integral β , and thus can be approximately described with reference to the degree of electronic orbital overlap between two electrons that compose the triplet. On organic molecules, where the donor and acceptor sites often are close together, this exchange interaction can be high. Typical values can vary between 0.2 eV for small overlap, to ~ 1 eV for closely located donor and acceptor sites.[3]

2.2.2 Triplet magnetic field effects

As the molecular triplet excited state has a net spin, it has a net spin magnetic moment. As such, while each triplet sub-level is approximately degenerate (though not exactly, as shall be discussed in Section 2.2.2.1), their degeneracy can be split using an applied magnetic field, due to an effect called the *Zeeman effect*[35], which is used in a range of spectroscopic techniques to identify triplet species. The energy splitting from an applied magnetic field can be found by starting from the expression with the spin magnetic dipole moment

$$\bar{\mu}_S = -\frac{g_S\mu_b}{\hbar}\mathbf{S} \quad (2.43)$$

where μ_b is the Bohr magneton, g_S is the spin g-factor, and \mathbf{S} is the spin angular momentum $|\mathbf{S}| = \hbar\sqrt{S(S+1)}$ [35]. A similar expression exists for the orbital angular momentum, which also contributes to the net magnetic moment possessed by the triplets[35].

$$\bar{\mu} = \bar{\mu}_s + \bar{\mu}_l \quad (2.44)$$

$$= -\frac{g_S\mu_b}{\hbar}\left(\sum_k \mathbf{S}_k\right) - \frac{g_L\mu_b}{\hbar}\left(\sum_k \mathbf{L}_k\right) \quad (2.45)$$

the index k corresponds to the electrons in the system to be considered, in the atom, molecule, or chromophore site. The weighting of these factors to the total sum is determined by the g-factor of each of the spin or angular momentum (g_s and g_l). While these are not integers, their values are very close to $g_s = 2$ and $g_l = 1$. Due to the difference between these factors, the magnetic moment μ cannot be simply related to the total angular momentum J .

To elucidate this relation, we consider the case of a magnetic field B applied along the $\hat{\mathbf{z}}$ axis. The resultant energetic splitting will be equal to[35]

$$\Delta E = -\bar{\mu}_J \cdot \mathbf{B} \quad (2.46)$$

$$= -\mu_{\hat{\mathbf{z}}} B \quad (2.47)$$

To find this, we need to find the component of the magnetic moment which is oriented along \mathbf{J} , which is given by

$$\bar{\mu}_J = |\bar{\mu}| \frac{\bar{\mu} \cdot \mathbf{J}}{|\bar{\mu}| |\mathbf{J}|} \hat{\mathbf{J}} \quad (2.48)$$

$$= \frac{\mu_b}{\hbar} \frac{(\mathbf{L} + 2\mathbf{S}) \cdot (\mathbf{L} + \mathbf{S})}{|\mathbf{J}|}. \quad (2.49)$$

The component of $\bar{\mu}_J$ in the direction of $\hat{\mathbf{B}}$ is given by[35]

$$\mu_{\hat{\mathbf{z}}} = |\bar{\mu}_J| \frac{\mathbf{J} \cdot \mathbf{B}}{|\mathbf{J}| |\mathbf{B}|}. \quad (2.50)$$

As the magnitude of B lies only in the $\hat{\mathbf{z}}$, this allows this equation to be reduced to[35]

$$\mu_{\hat{\mathbf{z}}} = |\bar{\mu}_J| \frac{J_z}{|\mathbf{J}|} \quad (2.51)$$

$$= \frac{\mu_b}{\hbar} \frac{(\mathbf{L} + 2\mathbf{S}) \cdot (\mathbf{L} + \mathbf{S}) J_z}{|\mathbf{J}|^2}. \quad (2.52)$$

By expanding the expression for $(\mathbf{J} \cdot \mathbf{J}) = (\mathbf{L} + \mathbf{S}) \cdot (\mathbf{L} + \mathbf{S})$, we can obtain an expression for[35]

$$\mathbf{L} \cdot \mathbf{S} = \frac{1}{2}(\mathbf{J} \cdot \mathbf{J} - \mathbf{L} \cdot \mathbf{L} - \mathbf{S} \cdot \mathbf{S}) \quad (2.53)$$

Thus, we can similarly expand the numerator $(\mathbf{L} + 2\mathbf{S}) \cdot (\mathbf{L} + \mathbf{S})$ and substitute the resultant equation for $\mu_{\hat{\mathbf{z}}}$ into the equation for the energetic splitting

$$\Delta E = \frac{\mu_b B J_z}{2\hbar |\mathbf{J}|^2} (3|\mathbf{J}|^2 + |\mathbf{S}|^2 - |\mathbf{L}|^2). \quad (2.54)$$

This can be expanded further as each spin component $|\mathbf{X}|^2$ has a definite definition of $|\mathbf{X}|^2 = \hbar^2 x(x+1)$ where x is the relevant quantum number of the variable and $J_z = m_j \hbar$ by definition[35]. This gives the final expression for the energy level splitting of the triplet due to the applied magnetic field

$$\Delta E = \mu_b B m_j \underbrace{\left(1 + \frac{j(j+1) + s(s+1) - l(l+1)}{2j(j+1)} \right)}_{\text{Landé factor}} \quad (2.55)$$

$$= \mu_b g_{\text{Landé}} B m_j \quad (2.56)$$

This value gives the amount by which each energy of the triplet sub-levels are changed by the Zeeman effect. The $|1, 0\rangle$ triplet state, however, has a total spin magnetic moment $m_j = 0$, resulting in a net 0 change in energy.[33–35]

2.2.2.1 Zero field splitting

Even in the absence of an applied magnetic field, however, the triplet energy levels are not exactly degenerate. This is because the electrons that form the triplet themselves possess a magnetic dipole moment that can interact with the other, and thus lift the degeneracy the triplet states[34]. The Hamiltonian for this interaction is

$$\hat{H}_{\text{dipole-dipole}} = \frac{\mu_0 \mu_b^2 g_s^2}{4\pi \hbar^2} \left[\frac{\hat{s}_1 \hat{s}_2}{|\mathbf{r}_{ee}^2|} - \frac{(3\hat{s}_1 \mathbf{r}_{ee})(\hat{s}_2 \mathbf{r}_{ee})}{|\mathbf{r}_{ee}^5|} \right], \quad (2.57)$$

where \mathbf{r}_{ee} is the inter-electronic displacement vector and g_s is the spin g factor. By converting from the spin operators of the individual electrons (\hat{s}_1, \hat{s}_2) to the total spin operator \hat{S} we obtain[34]

$$\hat{H}_{\text{dipole-dipole}}^{\text{spin}} = \frac{D}{\hbar^2} (\hat{S}_z^2 - \frac{1}{3} \hat{\mathbf{S}}^2) + \frac{E}{\hbar^2} (\hat{S}_x^2 - \hat{S}_y^2) \quad (2.58)$$

The parameters D and E here are called the *fine structure constants*, and determine the magnitude of the zero-field splitting. The resultant energetic splittings are

$$|T_x\rangle = D - E \quad (2.59)$$

$$|T_y\rangle = D + E \quad (2.60)$$

$$|T_z\rangle = 0 \quad (2.61)$$

thus lifting the degeneracy of the triplets with zero applied magnetic field.[34]

2.2.3 Excitons and Excimers - delocalised excitations

In the solid phase, adjacent molecules in an amorphous or crystalline state interact with one another in a number of ways, due to dipole-dipole interactions and the van-der-Waals effect. Considering the simplest case of two interacting molecules, their Hamiltonian can simply be represented by the sum of their individual Hamiltonians and a dipolar interaction term (neglecting vibrations and spin)[3]

$$H_{tot} = H_1 + H_2 + V_{12} \quad (2.62)$$

The ground state wavefunction of the two molecules can be similarly simply represented by the product of the two individual wavefunctions $\psi_1\psi_2$. This gives the energy of the ground state of the two-molecule system as[3]

$$E_g = \langle \psi_1\psi_2 | H_1 + H_2 + V_{12} | \psi_1\psi_2 \rangle = E_1 + E_2 + D; \quad (2.63)$$

$$D = \langle \psi_1\psi_2 | V_{12} | \psi_1\psi_2 \rangle \quad (2.64)$$

where D is a negative van-der-Waals energy interaction term, called the *gas-to-crystal shift* term. This term reduces the ground-state energy of the interacting molecules below a gas or liquid phase transition, attracting them to one another and allowing the material to remain in the solid or liquid state.

In the excited state, the molecules are no longer indistinguishable due to the presence of the excitation, the permutation of which amongst the two molecules is important. The resultant coupling between the two possible excited states leads to a splitting between two coupled *Dimer* states, which for identical molecules leads to[3]

$$\psi_{E\pm} = \frac{1}{\sqrt{2}}(\psi_1^*\psi_2 \pm \psi_1\psi_2^*) \quad (2.65)$$

$$E_{\pm} = E_1^* + E_2 + D' \pm \beta \quad (2.66)$$

in which D' is the gas-to-crystal shift term for the excited state state and β denotes the excited state resonance interaction. The observed result of this is to cause multiple

transition peaks in the absorption spectrum, and to cause a red shift to the emission spectrum, as the splitting results in emission from the lower split state. These shifts result from both the adjusted ground state as well as the adjusted excited state energies[3]:

$$\Delta E_{total} = \Delta E_1 + \Delta D \pm \beta \quad (2.67)$$

$$\Delta E_1 = E_1^* - E_1 \quad (2.68)$$

$$\Delta D = D - D' \quad (2.69)$$

Depending on the strength of the resonance interaction β , the behaviour of the excited state molecules can be significantly effected, which at higher values results in aggregation and a reduced vibrational coupling. This picture can be expanded to a crystalline model, by considering contributions from a larger number of molecules N , in a one-dimensional nearest neighbour model. This is represented via the Hamiltonian[3]

$$H = \sum_{i=1}^N H_i + \frac{1}{2} \sum_{i,j=1;i \neq j}^N V_{ij} \quad (2.70)$$

the ground and excited state wavefunctions

$$\psi_{GS} = \prod_{i=0}^N \psi_i^0 \quad (2.71)$$

$$\psi_E = \frac{1}{\sqrt{N}} \sum_{j=1}^N e^{ika} \psi_E^j; \quad \psi_E^j = \psi_j^* \sum_{i,j=1;i \neq j}^{N-1} \psi_i^0 \quad (2.72)$$

$$k = 0, \pm \frac{2\pi}{Na}, \pm \frac{4\pi}{Na}, \dots, \pm \frac{\pi}{a} \quad (2.73)$$

and energies

$$E_{GS} = \sum_{i=1}^N E_i^0 + D; \quad D = \langle \psi_{GS} | \frac{1}{2} \sum_{i,j=1;i \neq j}^N V_{ij} | \psi_{GS} \rangle \quad (2.74)$$

$$E_E(k) = \sum_{i,j=1;i \neq j}^N E_i^0 + E_j^* + D' + 2\beta \cos(ka); \quad D' = \langle \psi_E^j | \frac{1}{2} \sum_{i,j=1;i \neq j}^N V_{ij} | \psi_E^j \rangle \quad (2.75)$$

$$\beta = \langle \psi_E^i | \frac{1}{2} \sum_{i,j=1;i \neq j}^N V_{ij} | \psi_E^j \rangle \quad (2.76)$$

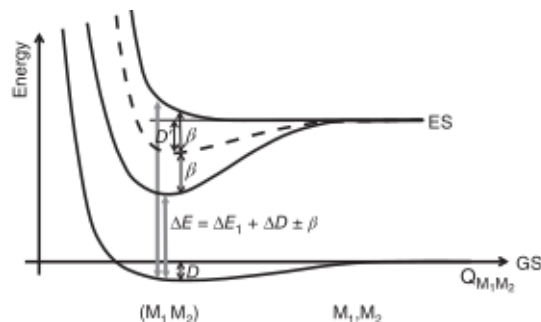


FIGURE 2.4: Splitting of the potential energy surface of the excited state due to intermolecular electronic coupling, showing how the D and β factors mediate the split energy levels, as well as how this splitting varies with the generalised intermolecular separation coordinate Q . Reproduced with permission from Köhler and Bäessler [3], © 2015 Wiley-VCH Verlag GmbH & Co. KGaA, Boschstr. 12, 69469 Weinheim, Germany.

These expressions represent an expansion of the intermolecular dipolar van-der-Waals interactions from the two-molecule picture into a nearest-neighbour representation of many molecules. The Hamiltonian is the sum of all individual Hamiltonians combined with the sum of all nearest-neighbour intermolecular interaction matrix elements, not including diagonal elements between the same molecules. The ground state wavefunctions are represented by a product of the individual ground state wavefunctions ψ_i^0 , combined with an antisymmetrisation operator \mathbb{A} which accounts for the necessary inclusion of the Pauli exclusion principle into the operator.

The excited state wavefunction is formed by considering a sum of each configuration of one excited and $N - 1$ unexcited molecules, each configuration of which is summarised in ψ_E^j . The total energies resulting from each of these configurations can be considered similarly to the dimer picture. The unaltered energies E^0 and E^* in the ground and excited states are combined with the gas-to-crystal shifts of the ground (D) and excited states (D') arising from the modified potential interaction between the modified wavefunctions, as well as the resonance interaction between the excited and unexcited molecules β . The primary difference in this picture is the phase component introduced by the $2 \cos(ka)$ term, in which a is the nearest neighbour spacing distance, and k is the wavevector of this delocalised quasi-particle.

The meaning of this result is that the excited state energy levels are split into a band of N states with energies modulated by the resonance interaction term (the maximum energy splitting is equal to 4β), in addition to the quantisation parameter k , which limits what wavelengths of light can excite the crystal by the relation $|k| = 2\pi/\lambda_{ph}$. This splitting is illustrated in Fig. 2.4. These states are spatially delocalised over multiple molecules, and are called *Frenkel Excitons*. The parameter β denotes by how much the crystalline lattice becomes deformed by the presence of the excitation[3].

2.2.3.1 Aggregates and changing transition dipole moments

The transition dipole moments of molecules for transitions in a solid state are altered by interactions between adjacent molecules. The transition dipole moment is a measure of the strength of coupling between two electronic states via an intermediate coupling to an electromagnetic field. Giving the dipole moments of between the ground and excited states of the isolated molecules as[3]

$$\bar{\mu}_1 = \langle \psi_1 | e\hat{\mathbf{r}} | \psi_1^* \rangle \quad (2.77)$$

$$\bar{\mu}_2 = \langle \psi_2 | e\hat{\mathbf{r}} | \psi_2^* \rangle \quad (2.78)$$

In the dimer picture, using the terms for ψ_G and $\psi_{E\pm}$

$$\bar{\mu}_{\pm} = \langle \psi_G | e\hat{\mathbf{r}} | \psi_{E\pm} \rangle \quad (2.79)$$

$$= \frac{1}{\sqrt{2}} \langle \psi_1 \psi_2 | e\hat{\mathbf{r}} | (\psi_1^* \psi_2 \pm \psi_1 \psi_2^*) \rangle \quad (2.80)$$

$$= \frac{1}{\sqrt{2}} (\langle \psi_1 \psi_2 | e\hat{\mathbf{r}} | \psi_1^* \psi_2 \rangle \pm \langle \psi_1 \psi_2 | e\hat{\mathbf{r}} | \psi_1 \psi_2^* \rangle) \quad (2.81)$$

$$= \frac{1}{\sqrt{2}} (\bar{\mu}_1 \pm \bar{\mu}_2) \quad (2.82)$$

This shows that the coupling strength as measured by the dipole moment between the two states of the combined 2-molecule system (shown in Fig. 2.4) are based on a vector sum/difference between the moments of the individual molecules. The vector sum results in 2 types of interaction, as the dipole moment is oriented along the length of the molecule[3]:

1. H-type interaction: When the molecules are oriented side-to-side, the dipole moments will be oriented in the same direction, and the moment corresponding to the lower energy state E_- , $\hat{\mu}_-$, is reduced to 0, whereas the higher energy state E_+ has an effective moment of 2μ with $|\hat{\mu}_1| = |\hat{\mu}_2| = \mu$. This results in a blue shifted absorption, as the higher energy absorption has a stronger electronic coupling to the excited state, but as the lower state E_- will rapidly become populated from non-radiative decay, the aggregated state will not be emissive.
2. J-type interaction: When the molecules are oriented head-to-head, the dipole moments will be oriented in opposite directions. Thus, the lower energy state E_- will

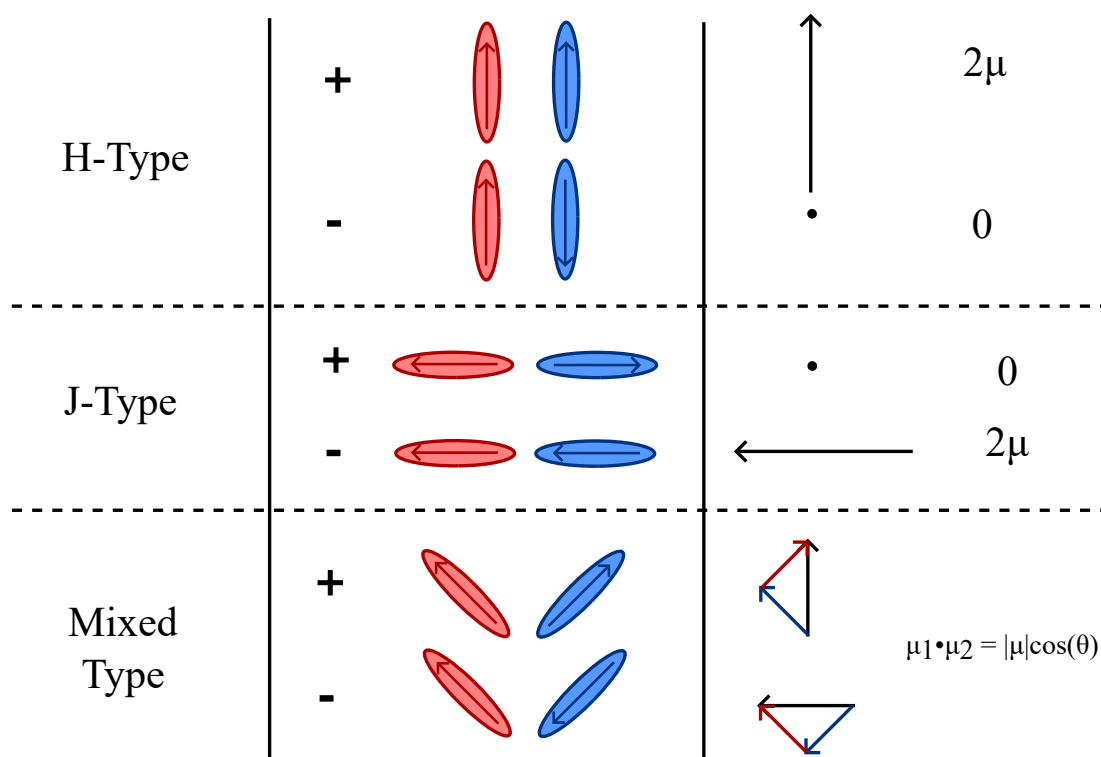


FIGURE 2.5: General geometry and resultant transition dipole moment of molecular aggregates

have a dipole moment of 2μ and the higher state E_+ has a moment of 0. This results in a red-shifted absorption to the lower energy state, and a correspondingly red-shifted strong emission from the same state.

Typically, a mix of two interactions will contribute towards the overall aggregate character of a molecular system in the solid state, and both must be accounted for when considering solid state absorption and emission spectra[3]. These interactions are schematically represented in Fig. 2.5.

2.3 Molecular dynamics

Adiabaticity, in general, describes a system in which energy is not transferred to a background environment or *bath*, typically referring to heat in a thermodynamic system. However, in the context of molecular dynamics, *adiabaticity* refers to a particular set of approximations.

2.3.1 The Adiabatic approximation

In the general form of the Schrödinger equation for a molecule, both the electrons and nuclei of the molecule need to be accounted for, resulting in the following[36–39]:

$$\hat{H}\psi_\alpha(\mathbf{r}_e, \mathbf{R}) = E_\alpha\psi_\alpha(\mathbf{r}_e, \mathbf{R}), \quad (2.83)$$

wherein \hat{H} is the Hamiltonian operator, $\mathbf{r}_{e,n}$ are the positions of the electrons and nuclei, respectively, and α indicates the dependence of the wavefunction ψ on the various quantum numbers, which will be derived more fully in later sections.

The Hamiltonian \hat{H} can be written in terms of the nuclear and electronic kinetic energy \hat{T}_n, \hat{T}_e , as well as the interactions between the nuclei, V_{nn} , the interactions between the electrons V_{ee} , and the interaction between the nuclei and the electrons V_{en} .

$$\hat{H} = \overbrace{(\hat{T}_n + V_{nn})}^{\hat{H}_n} + \overbrace{(\hat{T}_e + V_{ee} + V_{en})}^{\hat{H}_e}. \quad (2.84)$$

The adiabatic approximation is based on the assumption that the nuclei are far heavier than the electrons. This means that the positions of the nuclei are unchanging or slowly varying compared to those of the electrons due to their inertia, and that variations in the electronic positions \mathbf{r}_e have only a small, negligible impact on the nuclear positions \mathbf{R} .

This assumption is represented by the choice of solution of the general form[36, 39]:

$$\psi_\alpha(\mathbf{r}_e, \mathbf{R}) = \sum_j \chi_{\alpha j}(\mathbf{R})\Phi_j(\mathbf{r}_e, \mathbf{R}), \quad (2.85)$$

where the set of states Φ_j are orthogonal.

Inserting this trial equation into the Schrödinger equation above, and by expanding the nuclear terms and eliminating the electronic variables we obtain[36, 39]

$$\langle \Phi_k | \hat{H} | \Phi_j \rangle = \hat{T}_n \chi_{\alpha k} + \sum_j (U_{kj} + W_{kj}) \chi_{\alpha j} = E_\alpha \chi_{\alpha j}, \quad (2.86)$$

where

$$U_{kj}(\mathbf{R}) = \langle \Phi_k | \hat{H}_e | \Phi_j \rangle_e + V_{nn} \delta_{kj}(\mathbf{R}), \quad (2.87)$$

and represents a multidimensional potential energy hypersurface of dimensionality $3N$, where N is the number of nuclei in the system.

$$W_{kj} = \langle \Phi_k | [\hat{T}_n; \Phi_j] \rangle, \quad (2.88)$$

where $[\hat{T}_n; \Phi_j]$ is the commutation operator of \hat{T}_n and Φ_j . This variable is the vibronic coupling operator between electronic states k and j , a matrix which captures the interrelation between the vibrational motion of the nuclei and the energies of the electronic states. As the set of electronic wavefunctions $\Phi_j(\mathbf{r}_e, \mathbf{R})$ are orthogonal, we can choose them to be an infinite set of eigenfunctions of the electronic Hamiltonian \hat{H}_e .

This equation can be simplified further by considering two further approximations[39]: the *clamped nuclei approximation* and the *adiabatic approximation*. The former consists of ignoring the vibronic coupling term, setting $W_{jk} = 0$ in all cases. This corresponds to setting the positions of the nuclei as fixed parameters. Alternatively, the adiabatic approximation refers to considering only the diagonal elements of the vibronic coupling matrix W_{jj} . Physically, this means either holding that the nuclei do not move at all, in the former case, or that they move very slowly compared to the motion of the electrons and thus that no inter-state transfer can take place by perturbations induced by nuclear motion.

A benefit of this approximation is that we can expand the equation for the the potential energy hypersurface, using the eigenvalue property wherein $\langle \Phi_k | \hat{H}_e | \Phi_j \rangle_e = 0$ if $j \neq k$ [39].

$$U_{kj}(\mathbf{R}) = U_j(\mathbf{R})\delta_{kj}, \quad (2.89)$$

where

$$U_j(\mathbf{R}) = E_{ej}(\mathbf{R}) + V_{nn}(\mathbf{R}). \quad (2.90)$$

This allows the potential energy hypersurface to be defined without regard to the positions of the electrons \mathbf{r}_e . This approximation will be assumed throughout this paper, except when specified otherwise, and significantly reduces computational and theoretical complexity.

2.3.2 The adiabatic potential energy surface

Here we have defined $U_{kj}(\mathbf{R})$ as the multidimensional potential energy surface. More fully, this is a hypersurface with N dimensions, where N is the number of degrees of freedom possessed by the molecule. We have defined $U_{kj}(\mathbf{R})$ such that the potential

in which the nuclei and electrons move is independent on the position of the electrons, depending instead on the nuclei alone. The core assumptions that must be made to generate this surface are summarised below[40]:

1. The electrons move sufficiently faster than the nuclei, due to their lower mass, for the nuclei to be considered stationary.
2. The electronic energy eigenvalue, E_n^{el} , obeys the equation

$$\hat{H}^{el}(r_e, R)\psi_n^{el}(r_e, R) = E_n^{el}(R)\psi_n^{el}(r_e, R) \quad (2.91)$$

in which \hat{H}^{el} is the electronic Hamiltonian operator, ψ_n^{el} is the electronic wavefunction, n is the state quantum number, and r_e, R are as they have been defined previously. This means that the energy of an electron in a specific state is dependent only on the positions of the nuclei.

3. The potential energy surface is calculated by finding this eigenvalue over a range of R , and describes how the energy levels change with nuclear displacement.

When two of these potential surfaces are close to one another, i.e. when the energy eigenvalues of two states become close to degenerate for a particular combination of nuclear coordinates Q_n , there are two cases which can occur. The first is the case of an avoided crossing. Defining a single coordinate over which this nucleus takes place, Q_κ , Nohira and Nohira [41] define that these avoided crossings occur when[40]

$$\Delta Q_\kappa \gg \frac{h}{2\epsilon} \frac{dQ_\kappa}{dt}. \quad (2.92)$$

Here, ϵ denotes the splitting parameter of the crossing, which determines by how much the crossing is avoided; the two energy surfaces will be separated by 2ϵ . This means that, when ϵ is sufficiently large, i.e. the surfaces are far enough apart, compared to the nuclear velocity $\frac{dQ_\kappa}{dt}$, an avoided crossing will occur, and a transition between the two states will require a non-adiabatic transition, such as emission. In the opposite case, however, when[40]

$$\Delta Q_\kappa \ll \frac{h}{2\epsilon} \frac{dQ_\kappa}{dt}, \quad (2.93)$$

Then an avoided crossing does not occur, and with the right combinations of Q_n , the eigenvalues can be degenerate. This is called a non-avoided crossing, a diabatic transition, or, when this intersection occurs about a point, a conical intersection.

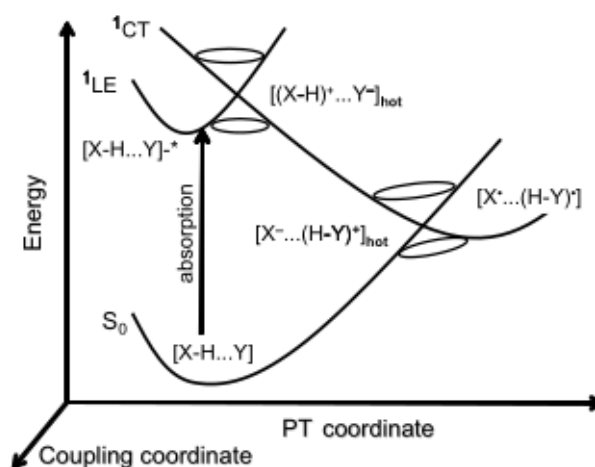


FIGURE 2.6: Generalised schematic representation of the rapid non-radiative decay pathway to the ground state S_0 from a locally excited (0LE) state via a pair of conical intersections with a charge transfer state potential energy surface, enabled via an electron driven proton transfer process. Reproduced with permission from Sobolewski and Domcke [4]

2.3.3 Conical Intersections and their properties

Conical intersections, despite the prevalence of the adiabatic approximation for treating potential energy surfaces, are found surprisingly commonly[42]. In fact, for certain nuclear coordinate configurations, such an intersection will exist in poly-atomic molecules with greater than two atoms. If the sign of a potential energy hypersurface changes when transported around a loop in the nuclear coordinate configuration space, then an intersection between two hypersurfaces of opposite symmetry will be found within the loop. [43]

It is surprising, however, due to the fact that for states with the same symmetry, the Pauli exclusion principle means the points of lowest energy will be where the potential surfaces are not degenerate; two states of like symmetry will repel one another to avoid degeneracy. [44]. This is called the *Jahn-Teller effect*, and states that for any symmetric molecule, at a conical intersection there will be some molecular normal coordinate Q where the gradient of the surface is negative, leading to a point on the surface of lower energy. This results in these intersections being less energetically accessible. However, this can be resolved in many ways, from symmetry breaking mechanisms such as proton transfer, to vibronic coupling between modes lifting degeneracy in different ways, or in molecules with lower symmetry (in which this problem will not arise) or in molecules with higher symmetry (in which degeneracies between three states are possible[45]).

At a conical intersection, decay between two states can proceed diabatically, proceeding from one electronic state to another without the need to emit energy via radiative or

vibration mediated coupling. The lack of this mediating mechanism means that these decays can proceed far faster than otherwise, leading to decays occurring over timescales ≤ 100 fs[46]. A schematic representation of a typical charge-transfer mediated conical intersection pathway is shown in Fig. 2.6.

2.3.4 Radiative transitions - Absorption and Emission

By the assumptions of the adiabatic approximation, transitions between electronic levels do not occur. The model can be adapted via introducing the dipole operator, $e\hat{\mathbf{r}}$, as a perturbative operator to the wavefunction of the initial state i , resulting in a transitive rate k_{if} by Fermi's golden rule[3]

$$k_{if} = \frac{2\pi\rho_f}{\hbar} |\langle\psi_f|e\hat{\mathbf{r}}|\psi_i\rangle|^2, \quad (2.94)$$

where ρ_f is the density of states of the final state f . The wavefunctions can be considered, by the adiabatic approximation, as products of the electronic, the spin, and the vibrational components of the wavefunctions[3]:

$$\psi_{total} = \psi_{el}(\mathbf{r}, \mathbf{R})\psi_{spin}(\uparrow, \downarrow)\psi_{vib}(\mathbf{R}), \quad (2.95)$$

where, also by the adiabatic approximation, we have said that the nuclear vibrations depend only on the nuclear positions and not on the electronic distribution. As only the electronic component ψ_{el} has a dependence on the electronic distribution $\hat{\mathbf{r}}$, the dipole operator operates only on this component. This physically represents that the more similar the electronic distributions in the initial and final states of a transition are, the easier and more rapid the transition will be.

In multi-atomic molecules, the nuclei vibrate as coupled oscillators, and we can replace the coordinate \mathbf{R} in the wavefunction of the nuclear with the normal nuclear coordinates Q_i which describe the set of nuclear normal modes. By taking slices along a given normal coordinate on the potential energy hypersurface, we can describe a 2D potential energy surface. The nuclei are considered to vibrate as harmonic oscillators, when their vibrational energy is low. Electronic transitions involving the absorption or emission of light do not immediately deform the molecule due to the adiabatic approximation, and thus these transitions can be represented on the potential energy surface representation as vertical lines[3]. While, for each transition, an electron can be excited to or decay to any vibrational level of the target electronic excited state, according to Kasha's rule[47], the rate of vibrational relaxation is much faster than that of electronic transitions, and

thus these transitions can be considered as taking place from the lowest vibrationally excited level of an electronic state.

The intensity of a given transition is proportional to the number of photons emitted or absorbed with time, as[3]

$$I = \hbar\omega * \frac{dn}{dt} \frac{1}{dA} = \hbar\omega \frac{1}{dA} k_{if}, \quad (2.96)$$

where $\hbar\omega$ is the photon energy. The intensity I is the quantity determining many of the experimental observables used in absorption, emission, transient absorption, and many other kinds of spectroscopy.

2.3.4.1 Electronic component of absorption

We begin by considering only the electronic component in the simplest picture, connecting the experimental observable of the intensity to the quantum mechanical factor by considering the Einstein coefficients A_{ul} for spontaneous emission, B_{lu} for absorption, and B_{ul} for stimulated emission. These coefficients are based on a probabilistic picture of thermodynamic equilibrium between an upper, u , and lower, l electronic state. The meaning of these coefficients are that the rates of each of these processes are proportional to these coefficients[48]:

$$k_{abs} = N_l B_{lu} \rho_\omega(\omega_{lu}) \quad (2.97)$$

$$k_{spont.} = N_u A_{ul} \quad (2.98)$$

$$k_{stim.} = N_u B_{ul} \rho(\omega_{ul}) \quad (2.99)$$

where N_i is the electronic population of state i , ρ_ω is the energy density of radiation per unit frequency in the system to be considered, and ω_{ij} is the transition frequency between states i , and j . By considering these equations to be balanced in thermal equilibrium, $k_{abs} = k_{spont.} + k_{stim.}$, we can find an equation for the relative population of states[48]

$$\frac{N_u}{N_l} = \frac{B_{lu} \rho_\omega(\omega_{lu})}{A_{ul} + B_{ul} \rho_\omega(\omega_{ul})}. \quad (2.100)$$

The general expression for the number of electrons in state i in thermal equilibrium, with each state having energy E_i , degeneracy g_i and the system has a temperature T is given by[48]

$$N_i = \frac{N g_i \exp(-E_i/kT)}{\sum_i g_i \exp(-E_i/kT)} \quad (2.101)$$

for a total number of electrons N . Using this expression, we can produce another expression for the relative state population based on thermodynamic considerations[48]

$$\frac{N_u}{N_l} = \frac{g_u}{g_l} \exp(-\hbar\omega_{ul}/kT) \quad (2.102)$$

which, by equating to the previous expression, we can obtain an expression for the energy density of radiation in terms of the A_{ul} , B_{ul} and B_{lu} coefficients[48]

$$\rho_\omega(\omega_{ul}) = \frac{g_u A_{ul} \exp(-\hbar\omega_{ul}/kT)}{g_l B_{lu} - g_u B_{ul} \exp(\hbar\omega_{ul}/kT)}. \quad (2.103)$$

This expression can be compared to Planck's law for a black body which gives the energy density as [48]

$$\rho_\omega(\omega) = \frac{\hbar\omega^3}{\pi^2 c^3} \frac{1}{\exp(\hbar\omega/kT) - 1}. \quad (2.104)$$

Using this comparison, stating that $g_u B_{ul} = g_l B_{lu}$ and using the known expression of the spontaneous emission constant A_{ul} , an expression for the absorption coefficient B_{lu} can be obtained in terms of the transition dipole moment[48]

$$|\langle\psi_u|\hat{\mathbf{e}}\mathbf{r}|\psi_l\rangle|^2 = |\mu_{ul}|^2 = |\mu_{lu}|^2 \quad (2.105)$$

$$B_{lu} = \frac{\pi e^2}{3\epsilon_0 \hbar^2} \frac{1}{g_l} |\mu_{lu}|^2 \quad (2.106)$$

This can be further related to experimental observables by utilising an additional expression for B_{lu} [3, 48]:

$$B_{lu} = \frac{\pi e^2 f_{lu}}{2\epsilon_0 \hbar m \omega_{ul}} \quad (2.107)$$

in which f represents the oscillator strength of a given transition lu . Experimentally, this can be related to the molar extinction coefficient[3]

$$f = \frac{4.39 \times 10^{-9}}{n_0} \int \epsilon(\nu) d\nu \quad (2.108)$$

The molar extinction coefficient is related to the intensity of absorbed light via[3]

$$I(\nu) = I_0 10^{-A(\nu)} = I_0 10^{-\epsilon(\nu)Cd} \quad (2.109)$$

where C is the molar concentration of absorbing species and d is the path length through the absorbing material. Thus, by substituting the extinction coefficient for the previously defined equations for B_{lu} in terms of f and $|\mu|^2$, the total absorbed light intensity can be written as

$$I = I_0 10^{\wedge} \left(2.278 \times 10^8 \times \frac{2}{3} \frac{n_0 m \omega_{ul}}{e \hbar g_i} |\mu_{lu}|^2 \right) \quad (2.110)$$

2.3.4.2 Vibrational component - the Franck-Condon factor

In general, there will be some shift in the normal coordinates ΔQ from the ground state potential energy surface and the excited state potential energy surface. As it has been established that optical decays and excitations in the potential energy surface representation are vertical, these shifts in nuclear coordinates will change the overlap between the vibrational component of the wavefunction of the ground and excited states. This overlap is known as the *Franck-Condon factor* F .

This factor is evaluated as a Poisson probability distribution from the 0^{th} vibrational energy level of the initial state to the m^{th} vibrational energy level of the final state[3]

$$F_{0-m} = |\langle \Psi_{vib,f} | \Psi_{vib,i} \rangle|^2 = \frac{S^m}{m!} e^{-S} \quad (2.111)$$

where i and f denote the initial and final state of a transition, and S denotes the strength of the overlap, and is referred to as the *Huang-Rhys parameter*. [3] This parameter is proportional to the square of the magnitude of the shift in molecular normal coordinate between the ground and excited state,

$$S = \frac{1}{2} M \omega_m \frac{\Delta Q^2}{\hbar} \quad (2.112)$$

in which ω_m is the angular frequency of transition m and M is the reduced mass of the harmonic oscillator. This equation describes the ratio of potential energy to the

vibrational quantum energy of the vibrating mode, which can also be interpreted as the number of vibrational quanta involved in the vibration, and is physically represented as the ratio of the intensity of the main peak in an absorption or emission spectrum to the subsequent peaks of mode m [3].

An equation to simulate the full absorption/emission spectrum of a non-distorted molecule can be found by including the consideration from line shape broadening, additional vibrational modes j , and correcting for the photon density of states. The resulting expression is[3]

$$I(\hbar\omega) = [n(\hbar\omega) \cdot \hbar\omega]^k \cdot \sum_{m_j} \prod_j \frac{S_j^{m_j}}{m_j!} e^{-S_j} \cdot \Gamma \cdot \delta(\hbar\omega - (\hbar\omega_0 - K \cdot \sum_j m_j \hbar\omega_j)) \quad (2.113)$$

where $\hbar\omega$ is the photon energy, $\hbar\omega_0$ is the 0-vibration electronic transition energy (also known as the 0-0 transition energy), $\hbar\omega_j$ is the energy of a vibrational normal mode labelled j , which has a quantum occupation number of m_j (for example the 0-1 transition for a particular normal mode has $m_j = 1$). S_j is the Huang-Rhys factor for vibrational normal mode j . S_j is a measure of the coupling strength between the electronic transition and the vibrational normal mode j , and is proportional to the square of the shift of the normal coordinate displacement between the ground and excited state potential energy surface $S_j \propto \Delta Q_j^2$ and to the intensity of the resonance Raman peak for mode j . To reduce the number of fitting parameters, the energies of the vibrational normal modes can be fixed to the values determined from resonance Raman spectroscopy[3]. Γ is a line shape function, taken to be Gaussian to account for coupling to low energy vibrations and dynamic and static disorder. $n(\hbar\omega)$ is the energy-dependent refractive index of the material and is included to accurately account for the photon density of states via $[n(\hbar\omega) \cdot \hbar\omega]^k$, where $k=3$ for emission spectra and $k=1$ for absorption (due to the electric field interacting with the sample multiple times, according to the Einstein relations). For solution samples, n does not vary significantly with photon energy and is assumed to be constant (this is not true for solid films). Finally, we set $K = -1$ for emission and $+1$ for absorption, as the energy of $m_j \neq 0$ transitions is lower for emission and higher for absorption[3].

After excitation or decay to an excited vibrational level, according to Kasha's rule [47], the molecule will experience vibrational relaxation to the lowest point on the electronic potential surface, out-competing any inter-state transfer processes. This vibrational relaxation can take place over a range of timescales of orders ~ 0.1 -10 ps. It is this change in energy by vibrational relaxation on both excitation and decay which is one major source of the *Stokes shift*, the shift in intensity maximum to lower energy seen

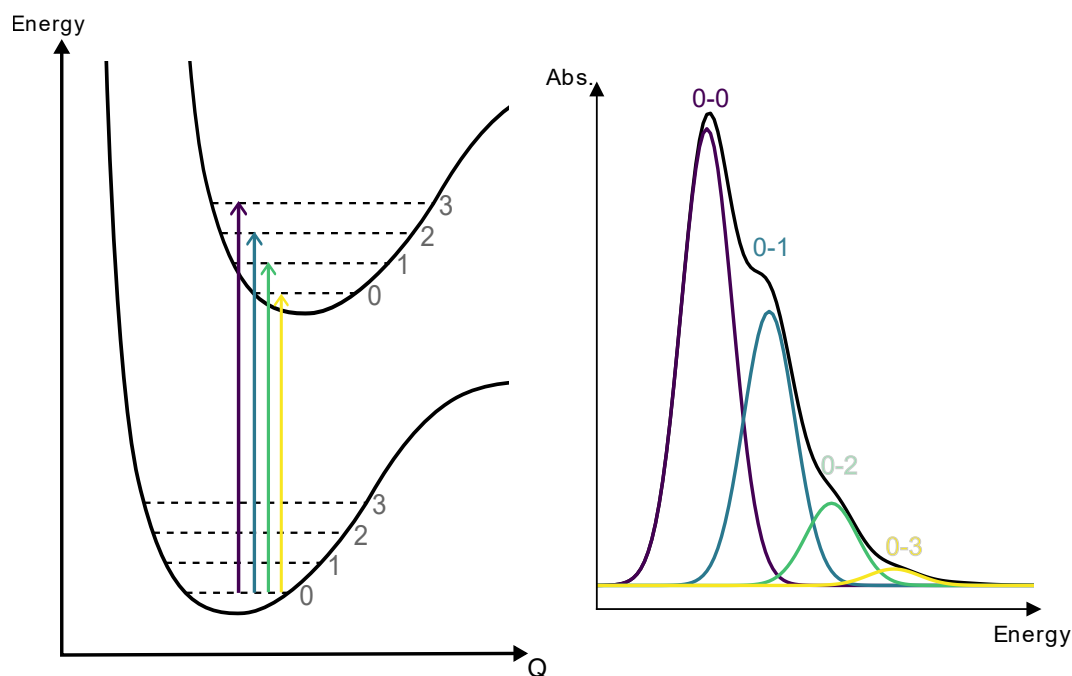


FIGURE 2.7: Correspondence of energy level transitions to steady-state spectra under the Franck-Condon model.

between the absorption and emission spectra[49]. This relationship between the potential energy surface and the steady state absorption and emission spectra is illustrated in Fig. 2.7.

2.3.4.3 The spin factor - spin-orbit coupling

The spin factor

$$\psi_{spin}(\uparrow, \downarrow) = \langle \psi_{spin,f} | \psi_{spin,i} \rangle \quad (2.114)$$

is, at the first approximation, fairly easy to consider. Due to the nature of spin states, the spin factor is simply 1 if the initial and final states have like spins, or 0 if the initial and final states have unlike spins. As the wavefunction components are combined multiplicatively, this means that transitions between singlet and triplet states are forbidden. However, as will be examined in a later section, many transitions between singlet and triplet states are observed experimentally[3].

This discrepancy is resolved by considering a perturbation in the form of a mixing between triplet and singlet wavefunctions via spin-orbit coupling, coupling between the transition-limiting electron spin and the orbital angular momentum. The transition that is considered here is that of *phosphorescence*, that is transition from the first triplet

excited state $|\psi_1\rangle$ to the ground singlet state $|\psi_0\rangle$ via emission of a photon. The applied spin-orbit perturbation Hamiltonian, \hat{H}_{SO} acts by mixing the triplet state with singlet states, and vice versa. The resultant perturbed triplet and singlet states are represented by [3, 33]

$$|{}^3\psi'_1\rangle = |{}^3\psi_1\rangle + \sum_k \frac{\langle {}^1\psi_k | \hat{H}_{SO} | {}^3\psi_1 \rangle}{E(T_1) - E(S_k)} |{}^1\psi_k\rangle \quad (2.115)$$

$$|{}^1\psi'_0\rangle = |{}^1\psi_0\rangle + \sum_k \frac{\langle {}^3\psi_k | \hat{H}_{SO} | {}^1\psi_0 \rangle}{E(S_0) - E(T_k)} |{}^3\psi_k\rangle \quad (2.116)$$

Using these expressions, the rate of phosphorescence is once again determined by Fermi's golden rule, using the perturbed wavefunctions and the dipole operator [3, 33]

$$k_{phos} = \frac{2\pi\rho f}{\hbar} |\langle {}^3\psi'_1 | e\hat{\mathbf{r}} | {}^1\psi'_0 \rangle|^2. \quad (2.117)$$

For simplicity, we define

$$\Omega_k^{ST} = \frac{\langle {}^1\psi_k | \hat{H}_{SO} | {}^3\psi_1 \rangle}{E(T_1) - E(S_k)} \quad (2.118)$$

$$\Omega_k^{TS} = \frac{\langle {}^3\psi_k | \hat{H}_{SO} | {}^1\psi_0 \rangle}{E(S_0) - E(T_k)} \quad (2.119)$$

Allowing the expanded expression for the rate of phosphorescence to be expressed as [3, 33]

$$k_{phos} = \frac{2\pi\rho f}{\hbar} |\langle {}^3\psi_1 | e\hat{\mathbf{r}} | {}^1\psi_0 \rangle|^2 \quad (2.120)$$

$$+ \sum_k \Omega_k^{TS} |\langle {}^3\psi_1 | e\hat{\mathbf{r}} | {}^3\psi_k \rangle|^2 \quad (2.121)$$

$$+ \sum_k \Omega_k^{ST} |\langle {}^1\psi_k | e\hat{\mathbf{r}} | {}^1\psi_0 \rangle|^2 \quad (2.122)$$

$$+ \sum_k \sum_j \Omega_k^{ST} \Omega_j^{TS} \langle {}^1\psi_k | e\hat{\mathbf{r}} | {}^3\psi_j \rangle|^2. \quad (2.123)$$

As we have previously defined, the first and final terms go to zero, as they involve overlaps with the unperturbed triplet and singlet states, while the middle two terms remain. Evaluating this further requires knowledge of the specific spin-orbit perturbing

Hamiltonian. This effect can arise from a number of sources, such as via the heavy atom effect, which will be discussed later, or via twisting nuclear vibrations.

2.3.5 Non-radiative transitions

Whilst a *radiative transition* is a process which emits a photon, and can be represented as a vertical arrow on a potential energy surface diagram, a *non-radiative transition* emits no photon, keeping the overall energy of the molecular system constant. Thus such transitions may be represented on a potential energy surface as isoenergetic, horizontal transitions, to a non-equilibrium point on the final state's energy surface. The excess vibrational energy is subsequently lost to the environment as thermal energy.

If said transition occurs between two states of the same spin multiplicity, such as a singlet \rightarrow singlet or triplet \rightarrow triplet transition, such a transition is called *internal conversion*. If states of different multiplicity are involved in the transition, most commonly singlet \leftrightarrow triplet transitions, in general such a transition is called intersystem crossing.

To formulate non-radiative decay quantitatively, we can follow a similar treatment to radiative decay via Fermi's golden rule[50], using a different perturbing Hamiltonian

$$k_{if} = \frac{2\pi\rho_f}{\hbar} |\langle \psi_{el,f} \psi_{vib,f} \psi_{spin,f} | \hat{H}' | \psi_{el,i} \psi_{vib,i} \psi_{spin,i} \rangle|^2 \quad (2.124)$$

$$= \frac{2\pi\rho_f}{\hbar} H_{if}^2 \quad (2.125)$$

where the perturbing Hamiltonian is given as $\hat{H}' = \partial/\partial Q$, the nuclear kinetic energy operator. Given that this transition is dependent on the motion of the nuclei, and that under the adiabatic approximation, the electronic states are eigenstates of the system with no overlap, we cannot work under the adiabatic approximation in this derivation. There is a non zero overlap that can be found by first integrating over terms with a dependence on the electronic coordinates[51]:

$$H_{if} = \langle \psi_{vib,f} | \hat{\mathfrak{S}} | \psi_{vib,i} \rangle \quad (2.126)$$

$$\hat{\mathfrak{S}} = \langle \psi_{el,f} \psi_{spin,f} | \hat{H}' | \psi_{el,i} \psi_{spin,i} \rangle. \quad (2.127)$$

Inserting an approximate expansion for \mathfrak{S} as a function of nuclear coordinates[51]

$$\mathfrak{S} = \sum_{n=1}^N \frac{\partial \mathfrak{S}}{\partial Q_n} (Q_n - Q_n^0), \quad (2.128)$$

wherein the modelled transition involves N vibrational modes, expanded in nuclear mode coordinate Q_n around the equilibrium position of said mode coordinate Q_n^0 . Thus, the resulting expression for H_{if} becomes[51]

$$H_{if} = \sum_n \frac{\partial \mathfrak{S}}{\partial Q_n} \langle \psi_{vib,f} | Q_n - Q_n^0 | \psi_{vib,i} \rangle. \quad (2.129)$$

The total vibrational wavefunction can be considered as a product of individual vibrational mode wavefunctions which contribute to a state, represented as[51]

$$\psi_{vib}(E) = \prod_n \chi_n(\nu_n), \quad (2.130)$$

where E is the energy of the vibrational mode relative to the lowest energy mode where the vibrational quantum $\nu_n = 0$. For the initial state, by Kasha's rule[47], we say that the system will be prepared in this lowest vibrational level, and that the initial state will have an electronic energy level greater than the final state $E_{i,el} > E_{f,el}$, $E_{el} = \hbar\omega$. Thus, we are considering a non-radiative *decay*, and the vibrational energy quantum will be greater than 0.

$$\psi_{vib,i}(0) = \prod_n \chi_n^i(0) \quad (2.131)$$

$$\psi_{vib,f}(E_n) = \prod_n \chi_n^f(\nu_n^f); \quad E_n = \sum_n \nu_n \hbar\omega_n^i. \quad (2.132)$$

Substituting these functions into 2.129 we obtain a function for H_{if} in terms of the modes m that contribute to the non-radiative transition:

$$H_{if} = \sum_m \frac{\partial \mathfrak{S}}{\partial Q_m} \left(\frac{\hbar\omega_m^i}{2k_m^f} \right) \times \quad (2.133)$$

$$[(\nu_m + 1)^{1/2} \langle \chi_m^f(\nu_m + 1) | \chi_m^i(0) \rangle + \nu_m^{1/2} \langle \chi_m^f(\nu_m - 1) | \chi_m^i(0) \rangle] \times \quad (2.134)$$

$$\prod_{n \neq m} \langle \chi_n^f(\nu_n) | \chi_n^i(0) \rangle \quad (2.135)$$

By the approximations of Siebrand [51], one of these modes will contribute to the transition significantly more than the others, and the perturbation applied to the wavefunctions is a small one. We denote the primary mode involved in the transition as the mode p . By this approximation,

$$\langle \chi_p^f(\nu_f) | \chi_p^i(\nu_i) \rangle = \delta_{\nu_i, \nu_f} \quad (2.136)$$

and we can separate the equation into two components:

$$H_{if} = JS(E) \quad (2.137)$$

where

$$J = \frac{\partial \mathfrak{S}}{\partial Q_p} \frac{\hbar \omega_p^i}{2k_p^i} \langle \chi_p^f(0) | \chi_p^i(0) \rangle \quad (2.138)$$

$$S(E) = \prod_{n \neq p} \langle \chi_n^f(\nu_n) | \chi_n^i(0) \rangle \quad (2.139)$$

As the transition involved in a non-radiative decay is horizontal, there is no difference from the total initial and final energies of the system. Therefore, by this energy conservation condition[51],

$$E = \hbar \omega_p^i + \sum_{n \neq p} \nu_n \hbar \omega_n^i \quad (2.140)$$

$$= \Delta E_{0-0} + \frac{1}{2\rho_f} \cos(\theta) \quad (2.141)$$

where ΔE_{0-0} is the energy difference between the minima of the initial and final states, ρ_f is the energy density function described in Fermi's golden rule, and θ is a phase parameter that takes values between 0 and 2π . This implies that the excess vibrational energy in the final state that results from the non-radiative decay are distributed in modes between energies[51]

$$\Delta E_{0-0} - \frac{1}{2\rho_f} \leq E \leq \Delta E_{0-0} + \frac{1}{2\rho_f} \quad (2.142)$$

Thus, the rate of non-radiative decay is given by[51]

$$k_{if} = \frac{2\pi\rho_f}{\hbar} |H_{if}|^2 \quad (2.143)$$

$$= \frac{2\pi\rho_f}{\hbar} J^2 \sum_E S^2(E) \quad (2.144)$$

where the sum over E is performed over each accessible mode. This sum in S^2 has also been defined previously as the Franck-Condon vibrational overlap interval, $F = |\langle \psi_{vib,f} | \psi_{vib,i} \rangle|^2$.

2.3.5.1 The Energy Gap Law

The evaluation of this overlap is a complex one containing difficult summations. Englman and Jortner [5] manage this by relating this factor to the classical absorption lineshape, and proposing a general form

$$F(E) = \frac{1}{\sum_k \exp\left(\frac{-E_{ik}}{k_B T}\right)} \left[\sum_k \sum_j \left| \prod_n \langle \chi_{f,n}(Q_n^{(f)}, \nu_{f,n}) | \chi_{i,n}(Q_n^{(i)}, \nu_{i,n}) \rangle \right|^2 \right] \quad (2.145)$$

$$\times \exp\left(\frac{-E_{ik}}{k_B T}\right) \delta(E_{fj} - E_{ik} - E) \quad (2.146)$$

where the contributions from each mode contributing to $F(E)$ has been taken into account via summations over the mode indices k and j , and the exponential terms account for finite temperature. Using an inverse Fourier transformation, they show the expression for the non-radiative decay rate becomes[5]

$$k_{if} = \frac{J^2}{\hbar^2} \exp(-G) \int_{-\infty}^{\infty} \exp\left(-\frac{i\Delta E t}{\hbar} + G_+(t) + G_-(t)\right) dt, \quad (2.147)$$

In which ΔE is the energy gap for the decay, from the bottom of the excited state potential energy surface to the ground state, and t is the result of the Fourier transform to the time domain from the frequency domain. The G terms are dimensionless quantities which relate to the change in the number of vibrational quanta involved in a given transition[5],

$$G = G_+(0) + G_-(0) = \frac{1}{2} \sum_j |\nabla_j|^2 (2\bar{n}_j + 1) \quad (2.148)$$

$$G_+(t) = \frac{1}{2} \sum_j |\nabla_j|^2 (\bar{n}_j + 1) \exp(i\omega_j t) \quad (2.149)$$

$$G_-(t) = \frac{1}{2} \sum_j |\nabla_j|^2 \bar{n}_j \exp(-i\omega_j t), \quad (2.150)$$

in which \bar{n}_j is the number of excited vibrations with vibrational frequency ω_j at thermal equilibrium

$$\bar{n}_j = \left(\exp\left(\frac{\hbar\omega_j}{k_B T} - 1\right) \right)^{-1} \quad (2.151)$$

and ∇_j is a term denoting the shift of the excited state surface minimum point with respect to that of the ground state in terms of the minimum of a given mode coordinate Q_j^0

$$\nabla_j = \left(\frac{M_j \omega_j}{\hbar} \right)^{\frac{1}{2}} \Delta Q_j^0; \quad (2.152)$$

$$\Delta Q_j^0 = Q_{j,f}^0 - Q_{j,i}^0 \quad (2.153)$$

where M_j is the effective mass of the oscillator.

We also define E_M as the difference between the transition from the lower energy potential energy surface to the higher and the transition from the higher to the lower, which in the radiative scheme would be analogous to the Stokes shift. In considering the behaviour of the above expression for G with temperature, we obtain two limiting cases, at low and high temperatures[5]:

$$G \approx \frac{E_M}{\hbar \langle \omega \rangle}; \quad \frac{\hbar \langle \omega \rangle}{k_B T} \gg 1 \quad (2.154)$$

$$G \approx \frac{2E_M}{\hbar^2 \omega^2 k_B T}; \quad \frac{\hbar \langle \omega \rangle}{k_B T} \ll 1 \quad (2.155)$$

in which $\hbar \langle \omega \rangle$ is the mean vibrational energy of a molecule. In the majority of our consideration, the low temperature limit is the most physically relevant. This, the upper equation, also defines two regimes[5]:

1. $E_M \gg \hbar \langle \omega \rangle$: The strong coupling limit, in which the intersection of the potential energy surfaces take place close to their equilibria, and the excited state potential surface is shifted significantly with respect to the ground state
2. $E_M \leq \hbar \langle \omega \rangle$: The weak coupling limit, in which the relative displacement of the potential surfaces is small and there is no or negligible intersection between them, far from the equilibrium.

In the weak coupling regime, the integral in the expression for the radiative decay rate in equation 2.147 is evaluated by the method of steepest descent wherein the solution to the integral is found from the roots of the equation[5]

$$\frac{1}{2} \sum_j \nabla_j^2 \hbar \omega_j \exp(i\omega_j t) - \Delta E = 0 \quad (2.156)$$

which, for large inter-state separations ΔE gives the solution for t as

$$t = -\frac{i}{\omega_M} \log \left(\frac{2\Delta E}{\sum_{M=1}^d \hbar \omega_M \nabla_M^2} \right) \quad (2.157)$$

in which the subscript M refers to the degenerate mode(s) which share the maximum frequency. In the approximation that we neglect all but the highest mode, we can write that the error resulting from the approximation is[5]

$$\epsilon = \frac{\hbar \omega_M \nabla_M^2}{\Delta E} \frac{\omega_M - \omega_m}{\omega_M} \quad (2.158)$$

Using this result, the expression for the non-radiative decay rate become[5]

$$k_{if} = \frac{J^2}{\hbar} \sqrt{\frac{2\pi}{\hbar \omega_M \Delta E}} \exp \left(\frac{1}{2} \sum_j \nabla_j^2 \right) \times \exp \left(\frac{\Delta E}{\hbar \omega_M} \left[\log \left(\frac{2\Delta E}{\sum_M \hbar \omega_M \nabla_M^2} \right) - 1 \right] \right) \quad (2.159)$$

Simplifying this equation by defining[5]

$$\gamma = \gamma(\Delta E, e_M, d) = \log \left(\frac{\Delta E}{de_M} \right) - 1 \quad (2.160)$$

$$e_M = \frac{1}{2} \hbar \omega_M \nabla_M^2 \quad (2.161)$$

$$de_M = \frac{1}{2} \sum_{M=1}^d \hbar \omega_M \nabla_M^2, \quad (2.162)$$

we obtain a very useful expression for the non-radiative decay rate[5]

$$k_{if} = \frac{J^2}{\hbar} \sqrt{\frac{2\pi}{\hbar\omega_M\Delta E}} \exp\left(-\gamma\frac{\Delta E}{\hbar\omega_M}\right). \quad (2.163)$$

This expression allows the generalised relation between the energy gap between two states and the non-radiative decay rate between them. The relation is approximately (though slightly stronger than) exponential, and many similar molecular systems can be compared using this equation, as they will share many of the pre-exponential factors. However, this law is only applicable to the weak coupling regime, when the two potential energy surfaces do not intersect near to the equilibrium position at the potential energy surface minimum.

2.3.5.2 The strong coupling limit

When there is a strong displacement between the initial and final states involved in a non-radiative transition, such that the intersection between the two occurs close to the equilibrium position, the decay between the states are best considered in the strong coupling regime. The difference between the weak and strong coupling limit is shown in Fig. 2.8

Quantitatively, this regime occurs when[5]

$$E_M \gg \hbar \langle \omega \rangle. \quad (2.164)$$

E_M can also be considered as the geometric reorganisation energy, or the difference between the point at which a transition intersects with a state's potential energy surface and the minimum of that surface. This gives the amount of vibrational energy which is lost on relaxation to the bottom of the energy surface and is given by

$$E_{rel} = \sum_j S_j \hbar \omega_j \quad (2.165)$$

wherein S is the Huang-Rhys parameter, or vibrational mode activity, of a given mode. In the limit of strong coupling, the dynamics of the molecule being determined by the reorganisation energy as well in addition to the energy gap ΔE [5]

$$k_{if} \propto \frac{1}{\sqrt{E_{rel}}} \exp\left(\frac{2E_A}{\hbar\omega}\right); \quad E_A = \frac{(\Delta E - E_{rel})^2}{4E_{rel}}. \quad (2.166)$$

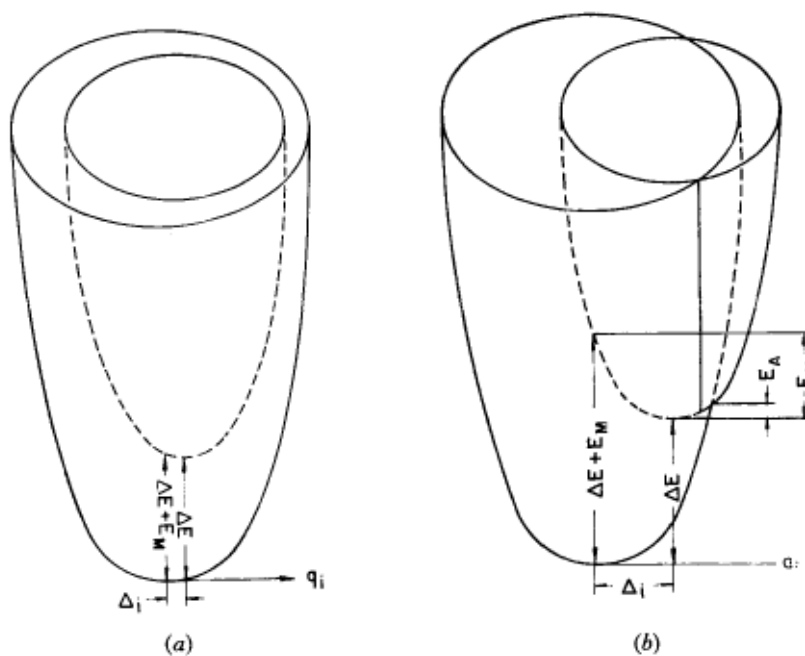


FIGURE 2.8: Schematic representation of the two electronic coupling limits. a) The weak coupling limit, in which the two surfaces do not intersect close to the surface minima, where the electronic decay is mediated by the energy gap between the two surfaces ΔE . b) The strong electronic coupling limit, in which the two surfaces intersect close to their minima. In this case, the rate of electronic decay is mediated by the quantities ΔE and E_A , which is the difference between the intersection energy and the energetic minimum of the excited state potential energy surface. Reproduced with permission from Englman and Jortner [5].

Here, the dependence of the non-radiative decay rate on the energy gap is gaussian rather than exponential.

2.3.5.3 Intersystem crossing and the Heavy Atom Effect

Non-radiative decay of the excited states of molecules by intersystem crossing and by internal conversion are only distinguished by the relative spin multiplicities of the initial and final states. If they are the same, such as most commonly a singlet \rightarrow singlet transition or a triplet \rightarrow triplet transition, it is referred to as internal conversion. If different, such as the decay of a triplet state to the ground singlet state, it is referred to as intersystem crossing. When the states are of different multiplicities, some perturbation must be applied to them in order to permit non-radiative transfer. The perturbation responsible for permitting this transition is spin-orbit coupling, and can be treated in the same way as has already been treated in the case of phosphorescence[3, 33].

The factor in spin-orbit coupling that has not yet been considered is the nature of the perturbing spin-orbit Hamiltonian. As there are multiple potential sources of spin-orbit coupling, the specific form depends entirely on which is chosen as the mechanism. We

will consider a common and relevant case, that of heavy-atom-effect induced spin-orbit coupling.

The heavy-atom effect is so called due to the dependence of the spin-orbit coupling strength on the atomic number of the nuclei to which the exciton spin couples. The spin-orbit Hamiltonian of the exciton state is given by[33]

$$H_{SO} = \xi(r) * \mathbf{l} \cdot \mathbf{s}; \quad (2.167)$$

$$\xi(r) = \frac{e}{2m_e^2 r c^2} \frac{\delta E}{\delta r}, \quad (2.168)$$

where \mathbf{l} is the electron's orbital angular momentum vector, \mathbf{s} is the electron's spin angular momentum, and $\xi(r)$ is the relativistic orbital distance (r) dependent prefactor, itself dependent on the electron charge e , the electron mass m_e , and the speed of light c , as well as the radial derivative of the electric field due to the nucleus, $\frac{\delta E}{\delta r}$. In a mono-atomic system, as an approximation, the electric field due to the atomic nucleus can be simply expressed as[33]

$$E = \frac{Ze}{4\pi\epsilon_0 r}, \quad (2.169)$$

where Z is the atomic number of the nucleus, and ϵ_0 is the vacuum permittivity. This substitution gives the formula for $\xi(r)$ as

$$\xi(r) = \frac{Ze^2}{8\pi\epsilon_0 m_e^2 r^3 c^2}. \quad (2.170)$$

For the case $l \geq 0$, the spin-orbit Hamiltonian matrix element on the quantum electronic state $\langle nlm_n m_l | H_{SO} | nlm_n m_l \rangle$ is non-zero, and can be separated into the spin-dependent component and radial component. The spin-dependent component[33],

$$\langle nlm_n m_l | \mathbf{l} \cdot \mathbf{s} | nlm_n m_l \rangle \quad (2.171)$$

is proportional to \hbar^2 . We write take the radial average of the remaining radial component as being proportional to hc , which, using the equation for $\xi(r)$, gives[33]

$$hc\zeta_{SO} = \langle nlm_n m_l | \xi(r) | nlm_n m_l \rangle \hbar^2 = \frac{Z\hbar^2 e^2}{8\pi\epsilon_0 m_e^2 c^2} \langle nlm_n m_l | r^{-3} | nlm_n m_l \rangle, \quad (2.172)$$

the solution to which is found by substituting for the *associated Laguerre function* corresponding to the state of the electron[33],

$$\langle nlm_n m_l | r^{-3} | nlm_n m_l \rangle = \frac{Z^3}{n^3 a_0^3 l(l + \frac{1}{2})(l + 1)}, \quad (2.173)$$

where a_0 is the Bohr radius. Rearranging equation 2.172 for ζ_{SO} , the final equation for the strength of the spin-orbit interaction that determines the rate of intersystem crossing is[33]

$$\zeta_{SO} = \frac{Z^4 e^2 \hbar^2}{8\pi\epsilon_0 m_e^2 h c^3 n^3 a_0^3 l(l + \frac{1}{2})(l + 1)}. \quad (2.174)$$

Simplifying this expression using the Rydberg constant for heavy atoms R_∞ and the fine structure constant α

$$R_\infty = \frac{m_e e^4}{8\epsilon_0^2 h^3 c}, \quad (2.175)$$

$$\alpha = \frac{e^2}{4\pi\epsilon_0 \hbar c}, \quad (2.176)$$

the equation for the spin-orbit coupling constant becomes[33]

$$\zeta_{SO} = \frac{Z^4 \alpha^2 R_\infty}{n^3 l(l + \frac{1}{2})(l + 1)} \quad (2.177)$$

From this equation[33], the strength of the spin-orbit coupling interaction is proportional to the fourth power of the atomic number, and thus we can qualitatively state that in a molecule, the inclusion of a heavy atom greatly increases the spin orbit coupling strength[52].

2.3.6 Singlet fission

While triplets can be generated in molecular systems via the spin-flip process of intersystem crossing, there is also a mechanism for the excitation to move from the singlet to the triplet manifold in a spin-conserved process, known as *singlet fission*. Singlet fission is a phenomenon mentioned first in Singh et al. [53], seen as a precursor to triplet-triplet annihilation in anthracene crystals.

In its most simple description, singlet fission is the conversion from a pair of one excited singlet and one ground singlet excitation on different excitation centres into two triplet excitations. As such, the occurrence of singlet fission is limited by an energetic condition on the state energy levels

$$E(S_1) = 2 \times E(T_1), \quad (2.178)$$

or, in other words, the triplet energy must be less than half the singlet energy.

In the most simplistic picture, singlet fission proceeds via a two step process, involving an intermediate paired triplet state, $^1(TT)$, which occurs due to the nature of spin conservation. The triplets, spin-1 excitons, are generated with opposing spin orientations, in order to preserve the initial spin-0 singlet state spin.

However, the decoherence of the coupled triplet pair state into free triplets $^1(TT) \rightarrow T_1 + T_1$ is a complex multi-step process in itself, first losing its electronic coherence (or regaining an unmodified triplet electronic state free from inter-triplet interaction effects) but retaining their spin coherence over a longer timescale. The resulting representation of the singlet fission pathway is[54]

$$S_1 S_0 \leftrightarrow ^1(TT) \leftrightarrow ^1(T\dots T) \leftrightarrow T_1 + T_1 \quad (2.179)$$

The most intuitive picture in which to represent the triplet pair/singlet state, which will be a four-spin excited state, will be via a single spin-product basis, which is given for a two-spin state:

1. $|\uparrow\uparrow\rangle$: Triplet, spin up, +1
2. $|\uparrow\downarrow\rangle$: Singlet, net spin 0
3. $|\downarrow\uparrow\rangle$: Singlet, net spin 0
4. $|\downarrow\downarrow\rangle$: Triplet, spin down, -1

in which $|\uparrow\rangle$ and $|\downarrow\rangle$ are the eigenstates of the spin operators of a single electron.

However, while this picture of the two-electron spin state wavefunctions is intuitive, the wavefunctions listed above are not eigenstates of the spin operator of a two-electron system. This has been explicitly stated above as[33]

1. $|S\rangle : \frac{1}{\sqrt{2}}(|\uparrow\downarrow\rangle - |\downarrow\uparrow\rangle)$
2. $|T_{-1}\rangle : |\downarrow\downarrow\rangle$
3. $|T_0\rangle : \frac{1}{\sqrt{2}}(|\uparrow\downarrow\rangle + |\downarrow\uparrow\rangle)$

$$4. |T_{+1}\rangle : |\uparrow\uparrow\rangle$$

These states are eigenstates of the total spin operator \hat{S} and the z-spin component of the electron spin. However, these are only valid when an external magnetic field exists to define a z direction, and are known as the high-field basis. In the absence of such a field, we have also defined previously the 2-electron zero-field basis[3, 34]:

1. $|S\rangle : \frac{1}{\sqrt{2}}(|\uparrow\downarrow\rangle - |\downarrow\uparrow\rangle)$; unchanged from the zero field basis
2. $|T_x\rangle : \frac{1}{\sqrt{2}}(|\downarrow\downarrow\rangle - |\uparrow\uparrow\rangle)$
3. $|T_y\rangle : \frac{i}{\sqrt{2}}(|\downarrow\downarrow\rangle + |\uparrow\uparrow\rangle)$
4. $|T_z\rangle : \frac{1}{\sqrt{2}}(|\uparrow\downarrow\rangle + |\downarrow\uparrow\rangle)$

This same approach can be applied to find the 4-spin state basis eigenstates, which are necessary to describe the triplet pair state. Burdett and Bardeen [55] and Bossanyi et al. [56] give the zero-field picture in a 9 state basis, using the zero-field triplet states (2-4 above) as components:

1. $|S^4\rangle : \frac{1}{\sqrt{3}}(|T_xT_x\rangle + |T_yT_y\rangle + |T_zT_z\rangle)$
2. $|T_x^4\rangle : \frac{1}{\sqrt{2}}(|T_yT_z\rangle - |T_zT_y\rangle)$
3. $|T_y^4\rangle : \frac{1}{\sqrt{2}}(|T_zT_x\rangle - |T_xT_z\rangle)$
4. $|T_z^4\rangle : \frac{1}{\sqrt{2}}(|T_xT_y\rangle - |T_yT_x\rangle)$
5. $|Q_a^4\rangle : \frac{1}{\sqrt{2}}(|T_xT_x\rangle - |T_yT_y\rangle)$
6. $|Q_b^4\rangle : \frac{1}{\sqrt{6}}(|T_xT_x\rangle + |T_yT_y\rangle - 2|T_zT_z\rangle)$
7. $|Q_x^4\rangle : \frac{1}{\sqrt{2}}(|T_yT_z\rangle + |T_zT_y\rangle)$
8. $|Q_y^4\rangle : \frac{1}{\sqrt{2}}(|T_zT_x\rangle - |T_xT_z\rangle)$
9. $|Q_z^4\rangle : \frac{1}{\sqrt{2}}(|T_xT_y\rangle - |T_yT_x\rangle)$

in which the superscript $(^4)$ denotes the 4 spin state these eigenstates are describing. Tayebjee et al. [57] and Sanders et al. [58] give the same description for the high-field basis:

1. $|S^4\rangle : \frac{1}{\sqrt{3}}(|T_{+1}T_{-1}\rangle - |T_0T_0\rangle + |T_{-1}T_{+1}\rangle)$

2. $|T_{+1}^4\rangle : \frac{1}{\sqrt{2}}(|T_{+1}T_0\rangle - |T_0T_{+1}\rangle)$
3. $|T_0^4\rangle : \frac{1}{\sqrt{2}}(|T_{+1}T_{-1}\rangle - |T_{-1}T_{+1}\rangle)$
4. $|T_{-1}^4\rangle : \frac{1}{\sqrt{2}}(|T_0T_{-1}\rangle - |T_{-1}T_0\rangle)$
5. $|Q_{+2}^4\rangle : |T_{+1}T_{+1}\rangle$
6. $|Q_{+1}^4\rangle : \frac{1}{\sqrt{2}}(|T_{+1}T_0\rangle + |T_0T_{+1}\rangle)$
7. $|Q_0^4\rangle : \frac{1}{\sqrt{6}}(|T_{+1}T_{-1}\rangle + |T_{-1}T_{+1}\rangle + 2|T_0T_0\rangle)$
8. $|Q_{-1}^4\rangle : \frac{1}{\sqrt{2}}(|T_0T_{-1}\rangle + |T_{-1}T_0\rangle)$
9. $|Q_{-2}^4\rangle : |T_{-1}T_{-1}\rangle$

In both these representations, Q denotes quintet states, that is, net spin 2 states. Due to the dependence of the exciton energy on magnetic field due to the Zeeman effect [3, 56] the presence of the triplet pair state in emissive materials can be investigated. Strong magnetic fields can shift the triplet pair state energy to permit or quench singlet fission rates, which can be seen in the prompt fluorescence intensity. Alternatively, the *delayed fluorescence* of a molecule which arises from triplet pair recombination to the singlet state, permitting radiative transition to the ground state, can contain information about the triplet pair states themselves.

The 2 electron, non-interacting states are not eigenstates of a 4 electron system[56], and thus when a system is prepared via excitation to the singlet state, it is not in a pure eigenstate. The initial state is thus a superposition of the eigenstates given above, depending on the required basis. The singlet character of a given eigenstate, and likewise the amount of a given eigenstate that is present in the isolated singlet state, can be found by the overlap between their respective wavefunctions;

$$|C_S^i|^2 = |\langle S | \psi_i \rangle|^2 \quad (2.180)$$

$$|C_i^S|^2 = |\langle \psi_i | S \rangle|^2 \quad (2.181)$$

The degree of singlet character present in a 9-state 4 spin triplet pair wavefunction (C_S^i) determines both the rate of return to the ground state, emissively or otherwise, as well as the rate of triplet fusion back to the excited singlet state. Similarly, a larger triplet or quintet character to a wavefunction will assist in the process of triplet pair dissociation.

As the triplet pair wavefunction is not prepared initially in an eigenstate of the system, the triplet pair wavefunction acquires a phase that will oscillate between the eigenstate,

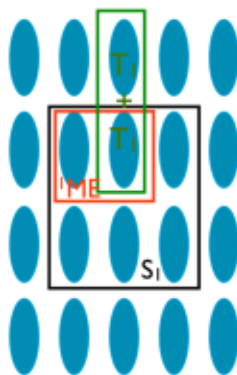


FIGURE 2.9: Illustration of the increase in entropy when transferring from the delocalised S_1 state to the localised triplet pair state ${}^1(TT) \rightarrow T_1 + T_1$. The S_1 state is delocalised over many molecules, and can only take a single configuration. The triplet pair state 1ME can form from any two molecules that form the singlet excitation, meaning that there are a large number of configurations that can form this state. The pair of free triplets $T_1 + T_1$ can form from any two molecules close to or part of the 1ME state. This has a larger configuration space, and the increase in entropy which results from this drives triplet pair dissociation. Reproduced with permission from Kolomeisky et al. [6], Copyright 2014 American Chemical Society.

rapidly losing singlet character. This oscillation will modulate the amount of singlet character that the triplet pair wavefunction has, and will thus affect the rate of delayed fluorescence. This results in a periodic oscillation in the delayed fluorescence intensity that is overlaid with the fluorescence decay kinetic, which is known as *quantum beating*. This phenomenon is unique to singlet fission and can help to identify it, though it is not seen in the case of strongly interacting triplet pairs[59].

Once the triplet pair state has been formed, what remains to be considered is the mechanism of triplet dissociation. The driving force behind triplet pair dissociation was not initially known, as often the triplet pair state can be bound with respect to the free triplet states due to triplet-triplet interactions. This would suggest that triplet dissociation is not energetically favoured. We can define the triplet binding energy as the difference between the quintet and singlet triplet pair states, as the quintet states are a major driver for triplet pair dissociation[60]. While the binding energy of the triplet pair appears as if it should prevent triplet dissociation from occurring, it can be overcome by considering thermodynamic effects, specifically the change in Gibbs free energy with the transition, via entropy as a driving force[6, 60, 61].

The Gibbs free energy change on the formation of the net-singlet triplet pair and a pair of free triplets from the initial singlet state is given below.

$$\Delta G_{S_1 \rightarrow ^1(TT)} = -E_{S \rightarrow 2T} - E_b - TS_{S_1 \rightarrow ^1(TT)} \quad (2.182)$$

$$\Delta G_{S_1 \rightarrow 2T_1} = -E_{S \rightarrow 2T} - TS_{S_1 \rightarrow 2T_1} \quad (2.183)$$

In which $E_{S \rightarrow 2T}$ is the electronic energy difference between the singlet and free triplet states, E_b is the triplet binding energy, and the final term in each case denotes the change in entropic energy from the transition from the singlet state to the net-singlet triplet pair state, and free triplets, respectively. While the exact entropic contributions are difficult to calculate, one can say qualitatively that an initial singlet state can be delocalised over several chromophores[6], whereas the triplet states deriving from singlet fission will be localised to a pair of adjacent chromophores. There will be a larger possible number of configurations for this localised state, resulting in an entropic gain on triplet formation. This results in a potentially negative, driving Gibbs free energy contribution, which can permit the dissociation of the triplet pair into free triplets even in the case that the electronic energy does not favour such an association. For tetracene, the entropic contribution is found to be <200 meV for $S_{S_1 \rightarrow 2T_1}$ and ~ 150 meV for $S_{S_1 \rightarrow ^1(TT)}$. This change in energy levels is illustrated in Fig. 2.10. It is shown in this figure that the electronic energy levels' contribution to the Gibbs free energy alone do not permit singlet fission, whereas with the inclusion of the entropic term, the process is energetically permitted.

It is this phenomenon in organic semiconductors that has motivated the following investigations into three dyes: Pigment Red 254, a derivative of diketopyrrolopyrrole, and BoDiPys 6 and 7, two derivatives of boron dipyrromethane which have been substituted with iodine and bromine, respectively. All three of these molecules have been predicted via density functional theory calculations to have singlet and triplet energies which fulfil the energetic requirement of singlet fission (eq. 2.178). Should this be true, these dyes would be very suitable for common applications of singlet fission, the most notable of which is in solar cells for multi-junction triplet sensitisation as previously discussed. However, in the following chapters, we shall demonstrate that these dyes do not show significant evidence of singlet fission due in all cases to loss mechanisms arising from common structural motifs associated with these pathways.

In the case of Pigment Red 254, we show that singlet fission is greatly out-competed by rapid picosecond-scale non-radiative decay via a conical intersection with the ground state, which is enabled via a hydrogen bond mediated proton transfer with adjacent molecules in the solid state. We demonstrate this via ultrafast transient absorption

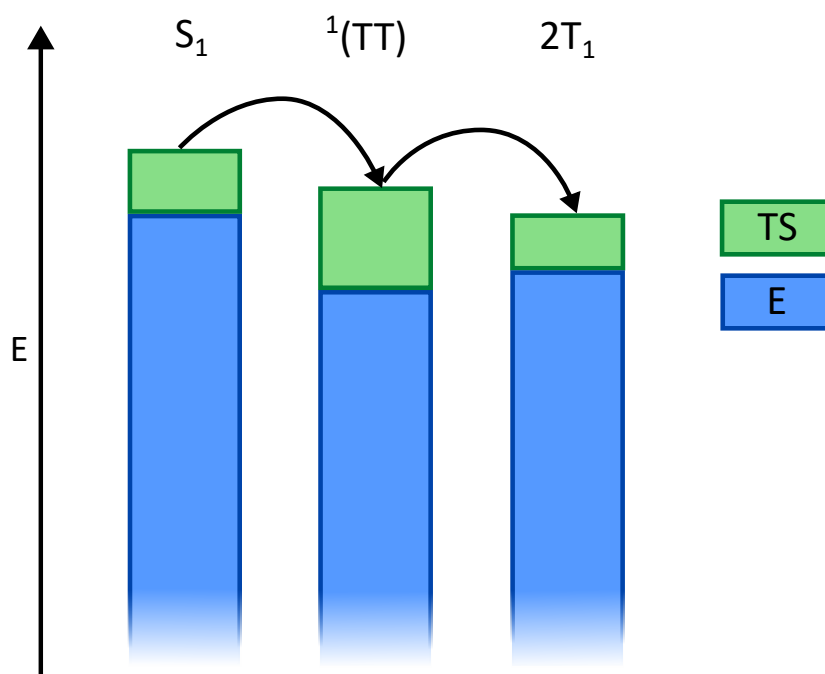


FIGURE 2.10: Energy level diagram showing the change in energy of the electronic states involved in singlet fission due to entropy. The base electronic energy levels (E) are shown in blue, and the contribution from entropy (TS) is shown in green.

and time-resolved infra-red spectroscopy. We demonstrate that this dye or a derivative thereof may be useful in a variety of photothermal applications.

In the case of BoDiPy 6 and 7, we demonstrate triplet production in both solution and solid states. However, due to the presence of triplet generation in the monomer (solution) transient absorption, as well as a pronounced heavy atom effect on the rate of triplet generation, we assign this triplet generation to heavy-atom induced intersystem crossing as opposed to singlet fission. We see a pronounced morphology dependence of the dynamics of the dyes in the solid state, with crystalline thin films showing no evidence of triplet generation in the case of BoDiPy 7, and showing a unique (between all dyes investigated) delayed fluorescence signal in its time resolved emission kinetics, suggesting some reverse triplet generation process is present.

Chapter 3

Methods

3.1 Sample preparation

Solid samples of Pigment Red 254 were prepared via thermal evaporation onto quartz coated glass, sapphire, calcium fluoride or silicon substrates (Ossila), while samples of BoDiPy 6 and BoDiPy 7 were prepared via spin-coating from concentrated solution in toluene. Substrates were first cleaned by sonication at 60 °C for 10 minutes in de-ionised water mixed with Helmanex III cleaning concentrate, followed by pure de-ionised water, acetone, and isopropanol. They were then cleaned further with a Bioforce Nanosciences UV-Ozone cleaner for 10 minutes.

Vacuum deposition of Pigment Red 254 was performed using an Angstrom Engineering vacuum deposition kiln with a target thickness of 200 nm at 0.2 \AA s^{-1} for UV-Vis samples, using PID control and thickness measured using a quartz microbalance. Sample thickness was measured using a Bruker DekTak profilometer to be ~ 40 nm. Samples of Pigment Red 254 on calcium fluoride substrates for infra-red measurements were prepared with a thickness of 80 nm.

Solution samples of Pigment Red 254 were prepared by adding 3 ml of dimethyl sulfoxide (DMSO) to 10 mg of dye in a glass vial. At this time, no solvation was visible. A magnetic stirrer bar was added to the mixture which was then stirred at 2000 rpm and heated to 195 °C using a hot plate under a ventilated fume hood. The cap was left on (unscrewed) to promote condensation of any vapours that arose. After 15 minutes, the solvent changed to a visibly yellow colour, indicating dissolution. Even so, there was undissolved solute remaining, as Red254 is very insoluble even in DMSO, and was filtered from the solution using a PTFE syringe filter. This solution was then diluted using DMSO by 100 times for use in transient absorption spectroscopy.

Once the solubility of Red254 was known, solution samples for concentration dependent emission were prepared by first producing a stock solution, with a concentration of $50 \mu\text{g/ml}$, by adding $800 \mu\text{g}$ of Red254 pigment to a glass vial, then covering with 16 ml of DMSO. Sample was then heated, stirred, and filtered as described above. Samples for steady-state spectroscopy were prepared by diluting the stock sample by 10 times ($5 \mu\text{g/ml}$), 100 times (500 ng/ml) and 1000 times (50 ng/ml) in order to test the concentration dependence of the sample emission. Steady state emission spectra were taken as described below with samples prepared in 1 mm thickness cuvettes (for the $50 \mu\text{g/ml}$ and $5 \mu\text{g/ml}$ samples) and 10 mm thickness cuvettes (for the 500 ng/ml and 50 ng/ml samples).

Solution samples of BoDiPy derivatives were prepared by dissolving the dye in a 5 mg/ml stock solution in toluene. For UV-Vis measurements, the sample was then diluted by 100 times in toluene for a final solution concentration of $50 \mu\text{g/ml}$. The solution was then prepared in a 1 mm cuvette as described above for Red254.

For amorphous thin films of BoDiPy derivatives, quartz-coated glass substrates were prepared as described above. Films were spin-coated using $40 \mu\text{l}$ of the 5 mg/ml stock solution at 2500 rpm for 45 s. More highly crystalline samples of BoDiPy derivatives were fabricated via thermal annealing of spin coated samples. Annealed samples were found to be less absorbing than amorphous samples, and thus were spin-coated using a higher concentration sample, of 25 mg/ml . After spin-coating, these films were heated to 130°C and annealed for 20 minutes, resulting in a highly polycrystalline film with visible spherulites.

3.2 Steady-state spectroscopy

Absorption and emission measurements of thin film samples, as well as the solution emission of the Pigment Red 254 solution and the absorption and emission of the BoDiPy derivatives were taken using an Ocean Insight Flame fibre coupled mini spectrometer. For the absorption spectrum, the light source used was a Halogen-Deuterium Ocean Insight DH 200 BAL lamp. The absorption spectrum was inferred based on the percentage transmission of the lamp's light through the sample. The light source used for emission measurements was a 405 nm CW semiconductor diode laser with laser power 2.85 mW.

Absorption measurements of Pigment Red 254 in solution of DMSO were performed using a Horiba Fluoromax 4 spectrofluorometer.

Concentration dependent emission spectra were taken using the same CW laser setup as used for the thin film steady state emission measurement. The concentrations used

are described above, being 50 $\mu\text{g}/\text{ml}$ and 5 $\mu\text{g}/\text{ml}$ in 1mm cuvettes and 500 ng/ml and 50 ng/ml samples in 10mm cuvettes.

3.3 Transient Absorption Spectroscopy

Transient absorption is a technique for investigating the dynamics of molecules in the excited state, using white supercontinuum laser light to probe the time-resolved UV-Vis spectrum of the material at a time t after an initial excitation or pump at time t_0 . Highly temporally resolved pump laser pulses, of a wavelength at which the material to be investigated absorbs is focused onto a thin sample of the material, either as a dilute solution in a thin cuvette or in thin-film format, prepared on a transmissive substrate via spin-coating, drop casting, or spray coating from solution onto the substrate, or via vacuum deposition from the solid state. The transmitted light is then dumped onto a beam block to prevent it reaching the detectors.

The probe beam is prepared by focusing an intense beam with a repetition rate twice that of the pump beam, in the cases explored in this work at 800 nm, onto a crystal of either sapphire or calcium fluoride to produce a broad coherent spectrum of light via non-linear light-matter interactions. In particular, second- and third-harmonic generation, as well as spectral broadening and temporal narrowing of these harmonic peaks, contribute to producing a spectrum that spans between ~ 350 nm and ~ 700 nm. The pump for the white light generation is filtered out of the resulting white light spectrum and is then also focused onto the sample, and made to overlap with the focused spot of the pump laser.

Either via an electronic synchronisation signal or through a spatial delay applied via changing of the optical beampath and adjustable via the use of a movable delay stage, the delay of the probe pulse with respect to the pump pulse t is adjustable. The transmitted white light spectrum is collimated and focused into the spectrometer optics. This spatiotemporal overlap is shown in Fig. 3.1.

The transient absorption signal is found by taking a difference spectrum between the transmitted spectrum without the pump pulse triggering and the transmitted spectrum when the material has been pumped by the less-frequent pump pulse. Transmittance is measured as the ratio of the measured intensity of light before and after the light is transmitted

$$T = I/I_0. \tag{3.1}$$

The change in transmittance, therefore, is given by

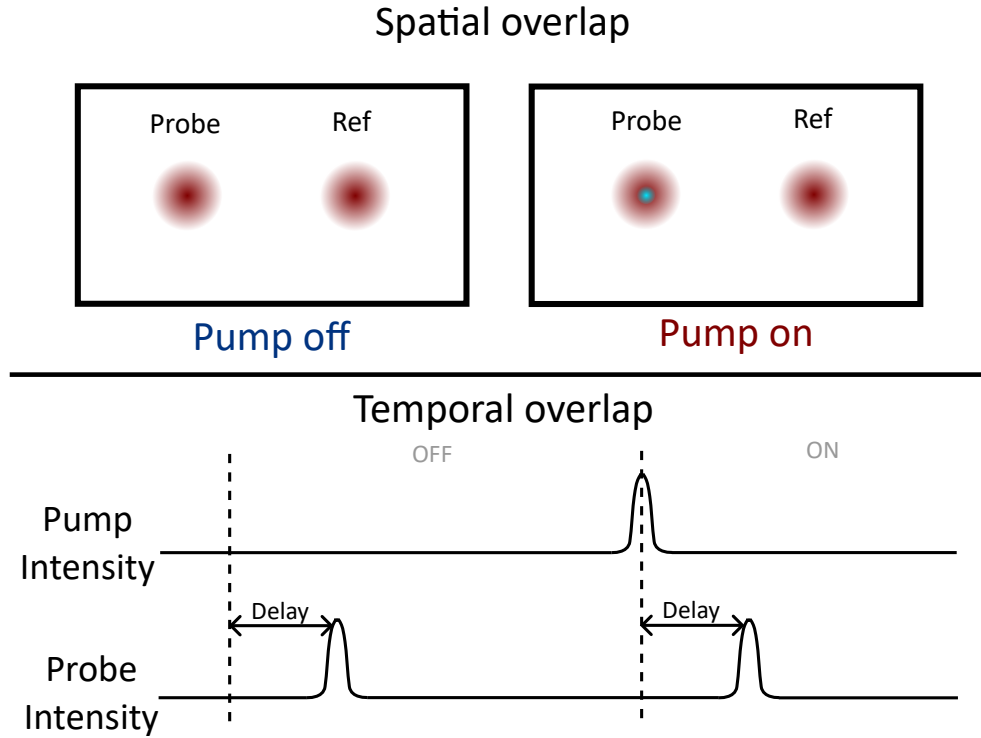


FIGURE 3.1: Schematic representation of the spatial overlap (top) and temporal overlap (bottom) of the pump and probe beams in pump-probe spectroscopy. Two probe type beams, marked "probe" for the pumped beam and "ref" for an unpumped reference beam are shown in the upper figure, as this setup is used in the Solstice setup detailed below. The temporal overlap is shown over one full TA cycle, with and without the pump. It is worth noting that the two pulses, pump on and pump off, are not necessarily sequential.

$$\Delta T = \frac{I_{ON}}{I_0} - \frac{I_{OFF}}{I_0} \quad (3.2)$$

where I_{ON} is the intensity measured with the pump laser on, and conversely for I_{OFF} .

As the untransmitted intensity is not typically measured, the above equation can be multiplied by $T_{OFF}^{-1} = I_0/I_{OFF}$, and thus the parameter measured is not ΔT , but rather

$$\frac{\Delta T}{T} = \frac{I_{ON}}{I_{OFF}} - 1 \quad (3.3)$$

Alternatively, the transient absorption signal can be presented in units of absorption, as

$$T = 10^{-A} \quad (3.4)$$

Thus, we can state that

$$\Delta A = -\log_{10} \left(\frac{I_{ON}}{I_{OFF}} \right) \quad (3.5)$$

Whichever way the signal is represented, once the signal from the transmitted white light laser is detected, the signal may be optimised by varying the position of the focused spot on the sample, as well as the relative delay between the pump and probe pulse. The zero time (t_0) for taking measurements is then set according to the rise time of the signal.

Once the signal has been found, the power of the pump and probe beam can be adjusted via filters to the desired levels, and the polarisation of the probe light can be set to minimise anisotropy effects from the material, using a half wave plate and a Glann-Taylor prism to set the polarisation of the probe to 54.7° of the pump beam. In addition, pump power and beam spot statistics should be recorded at this point for fluence- or excitation density-dependent measurements.

Measurements can be recorded now by choosing an array of time points using the electronic delay or physical delay stage, and the transient absorption ΔA or $\Delta T/T$ signal is recorded using the spectrometer at each wavelength, producing a 2 dimensional temporally and spectrally resolved dataset which traces the decay of the pumped excited state spectra with time.

Various data processing techniques should then be applied to the dataset, including chirp correction, which involves fitting a polynomial to the data to correct for spectrally resolved time-zero differences, background correction, to remove any non-time-resolved signal from the data, and pump removal, to remove the region of the spectrum at the pump wavelength to prevent contamination of the dataset from the scattered light of the pump laser.

In interpreting this resulting time-resolved spectrum, there will be 3 common types of signal that will be observed. The first is referred to as Ground State Bleach (GSB). This arises as the sample is excited by the pump laser, there will be fewer chromophores present in the ground state. This will result in a reduction or bleach at the absorption band of the material, as more light is transmitted there in the excited state. This can often be easily found by comparing the spectral location with the absorption spectrum of the material.

The second is Stimulated Emission (SE). In molecules which exhibit fluorescence, emission of light will be associated with a reduction in absorption, as more light will be seen at this wavelength than in the ground state. However, spontaneous emission will not be seen as it will not be temporally resolved. For a molecule in the excited state,

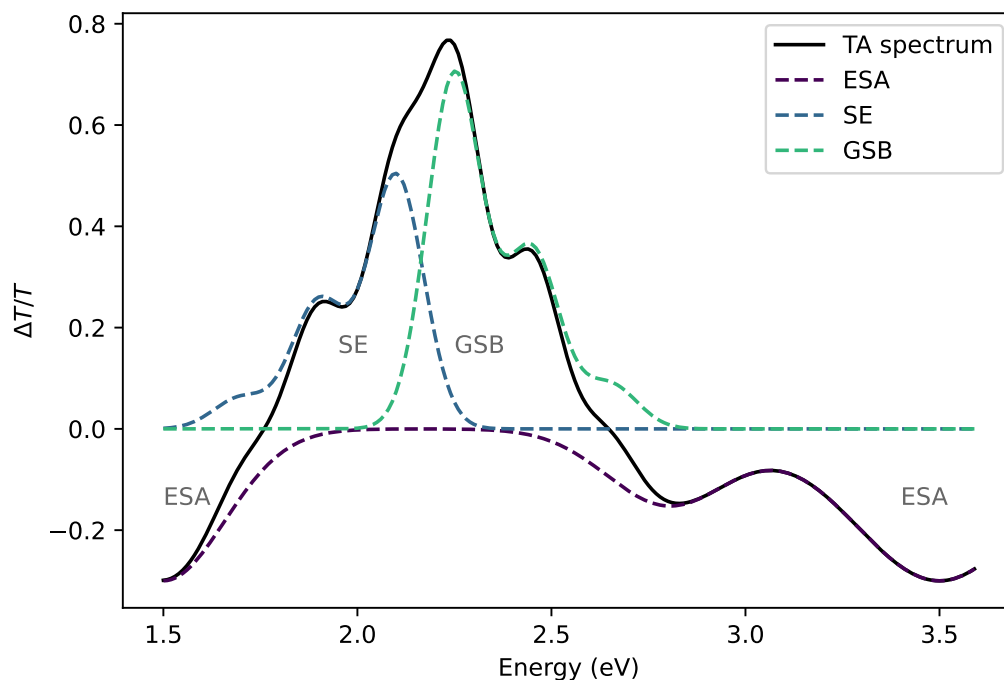


FIGURE 3.2: Example transient absorption spectrum, constructed from summation of gaussian models. Shown are typical configurations of Ground State Bleach (GSB) features, Stimulated Emission (SE) features, and multiple Excited State Absorption (ESA) features.

incident light from the probe beam can induce the sample to emit via stimulated emission, causing the SE feature in the TA to be observed at the emission wavelength of the sample.

The final type of signal is PhotoInduced Absorption (PIA) or Excited State Absorption (ESA). This signal arises because when the molecule is in the excited state, the incident probe beam can be absorbed by transitions from the excited state to higher excited levels. This results in a reduced transmission of light at these wavelengths as more light is absorbed, resulting in a signal opposite to that of the GSB and SE features.

A typical transient absorption spectrum will have all of these features overlapped with one another. Often these features will not be easily resolved, and more complex analysis is required to separate these features. This is illustrated by the simulated TA spectrum shown in Fig. 3.2.

This technique is also usable with broad infra-red spectra as probe light, allowing excited state measurements of the vibrational absorption, with two key differences. The first is, as with many infra-red techniques, that the experimental setup must be purged from water vapour, as water is a highly infra-red active molecule, and will significantly contaminate the IR spectrum. Secondly, infra-red spectra are often much broader than visible spectra, and to scan multiple vibrational features, it is common to have multiple

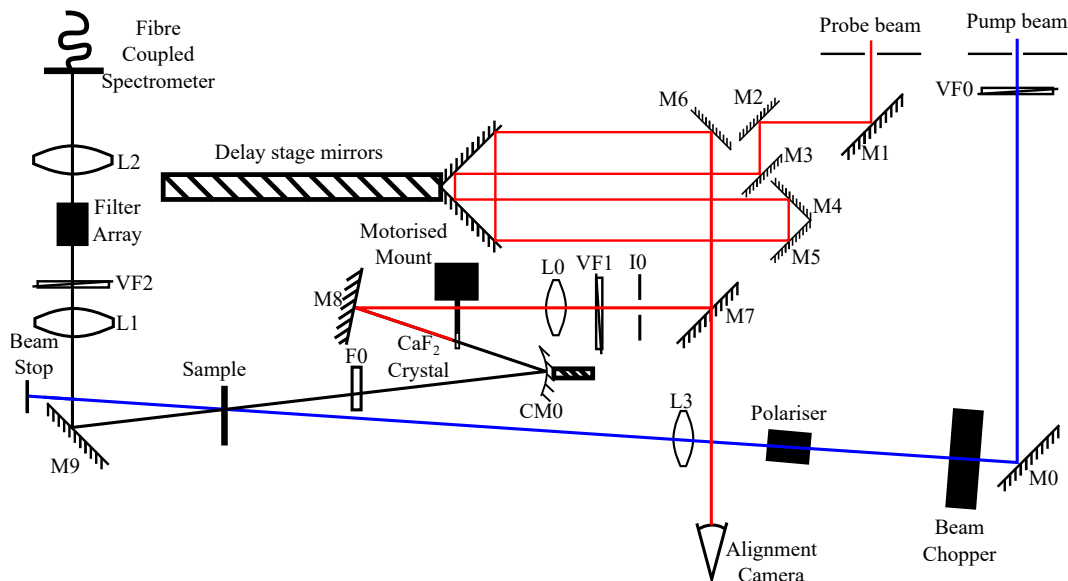


FIGURE 3.3: Ultrafast Systems Helios transient absorption spectrometer used for femtosecond transient absorption measurements. Key for abbreviations: M: Mirror, CM: Curved Mirror, L: Lens, F: Filter, VF: Variable Filter, I: Iris.

spectrometers to measure a broader spectrum of light. In this case, this technique is referred to as Time-Resolved Infra-Red spectroscopy, or TRIR.

3.3.1 Femtosecond transient absorption spectroscopy

Femtosecond transient absorption spectroscopy was performed using an Ultrafast Systems Helios transient absorption spectrometer, described in detail elsewhere [62], and its beam path is shown in Fig. 3.3.

Ultrafast femtosecond laser pulses are generated through exploiting the dispersive properties of chirped optics, which can compress seed pulses by preferentially slowing certain spectral regions of the input. One way this is done is using self-phase modulation via the nonlinear Kerr effect to shift the leading and trailing temporal edges of the pulse to longer and shorter wavelengths due to the varying refractive index induced by the pulse as it propagates. This allows the pulse to be either dispersed or compressed by using normal or anomalous dispersion, permitting the generation of ultrafast laser pulses.

These pulses can be generated directly in a lasing medium, or through the use of nonlinear processes. However, this can limit the power of the resultant pulses due to the damage threshold of the gain medium. To bypass this, a technique called Chirped Pulse Amplification is employed, which involves reducing the peak power of the pulse via the use of chirped optics, which also extend the pulse in time. Any desired amplification or nonlinear processes can then be applied to the lower peak energy beam, then the pulse

re-compressed to regain the peak power. Thus, high-power ultrafast laser pulses can be generated without damaging the gain media of laser, OPA, or other components.

The probe beam was generated using the output from an amplified 10 kHz Ti:Sapphire laser (Spectra Physics Spitfire Ace) at 800 nm to pump a calcium fluoride plate that produced a supercontinuum white light beam. The pump laser used was the output of a Light Conversion TOPAS Prime 10 kHz 80 fs parametric amplifier, driven by the output of the same Spectra Physics laser. The pump beam is triggered at 10 kHz also, however half of the pump pulses are removed using a synchronised beam chopper. This results in an overall repetition rate of 5 kHz, half that of the probe laser.

The data for Pigment Red 254 was acquired at pump powers between 0.5–1 mW and pump diameters on the order of 700–1200 μm (probe spot 100–400 μm diameter). We observed no measurable fluence dependence. The pump wavelength used for these measurements was 532 nm.

Transient absorption spectra for the solution and amorphous solid samples of BoDiPy 6 and 7 were obtained with pump wavelengths of 520 nm, and pump powers of 500 μW . Transient absorption spectra of the crystalline samples of BoDiPy 6 and 7 were taken with varied pump wavelength and power, to excite both to the primary absorption $S_0 \rightarrow S_1$ and the secondary weaker absorption seen in the steady state absorption spectra $S_0 \rightarrow S_2$. To this end, TA was done on these crystalline samples at both 400 nm and at 530 nm. The pump powers used for the acquisition of the fluence dependent transient absorption spectra, as well as the beam parameters and resultant beam energy densities are summarised in Tables C.1 and C.2.

3.3.2 Nanosecond transient absorption spectroscopy

Nanosecond transient absorption spectroscopy of Pigment Red 254 is performed using the output from a 1 kHz 90 fs Spectra Physics Solstice ultrafast amplifier at 800 nm to pump a sapphire plate, generating a broadband white light spectrum from ~ 450 –700 nm. Residual fundamental is filtered out with a shortpass filter. This white light supercontinuum is split with a 50/50 beamsplitter and used as a probe and reference beam for the transient absorption measurement. For a pump we used the second harmonic (532 nm) of an 800 ps Q-switched Nd:YVO4 Innolas Piccolo laser, externally triggered at 500 Hz.

Pump, probe, and reference are all focused onto the sample, and the pump and probe are overlapped with one another. The reference beam is focused ~ 1 cm from the pump and probe, to prevent the reference beam from detecting any pumped species. After exciting the sample, the pump is filtered out using a 532 nm notch filter. The magic angle of

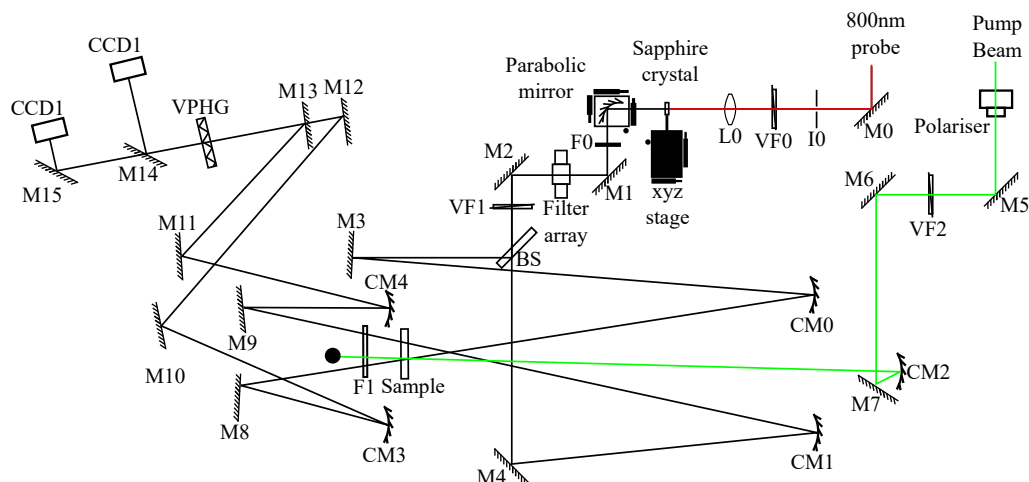


FIGURE 3.4: Schematic of the beam path of the long-time nanosecond scale transient absorption setup used in this work. Key for abbreviations: M: Mirror, CM: Curved Mirror, L: Lens, F: Filter, VF: Variable Filter, I: Iris, BS: BeamSplitter, CCD: Charge Coupled Device, VPHG: Volume Phase Holographic Grating.

polarisation between the two beams are set using a $1/2$ wave plate and Glann-Taylor prism.

After focusing onto the sample, the transmitted probe and reference beams are made incident onto a Wasatch volume phase holographic grating and made incident on two Hamamatsu S7030 silicon 1D CCDs (charge coupled devices). The resultant spectrum is calibrated using a filter wheel with 10 nm bandpass filters at 500, 600 and 700 nm. Acquisition is triggered at 1 kHz electronically using a Stanford DG645 digital delay generator, with data acquisition being triggered by a Entwicklungsbuero Stresing custom built data acquisition board. Triggering, data acquisition and preview, temporal overlap and device connection were all managed by home-built software. The resultant beam path schematic is shown in Fig. 3.4.

Solution data was acquired with a higher pump power than solid samples due to less concern of damage to the sample, at 2 mW. The data from the solid samples was acquired at pump powers between 0.4–0.8 mW and we observed no measurable fluence dependence at long time, as before.

3.3.3 Time Resolved Infra-Red Spectroscopy

Time Resolved Infra-Red (TRIR) spectroscopy of Pigment Red 254 was taken using the ULTRA spectrometer at the Rutherford Appleton Laboratory. The pump and probe beams are generated using a Femtolaser oscillator with a 20 fs pulse length and 50 nm bandwidth, which feeds a Thales Laser Ti-Sapph chirped pulse amplifier. The output

of this amplifier which was used gives 10 kHz frequency pulses with a 40-80 fs pulse at 0.8 mJ pulse energy, at a wavelength of 800 nm. These laser pulses are shaped by a telescope system to 0.6 cm, and sent through a compressor which can select pulse lengths of 1–3 ps.

The pump and probe beams are generated separately using the light conversion system, consisting of a set of Optical Parametric Amplifiers (OPAs) which allows the selection of a pump wavelength between 200–20000 nm with a pulse energy of 0.4 mJ. The pump wavelength used for these experiments was at 520 nm, and the power was adjusted to 0.5, 1, 2.5, and 5 mW for pump power dependent measurements. A 10 μ J portion of the Thales amplifier output is used to generate a broad infra-red white light spectrum within this same region. The light range used in these measurements were 1300–1900 cm^{-1}

The triggering between the two beams were adjusted by modulating the repetition rate of the pump from 10 kHz to 5 kHz, using a TTi C-995 phase chopper. The delay between the two beams are set using multiple Newport IMS600LM delay stages, to physically induce delay.

The detection system used is a pair of 256 pixel InGaAs detectors which are aligned in post-processing to probe a broad range of the infra-red spectrum. Further details of the setup and other uses of the ULTRA spectrometer are given in Greetham et al. [63].

3.4 Temperature dependent absorption

Temperature dependent absorption measurements of solid state thin films of Red254 on sapphire and quartz-coated glass were performed by attaching each sample to a brass flow-through sample holder connected to a water immersion heater. The room-temperature absorption spectrum was acquired using a Cary50-Bio spectrofluorometer at high sensitivity acquisition settings, with an average time of 10 s, a spectral resolution of 5 nm, a scan rate of 30 nm/min, and a wavelength range of 400-680 nm. The temperature of the water bath was then incremented by 5 °C, and the temperature on the back face of the sample measured using a mercury thermometer. Hot absorption spectra were measured using the same settings and subtracted from the room temperature spectrum to give temperature dependent difference spectra.

3.5 Resonance Raman Scattering

For free-space ultra-low frequency Raman spectroscopy of Pigment Red 254, the sample is placed on a motorised xyz stage (STANDA-8MTF). The sample is excited using a

532 nm single mode solid state diode pumped laser (Cobolt, 04-01) with a 10 cm^{-1} Bragg notch filters (OptiGrate, BragGrate) used to filter the excitation beam. The beam is then focused onto the sample using a $50\times$ objective (M Plan Apo $50\times$, Mitutoyo), with numerical aperture = 0.55, providing a spatial resolution of $\approx 1\text{ }\mu\text{m}$. Laser power at the sample is typically 0.5 mW (Power density $\approx 6.34 \times 10^4\text{ W cm}^{-2}$).

Emission is collected by the same objective. The laser line is attenuated with further 10 cm^{-1} Bragg notch filters and is then coupled to a spectrometer (Princeton Instruments, SP2750) equipped with a high-sensitivity liquid nitrogen cooled charge-coupled device (Princeton Instruments, PyLoN). A 1800 g/mm grating used provides a spectral resolution of $\approx 0.4\text{ cm}^{-1}$. Polarisation optics in both excitation and collection beam paths allow the measurement of co-linear and cross-linear polarisations.

Raman scattering was performed by Daniel J. Gillard of the University of Sheffield.

3.6 Atomic Force Microscopy (AFM)

Atomic force microscopy (AFM) was taken using a Dimension 3100 (Veeco) microscope, equipped with a Nanoscope 3A feedback controller and a Scout 350 RAI (NuNano) cantilever. The resonant frequency of this cantilever was 350 kHz and its spring constant was 42 N/m. The data was processed using Gwyddion Version 2.60 [64], by aligning rows in the software via the median method, levelling the data via mean plane subtraction, correcting for horizontal scars and applying a zero correction. RMS roughness values were extracted using the 1D method used in the Gwyddion software extrapolated to 2D, using the equation

AFM was performed by Rachel Kilbride of the University of Sheffield.

$$R_{RMS} = \sqrt{1/N \sum_{ij}^N r_{ij}}, \quad (3.6)$$

where N is the number of image pixels and r_{ij} is the height of the image at index ij . The resultant AFM image is shown in Fig. 4.1(b).

3.7 Grazing Incidence Wide Angle X-ray Scattering (GIWAXS)

Grazing incidence wide X-ray scattering (GIWAXS) at I07 (Diamond Light Source, Rutherford, U.K.) were performed at an X-ray beam energy of 12.4 keV. Scattering patterns were recorded on a vertically-offset Pilatus 2M detector with a sample to detector distance of 635.62 mm, calibrated using a silver behenate standard to achieve a Q range of 0.045–2.1 \AA^{-1} . Alignment was performed via three iterative height (z) and rocking curve (Ω) scans, with the final grazing incidence angle set to $\Omega = 0.3^\circ$. The two-dimensional scattering patterns were masked to remove the sample horizon, detector module gaps and beam-stop and radially integrated from the apparent beam centre.

Grazing incidence small- and wide-angle X-ray scattering (GIWAXS) at the University of Sheffield were performed on the Xeuss 2.0 instrument equipped with an Excillum MetalJet liquid gallium X-ray source. Alignment was performed on silicon substrates via three iterative height (z) and rocking curve (Ω) scans, with the final grazing incidence angle set to $\Omega = 0.2^\circ$. Scattering patterns were recorded on a vertically-offset Pilatus 2M detector with a sample to detector distance of 0.323 mm for Pigment Red 254 and 0.313 mm for the BoDiPy dyes, calibrated using a silver behenate standard to achieve a Q -range of 0.1–2.0 \AA^{-1} . Two-dimensional images were recorded with exposure times of 600 s. The images were masked to remove the sample horizon, detector module gaps and beamstop, and radially integrated from the apparent beam centre.

Data correction and reduction was performed using the GIXSGUI MATLAB toolbox.[65] Two-dimensional scattering data was reduced to one-dimensional via radial integration, which was performed with a mask to remove contributions from “hot pixels”, the substrate horizon, and reflected beam.

GIWAXS was performed by Daniel T. W. Toolan of the University of Sheffield, both at the University of Sheffield and the Diamond Light Source.

3.8 Quantum Chemical Calculations

Quantum chemistry calculations have been done with the Gaussian16 suite of programs[66]. The molecular geometry used in these energetic calculations followed the structure found via X-Ray powder diffraction methods by Ivashevskaya [67] IR spectra were obtained from the calculated DFT intensities and the vibrational wavenumbers uniformly scaled by 0.96[68]. Every band was represented by a Gaussian function of 10 cm^{-1} half-height width.

Quantum chemical calculations were performed by Dr. Samara Medina Rivero of the University of Sheffield, with assistance from Daniel Hook.

3.9 Fourier Transform Infra-Red Spectroscopy

Fourier transform infrared spectroscopy (FTIR) is a method of measuring the change in a broad infrared spectrum of light as it passes through a material, and is analogous to UV-Vis spectroscopy in that it can measure the light absorption of a sample. While very few atoms or molecules have low enough energy transitions to absorb the infrared light electronically, the vibrational modes of a molecule can be IR active and absorb light. This can be used to probe the chemical structure of a molecule by measuring typical bond absorption.

FTIR is performed with the use of a Michelson Interferometer^[69], an optical setup which consists of a beamsplitter to generate two paths or *arms* of the interferometer, each with a retro-reflecting mirror. One of these mirrors is mobile and can be moved back and forth in the directions of propagation of the laser, and one is fixed. These beams are then recombined at the beamsplitter and made incident on a detector. An interferogram is formed by translating the movable mirror, as the differences in phase of the light at different mirror positions and optical path lengths will result in constructive and destructive interference between the beams from the different arms of the interferometer.

Different wavelengths of light will have different phase differences at different path length differences which will result in a complex interferogram comprised of many different frequency components. This interferogram can be processed to find the spectrum of the beam of light in reciprocal space using a Fourier transformation, which will give the spectrum of the light intensity as a function of wavenumber (cm^{-1}), the typical format for an infra-red spectrum.

Apart from the use of the interferometer and the Fourier transform, this experiment can be run in the same manner as an absorption spectrometer, by measuring the difference in the IR spectrum with and without the thin sample in place. In this manner, an infrared absorption spectrum can be obtained.

Fourier transform infra-red spectroscopy (FTIR) on thin film samples of Pigment Red 254 on calcium fluoride substrates was performed using a Nicolet iS10 FTIR spectrometer purged with nitrogen to prevent infra-red absorption from water vapour.

3.10 Time Correlated Single Photon Counting (TCSPC)

Time Correlated Single Photon Transfer (TCSPC) is a method of measuring the emissive decay lifetime of a sample with high sensitivity. Using a laser that is triggered from the TCSPC electronics, the sample is excited in the same manner as standard emission spectroscopy. However, instead of the resultant emitted light being sent to a spectrometer, it is instead filtered through a monochromator to remove all scattered pump light and select the emission wavelength that is desired. This light is taken from the output of the monochromator and made incident onto an avalanche photodiode detector. This detector is formed of a capacitor which is simultaneously triggered with the laser, at which time it begins to increase the charge stored on it. On the detector receiving a single photon, this is enough to trigger the discharge of the capacitor, releasing a charge that is proportional to the time since the triggering of the laser. Even for low emission, over time, the time-resolved single photon emission detection will build up a kinetic trace of the decay.

Due to the specifics of this technique, the light emitted and especially the scattering and background light, must be kept low, as a large enough photon flux at the detector can saturate it, ensuring a photon always reaches the detector at early times, leaving the later time emission completely immeasurable.

TCSPC measurements of BoDiPy 6 and 7 were performed using a Picoquant LDH P-C 510b semiconductor diode laser, together with a monochromator which allowed the selection of a specific wavelength of light from the emitted spectra. The resultant monochromatic light is focused onto a Micro Photonic Devices avalanche photodiode, connected to a dedicated TCSPC card in the lab computer. Visualisation of the decay and acquisition was performed using the Timeharp 260 software.

3.11 Data Processing Algorithms

3.11.1 Franck-Condon

Franck-Condon fitting of steady state spectra was accomplished using a Franck-Condon fitting python module by Bossanyi [70]. Franck-Condon for Pigment Red 254 fitting was performed using effective vibrational modes extracted from the resonance Raman scattering spectrum in figure 4.2 (top-right) using the following weighted sum equation from Köhler and Bässler [3] for the effective Franck-Condon vibrational mode,

$$E_{vib}^{eff} = \sum_i E_i^{vib} \sigma_i^{Raman} / \sum_i \sigma_i^{Raman} \quad (3.7)$$

where E_i^{vib} is the vibrational energy of a particular resonance Raman mode i , and σ_i^{Raman} is the resonance Raman intensity of this i^{th} mode.

Franck-Condon fitting of BoDiPy steady state UV-Vis spectra was accomplished by using the vibrational mode wavenumbers as parameters, allowing them to vary freely.

Visualisation of molecular crystal structure of Red254 was accomplished using the open source Vesta 3D molecular plotting software[71]. The 2D chemical structure of Red254 was displayed using the PerkinElmer ChemDraw chemical drawing tool.

3.11.2 Multivariate Curve Resolution - Alternating Least Squares global fitting

Multivariate Curve Resolution - Alternating Least Squares (MCR-ALS) is a global fitting algorithm which uses the alternating least squares fitting algorithm to fit a 2-dimensional decay spectrum with a number of representative spectra equal to the expected number of species. The algorithm used to fit the decays of the BoDiPy picosecond TA spectra is the MCR-ALS MATLAB GUI toolbox by Jaumot et al. [72]. The initial spectra used for the fits are determined by the spectra at early times, between 1-2 ps, held to correspond to a mostly excited singlet state. The late time spectra used are between 3-5 ns, which is held to be mostly triplet state. No constraints were applied to the spectral fitting, as non-negativity, unimodality, closure, and equality do not apply to arbitrary spectra. Non-negativity was set to apply to the concentrations of each spectrum, as the concentration should never be negative for an electronic species.

Chapter 4

Pigment Red 254: a potential candidate for singlet fission

4.1 Introduction

Singlet fission is a form of multi-exciton generation in which one singlet exciton can produce two triplet excitons[73]. Generating two lower energy triplets per photon could overcome thermalisation losses in solar cells if properly harnessed. Therefore, singlet fission sensitised devices could bypass the fundamental single-junction thermodynamic limit, increasing the maximum achievable efficiency of solar cells from 33.7 % to ~45 % [32, 74].

However, the library of existing molecules which exhibit singlet fission is limited[75], and none are yet suitable for solar cell applications. In addition to simply undergoing singlet fission, candidate materials must have [32]: (1) good stability in oxygen-rich, humid, high fluence environments; (2) strong absorption in the visible region of the solar spectrum; (3) high triplet mobility and lifetime; (4) favourable triplet pair dissociation rates; and (5) triplet energies corresponding to efficient photovoltaic semiconductor bandgap energies (e.g. silicon). To these we add an additional condition: (6) facile synthesis and the possibility of cheap mass-production.

The process of experimentally screening materials for singlet fission and properties (1)-(6) is slow. To expedite this process, Padula *et al.*[1] developed an algorithm that uses big data, searching the Cambridge Crystallographic Database for solid-state materials that satisfy the basic criteria for singlet fission: $E(S_1) > 2 \times E(T_1)$ and $E(T_2) > 2 \times E(T_1)$, where $E(S_1)$ is the energy of the first singlet excited state (S_1) and $E(T_i)$ is the energy

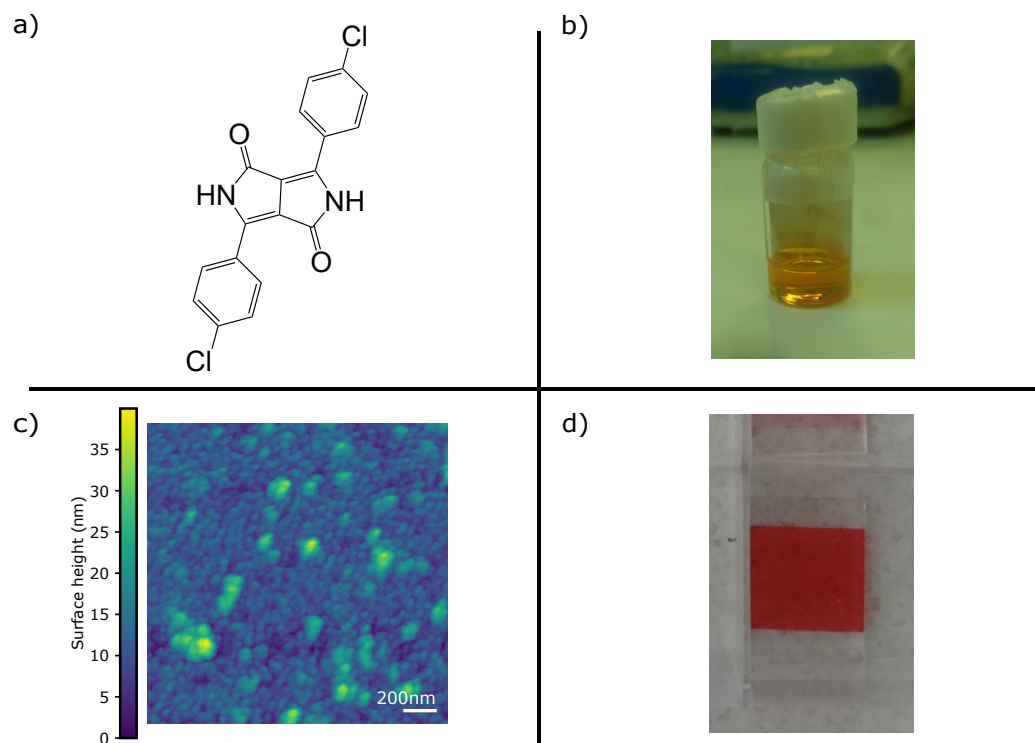


FIGURE 4.1: Structural data on samples of Red254. (a) molecular structure of Red254. (b) sample image of Red254 in solution of DMSO, (c) Atomic Force Microscopy (AFM) plot of thermally evaporated thin films of Red254 on quartz-coated glass. These films are visibly polycrystalline, with a height of 38.87 nm and an RMS roughness of 12.75 nm and (d) sample image of Red254 as a evaporated thin film on quartz-coated glass. The hypsochromic shift as the change in colour in solution vs solid states is easily visible; the solution transmits yellow light, whereas the solid predominantly transmits red light.

AFM was performed by Rachel Kilbride of the University of Sheffield.

of the i^{th} triplet state. The latter condition prevents intersystem crossing to a higher triplet state from occurring as a loss pathway.

One predicted result that shows exceptional stability, high absorption in the visible region, a predicted triplet energy of 1.20 eV and that is already cheaply mass-produced for commercial purposes is 4-bis(4-chlorophenyl)-2,5-dihydropyrrolo[3,4-c]-pyrrole-3,6-dione, also known as Pigment Red 254, p-Cl-DPP or Ferrari red, shown in Fig. 1(a, c). In this work this molecule will be referred to as Red254. Red254 is a diketopyrrolopyrrole derivative dye that is famously stable in hot, bright, humid environments; sufficiently so to be used as a pigment in car paint[76–80].

However, despite these excellent properties, and its favourable calculated energies for singlet fission [1], the excited-state dynamics of Red254 have not been comprehensively

investigated. Here we investigate the photophysical properties of Red254 and its potential as a singlet fission sensitiser. This work tests whether Padula *et al.*'s algorithm has sufficient information to predict singlet fission capability.

Red254 has not been investigated previously in part due to its insolubility[79, 81–83] in most organic solvents because of strong intermolecular interactions between molecules that promote aggregation and prevent formation of solution-processed thin films.

Red254 is soluble at low concentrations in some organic solvents, such as propylene glycol methyl ether acetate (PGMEA)[82], dimethyl sulfoxide (DMSO)[84] and 1-methyl-2-pyrrolidone[79]. However, the solubility limit is too low for film formation even from these solvents. Therefore, most studies on diketopyrrolopyrrole (DPP) molecules related to Red254 have focused on derivatives that have been designed to be more soluble, for example by substituting the side hydrogen groups of the core DPP for longer molecular chains, such as alkyl groups, or by polymerisation to form dimers.[79, 82, 85, 86].

Singlet fission has been observed in solution-processed thin films of DPP derivatives similar to Red254. Hartnett *et al.*, examined the singlet fission efficiencies of soluble 3,6-bis(thien-2-yl) DPP (TDPP), 3,6-diphenyl-DPP (PhDPP), and 3,6-bis(5-phenylthien-2-yl)-DPP (PhTDPP) derivatives [87]. Of these, they found that PhTDPP and TDPP underwent singlet fission via an excimer precursor. The PhDPP derivative did not undergo singlet fission. They correlated the lack of singlet fission in PhDPP with long $\pi - \pi$ packing distance ($\sim 3.9 \text{ \AA}$) as both PhTDPP and TDPP packed more closely ($\sim 3.5 \text{ \AA}$ $\pi - \pi$ stacking). PhTDPP in particular was found to undergo singlet fission with a high yield of $165 \pm 30 \%$. As the molecular $\pi - \pi$ stacking distance of Red254, 3.87 \AA [67], is similar to PhTDPP and TDPP, Red254 shows promise as a singlet fission sensitiser.

Investigation of TDPP was continued by Mauck, *et al.* by functionalising the NH side groups with methyl, n-hexyl, triethylene glycol and 2-ethylhexyl, in order to fine-tune the stacking of the molecules in polycrystalline thin films, and thus the intermolecular coupling and its effect on singlet fission.[88]. They found that for all but triethylene glycol-TDPP, an increase in the singlet fission rate and yield was linked to the coupling energy between adjacent molecules. The coupling energy is strongly effected by the π -stacking and slip-stack parameters of the crystal and is thus highly sensitive to complex intermolecular packing.

Further work emphasises the importance of intermolecular coupling in diketopyrrolopyrroles with Miller *et al.* [89] demonstrating the role that charge transfer and excimer states play in their excited state dynamics. They develop two models, one describing a charge-transfer mediated superexchange pathway to singlet fission, and another via

lower energy excimer which acts as a trap state when the charge transfer state energy is too high, slowing the rate of singlet fission. They test this model using the singlet fission rates and coupling parameters of Me-TDPP, C6-TDPP, EH-TDPP, PhDPP, PhTDPP, and a set of rylene derivatives. While many of these molecules' singlet fission rates are correctly predicted to within factors of 3-6, the molecules based on TDPP are much less accurate, off by factors of >10 . They attribute this larger error to oversimplifications in determining the energy of the excimer intermediate. This demonstrates both how easily DPP derivatives form excimer states and how integral they can be to their excited state dynamics, subject to the degree of coupling to different states and to other molecules.

We have summarised here the importance of small variations in intermolecular interaction strength to the excited state dynamics of many diketopyrrolopyrrole derivatives. However, due to the insolubility of unsubstituted diketopyrrolopyrrole derivatives, the effect of the strong hydrogen bonding present in these derivatives (including Red254) on their excited state dynamics have not been investigated. Investigation of the dynamics of Red254's excited state may elucidate how these intermolecular interactions can be exploited as a tool in opto-electronics.

Here we show that an observed long lived signal in Red254 is due to a thermal artefact arising from rapid non-radiative decay to the ground state, and demonstrate that this non-radiative decay is much more rapid than the trend defined by many similar diketopyrrolopyrrole derivative monomers. Therefore, we find that the prediction made by Padula *et. al.*[1] is incorrect in the case of Red254, as any potential singlet fission is out-competed by picosecond-scale non-radiative decay. In addition, the mechanism of non-radiative decay in the polycrystalline thin film is one much more rapid than a simple adiabatic gap law transition.

4.2 Results

4.2.1 Steady state characterisation

Due to the strong intermolecular hydrogen bonding in Red254[67, 86], solution processing solid films is unreliable. Here we study thin films made by thermal evaporation (details in the methods section). An atomic force microscopy (AFM) image of a typical film in Fig. 4.1c) indicates that films produced in this way likely have some crystalline character, with grain sizes on the order of 10s of nm. The photograph of a film in panel d) shows that the film is homogeneous and strongly absorbing.

Fig. 4.2(a) shows the steady state absorption and emission of Red254, both in solution of DMSO (top), and in sublimated thin film on quartz-coated glass substrate (bottom). The maxima of the 0-0 peaks of each transition are shown in Table 4.1. In addition, we have reproduced the values calculated by Padula *et. al.* for the singlet and triplet energies of Red254 in the solid state. In solution, we observe a small Stokes shift of the emission maximum with respect to the absorption of 61 meV, and the emission and absorption spectra show similar vibronic structure. The emission spectrum shown was taken at a concentration of 50 ng/ml, to minimise self-absorption effects, as explained below. The optical density of the absorption maximum of the solution sample was 0.39.

The solution absorption and emission spectra were further analysed by using a Franck-Condon fit. Using eq. 2.113, and taking the peak broadening (via the Gaussian contribution), 0-0 energy, vibrational mode energy, and Huang-Rhys factor as variables, as well as collecting linear scaling factors into an empirical scaling factor, the experimental spectra can be fit using a least-squares fitting algorithm, as described in the methods section[70]. This was applied to the absorption spectrum of the solution of Red254 in DMSO. The vibrational mode energies are fixed by considering resonance Raman measurements of the solid film of Red254 excited at 532 nm, shown in Fig. 4.2(b). From eq. 3.7, we can take a weighted mean of the modes seen in the Raman spectrum to give us these effective Franck-Condon modes, using the highest-wavenumber modes, between $1550\text{-}1600\text{ cm}^{-1}$ and $1300\text{-}1400\text{ cm}^{-1}$ to generate two vibrational modes to fit. The Huang-Rhys parameters were allowed to vary freely.

For the emission spectrum, the same vibrational modes were used, and instead the Huang-Rhys parameters were fixed, allowing only the 0-0 transition energy, broadening, and scaling factor parameters to vary. The resultant fits are shown as dashed lines overlaid with the solution absorption and emission spectra, and the fitting parameters are shown in Table 4.2.

Fig. 4.2(a) (bottom) shows the absorption and emission spectra of a sublimated film of Red254 on quartz-coated glass. The film has a maximal optical density of 0.34, and the maximum absorption energy is shifted by 0.15 eV compared to the solution. These spectra were not able to be fit with a Franck-Condon model in the same way as the solution spectra.

The emission yield in the thin film is significantly lower than the solution emission (the film emission was almost immeasurable on our setup, despite the strong absorption, and is relatively featureless with a tail extending to energies above the absorption edge at 2.2 eV. The low emission yield indicates a non-emissive pathway for excited state decay in the solid film. In addition to this featureless emission, a large Stokes shift of 330 meV suggests that either there is self-absorption present in the highly absorbing solid state

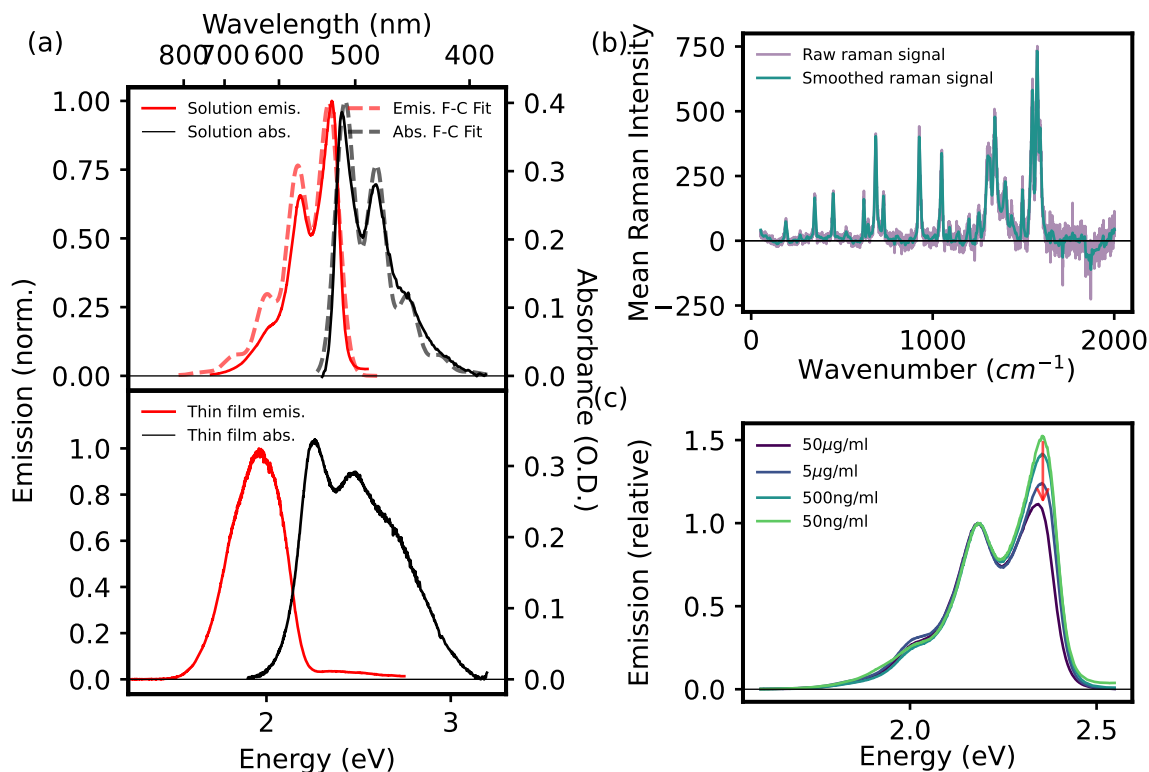


FIGURE 4.2: Steady state spectroscopic characterisation of Red254. UV-vis spectroscopy of Red254 is shown in subfigure (a), containing absorption and emission spectra of a solution phase sample of Red254 in DMSO (top) and absorption and emission spectra of evaporated thin films of Red254 on a quartz-coated glass substrate. The emission spectrum was taken with an excitation of 405 nm. The dashed line plots overlaid with the solution-phase spectra are Franck-Condon fits to the data, full details of which are displayed in the main body of text, in Figs. SA.1 and SA.2 and in Table 4.2. Averaged resonance Raman spectrum of thin films of Red254 on quartz coated glass substrates is shown in subfigure (b). This scattering spectrum was taken with an excitation wavelength of 532 nm. This spectrum is overlaid with a smoothed spectrum using fourier transform filtering to remove noise effects to make the peak locations clearer. The peaks used to generate the vibrational modes used in Franck-Condon fitting are the highest-wavenumber modes, between $1550\text{-}1600\text{ cm}^{-1}$ and $1300\text{-}1400\text{ cm}^{-1}$, generating effective modes using equation 2.113 Concentration dependence of the solution phase emission spectra with an excitation wavelength of 405 nm is shown in subfigure (c) to illustrate the effect of self-absorption. Raman scattering was performed by Daniel J. Gillard of the University of Sheffield.

thin film, or that there is a high level of molecular vibrational reorganisation in the excited state, which could be caused by such things as strong vibronic coupling[5, 21] or excimer formation due to strong dipolar coupling[21].

This type of intermolecular interactions are also shown in the solid state absorption spectrum, seen from its red shift and change in shape going from solution to thin film. The red shift is likely due to out-of-plane $\pi-\pi$ orbital overlap interacting with the $\pi-\pi^*$ transition energies in the film[87, 90–92], causing a reduction in the transition energy, which is common in diketopyrrolopyrrole derivatives. This is likely, as Ivashevskaya [67] demonstrates a relatively coplanar crystal structure for Red254 in the solid state. The

TABLE 4.1: 0-0 vertical (absorption) and adiabatic (emission) transition energies of Red254. Calculated singlet energy and triplet energies from Padula *et al.* [1].

	Solution Singlet	Solid Singlet	Calc. Singlet	Calc. Triplet
Abs. energy (eV)	2.41	2.26		
Em. energy (eV)	2.35	1.959	2.451	1.203

TABLE 4.2: Franck-Condon fitting parameters for Red254 steady-state solution spectra. Values presented with an asterisk (*) in the solution absorption indicate where fitting parameters were allowed to vary freely.

	0-0 En. (eV)	Vib. 1 (eV)	Vib. 2 (eV)	HR 1	HR 2	Overall RMSE
Abs.	2.426*	0.195	0.166	0.115*	0.662*	0.0567
Em.	2.339*	0.195	0.166	0.115	0.662	0.0343

broadening and non-Franck-Condon character of the absorption spectrum may be due to a number of factors, such as disorder in the polycrystalline film, including inhomogeneity such as the presence of crystal defects, or a non-typical distorted excited state potential energy surface altering the absorption characteristics of the film. This effect could originate from a number of sources, such as the presence of a charge transfer state close to the energy of the S_1 state[93, 94], which could affect the shape and nature of the excited state. The broadening of the excited state may also result from a dynamic shift due either to a large displacement of the excited state along a vibrational mode coupled to the excited state[3, 5], or to excimer formation[3], which has also been proposed as a source of the large stokes shift and weak vibration structure in the thin film emission spectrum.

Fig. 4.2(c) shows the change in normalised emission spectra of solutions of Red254 in DMSO for a range of concentrations: 50 $\mu\text{g/ml}$, 5 $\mu\text{g/ml}$, 500 ng/ml , and 50 ng/ml . This was taken to examine how solution spectrum used for steady state characterisation was affected by self-absorption effects. We observe a comparative reduction in the 0-0 peak of the emission as a function of increasing concentration, which indicates the onset of self absorption. The maximum of the secondary peak is found at 0.644 (in relative units to the first spectrum) at 50 ng/ml , at 0.700 (relative units) at 500 ng/ml , at 0.803 (relative units) at 5 $\mu\text{g/ml}$ and at 0.896 (relative units) at 50 $\mu\text{g/ml}$, forming an approximately logarithmic relation. We also observe a slight red shift of ~ 10 meV present only in the emission spectrum of a 50 $\mu\text{g/ml}$ sample, a telltale sign of self-absorption at the high energy edge. As a result we can confidently say that at 5 $\mu\text{g/ml}$ concentration and below, self-absorption has a reduced effect. For the steady state emission measurements in solution, we have used the lowest concentration of the prepared samples, to reduce self-absorption as much as possible.

4.2.2 Transient absorption spectroscopy

To test whether the significant non-radiative decay in Red254 thin films is due to SF, we used transient absorption spectroscopy (TA). As a control, we first measured the dilute solution of Red254 in DMSO, shown in Fig. 4.3, using a pump wavelength of 532 nm.

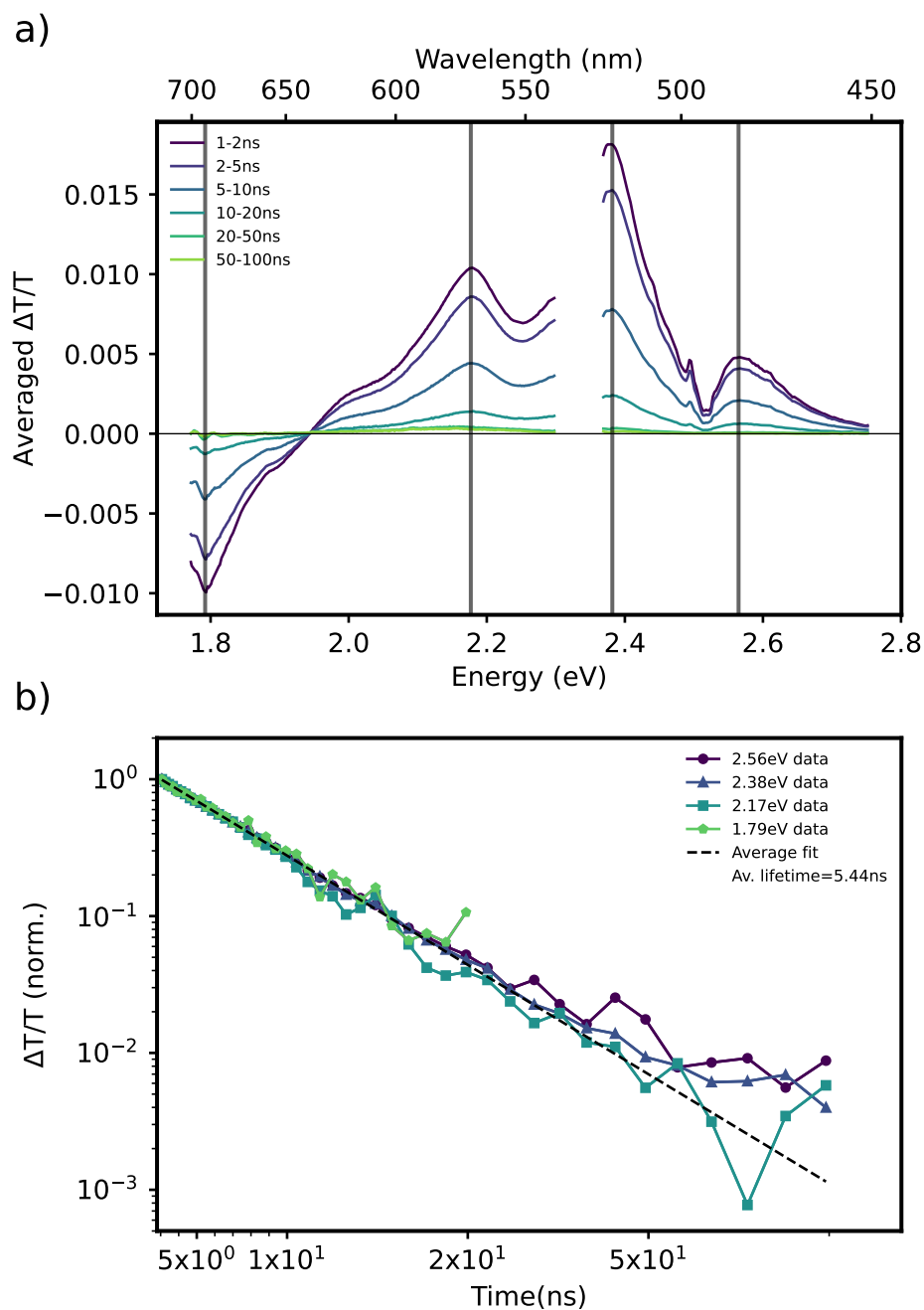


FIGURE 4.3: Nanosecond scale transient absorption (a) spectra and (b) kinetics of solution of Red254 in solution of DMSO, with an excitation wavelength of 532 nm. The energies used for the kinetics are marked by vertical lines on subplot (a). The kinetics are well fit by a mono-exponential decay with a lifetime of 5.44 ± 0.02 ns, representing the emissive lifetime of the Red254 monomer.

The solution-phase nanosecond transient absorption spectra are dominated by features from the S_1 population: the positive features correspond to Ground-State Bleach (GSB) and Stimulated Emission (SE) (they are overlapped with the ground-state absorption and fluorescence spectra in Fig. 4.1a, see Fig. A.6). The negative feature, peaking at 1.8 eV is an $S_1 \rightarrow S_n$ excited-state absorption feature, evidenced by the presence of an isosbestic point at $\Delta T/T = 0$ around 1.95 eV. The normalised kinetics of Red254 shown in Fig. 4.3(b) decay mono-exponentially ($\tau = 5.44 \pm 0.02$ ns). We conclude that in solution we observe only singlet decay with no evidence of triplets, tautomerization or other excited-state decay pathways.

The solid state TA spectra and kinetics, using the same excitation wavelength as the solution, show more complex behaviour than the solution. Fig. 4.4 (left) shows the TA spectra of Red254 sublimated thin film on quartz-coated glass substrate, on picosecond timescales (top) and on nanosecond timescales (bottom), and shows similar spectra in Fig. 4.4 (right) of Red254 sublimated thin film on a sapphire substrate. At early times (~ 10 -100 ps), the spectra on quartz-coated glass can be identified by comparison to the steady state UV-Vis spectroscopy, as before, with the positive feature corresponding to the GSB, matching the steady state absorption spectrum, and the negative feature at < 2.00 eV corresponding to ESA to higher singlet levels. There is no visible SE feature even at the earliest times, indicating that the population of the emissive state is sufficiently low even at early times that it is masked by the ESA feature. On nanosecond timescales (bottom), the spectra are more difficult to identify, and there appears to be a negative feature overlaid with the GSB (evident at ~ 2.1 eV and at ~ 2.6 eV). In addition, the negative ESA feature is no longer present, indicating the excited singlet state has been depopulated.

For the sample on the sapphire substrate shown in Fig. 4.4 (right), on picosecond timescales (top), there is little change to the spectrum, aside from an enhancement of the ESA, on nanosecond timescales (bottom) the positive features aside from the main central peak have been suppressed and in some cases (~ 1.8 eV, ~ 2.3 eV, 2.75 eV) have been overtaken by negative features. This difference is more clearly seen in the solid state transient absorption kinetics. Fig. 4.5 shows the kinetics of the sample on quartz (top) and on sapphire (bottom). The lifetimes of approximate fits to the decays of the GSB and ESA features are shown in Table 4.3.

The ESA features both decay mono-exponentially with lifetimes of the order of 10 ps. By contrast, the GSB feature is best described with an approximate bi-exponential decay model, which is described in full in Appendix A.

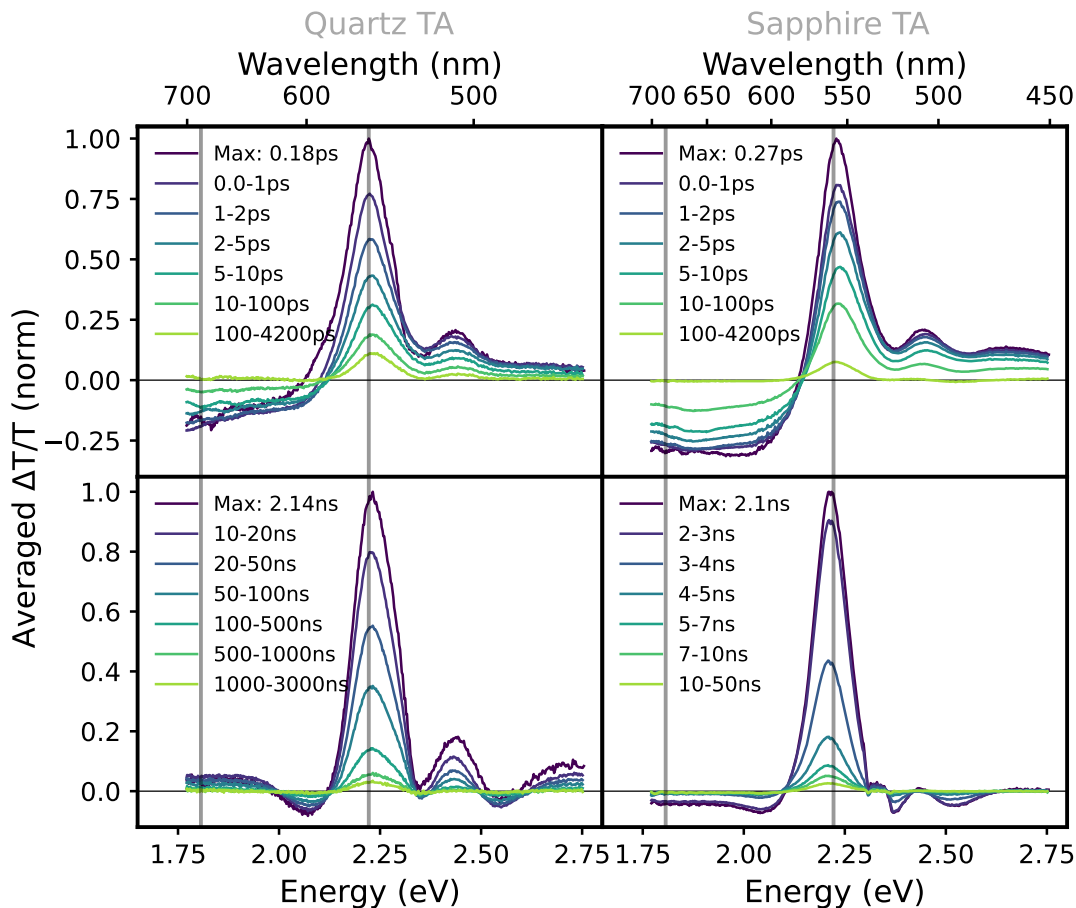


FIGURE 4.4: Transient absorption spectra of sublimated thin films of Red254 on quartz (left) and sapphire (right) at picosecond (top) and nanosecond (bottom) timescales with 532 nm excitation. The energies from which the kinetics (Fig. 4.5) were taken are shown on this figure in blue.

While this model is empirical and inexact, it allows us to identify the approximate timescales present in the complex decays of Red254 thin films. The short-lived component of the GSB has a lifetime of 5.4 ± 0.2 ps for the sample on quartz, and 4.0 ± 0.3 ps on sapphire. While these lifetimes are similar, the nanosecond-scale component varies more drastically with substrate, with the lifetime on quartz being 24 ± 3 ns, and the lifetime on sapphire being reduced by a factor of ~ 100 , to 154 ± 9 ps.

We suggest that the nanosecond-scale signatures are due to non-radiative decay populating vibrationally excited levels of the ground state, similar to that seen in Rao et al. [95] and Albert-Seifried and Friend [96]. This results in an artefact signal in the transient absorption spectra at long times, resulting from the hot ground state population causing a shift to the ground state absorption spectrum. In addition, this is the cause of the difference in the longer decay component of the biexponential fits to the data in Fig. 4.5 between the sapphire and quartz-based substrates. Sapphire has a thermal conductivity ~ 24 times that of quartz[97], and thus the vibrational energy is more efficiently

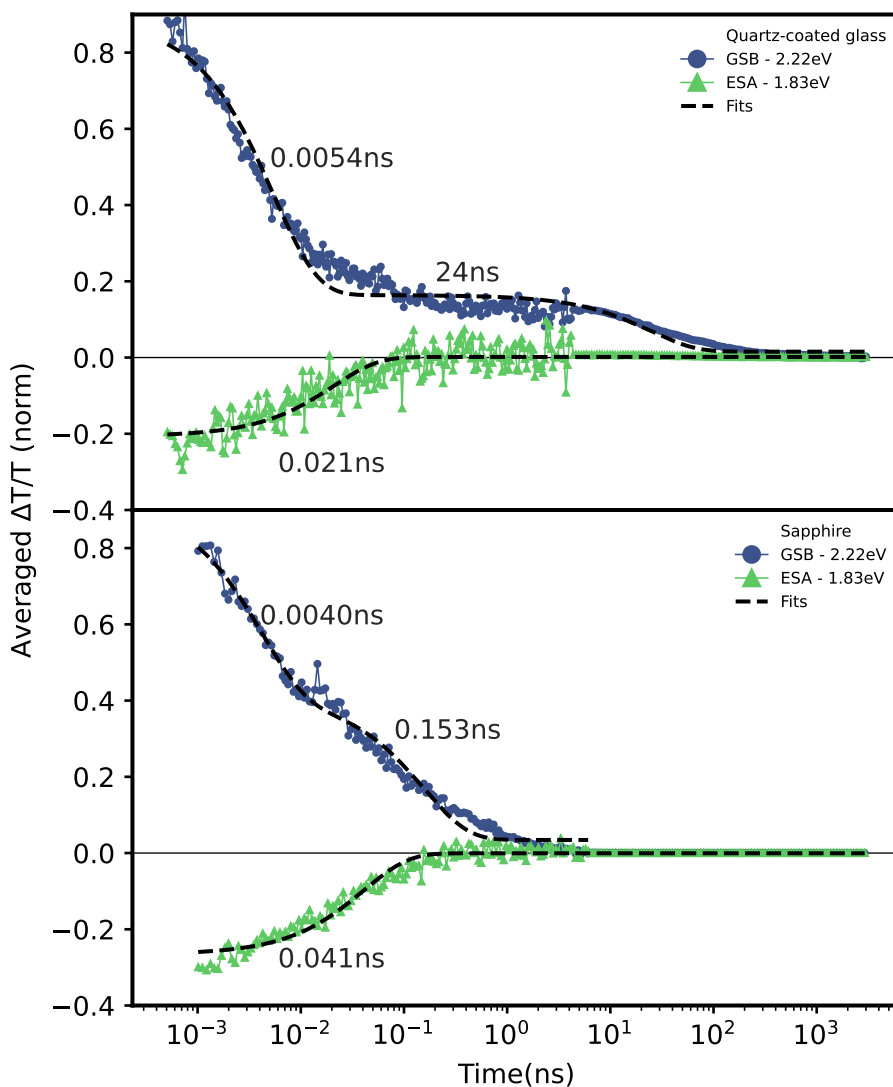


FIGURE 4.5: Transient absorption kinetics of sublimated thin films of Red254 on quartz-coated glass (top) and sapphire (bottom) substrates using a 532 nm excitation, with the data from picosecond and nanosecond timescales combined. The nanosecond-scale data has been normalised to its overlap with the picosecond-scale data. The kinetics of the two energies shown correspond to the primary peak of the GSB in the TA signal (2.22 eV) and the low-energy ESA feature (1.83 eV). While the ESA features can be fit with monoexponential decays with lifetimes of 21 ± 2 ps (quartz) and 41 ± 2 ps (sapphire), the GSB feature’s decays are best reproduced by a biexponential decay with the quartz decay having lifetimes of 5.4 ± 0.2 ns and 24 ± 3 ns and the sapphire substrate sample having a decay with lifetimes of 4.0 ± 0.3 ps and 154 ± 9 ps.

dispersed by this substrate in the form of heat, resulting in a faster decay of the hot ground-state signal.

This suggests that the second component results from a temperature dependent component being quenched by the higher thermal conductivity of sapphire. However, this

TABLE 4.3: Lifetimes and uncertainties of the decays of sublimated thin film samples of Red254 on quartz and sapphire substrates

	Excited-State Absorption		Ground state bleach			
	τ_{ESA} (ps)	$\delta\tau_{ESA}$ (ps)	τ_1 (ps)	τ_2 (ns)	$\delta\tau_1$ (ps)	$\delta\tau_2$ (ns)
Quartz	21	2	5.4	24	0.2	3
Sapphire	41	2	4.0	1.54×10^2	0.3	0.9×10^2

is not definitive, as it does not rule out substrate-sample interactions, nor explains the altered ESA signal.

4.2.3 Temperature dependent absorption

To verify this heating artefact, the temperature dependence of the ground state absorption of the thin film samples of Red254 is shown in Fig. 4.6, for both the quartz substrate sample (top) and the sapphire substrate sample (bottom). These plots were generated by taking the steady state absorption of the sample both at room temperature, and when heated to a range of temperatures shown in Table A.1. These heated ground state absorption spectra were subtracted from the room temperature spectrum. This is plotted together with the transient absorption spectra of the quartz and sapphire substrate for comparison. It is clear that the resultant difference spectra from the heated ground state absorption accurately reproduce the nanosecond transient absorption spectra, confirming that the long-lived transient absorption features result from a hot ground state.[95, 96].

As this hot ground state signal is the origin of the nanosecond-scale component seen in the TA data, we suggest that singlet fission does not occur in this molecule in the solid state.

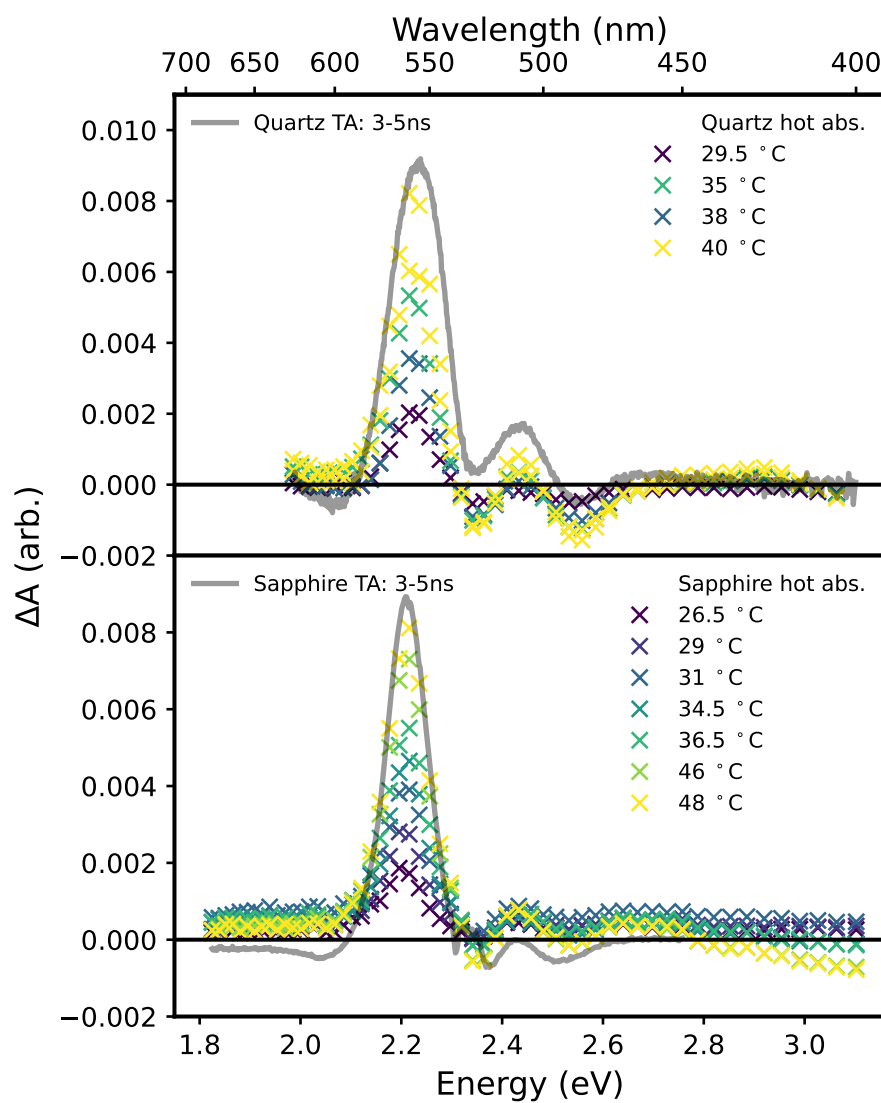


FIGURE 4.6: Temperature dependent difference spectra of sublimated thin films of Red254 on a quartz (top) and a sapphire substrate (bottom). The maxima of the ns transient absorption spectra as indicated in Fig. 4.4 (2.1 ns) are plotted on alongside their respective difference spectra to illustrate that the features of the TA spectra are reproduced by these difference spectra, as well as the differences between the quartz and sapphire substrates.

4.3 Discussion

With the transient absorption (TA) spectrum of Red254 on sapphire, as well as the temperature dependent absorption spectra, we have demonstrated that the nanosecond TA signal is due to a long-lived pump-induced thermal artefact. This suggests that solid films of Red254 possess an alternative decay pathway that out-competes any signal that may be due to singlet fission, and that if singlet fission does occur, it does so with a very low yield. The low fluorescence intensity and rapid initial decay in the solid state, which has an approximate lifetime of 5 ps, compared to the lifetime of 5.44 ns found for the excited state decay of the solution, indicates a rapid non-radiative decay pathway made available in the solid state, which results in the population of higher vibrational modes in the ground state, resulting in the pump-induced heating seen in the TA spectra. This pathway is likely associated with the intermolecular hydrogen bonding, as it is not observed in other diketopyrrolopyrrole derivatives for which the hydrogen has been substituted.

Mizuguchi and Wooden [94] performs a steady-state characterisation of three diketopyrrolopyrrole derivatives, including diphenyl diketopyrrolopyrrole, a very similar molecule to Red254. They associate the shape and red-shift of the steady state absorption spectrum with intermolecular hydrogen-bond mediated charge-transfer characteristics in the solid state, measuring the conductivity and absorption spectrum as a function of a strong basic additive tetrabutylammonium hydroxide (TBAH), finding that the disruption of the acidic hydrogen bonds by this base resulted in radical changes to the absorption spectrum. They propose a scheme by which strong charge transfer interactions between the N-H group and C=O group on the adjacent molecule result in greater electron density on the nitrogen atom and thus the pyrrole chromophore, causing a strong bathochromic shift. This model explains the non-Franck-Condon character of the solid state absorption spectrum, due to the presence of charge transfer interactions.

We propose that this interaction results in the observed rapid non-radiative decay, a scheme which will be expanded and investigated in the following chapter.

4.4 Conclusion

In conclusion, Pigment Red 254 does not exhibit singlet fission in the solid state, but rather undergoes rapid non-radiative decay to the ground state, with a lifetime of 5.4 ± 0.2 ps on a quartz substrate, which produces a population of vibrationally excited ground state species causing a nanosecond-scale thermal artefact in the transient absorption spectrum. On quartz substrates, this artefact has a lifetime of 24 ± 3 ns, and on sapphire

substrates, with a higher thermal conductivity, it has a lifetime of 154 ± 9 ps, two orders of magnitude shorter than on quartz. This indicates some pathway is activated by the intermolecular interaction between molecules in the excited state that is unavailable in the solution state.

Chapter 5

Infra-Red investigations of proton transfer in Pigment Red 254

5.1 Introduction

In the previous chapter we have demonstrated that in a poly-crystalline thin film, Pigment Red 254 undergoes a rapid non-radiative decay to the ground state that is not exhibited in the solution phase. We have shown that this non-radiative decay out-competes any potential singlet fission or triplet generation processes as well as radiative or gap-law mediated non-radiative decay, granting it its short excited state lifetime.

While this does prevent other complex excited-state mechanisms such as triplet formation from occurring, understanding the mechanism of non-radiative decay in Red254 is desirable to facilitate the intelligent engineering of future molecules, both to prevent non-radiative decay as a loss mechanism where a long-lived or radiative electronic excited state is preferable including charge generation, triplet formation, and OLED applications.

In addition, understanding the mechanism behind this rapid non-radiative decay is useful for applications where the non-radiative decay process itself is desirable. These may include photoprotection, in a mechanism similar to that shown by DNA nucleotides, as well as phototherapeutic applications, exploiting the generation of heat by non-radiative decay for photo-induced ablation of organic tissue such as cancer cells[98].

The energy gap law dependence of non-radiative decay is described in depth in Section 2.3.5.1. As we find that non-radiative decay is sufficiently rapid to out-compete singlet fission in the case of Red254, and as the semi-empirical gap-law could be used to screen large datasets such as the Cambridge Crystallographic Database for singlet

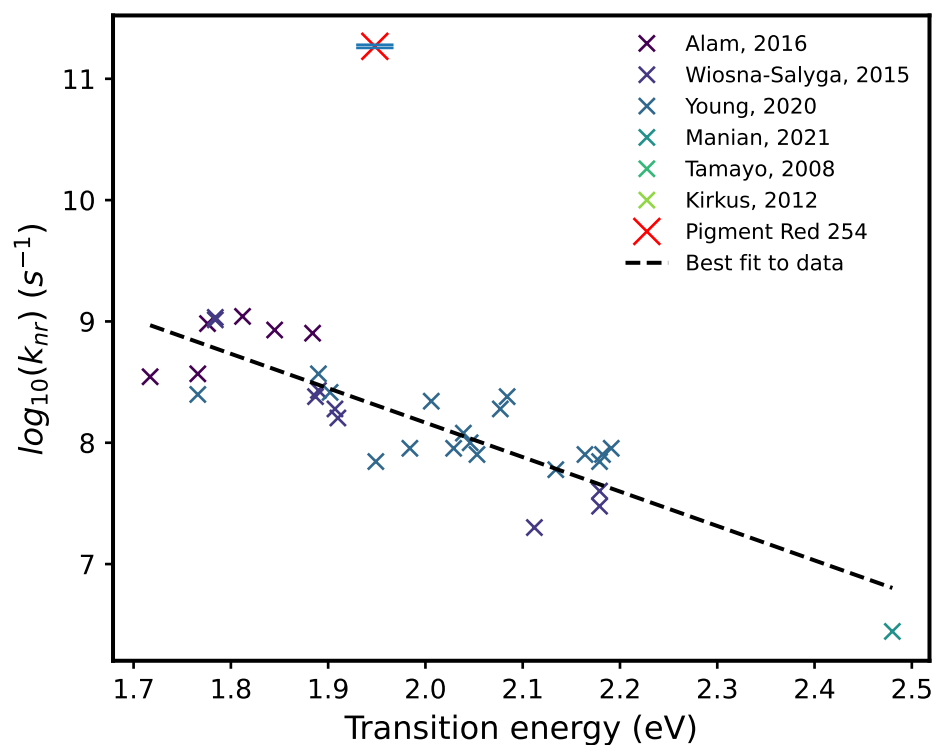


FIGURE 5.1: Comparison of the energy gap law relationship in diketopyrrolopyrrole derivatives, plotting the natural logarithm of the non-radiative decay rates of a range of molecules with diketopyrrolopyrrole cores against their transition energy from the excited state to the ground state. This data was collected from Manian et al. [99], Alam et al. [100], Wiosna-Salyga et al. [101], and Young et al. [91]. Also marked on this graph is the rate and energy of the non-radiative decay of Red254, demonstrating that said non-radiative decay takes place over much faster timescales than is typical of molecules of this type, indicating a different mechanism of decay.

fission materials [1], we aim to determine whether the non-radiative decay we observe also follows gap-law behaviour by comparing it to similar molecules which should have similar coupling coefficients.

Fig. 5.1 shows the non-radiative decay rate of several similar diketopyrrolopyrrole derivatives [91, 99–101] which exhibit non-radiative decay. They follow a consistent transition energy-lifetime relation according approximately to an exponential gap-law dependence (dashed line). However, the non-radiative decay rate of Red254 is ~ 900 times faster than if it followed the diketopyrrolopyrrole gap-law behaviour. This suggests that non-radiative decay in Red254 may occur via strong (large ΔQ) interstate coupling between the first excited- and ground-state potential energy surfaces [5], rather than a non-adiabatic transition between weakly coupled states.

There has not been much explicit research into non-radiative decay in diketopyrrolopyrroles, especially in the solid state. This lack of research has been driven by the difficulty

of dissolving and film-processing the unsubstituted diketopyrrolopyrrole dye[79, 81–83, 85, 86], as well as different properties of the versatile diketopyrrolopyrrole molecule and its derivatives taking the focus of research. These include singlet fission, as has been previously discussed[87, 88, 102], and the high fluorescence of some N-H substituted derivatives in the long wavelength region of the visible spectrum[85, 91, 103].

The clearest distinction between Red254 and many of the investigated diketopyrrolopyrrole derivatives is their luminescence, and the lack of Red254's characteristic intermolecular hydrogen bonding. This bonding promotes aggregation of the molecules, which contributes to its lack of solubility in many organic solvents, as well as the large Stokes shift in the solid phase. The most common strategy in working with diketopyrrolopyrrole derivatives, especially in solution, is substitution of the N-H bonds, replacing the hydrogen atom with a longer alkyl chain, or other organic group[80]. This substitution increases the spacing distance between molecules and reduces the intermolecular interactions. Hence, it is likely that hydrogen bond present in Red254 is integral in mediating the rapid non-radiative decay.

This is supported by Mizuguchi [104], in which they find that the formation of the hydrogen bond in Red254 is responsible for the bathochromic shift of the S_0 - S_1 transition overcoming the hypsochromic contribution from the Van der Waals interaction, resulting in the overall red-shift to the ground state absorption spectrum, similar to that in Mizuguchi and Wooden [94].

The impact of the hydrogen bonding nature and strength is highlighted by Suna et al. [105], in which thin films of unsubstituted PhDPP are prepared by thermal shearing of solubilising tert-butoxycarbonyl groups at 200 °C. After regenerating the intermolecular hydrogen bonds in these thin films, the hole mobility in these films were increased by 2-3 orders of magnitude. This further demonstrates the importance of the hydrogen bonding to the electronic distribution and dynamics in these molecules.

We suggest that the intermolecular hydrogen bond that is formed in non-substituted diketopyrrolopyrrole derivatives is responsible for the rapid deactivation of the Red254 excited state. We hypothesise that the mechanism by which this non-radiative decay occurs is by partial proton transfer across the N-H...O hydrogen bond between adjacent molecules, forming a non-permanent tautomer form of the molecule under excitation. This scheme is illustrated in Fig. 5.2.

Proton transfer has been observed to facilitate non-radiative decay in a number of molecular systems. It is well known to occur between DNA nucleobases, which functions as a photoprotection mechanism to avoid solar damage in organisms[106, 107].

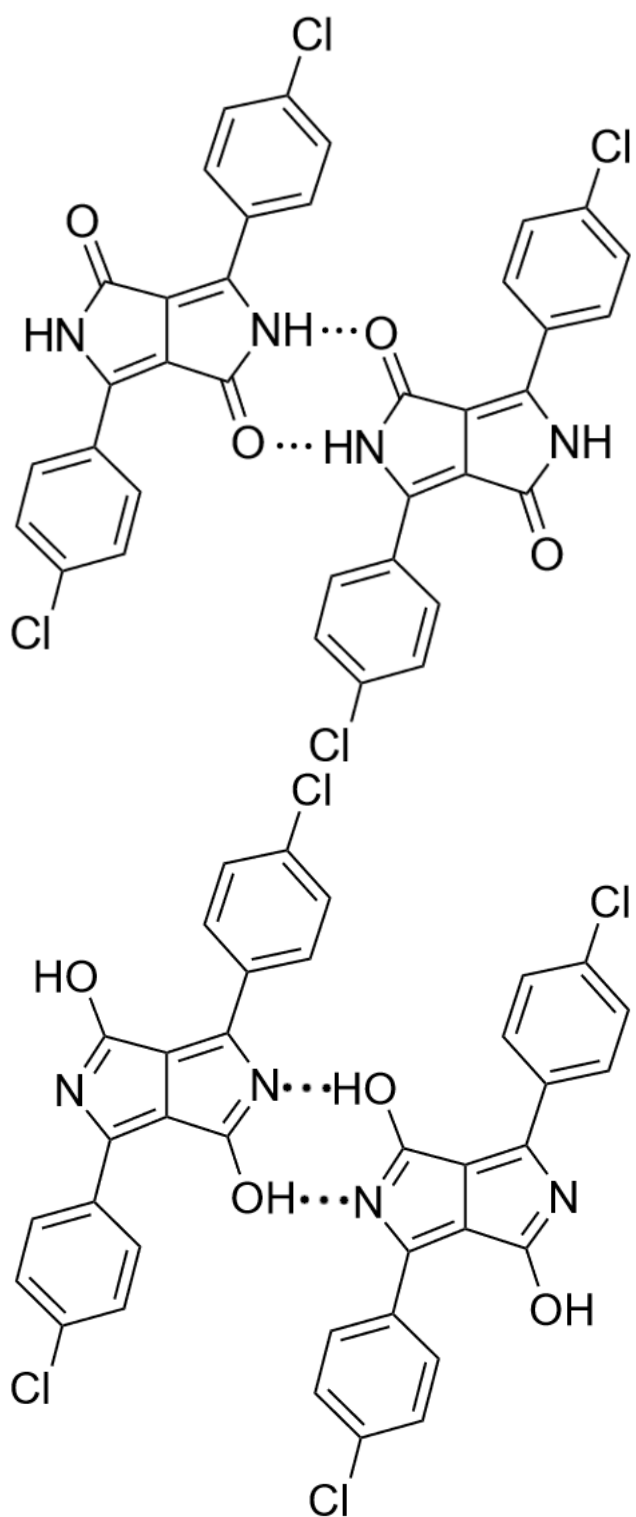


FIGURE 5.2: Proposed structure of intermolecular tautomerisation of Red254 in the solid state. The upper figure shows the un-tautomerised molecule, with the N-H...O interaction highlighted with dotted lines. The lower figure shows the proposed form of the tautomerised molecule, in which the hydrogen atom has been transferred to the oxygen, slightly altering the conjugation of the pyrrole core.

Non-radiative decay due to hydrogen-bond induced proton transfer has been observed in fluorenone derivatives in alcoholic solutions[23, 25, 108]. In this environment, there is strong hydrogen bonding between the fluorenone and solvent that strengthens in the excited state, reducing the excited state energy and enhancing vibronic relaxation[23, 25], over timescales that can be as short as femtoseconds[108].

To verify this hypothesis, we have performed ultrafast time-resolved infra-red spectroscopy and density functional energy calculations in order to find which bond vibrations are involved in the non-radiative decay process of Red254. We anticipate that the process of proton transfer will be visible in the transient infra-red spectra by a bleaching of the carbonyl bond signal, due to the replacement of the carbon-double-bond with a single C-O bond. Simultaneously, we would expect an additional excited-state absorption feature in the same region as other carbon-double-bond signals, which would correspond to the newly formed C=N feature. We expect to see some component of the time-resolved infra-red decay to decay with the same lifetime as the excited state decay of the UV-Vis TA signal seen in Fig. 4.4.

5.2 Results

5.2.1 Density functional theory (DFT) calculations

The resultant calculated modes from the density functional theory (DFT) calculations are shown in Fig. 5.3. Four modes were selected by virtue of their IR strength intensity as well as their relevance to modes of interest, specifically phenyl hydrogen wagging modes and stretching modes (Fig. 5.4a), 1410 cm^{-1} , purple), a C=O stretching and pyrrole C=C stretching mode (Fig. 5.4b), 1684 cm^{-1} , blue) a similar pyrrole C=C stretching combined with internal intermolecular carbonyl stretching mode (Fig. 5.4c), 1751 cm^{-1} , teal) and external intermolecular carbonyl stretching mode with minimal contribution from the internal pyrrole modes (Fig. 5.4d), 1793 cm^{-1} , green).

In addition, the high-energy modes around $3200\text{--}3600\text{ cm}^{-1}$ are identified with vibrations involving hydrogen single bonds, such as C-H and N-H bonds. Mizuguchi and Wooden [94] identifies this mode in Diphenyl-DPP as corresponding to broad N-H IR absorption,

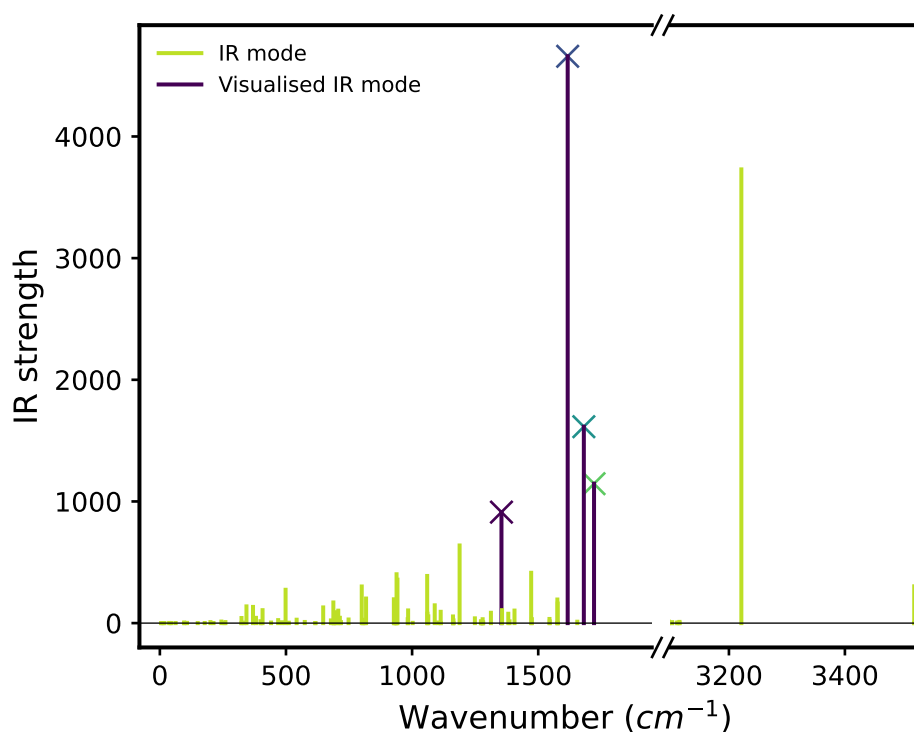


FIGURE 5.3: Spine plot of modes found via density functional theory calculations, shown with vertical lines against their predicted infra-red activity strength. Modes which are visualised and shown in Fig. 5.4 are shown in purple, with colour-coded *X* markers at their maximum value, while those not visualised are shown in green. These quantum chemical calculations were performed by Dr. Samara Medina Rivero of the University of Sheffield.

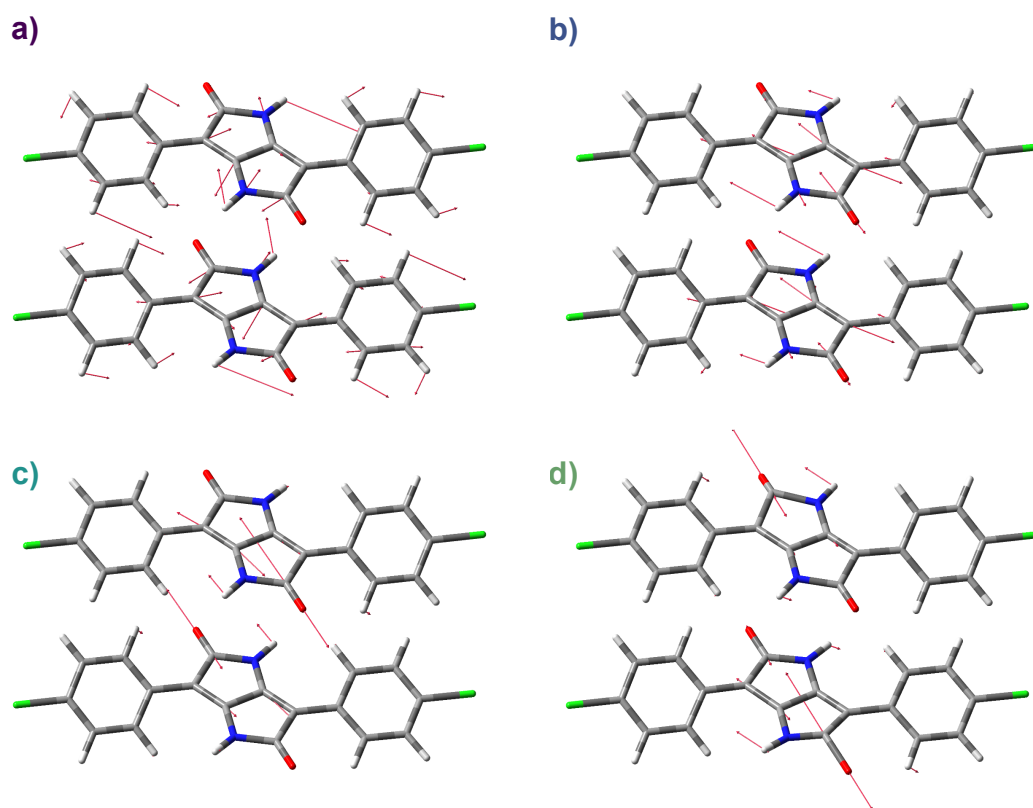


FIGURE 5.4: Vector plots of vibrational modes of Red254 dimers as found via DFT calculations. The modes shown are (a) 1410 cm^{-1} , (b) 1684 cm^{-1} , (c) 1751 cm^{-1} and (d) 1793 cm^{-1} . These quantum chemical calculations were performed by Dr. Samara Medina Rivero of the University of Sheffield.

suggesting this mode represents stretching of the hydrogen side group bond attached to the nitrogen atom.

These mode energies are unlikely to be exact, due to this molecule not being modelled in a crystalline lattice for simplicity, resulting in energetic differences due to a lack of $\pi - \pi$ stacked adjacent molecules and the presence of external modes which aren't effected by intermolecular interactions.

This is shown by the difference in the energy of carbonyl stretching between the modes shown in Fig. 5.4c) and d). However, these are a useful approximation to aid in mode identification, together with previous mode identifications in similar molecules from the literature.

5.2.2 Fourier Transform Infra-Red spectroscopy

Fig. 5.5 shows the Fourier Transform Infra-Red (FTIR) spectrum of Red254 thermally deposited on a calcium fluoride substrate, background corrected with a blank calcium

fluoride window.

The high energy feature in the FTIR spectrum at $\sim 3000\text{cm}^{-1}$ is assigned to a broad N-H stretching mode, based on the paper by Soberats et al. [109] and on the analysis of the similar molecule by Mizuguchi and Wooden [94]. This assignment corresponds to the high-energy modes around $3200\text{-}3600\text{cm}^{-1}$ in the DFT calculations, showing agreement within $\sim 500\text{cm}^{-1}$ between experiment and calculation. As this bond's vibrational modes are the most likely to be affected by inclusion of more molecules in simulation due to the N-H bond's importance to the intermolecular interactions in diketopyrrolopyrroles[104, 105], this level of accuracy is sufficient for this assignment.

Below 1723cm^{-1} , the density of peaks increases, and thus is shown in Fig. 5.5 with a scaled axis. The most prominent peaks in this spectrum are two peaks between $\sim 1600\text{cm}^{-1}$ and $\sim 1650\text{cm}^{-1}$. These bonds occur in a region commonly associated with carbon double-bond stretching modes[110, 111]. We specifically assign the lower peak at 1626cm^{-1} to a C=C stretching mode, and the higher peak at 1640cm^{-1} to C=O

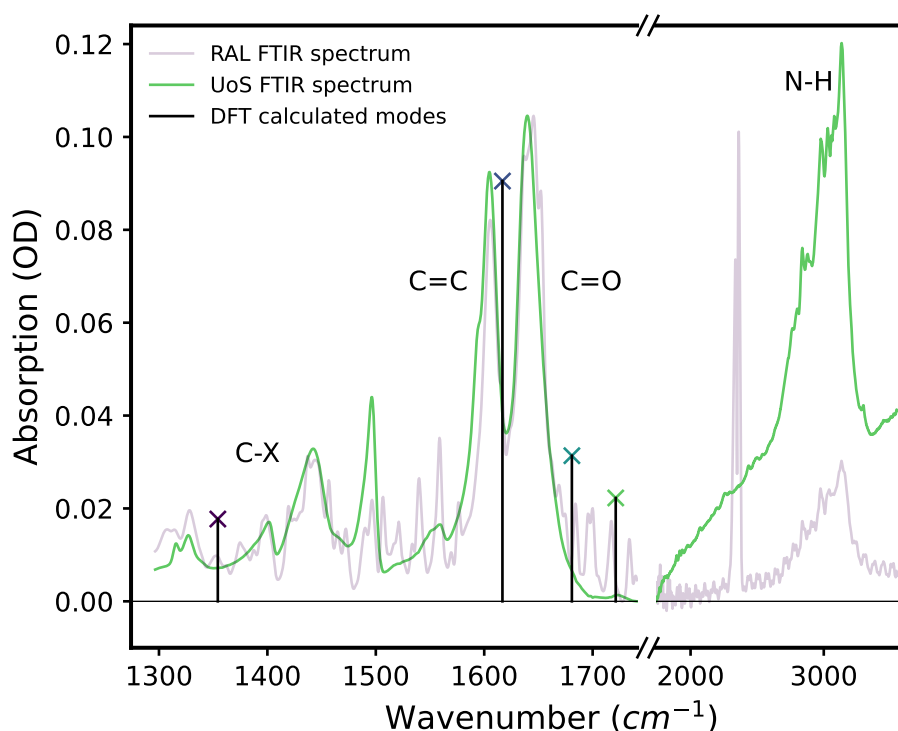


FIGURE 5.5: Fourier Transform Infra-Red (FTIR) spectra of thermally sublimated film of Red254 on a calcium fluoride substrate. The spectrum in purple was taken using the instrument at the Rutherford Appleton Laboratory. The spectrum in green was taken using the instrument at the University of Sheffield. The FTIR is shown on two different wavenumber scales, as the peaks between $\sim 1350\text{cm}^{-1}$ and 1723cm^{-1} are much more tightly spaced than the longer wavenumber spectrum. The modes shown in vector plot Fig. 5.4 are marked on this plot with normalised vertical black lines, and colour coded X markers.

stretching. We make these identifications partially due to the modes highlighted in the DFT calculations (Fig. 5.3, 5.4), in which the lower energy intense peaks have a large contribution from pyrrole C=C bond stretching, whereas the higher energy modes have large C=O stretching contributions, as well as from assignments made by Mizuguchi and Wooden [94].

There are many low-intensity peaks present in the FTIR spectrum below 1600 cm^{-1} , and it is difficult to identify each of them individually, especially as the DFT calculations are not exact. However, this region is associated with C-N and C-C stretching modes [111]. From the DFT calculations in Fig. 5.3 and Fig. 5.4a), many modes in this region are associated with breathing and stretching modes associated with the phenyl groups, as well as hydrogen wagging modes.

5.2.3 Time-Resolved Infra-Red spectroscopy

To examine how the molecular vibrations change over time on excitation, time resolved infra-red spectroscopy (TRIR) was performed on the thin film sample, using an excitation wavelength of 520 nm. The resultant spectra and kinetics are shown in Fig. 5.6 (top) and (bottom) respectively, for a pump power of 5 mW.

The TRIR spectra show two negative bleach signals corresponding to the C=O and C=C stretching mode peaks at 1643 cm^{-1} and at 1610 cm^{-1} , respectively. This assignment is made due to their overlap with the previously assigned modes from the FTIR spectrum, in addition to the previous assignments from the literature[94, 110, 111].

These bleach signals overlap with an excited state absorption (ESA) feature, from $\sim 1600\text{ cm}^{-1}$ to $\sim 1650\text{ cm}^{-1}$. We suggest that this mode corresponds to a C=N stretching mode, as it is in the same region as the other carbon-double-bond mode assignments, and its energy lies between that of the C=O and C=C bond stretching mode energies. This corresponds well with the proposed model of proton transfer, in which the C=O bond has been bleached and a C=N ESA feature has appeared.

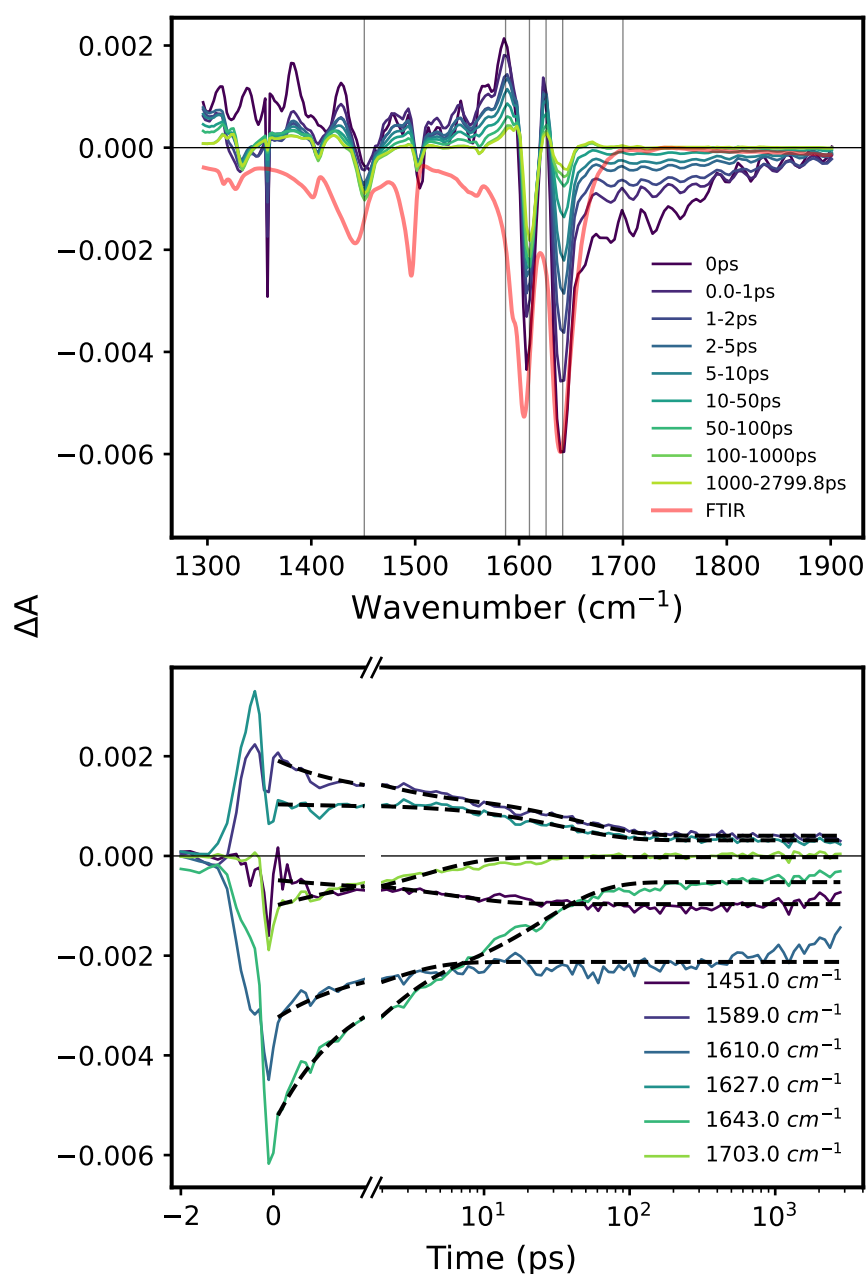


FIGURE 5.6: Time Resolved Infra-Red (TRIR) spectra (top) and kinetics (bottom) of thin film of Red254 on calcium fluoride window substrate, using a pump wavelength of 520 nm and power of 5 mW. An additional broad electronic signal was seen in all TRIR spectra, and was subtracted from the overall spectrum by subtracting the signal between 2000-2100 cm^{-1} , as the signal appeared the same across the spectrum. The subtracted kinetics are shown in Fig. 5.7. Overlaid with these spectra is the inverted Fourier Transform Infra-Red (FTIR) obtained from the Rutherford Appleton Laboratory spectrometer, to assist in identifying the peaks. The locations of the kinetic slices used in TRIR kinetics (bottom) are marked by grey lines on the figure. Exponential and bi-exponential fits to the data are shown on this graph as dotted black lines.

TABLE 5.1: Table of different wavenumbers (ν) assigned to vibrational modes in the DFT calculations, FTIR spectrum, and TRIR spectra. C-X refers to a generic, approximate or representative carbon single-bond mode. "s" denotes a stretching mode, while "w" denotes a waving or bending mode.

Bond	DFT ν (cm^{-1})	FTIR ν (cm^{-1})	TRIR ν (cm^{-1})
C-X s/w	~ 1410	1443	~ 1451
C=N s (1)	-	-	1589
C=C s	~ 1684	1605	1610
C=N s (2)	-	-	1627
C=O s	1751/1793	1642	1643

A broad time dependent signal was observed in the TRIR spectra, and was present across the whole examined region. This signal was assigned to an electronic signal overlaid with the vibrational peaks, and the average of this signal between $2000\text{-}2100\text{ cm}^{-1}$ was subtracted from the overall transient infra-red spectra, using the approximation that the broad signal varies only a small amount across the region of interest. The TRIR spectra shown in this paper are all corrected for the electronic signal in this manner. The subtracted kinetics, for pump powers 0.5 mW, 1 mW, 2.5 mW, and 5 mW, are shown in Fig. 5.7, and have a lifetime of 11 ± 1 ps. The uncorrected spectra are shown in Figs. B.1-B.4.

At lower energies, there are bleached peaks corresponding to the smaller peaks which we have previously assigned to miscellaneous phenyl and C-N stretching modes, as well as C-C and ring breathing modes.

Table 5.1 shows the differences between the calculated and experimentally determined wavenumbers as assigned to each mode: approximate carbon single-bond modes, C=O, C=C, and C=N stretching modes. As the C=N feature only appears as an excited-state feature, and does not appear in the FTIR or DFT spectra, these do not appear for comparison.

The kinetic decays of the TRIR are shown in the lower figure. At negative times there is a coherent artefact response, and as such the time-zero point is set after the decay of the initial strong signal. The decay of the bleach signals $< 1600\text{ cm}^{-1}$, which have been identified with carbon-single-bond modes such as phenyl modes, are separated into two groups: the bleaches at 1383 cm^{-1} and 1426 cm^{-1} decay with the same lifetime as the C=N ESA peak at 1582 cm^{-1} , and similarly to the 1623 cm^{-1} ESA peak, and thus are not represented in the kinetics.

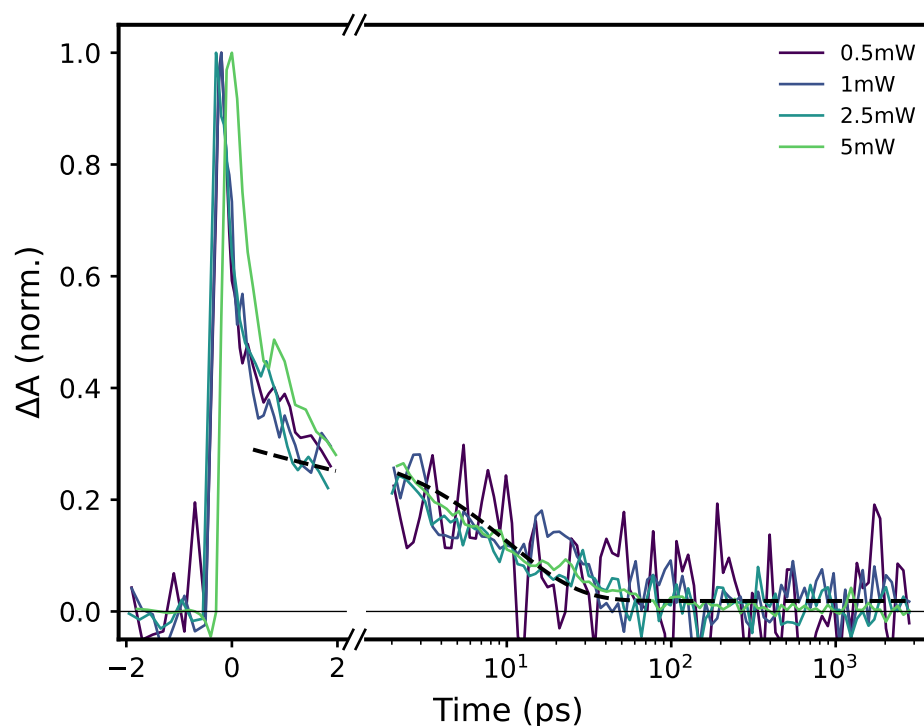


FIGURE 5.7: Normalised kinetic decays of the $2000\text{-}2100\text{ cm}^{-1}$ kinetic slice of time-resolved infra-red spectrum of Red254 evaporated thin film on calcium fluoride substrate, using an excitation wavelength of 520 nm , at fluences 0.5 mW , 1 mW , 2.5 mW , and 5 mW . These decays are fitted with exponential decays after 1 ps , and the average of these lifetimes are displayed as a black dotted line.

The ESA at the low-energy end of the spectrum at 1334 cm^{-1} as well as the bleach peak at 1504 cm^{-1} decay with the same kinetic shape as the bleach at 1451 cm^{-1} . As the 1451 cm^{-1} peak is the most intense, this decay is plotted on Fig. 5.6. The broad high energy bleach at 1700 cm^{-1} as well as the C=C and C=O bleach features (at 1610 cm^{-1} and 1643 cm^{-1}) decay on distinct timescales and thus are shown as well.

This is done to group together redundant decays, as well as to identify which modes are related in different excited states. In TRIR spectra, each peak corresponds to a different vibration which may decay on its own timescale, which contrasts with transient absorption spectra in which the signals arise from typically one or two electronic excited states at a time. In making these comparisons, we have said that the complex spectrum below $\sim 1600\text{ cm}^{-1}$ represent two different associated sets of vibrations: one which decays at the same rate as the tautomer, evidenced by the C=N ESA features decaying with a similar lifetime, and one which has distinct decay dynamics. In addition, the decay of the C=C and C=O bleaches are distinct, meaning that the C=C bleach feature is not uniquely associated with the proton-transfer induced tautomerisation.

TABLE 5.2: Lifetimes of excited vibrational decays from Time-Resolved Infra-Red spectroscopy kinetics as shown in Fig. 5.6. The pump power used for these measurements was 5 mW

Wavenumber (cm ⁻¹)	τ_1 (ps)	τ_2 (ps)	$\delta\tau_1$ (ps)	$\delta\tau_2$ (ps)
1451 (C-X)	6	-	1	-
1589 (C=N)	1.7	43	0.2	4
1610 (C=C)	1.9	-	0.3	-
1627 (C=N)	36	-	3	-
1643 (C=O)	1.5	25	0.1	2
1703 (electronic)	3.7	-	0.3	-

Fits to the kinetic decays are shown on these figures as dotted black lines. The 1451 cm⁻¹, 1610 cm⁻¹, 1627 cm⁻¹, and 1700 cm⁻¹ kinetic slices are modelled as exponential decays, whereas for the 1587 cm⁻¹ and 1643 cm⁻¹ component, it was found to be best modelled with two exponential components, as an approximation to estimate the lifetimes of the decays, similar to the transient absorption data in Fig. 4.4. The lifetimes extracted from these plots via the fits are shown in Table 5.2 for the highest pump power plot, at 5 mW.

The decay seen at 1700 cm⁻¹ decays with a single lifetime component of 3.7±0.3 ps, and is well described with a monoexponential decay, leaving very little residual signal. This timescale matches well with the excited state decay seen in the transient absorption data, which had a lifetime of ~5 ps (Chapter 4). This further corroborates the assignment of the broad signal to the electronic excited state decay.

The 1451 cm⁻¹ kinetic grows with time, which with an exponential model has a time constant for this growth of 6±1 ps, which is also similar to the lifetime of the electronic excited state decay. This indicates that as the non-radiative decay occurs from the excited state, the resultant thermal artefact enhances some of the low-energy signals in the TRIR spectrum. This may be via classical heating artefact which changes the local refractive index of the sample. However, as this artefact is not consistent across this region, with some instead decaying concurrently with the C=N mode, this could be interpreted as population of quantised vibrational energy levels, localised on carbon-single-bond and phenyl modes. Due to the overlap of signals in this region, however, it is difficult to make a definitive statement.

There are four peaks that will be analysed in the carbon double-bond region: an excited-state absorption (ESA) peak at 1582 cm⁻¹, a ground-state bleach (GSB) peak at 1610 cm⁻¹, another ESA peak at 1627 cm⁻¹ and a final GSB peak at 1643 cm⁻¹. As described previously, the two ESA peaks represent a single C=N ESA peak overlapped with the lower energy C=C stretching GSB, at 1610 cm⁻¹. The low-wavenumber ESA peak, as well as the two GSB peaks, have an initial short decay lifetime component of

1.7 ps, 1.9 ps and 1.5 ps, for the 1587 cm^{-1} C=N ESA peak, C=C GSB peak, and C=O GSB peak respectively. The 1627 cm^{-1} C=N ESA peak does not have this lifetime, which may be due to its overlap with the C=C counteracting this decay component.

The 1610 cm^{-1} peak, associated with the C=C stretching mode of the diketopyrrolopyrrole core, decays slightly with this lifetime before plateauing, and the final decay of the peak takes place over longer timescales than those that were available for the ULTRA TRIR spectrometer. This indicates that the reduction in IR strength of the C=C mode lasts for a much longer timescale than the electronic excitation, and that this mode plays a significant part in the long-lived thermal artefact that was observed in the TA data.

For the remaining carbon-double-bonded peaks, there is a longer-lived decay component with lifetimes of 43 ps, 36 ps, and 25 ps for the 1589 cm^{-1} and 1627 cm^{-1} C=N ESA as well as the 1643 cm^{-1} C=O GSB kinetics, respectively. As this lifetime is associated with the C=O bleach, it can be assigned to the decay of the proposed proton-transfer tautomer bond, as the recovery of the un-tautomerised conformer would result in a recovery of the carbonyl bond. This further confirms that the ESA peak overlaid with the C=O and C=C peaks is due to the formation of C=N bonds in the tautomer.

Finally, these three peaks also retain some population at long times, that do not decay over the course of the experiment. This can be explained via the same thermal artefact seen in the lower energy region as well as in the UV-Vis Red254 TA (Fig. 4.4), with the C=C GSB retaining the most intensity due to the higher population of C=C bonds in the molecule.

The difference between the fitted lifetimes of these peaks can be explained due to the close spacing of the peaks in the $<1650\text{ cm}^{-1}$ region, resulting in a difficulty of separating them, as well as potential overlap with any residual excited electronic signal.

5.2.4 Fluence dependent TRIR

TRIR of thin films of Red254 were performed with a range of pump powers, to investigate the effect of varying fluence on the excited state decay of the molecule. Full spectra and kinetics for pump powers 0.5 mW, 1 mW, and 2.5 mW are shown in Appendix B, and the fitted decay lifetime parameters for these pump powers are summarised in Table B.1.

Each previously discussed kinetic at each pump power taken (0.5 mW, 1 mW, 2.5 mW and 5 mW), grouped by wavenumber (1451 cm^{-1} , 1589 cm^{-1} , 1610 cm^{-1} , 1627 cm^{-1} , 1643 cm^{-1} , and 1703 cm^{-1}), are shown in Figs. 5.8, B.8, 5.9, B.9, B.10, B.11 respectively. Decay fits of each kinetic were performed in the same manner as for the 5 mW

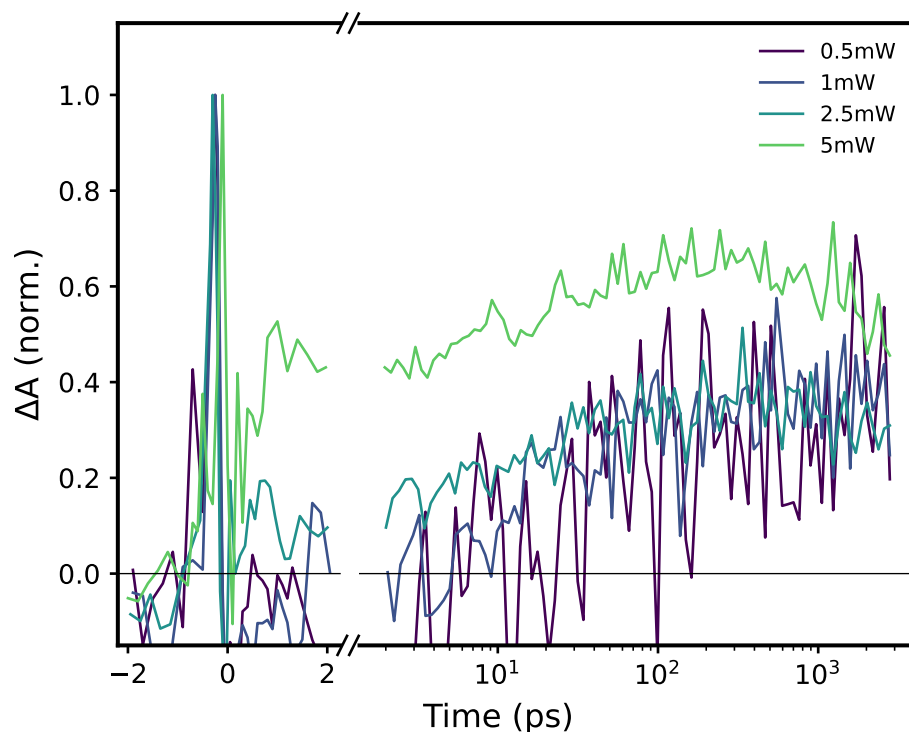


FIGURE 5.8: Normalised kinetic decays of the 1451 cm^{-1} kinetic slice of time-resolved infra-red spectrum of Red254 evaporated thin film on calcium fluoride substrate, using an excitation wavelength of 520 nm , at fluences 0.5 mW , 1 mW , 2.5 mW , and 5 mW . At higher fluence, the immediate picosecond-scale signal is greater, while the signal converges after $\sim 100\text{ ps}$. This indicates the presence of a short-lived fluence dependent vibration that manifests as an excited-state absorption at early times.

kinetics, and the pump power dependence of each lifetime are shown in Figs. [B.12](#), [B.13](#), [B.14](#), [B.15](#), [B.16](#), [B.17](#) respectively.

In the 1451 cm^{-1} kinetics, corresponding to carbon-single-bond modes, the shape of the 5 mW kinetic is different from the 2.5 mW and 1 mW kinetics, being significantly more absorbing at early times. There is not a significant trend in the resultant lifetimes shown in Fig. [B.12](#) that do not appear to be related to the lower signal to noise ratio at lower pump powers. This early signal suggests that above a certain pump power, a pump induced signal is present at early times and lasts until \sim nanosecond timescales. This may be related to the aforementioned classical thermal artefact or through the population of lower energy C-H, C-C and phenyl modes.

In the 1610 cm^{-1} kinetics, which correspond to the C=C stretching mode, shown in Fig. [5.9](#), the signal of the 5 mW kinetic is enhanced compared to the lower pump power kinetics, at earlier times and persisting out to \sim nanosecond timescales, in a manner similar to the 1451 cm^{-1} kinetic. The lifetime comparison in Fig. [B.14](#) does not

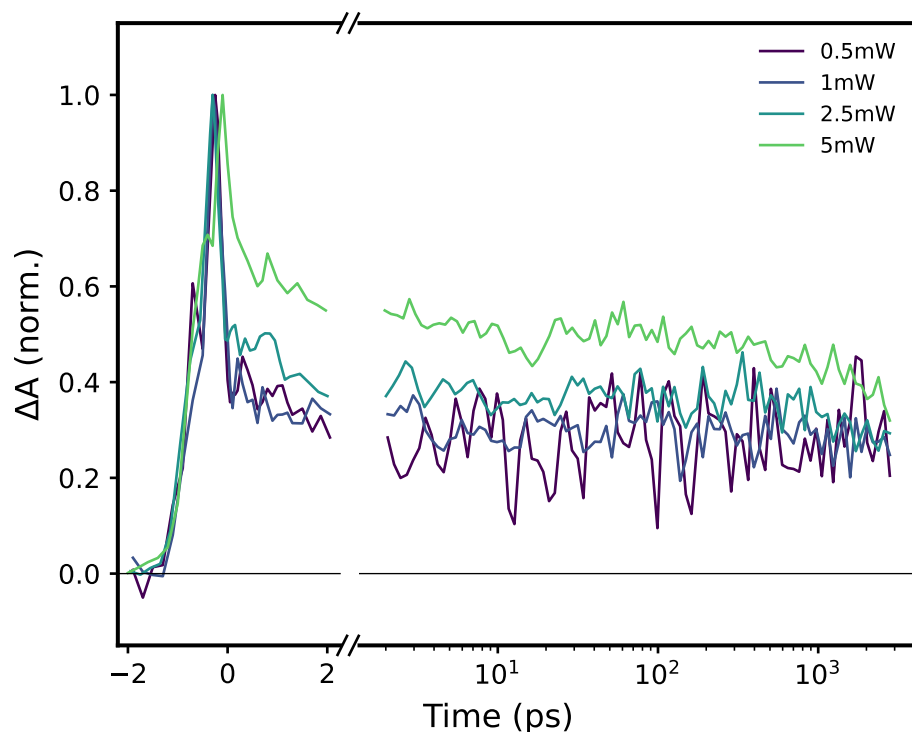


FIGURE 5.9: Normalised kinetic decays of the 1610 cm^{-1} kinetic slice of time-resolved infra-red spectrum of Red254 evaporated thin film on calcium fluoride substrate, using an excitation wavelength of 520 nm at fluences 0.5 mW , 1 mW , 2.5 mW , and 5 mW . The 5 mW fluence kinetic is more intense than the others, and the 0.5 mW fluence kinetic has more noise than the rest, but is less noisy than the the previous 0.5 mW kinetics.

otherwise show a clear trend. As this fluence dependence is observed in carbon-carbon single- and double-bonds, and in no other feature of the TRIR kinetics, this suggests this feature is vibrationally relevant and not just pump-induced heating. However, as this feature appears to decay by the end of the kinetics on \sim nanosecond timescales, this effect appears to be distinct from the thermal artefact observed in the TA (Fig. 4.4).

The kinetics of the C=N ESA features at 1589 cm^{-1} and 1627 cm^{-1} , as well as the C=O bleach at 1643 cm^{-1} and the residual electronic signal at 1703 cm^{-1} do not show significant variation with pump power that are not explained via the significantly lower signal to noise ratio at low powers. The remaining kinetic comparisons are shown in Figs. B.8, and B.9 for the C=N ESA features, Fig. B.10 for the C=O bleach, and Fig. B.11 for the residual electronic signal. Graphical illustrations of the differences in fitted lifetimes to the decays, are shown in Section B.5.

The difference in spectral shapes with fluence between $1\text{-}2\text{ ps}$ and $1000\text{-}2800\text{ ps}$ are shown in Figs. 5.10 and 5.11, respectively. At early times, there are minor differences in the spectra, primarily at low wavenumbers $<1700\text{ cm}^{-1}$. At these energies, there is a slightly increased signal at low fluence. This broad difference is likely due to errors in

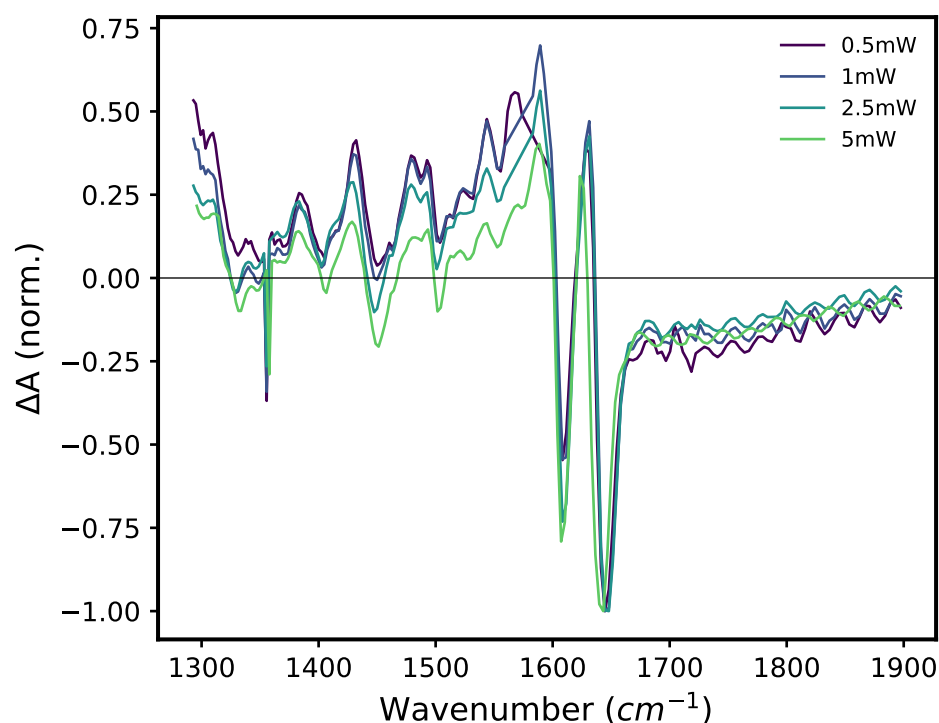


FIGURE 5.10: Early-time time-resolved infra-red fluence dependent spectra of Red254 thin film on calcium fluoride substrate, using an excitation wavelength of 520 nm averaged between 1-2 ps. At high wavenumbers, above $\sim 1600\text{ cm}^{-1}$, there is little to no change in the spectrum with fluence. However, at lower wavenumbers, there are complex changes in the spectral shape, with peaks at 1384 cm^{-1} and 1492 cm^{-1} being proportionally higher at higher fluence, and the location of the highest-signal peak around 1590 cm^{-1} is shifted slightly in the 0.5 mW spectrum. In addition, the higher fluence spectra are shifted slightly to negative signal, indicating the removal of the broad electronic signal by single-point correction at high wavenumber was not perfect.

the approximation made to correct for the broad electronic signal. This suggests that at higher fluence the electronic signal is broader and more featureless, resulting in a better approximation and a more efficient background removal. In addition, there are some differences in the peaks below $\sim 1600\text{ cm}^{-1}$, such as in the features at 1384 cm^{-1} and 1492 cm^{-1} , in which these peaks are proportionally higher than their neighbours at higher fluence. This further supports the previous assertion, that the phenyl-localised modes are enhanced in response to thermal artefacts, and increase at higher fluence due to pump induced heating. In addition, the origin of the difference in the 0.5 mW kinetic at 1587 cm^{-1} can be seen in this spectrum; the maximum of this peak is displaced compared to the other readings.

At late times, there are broad differences across the whole spectrum, with a more negative signal being observed at low fluence. This also is likely to arise from the correction for the broad electronic signal, which is once again most accurate for the highest fluence 5 mW.

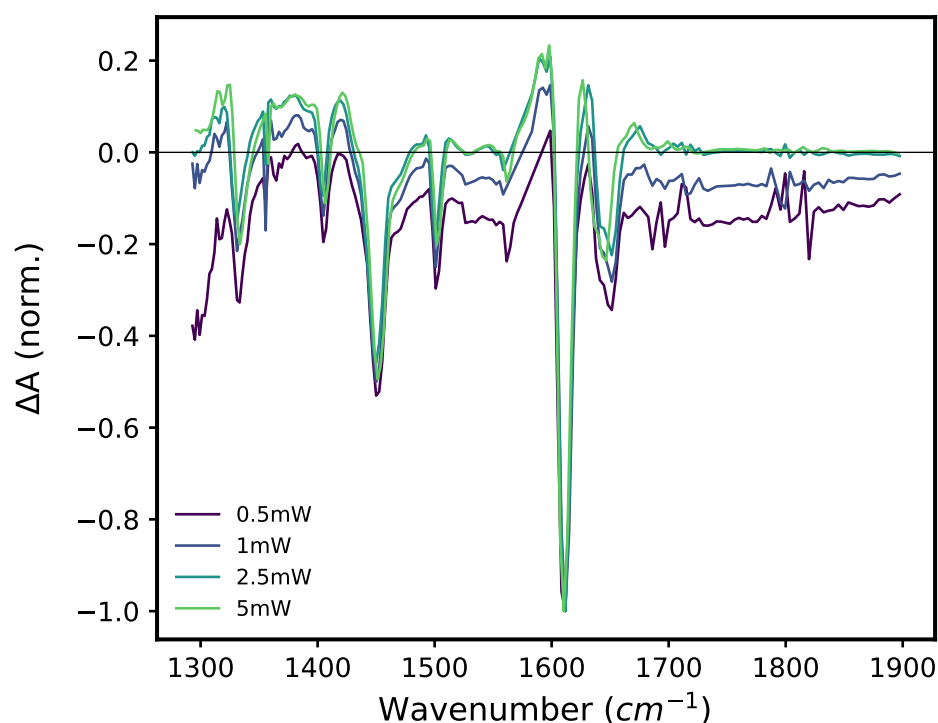


FIGURE 5.11: Late-time time-resolved infra-red fluence dependent spectra of Red254 thin film on calcium fluoride substrate, using an excitation wavelength of 520 nm averaged between 1000-2800 ps. There is broad signal overlapped with the peaks throughout, indicating that the broad electronic signal is not well removed at late times. This indicates that this signal is broader and more featureless in the 5 mW fluence measurement.

5.3 Discussion

While the modelling proposed above is imprecise, it demonstrates that there are ~ 3 separate decay lifetimes that are visible: There is a very rapid, 1-2 ps timescale decay, that is visible in the 1589 cm^{-1} , 1610 cm^{-1} and 1643 cm^{-1} kinetic traces, all of which we have identified with carbon-double-bond features: C=N, C=C, and C=O. There is also a 3.5-5 ps lifetime that we have compared to the ESA decay lifetime in the TA, that is visible in the 1451 cm^{-1} kinetic trace as a growth feature, as well as in the the 1703 cm^{-1} kinetic trace which is associated with the electronic excited state. Finally, there is a >10 ps lifetime, which is present in the carbon-double-bond features: 1589 cm^{-1} , 1610 cm^{-1} , 1627 cm^{-1} and 1643 cm^{-1} . In addition, there is signal in the TRIR that lasts beyond the range of the experiment, primarily shown in the 1610 cm^{-1} and 1451 cm^{-1} decays.

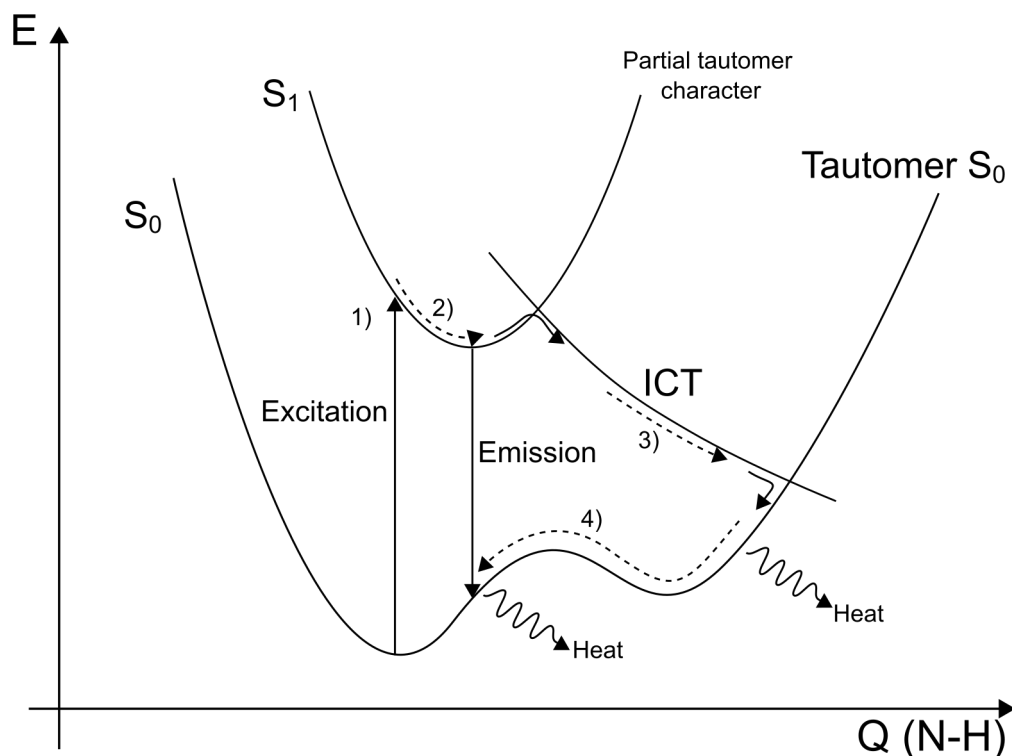


FIGURE 5.12: Model of the non-radiative decay of Red254, following the model detailed in this chapter. Shown on Axes of Energy E vs molecular normal coordinate Q , which has some character mediating the N-H inter-nuclear distance. Step 1) Excitation of the molecule into the excited S_1 state, which has partial tautomer character due to changes in charge density on the diketopyrrolopyrrole core. Step 2) 1-2 ps timescale of vibrational relaxation according to Kasha's Rule [47]. Step 3) Conical intersection with an intermolecular charge transfer state, resulting in rapid ~ 5 ps timescale relaxation to the ground state which still maintains tautomer character. This charge transfer state results in the hydrogen atom being driven to form a semi-stable tautomer. Step 4) The tautomer is unstable, resulting in a relatively slow recovery of the un-tautomerised ground state. The excess energy in this and the previous step are lost to the environment as heat (step 5 of the model below, not visible on the potential energy surface.)

We propose a model for these observations, taking into consideration the observed lifetimes in the transient absorption spectra previously examined:

1. **Initial excitation and tautomer formation:** Due to the lack of growth of the tautomer-associated signals (the C=N identified ESA at 1589 cm^{-1} and 1627 cm^{-1}), we suggest that hydrogen-bond induced proton transfer happens very rapidly, with a timescale sufficiently short to be obscured by short-time artefacts and chirp correction. Due to the extremely rapid timescale of the tautomer formation, occurring on a timescale < 1 ps, we consider that the excited state itself has partial tautomer character; a change in the charge density on the diketopyrrolopyrrole core in the excited state results in the broad, red-shifted excited state potential energy surface that allows the molecule to tautomerise via vibrational relaxation. This can

be considered qualitatively as the hydrogen nucleus becoming more mobile in the excited state, and being attracted to the oxygen site on the adjacent molecule.

- 2. Vibrational relaxation:** After excitation, the partially-tautomer S_1 state is prepared in a non-equilibrium vibrational state. As Kasha's rule states that vibrational decay happens over \sim ps timescales, we assign the 1-2 ps decay lifetime of the carbon-double-bond features around 1580 cm^{-1} - 1650 cm^{-1} to vibrational decay to the excited state potential energy surface minimum.
- 3. Conical intersection with Charge Transfer state:** We know that the excited state that is observed in the TA is lost over a \sim 5 ps timescale. As such, we identify the following 3.5-5 ps timescale decay observed in the TRIR with a non-avoided conical intersection with a dark charge transfer state which permits rapid non-radiative relaxation to the ground state, which itself has tautomer character. The picosecond scale lifetime of this decay suggests a small energy barrier to the decay at this intersection. We identify this state as a dark charge transfer state rather than a non-bonding $n\pi^*$ orbital due to the presence of the near-IR electronic signal that has been previously discussed. This broad near-IR absorption is typical of molecular polaronic states. In addition, the presence of charge transfer states has previously been used to explain the broad red-shifted steady state absorption spectrum [94, 104, 112]. The presence of the charge transfer state broadens the S_1 potential energy surface via resonant interactions. The high rate of this conical intersection mediated non-radiative decay is responsible for the negligible emissivity of Red254 in the solid state. That it decays to a tautomer state is demonstrated by the persistence of the C=N feature, and we know that this decay is significant as the ESA visible in the UV-Vis TA (Fig. 4.4) disappears along this timescale, the electronic state at 1703 cm^{-1} disappears on this timescale, and the phenyl associated single-carbon bonds below \sim 1600 cm^{-1} increase in intensity on this timescale.
- 4. De-Tautomerisation:** After decaying to the tautomer ground state local minimum, the original form of the molecule is recovered over an approximate 10-50 ps timescale, as the ESA peaks associated with the C=N bond, as well as the C=O bleach, decay on this timescale, indicating the re-formation of the N-H and C=O bonds. This longer timescale governing the loss of the C=N bond is what suggests that the tautomerised conformer is not stable, and the un-tautomerised ground state minimum is a lower energy configuration.
- 5. Thermal relaxation:** The residual signal present beyond the timeframe accessible by the ULTRA TRIR spectrometer is likely due to the same thermal artefact

seen in the UV-Vis TA spectrum at late times, that is a classical heating artefact arising from the excess vibrational energy.

This model is illustrated by the schematic in Fig. 5.12. In step 3, we do not have direct evidence to say definitively whether a conical intersection occurs. However, these crossings are known to occur in systems mediated by proton transfers due to changes in the symmetry of the molecule permitting these diabatic crossings. As such, the lifetime of this decay is either determined by a rate-limiting energy barrier in the excited state potential energy surface, or the decay proceeds with a gap law decay via a reduced, ~ 0.9 eV energy gap. This value is based on the trend of the energy-gap-law mediated non-radiative decay from literature found in Fig. 5.1, by extrapolating the expected energy value of Red254 with its 5 ps lifetime on this trend line.

This model is supported by previous research into the charge transfer states of diketopyrrolopyrrole derivatives. Głowacki et al. [84] have used Density Functional Theory calculations to link the strength of the charge transfer character in DPP derivative dyes including Red254 to the strength of the intermolecular hydrogen bond. They study Phenyl-substituted DPP (PhDPP) as well as p-position Bromine substituted and Chlorine substituted DPP, p-Br-PhDPP and p-Cl-PhDPP, the latter molecule being synonymous with Red254. They demonstrate that while in p-Br-PhDPP and p-Cl-PhDPP the contributions to the charge carrier mobility are lower than in unhalogenated PhDPP, its contribution is at least 12% in all three molecules.

The charge transfer state for which the hydrogen bonding behaviour is a strong mediating force has been used to affect the decay pathways of the excited state in multiple ways. A series of papers by Mauck et. al have demonstrated that in a range of phenyl-DPP derivatives, the charge transfer state can be an intermediate state for generating triplet pairs via singlet fission. While singlet fission does not occur in Red254, these papers demonstrate the energetic relaxation which occurs due to excited state conversion to charge transfer states in diketopyrrolopyrroles, which is observed in Red254's highly Stokes shifted low-yield fluorescence.[87, 88, 102]

Similar charge transfer state-mediated non-radiative decay has been seen in Liang et al. [26], where a ferrocenyl DPP derivative is used as a dye for cancer-treating photothermal therapy. In this work, a photo-induced electron transfer mechanism is proposed, forming a charge transfer state which quenches singlet and triplet populations to produce heat via non-radiative decay, similar to the effect seen in the nanosecond scale transient absorption measurement of Red254 (Chapter 4).

Charge transfer states have also been linked with proton transfer in Red254 previously. It is noted in Mizuguchi and Wooden [94] that proton transfer occurs as a possible result

of the charge transfer formation changing the electron density on the nitrogen atom of diphenyl-diketopyrrolopyrrole. In addition, Ruiz-Carretero et al. [112] identifies both the oxygen and nitrogen atoms as being involved in hydrogen bonding behaviour. As such, we confidently assign the intermediate dark state observed in this process as a dark charge transfer state which drives the intermolecular proton transfer between the nitrogen and oxygen of adjacent molecules.

By the arguments presented in this and the previous section, we have determined that Pigment Red 254 does not undergo singlet fission as predicted by the work of Padula et al. [1], but rather undergoes efficient picosecond-scale non-radiative decay to the ground state via proton transfer tautomerisation enabled, likely charge transfer state mediated conical intersection with the ground state, and produces a significant thermal artefact in the long time TA and TRIR spectra that is reproducible via sample heating. This highlights the importance of considering more than singlet and triplet energies when predicting a material's viability for singlet fission sensitisation, as the presence of intermolecular hydrogen bonding is known[4] to encourage proton transfer and non-radiative decay, which results in a loss mechanism for singlet fission.

However, despite the lack of singlet fission found in Red254, its rapid, efficient non-radiative decay may prove of interest to the fields of photothermal therapy, if the molecule is found to be safe *in vivo*, or as a building block for a larger, polymerised photothermal therapy sensitiser. In addition, its stability in harsh environmental environments would make it ideally suited for solar-driven water purification.

5.4 Conclusion

In conclusion, in this section we have found evidence for non-radiative decay in thin films of Red254, via tautomerisation due to hydrogen-bond mediated proton transfer over a ~ 5 ps timescale. We have proposed a model for this non-radiative decay involving a proton-transfer induced conical intersection with the ground state which results in long-lived artefact signals in the nanosecond TA and TRIR spectra due to dispersal of the excited state energy as heat. We suggest based on related research on Red254 and similar molecules that the intermediate state that causes the conical intersection is a dark charge transfer state, which also gives rise to the electronic signal seen in the TRIR spectra as well as the broad, shifted steady state emission and absorption spectra.

Chapter 6

Investigating singlet fission predictions in BoDiPy dye derivatives

6.1 Introduction

BoDiPy, also known as 4,4-difluoro-4-bora-3a,4a-diaza-s-indacene, or Boron Dipyrromethane, and its derivatives, are a series of organic and hybrid organic-inorganic dyes, the first of which was discovered in 1968 by Treibs and Kreuzer [113]. Since then, BoDiPy derivatives have received significant attention for their high absorption and emissive yields, as well as high stability and solution-processibility [114–117].

The BoDiPy derivatives 2,6-di-iodo,4-mesityl BoDiPy and 2,6-di-bromo,4-mesityl BoDiPy, referred to in this section as BoDiPy 6 and BoDiPy 7 respectively, were synthesised and supplied to us by Marco Cavazzini (described in Pidgeon [2]). The structures of these molecules are shown in Fig. 6.1.

The potential for singlet fission has been previously investigated in other BoDiPy dyes. However, whether or not the experimental evidence has confirmed the presence of singlet fission has been contentious. Particular derivatives of the BoDiPy subunit, TM-BoDiPy dimers, have been a centre for this controversy. Via complete active-space self-consistent field (CASSCF) and density functional theory (DFT) calculations, Duman et al. [118] predicted the presence of an S_1 state with $^1(TT)$ -like character as a precursor to ISC in TM-BoDiPy dimers, and Montero et al. [119] experimentally found long-lived triplet signal in transient absorption spectra of such dimers in cyclohexane, chloroform, and acetonitrile. By examining the decay associated spectra and calculating the expected

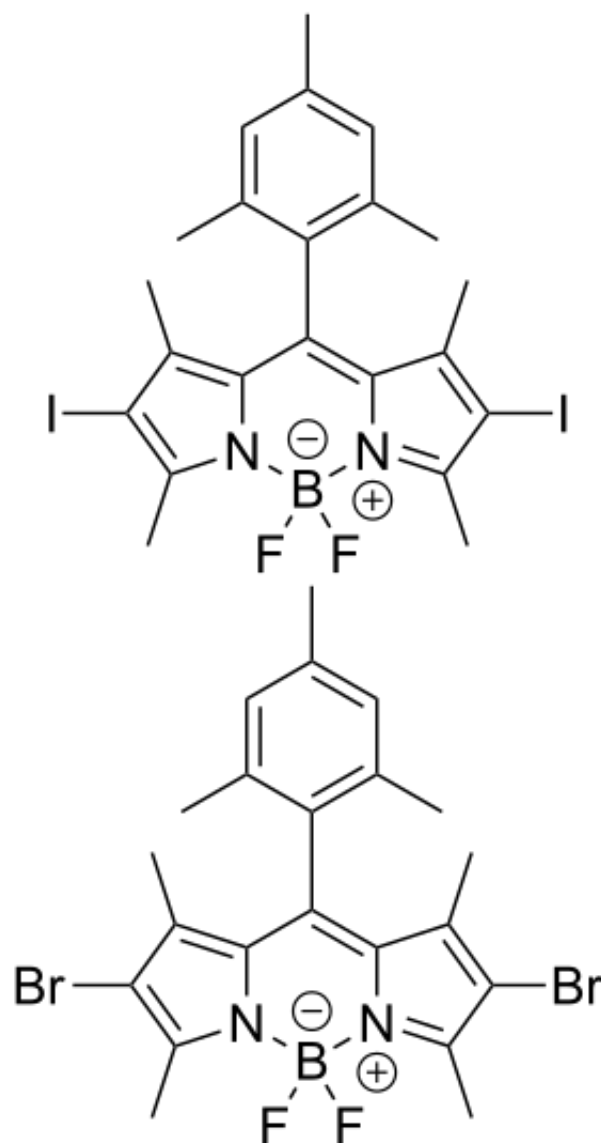


FIGURE 6.1: Molecular structures of BoDiPy 6 (top) and BoDiPy 7 (bottom)

phosphorescence quantum yield for each of these solutions, they argued for the presence of $^1(TT)$ spectra before free triplet formation, and predicted that the phosphorescence quantum yield for cyclohexane and chloroform were greater than 1, an indicator of multiexciton generation.

However, Wen et al. [120] demonstrated by the use of MS-CASPT calculations that the energetic requirement for singlet fission ($E(S_1) \geq 2 \times E(T_1)$) was not fulfilled in the bodipy dimer molecule. In addition, Kandrashkin et al. [121] demonstrated through the use of transient EPR spectroscopy that the expected quintet triplet pair state $^5(TT)$, often thought to be an intermediate in the separation of free triplets in the singlet fission process, does not appear for this BoDiPy dimer in low temperature glassy solvents. In addition, the EPR signal of each subunit of the dimer was different, indicating that the

triplets on each subunit did not arise from geminate pair generation through singlet fission.

These assertions were then confirmed by Montero et al. [122] in a correction to their earlier paper, showing through phosphorescence measurements that the triplet energy, as measured for separately donor- (Ph-NH₂) and acceptor-substituted (Ph-NO₂) BoDiPy monomers, would not permit singlet fission to occur, being 1.62 eV compared to the singlet energy of 2.48 eV.

This discussion is not yet concluded, however, as Tsuneda and Taketsugu [123] have continued to investigate singlet fission in BoDiPy, asserting that the solvent dependence as seen by Montero et al. [119] in the BoDiPy dimer, as well as in a new pi-stacked BoDiPy dimer similar to Montero et al. [119]'s, were due not to the occurrence of charge transfer states, but to differences in solvent adsorption to the molecule in solution altering the $\pi - \pi$ energy of the stacked dimers. In addition, they found that the S_2 energy of this dimer was near-isoergic with the $^5(TT)$ state, potentially allowing singlet fission from a higher singlet state. These were found using Long-range Correlated Kohn Sham Density Functional Theory (LC DFT), as well as the time dependent and spin flip variants of the technique. In addition, Xue et al. [124] used ab initio molecular dynamics simulations and TDDFT calculations to examine the solvent-solute dynamics for the same TMBodiPy dimers as Montero et al. [119] in chloroform and cyclohexane, demonstrating that variations in intramolecular vibrational modes due to the solvent-solute interactions result in variations in the S_1 , T_1 , and charge transfer state energies. These effects can combine to create a non-zero probability of singlet fission occurring in the dimer, as there are times when the primary condition for exothermic singlet fission is fulfilled.

Recently, there has been a paper from Zhou et al. [125], who identify the presence of singlet fission from the S_2 state of the Phenyl-BoDiPy heavy atom free molecule. They identify long-lived triplet transients in the nanosecond transient absorption spectrum of this molecule in solid crystalline films as well as in single crystals, and compare them to calculated triplet spectra for this molecule, demonstrating the presence of triplets. Via global analysis, they assign a three-lifetime-component model to the decay, with the shortest lifetime component being on ultrafast timescales (~ 30 fs). However, while they assign this decay component to the depopulation of the S_2 excited state via $^1(TT)$ formation, this evidence is difficult to base such a claim on, as it may be due to group velocity dispersion based artefacts on ultrafast timescales, and they clarify that there are other potential origins for this late-time triplet transient, such as SOCT-ISC, or ISC from S_2 to higher energy triplet states.

As the determination of the presence of single fission in BoDiPy-based dyes has been difficult, it is important to also consider alternative methods of triplet generation in BoDiPies, as singlet fission is not the only option. The most prominent method of triplet generation in BoDiPys is that of intersystem crossing, commonly via the heavy atom effect (Section 2.3.5.3). This heavy-atom effect induced intersystem crossing is a well known and common technique in BoDiPy dye derivatives, often by halogen substitution, typically using iodine as the heavy atom[52, 126–130] It has been found by [52, 128, 130] that the intersystem crossing yield is, in general, increased by increasing the halogen loading, though it can result in diminishing returns. In addition, substitution of the halogen atoms at some positions can hinder intersystem crossing by increasing the steric hindrance of the *meso*-substituted group twisting[130], which may indicate that this vibrational twisting mode is in part responsible for the intersystem crossing in *meso*-substituted BoDiPy derivatives.

The heavy atom effect is not the only pathway for intersystem crossing in BoDiPys, however. Another method of intersystem crossing that should be considered is Spin Orbit Charge Transfer Intersystem Crossing (SOCT-ISC). This pathway to triplet generation occurs due to the formation of an intermediate charge transfer state in a system containing an electron donor and an acceptor, which can induce changes in the orbital angular momentum when the dihedral angle between the two subunits is high. This has been observed in a range of *meso*-substituted BoDiPy derivatives, beginning with C_{60} in Ziessel et al. [131], and has been observed in many BoDiPys since then[98, 106, 117, 123, 129]. The primary criteria for the additive donor/acceptor subunit to BoDiPy enabling SOCT-ISC is that it be a large, bulky molecule, which induces a large dihedral angle between the two subunits. This in turn means that as electron transfer takes place from the core BoDiPy, the orbital angular momentum of the undergoes a large change, which permits transfer to the triplet manifold. As the mesityl group in BoDiPy 6 and 7 extends close to the main BoDiPy core, it is necessary to consider this ISC pathway as a possibility in the excited state decay.

This pathway has a number of advantages over conventional heavy-atom-effect induced ISC, including a lack of the toxicity often associated with halogen- or metal-including hybrid organic molecules, which is problematic for the in-vitro application of photodynamic therapy where BoDiPys are often used. In this application, triplets that are generated on the sensitising molecule transfer to create toxic singlet oxygen (1O_2) species, which can be used in location specific treatments to kill cancer cells.

In addition, for charge harvesting purposes, high degrees of spin-orbit coupling which can arise from the presence of heavy atoms may cause high phosphorescence quantum

yields, and are thus undesirable due to the resultant shortening of the triplet excited state lifetime[132].

The molecular structure of two BoDiPy dyes, herein referred to as BoDiPy 6 and BoDiPy 7, are shown in Fig. 6.1. These dyes were synthesised by Marco Cavazzini of the Istituto di Scienze e Tecnologie Molecolari (ISTM), Consiglio Nazionale delle Ricerche (CNR), and were sent to Dr. James Pidgeon together with additional BoDiPy derivatives to assess for their viability in polariton based microcavity research[2].

In this chapter, we shall investigate the excited state dynamics of these dyes and their potential as triplet sensitisers. We hypothesise that we shall observe long-term nanosecond scale signal in transient absorption spectroscopy, however the mechanism behind triplet generation is to be determined. We shall investigate both the morphology dependence of the excited state behaviour of these dyes, performing femtosecond ultrafast transient absorption spectroscopy on solutions of these dyes in toluene, as well as in spin-coated amorphous films, as well as highly crystalline thermally annealed films. As singlet fission requires multiple chromophores as sites for excitation, it is likely that adjusting the degree of intermolecular interaction in this manner will result in observable differences in the dynamic excited state behaviour of these dyes.

6.2 Results

6.2.1 Atomic Force Microscopy (AFM)

Atomic Force Microscopy (AFM) of the un-annealed (Fig. 6.2) and annealed (Fig. 6.3) thin films of BoDiPy 6 and 7. Fig. 6.2 (top) shows the AFM of the un-annealed thin film of BoDiPy 6. The surface is seen to be very smooth, with a Root Mean Square (RMS) roughness of 2.85 nm. This indicates that the un-annealed thin film of BoDiPy is very amorphous, with no evidence of crystal formation observed. In addition, the BoDiPy 7 amorphous film AFM is shown in Fig. 6.2 (bottom). However, it was observed during the measurement process that the BoDiPy pristine film was rapidly crystallising under the microscope, corroborating the observed degradation of both BoDiPy

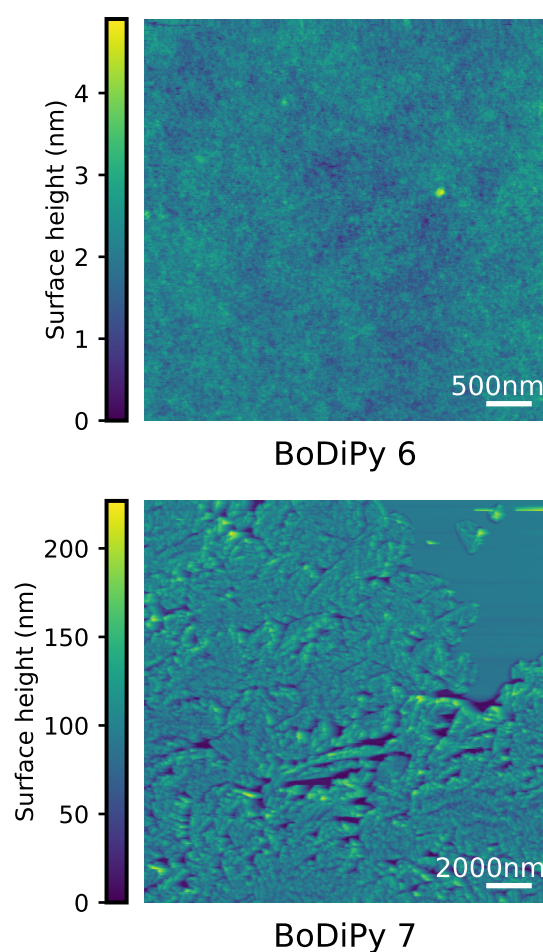


FIGURE 6.2: Atomic force microscopy images of amorphous films of BoDiPy 6 (top) and BoDiPy 7 (bottom). The BoDiPy 7 sample was observed to crystallise rapidly over the course of the experiment, and thus the sample is much more crystalline than the BoDiPy 6 film. However, the region in the upper right in this image has retained its amorphous nature. The image size is indicated by the length bar to the bottom right of the image. AFM was performed by Rachel Kilbride of the University of Sheffield.

6 and BoDiPy 7 un-annealed films when performing Transient Absorption Spectroscopy and steady state spectroscopy. Thus, we suggest that the heat from the illumination in the spectrometers result in crystallisation of both films. As the sample of BoDiPy 7 crystallised so rapidly, only a small amorphous region could be imaged (Fig. 6.2, bottom subfigure, top-right quadrant). The overall section of this film was found to have an RMS roughness of 120 nm, and the amorphous region was found to have an RMS roughness of 8.60 nm.

Fig. 6.3 shows the AFM of annealed films of BoDiPy 6 (top) and BoDiPy 7 (bottom), both with a region of interest (ROI) of $5\ \mu\text{m}$ (left) and $10\ \mu\text{m}$ (right). The smaller ROI is located on each larger ROI, and are designated with a red square. The colour range of each AFM plot is normalised with respect to the others for the sake of comparison.

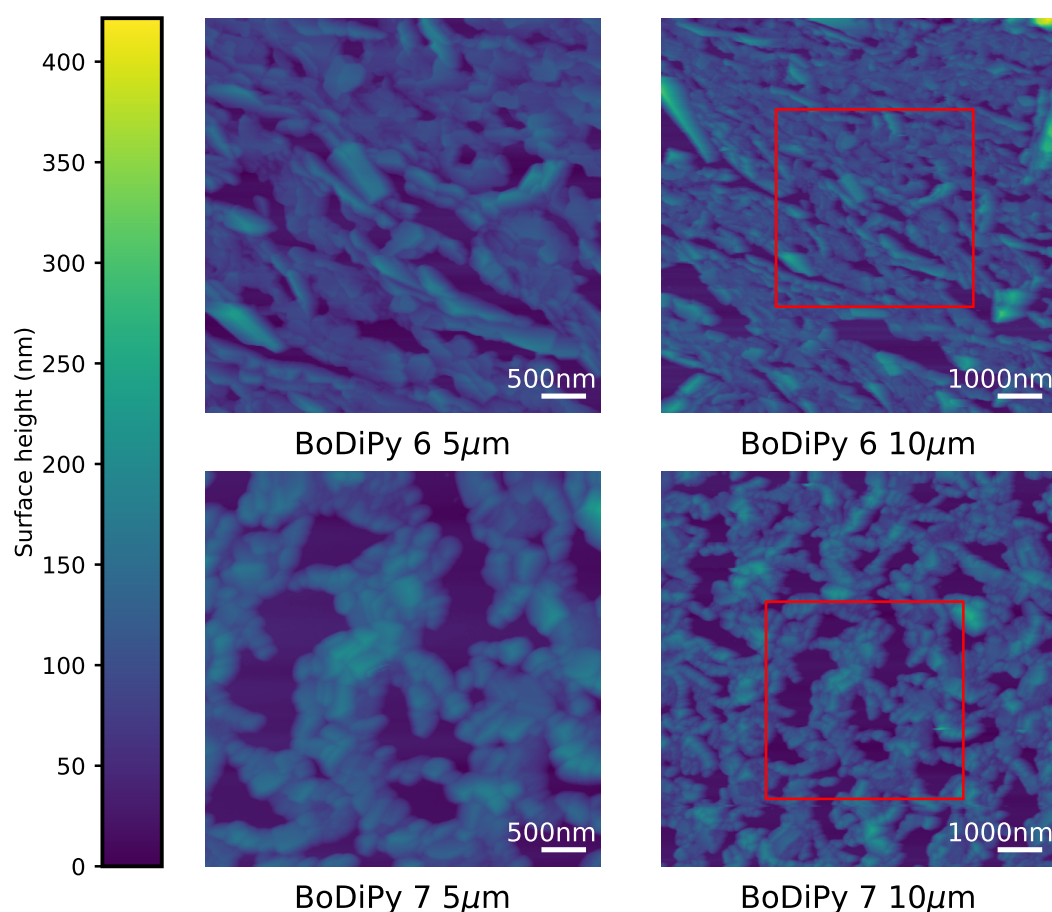


FIGURE 6.3: Atomic force microscopy images of thermally annealed films of BoDiPy 6 (top) and BoDiPy 7 (bottom). The height scans are normalised to the same points for ease of comparison. The position of the smaller images (left) on the larger, more zoomed-out images (right) are indicated by the red square. The image size is indicated by the length bar to the bottom right of the image. There is potential long-range structure visible in the BoDiPy 7 film, with aligned crystallites in the region of the smaller figure (bottom-left). AFM was performed by Rachel Kilbride of the University of Sheffield.

The BoDiPy 6 annealed film appears more crystalline than the pristine film, with an RMS roughness of 88 nm in the 5 μm plot, and of 100 nm in the 10 μm plot, due to a rougher region being visible in the top right of the image. The image shows that while the film shows many discernible domains, their size varies significantly, and there is little long-range order to be seen. This indicates that over long ranges, the annealed BoDiPy 6 film is quite disordered.

The BoDiPy 7 annealed film is similarly crystalline, with an RMS roughness of 98 nm in the 5 μm plot, and of 97 nm in the 10 μm plot, indicating a more uniform crystallinity. The crystalline domains seen in this film are much more uniform and smaller in size than those observed in the BoDiPy 6 films, and in the 10 μm plot, it appears that the crystals have formed aligned chains, indicating some level of self organisation or long-range structure in the crystal formation of BoDiPy 7, especially in the bottom two thirds of the AFM image.

Due to this characterisation, we refer to the un-annealed films as amorphous thin films, and the annealed films as crystalline thin films going forward.

6.2.2 Steady State Absorption

The steady-state UV-Vis absorption and emission spectra for BoDiPy 6 in toluene solution, in amorphous, un-annealed film, and in thermally annealed crystalline film are shown in Fig. 6.4. Franck-Condon fitting was performed on each spectrum, and where it was successful in recreating the shape of the spectrum, the fit is shown overlaid with the spectrum as a dashed grey line. The absorption and emission spectra for BoDiPy 6 in solution and in amorphous film are qualitatively similar. Both their absorption spectra possess narrow peaks between 2.0 and 2.5 eV, with a higher energy shoulder corresponding to vibronic character which is well modelled by Franck-Condon fitting. In addition, there is a broad absorption feature between 2.8 and 3.5 eV. We assign the lower energy absorption to the $S_0 \rightarrow S_1$ transition as they are the lowest energy, most intense features, and are mirrored with the emission spectra. We assign the higher energy absorption feature to the $S_0 \rightarrow S_2$ transition. The emission spectra are also narrow, with only a small shoulder at lower energy.

The absorption spectrum of the amorphous film is broader than that of the solution, while the corresponding emission spectrum is narrower. In addition, the spectra of the amorphous film are red-shifted from solution, by 0.074 eV for the absorption spectra, and by 0.049 eV for the solution spectra. This represents a reduction in the stokes shift in the amorphous thin film compared to the solution: 0.104 eV for the solution, and

0.079 eV for the film. This may be due to the increased broadening of the amorphous film spectra.

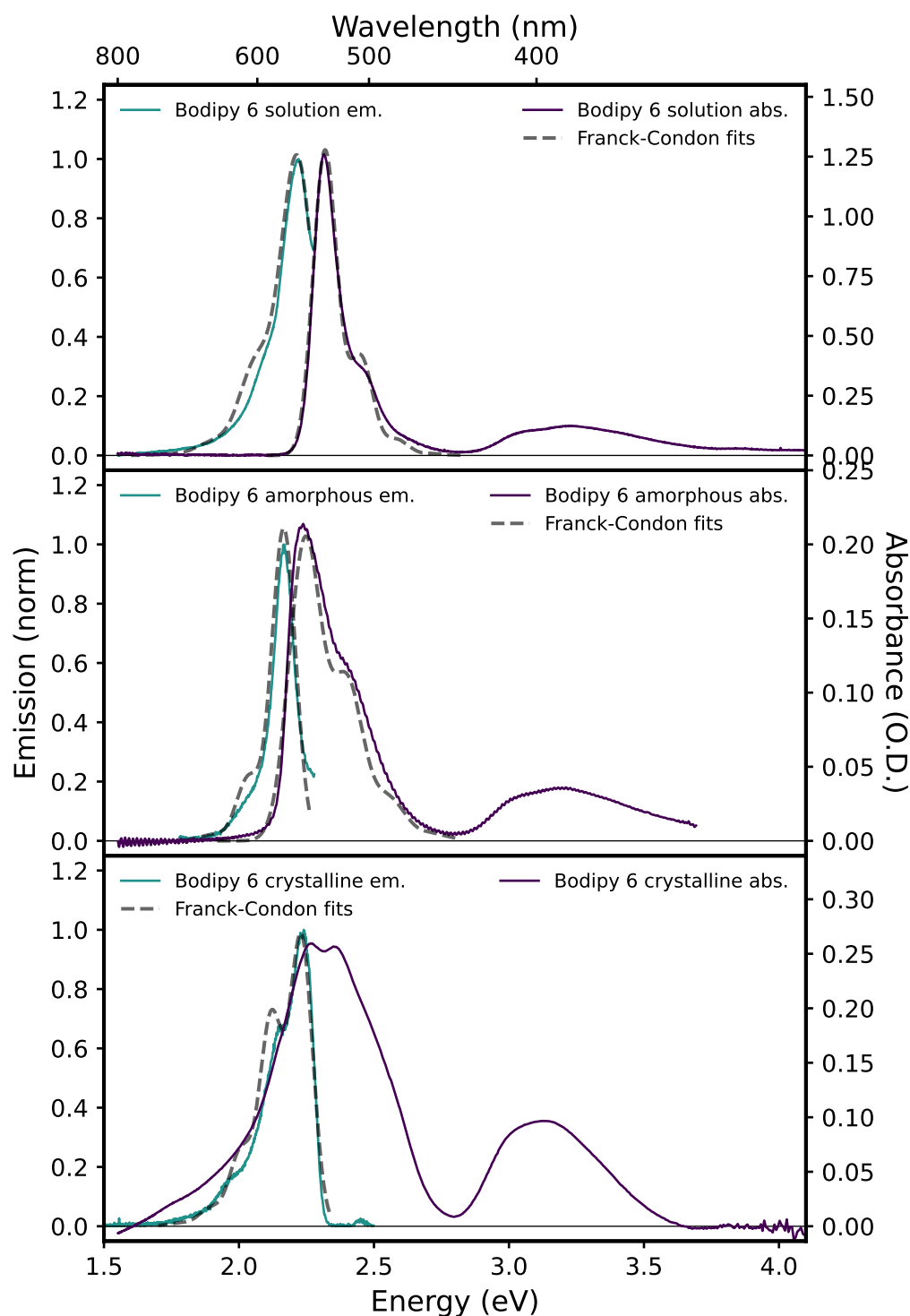


FIGURE 6.4: Steady state UV-Vis absorption and emission spectra for solutions, amorphous films, and crystalline films of BoDiPy 6. Absorption spectra show two peaks, an intense peak at around 2.3 eV, and a less intense absorption feature around 3 eV. The Franck-Condon fits to the data are shown with grey dotted lines.

The intensity of the $S_1 \rightarrow S_2$ absorption feature is also greater in the amorphous film spectrum as compared to the solution spectrum. All of this indicates that in the amorphous film sample, small intermolecular interactions allowed by greater molecular proximity have had small effects on both the potential energy landscape of the molecule, as well as the relative strengths of the dipole transition moments of the S_1 state compared to the S_2 state; either it has strengthened the S_2 dipole moment or reduced the S_1 dipole moment. The change in potential energy landscape can be quantified by the differences in the Franck-Condon fitting parameters in table 6.1, where the changes in the vibrational mode energy contributing to the spectra are small compared to differences in the Huang-Rhys parameter of said mode, which indicates a change in wavefunction overlap between the potential energy surfaces of the ground and excited states.

The crystalline film spectra show even greater broadening and increased vibrational character than the solution and amorphous film samples due to stronger intermolecular interactions. The S_2 transition feature is more strongly enhanced, and the Stokes shift is more strongly reduced between the S_1 state absorption and emission. In fact, the absorption and emission of this feature are almost overlapped, due to the broad tail of the absorption peak. This broad tail is similar to that noted in Zhou et al. [125], where they attribute it to both Mie and Rayleigh scattering from the crystalline film, as well as to an Urbach tail that arises from disorder in the film[133]. Thus, this tail may either arise from scattering or from contributions from disorder.

The steady state UV-Vis absorption and emission features of BoDiPy 7 are shown in Fig. 6.5. While the features of these spectra are broadly similar to those of BoDiPy 6, there are notable differences, especially in the crystalline film. The qualitative features of the absorption and emission spectra of BoDiPy 7 solution are the same as those of BoDiPy 6, with relatively minor quantitative shifts. The intense $S_0 \rightarrow S_1$ and $S_1 \rightarrow S_0$ features are both blue shifted compared to those of BoDiPy 6 by 0.028 eV and 0.061 eV respectively, leading to a larger Stokes shift of 0.079 eV compared to that in BoDiPy 6. The Franck-Condon fitting parameters, shown in Table 6.1, are identical to those in BoDiPy 6 for the absorption spectra. However, for the emission spectra, the difference is larger, with the vibrational mode energy being lower and the H-R parameter being higher in BoDiPy 7, indicating a smaller energy shift in the excited state and a larger wavefunction overlap. Both solutions also share the high energy absorption feature, which similarly to BoDiPy 6 we assign to the $S_0 \rightarrow S_2$ transition.

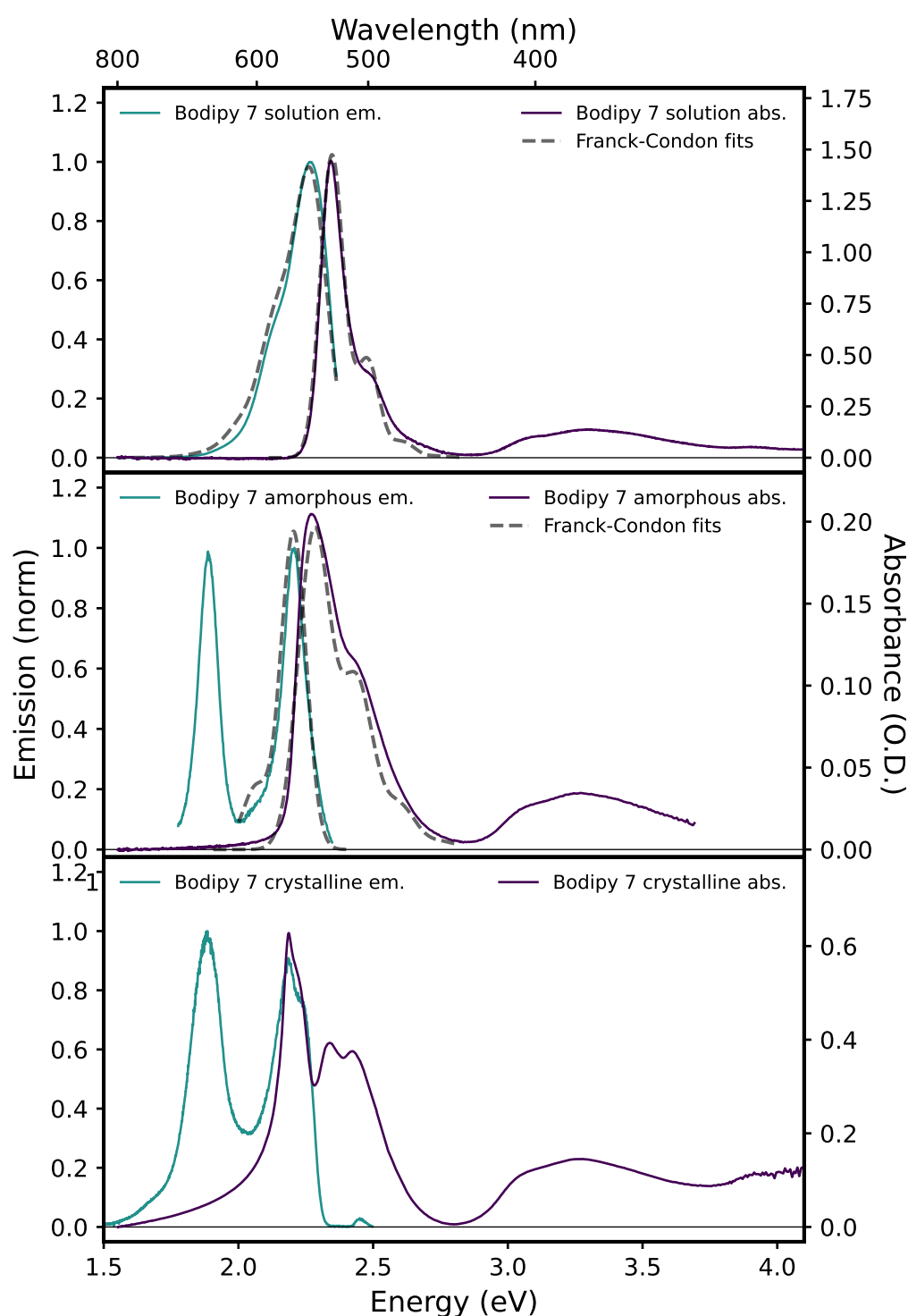


FIGURE 6.5: Steady state UV-Vis absorption and emission spectra for solutions, amorphous films, and crystalline films of BoDiPy 7. Absorption spectra show two peaks, an intense peak at around 2.3 eV, and a less intense absorption feature around 3.2 eV, and in the crystalline film the absorption extends to higher energies. In the emission spectra, there are two distinct peaks - one monomer like peak around 2.15 eV that is partially overlapped with the absorption spectra which has minor vibrational character in the amorphous spectrum, as well as a lower energy emissive peak around 1.8 eV. The Franck-Condon fits to the data are shown with grey dotted lines.

In the case of the amorphous film of BoDiPy 7, the absorption spectrum differs from the solution spectrum similarly to how the amorphous film and solution differ for BoDiPy 6; The $S_0 \rightarrow S_2$ feature is relatively enhanced in intensity, and the changes to the vibrational mode energy and H-R parameter of the $S_0 \rightarrow S_1$ transition feature shoulder are identical to in BoDiPy 7. This indicates that in the amorphous film, the intermolecular interactions are identical to those in the BoDiPy 6 film, and that the interactions are not of a type where the difference between the bromine and iodine substituted side groups contribute significantly. This suggests that any intermolecular interactions are mainly of an out-of-plane $\pi - \pi$ wavefunction-overlap type.

In the emission spectrum of this amorphous film sample, however, while the primary $S_1 \rightarrow S_0$ is comparable to that in BoDiPy 6, having a very small vibrational shoulder and very similar Franck-Condon fitting parameters (Table 6.1), there is an additional emissive peak at ~ 1.89 eV. This peak we assign to a low energy trap state in BoDiPy 7 which arises due to intermolecular interactions, as Pidgeon [2] shows that this state arises proportionally to the concentration of BoDiPy 7 in a polymer matrix. Further speculation on the nature of this state will be explored later in this chapter.

TABLE 6.1: Franck-Condon fitting parameters, where applicable, for BoDiPy 6 and BoDiPy 7. A (*) sign indicates the parameter was not obtained through Franck-Condon fitting, but from the maximum point of the spectrum, and thus does not correspond to the "true" 0-0 peak

Spectrum	0-0 energy	Vib. energy	H-R
BoDiPy 6 Absorption			
Solution	2.319	0.133	0.320
Amorphous film	2.245	0.156	0.521
Crystalline film	2.305	-	-
BoDiPy 6 Emission			
Solution	2.215	0.154	0.298
Amorphous film	2.166	0.131	0.200
Crystalline film	2.231	0.112	0.716
BoDiPy 7 Absorption			
Solution	2.347	0.132	0.321
Amorphous film	2.281	0.158	0.520
Crystalline film	2.19*	-	-
BoDiPy 7 Emission			
Solution	2.268	0.129	0.469
Amorphous film	2.205	0.141	0.193
Crystalline film	2.191	-	-

In the crystalline film absorption and emission spectra, the features observed in the amorphous film spectra are enhanced. The peaks in the emission spectra are broader than in the amorphous film, resulting in attempts to fit this spectrum with a Franck-Condon progression being unsuccessful. In addition, in the absorption spectrum, the $S_0 \rightarrow S_2$ absorption transition is more intense, and the $S_0 \rightarrow S_1$ transition has more intense vibronic peaks. The absorption spectrum also has an intense peak which overlaps with the emission spectrum at 2.19 eV, with a broad tail which overlaps with the lower-energy peak of the emission spectrum.

6.2.3 Time Correlated Single Photon Counting

Time-Correlated Single Photon Counting (TCSPC) decays of BoDiPy 6 and BoDiPy 7 are shown in Fig. 6.6 (top) and (bottom), respectively, in solution, in amorphous film, and in crystalline film, for comparison. Exponential fits (or biexponential in the case of BoDiPy 6 crystalline film) are shown as dotted lines overlaid with the decays. For the BoDiPy 6 amorphous film and the BoDiPy 7 crystalline film decays, their lifetimes are different enough to be separable into two distinct regions and fit with independent exponential decays, while for the BoDiPy 6 crystalline film, the initial decay is too small compared to the later decay to be fit separately.

In BoDiPy 6, the decays of the solution emissive state and the initial emissive decay of the amorphous film occur on similar timescales. Lifetimes components of the (bi)exponential decays and their uncertainties are recorded in full in Table 6.2. Both the early-time amorphous film and solution lifetimes occur on an approximately ~ 400 ps timescale, which indicates that in the amorphous film there is little change to the monomer-like dynamics of the dye in solution. There is insufficient data, and what is there is too noisy, for much to be concluded from the late-time section of the BoDiPy 6 amorphous film. However, the possible presence of a delayed component to the fluorescence of this sample supports the presence of triplet generation in the amorphous film.

The decay of the BoDiPy 6 emissive state in crystalline film is well modelled by a biexponential decay. While the first decay component is similar to those of the amorphous film and solution decays (680 ± 40 ps compared to ~ 400 ps), the second component is much longer, having a decay lifetime of 8.5 ± 0.7 ps. This long timescale decay is indicative of some back-conversion process in BoDiPy 6 from the non-fluorescent triplet state, such as Reverse InterSystem Crossing (RISC) or Triplet Fusion (TF), resulting in the observed delayed fluorescence.

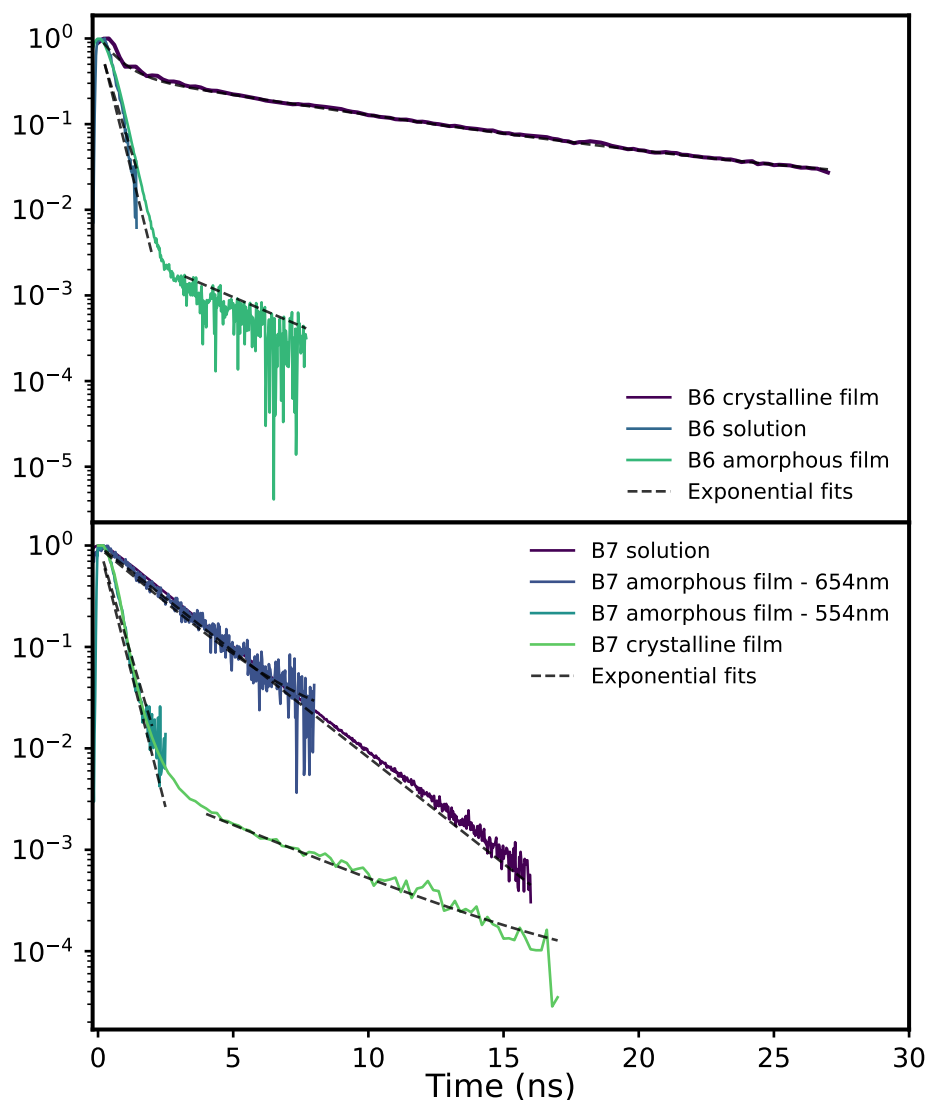


FIGURE 6.6: Time-correlated single photon counting plots of the emissive decay of BoDiPy 6 (top) and BoDiPy 7 (bottom). Fitted decays are shown as dashed lines overlaid with the plots. The emissive lifetimes of BoDiPy 6 in solution (top, blue) and in amorphous solid (top, green) film, as well as those of the high energy BoDiPy 7 amorphous film emission (bottom, light blue) and the BoDiPy 7 crystalline film emission (bottom, green), and the BoDiPy 7 low energy amorphous film emission (bottom, dark blue) and the BoDiPy 7 solution emission (bottom, purple), are similar and overlapped with one another. The emission of the BoDiPy 6 crystalline films was only fit using multiple decay components, and has a much longer lifetime than that of BoDiPy 6 in solution and in amorphous films.

The decay of the BoDiPy 7 crystalline film decays on the same shorter ~ 400 ps timescale as the main BoDiPy 7 amorphous film emission, similar to the main emissive lifetimes of BoDiPy 6. The longer lifetime component in the crystalline film decays with a lifetime of 3.9 ± 0.4 ns, and similarly to the BoDiPy 6 samples, indicates the presence of delayed fluorescence due to some reverse-triplet-generation process, though to a lesser degree

TABLE 6.2: Lifetimes of emissive decays from Time-Correlated Single-Photon Counting decays as shown in Fig. 6.6.

Decay	τ_1 (ns)	τ_2 (ns)	$\delta\tau_1$ (ns)	$\delta\tau_2$ (ns)
BoDiPy 6				
Solution	0.42	-	0.02	-
Amorphous film	0.34	3	0.01	30
Crystalline film	0.68	8.5	0.04	0.7
BoDiPy 7				
Solution	2.07	-	0.003	-
Amorphous film 654 nm	1.92	-	0.03	-
Amorphous film 554 nm	0.42	-	0.01	-
Crystalline film	0.48	3.9	0.07	0.2

than that observed in the crystalline BoDiPy 6 film. The presence of delayed fluorescence in the BoDiPy 6 amorphous and crystalline films as well as the BoDiPy 7 crystalline films indicates a triplet generation process in these films. This does not eliminate the possibility of similar processes occurring in the remaining samples due to higher noise and the consequently limited time range of the experiments.

The longer wavelength feature observed in the BoDiPy 7 steady state emission spectrum (Fig. 6.5) was also examined using TCSPC. This feature decays with a timescale of 1.92 ± 0.03 ns, which is very similar to the solution emissive lifetime of 2.07 ± 0.03 ns. This indicates that the second emissive feature in the BoDiPy 7 amorphous and crystalline film is monomer-like, and experiences similar dynamics to the emissive state in solution.

6.2.4 Transient Absorption Spectroscopy

Transient absorption spectroscopy (TA) was performed on solution, amorphous film, and crystalline film samples of BoDiPy 6 and 7. In addition, the TA of the crystalline film was performed using an excitation wavelength of 400 nm (3.1 eV) and 530 nm (2.3 eV), as well as at a range of fluences from 500 uW to 1500 uW. The transient absorption spectra and kinetics of BoDiPy 6 in solution is shown in Fig. 6.7, those corresponding to the amorphous film in Fig. 6.8, and those corresponding to the crystalline film on the right hand side Fig. 6.9, with the resultant fits shown on the plots as dashed lines. The lifetimes of the decays are shown in Table 6.3.

The BoDiPy 6 solution spectrum (Fig. 6.7, top) shows an intense positive feature corresponding to a combined Ground State Bleach (GSB) and Stimulated Emission (SE) feature, as they occur at the same energies as those appearing in the steady state spectra. In addition, there are negative signals at higher energy which represent Excited State Absorption (ESA) features. Due to the presence of the S_2 absorption in the steady

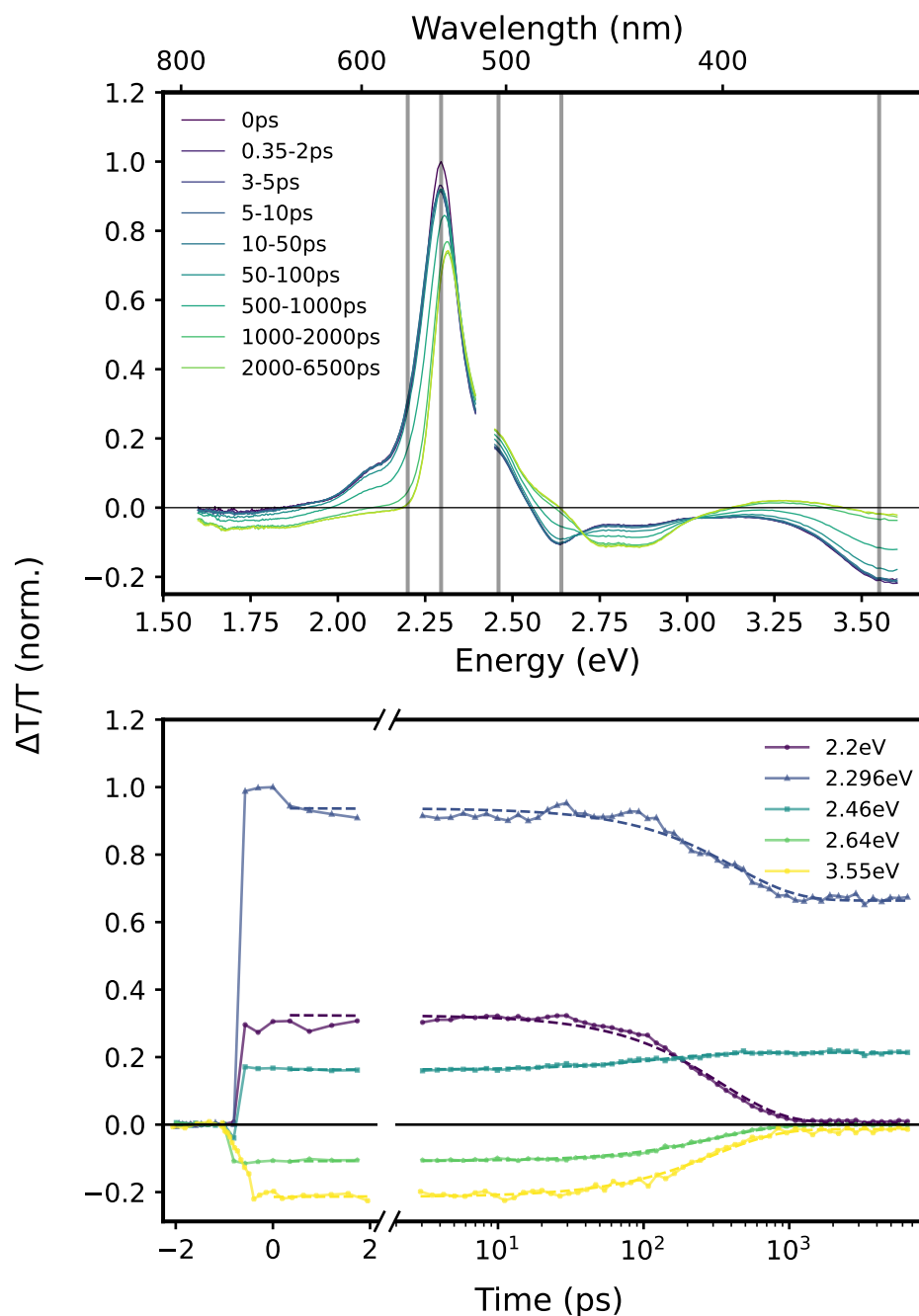


FIGURE 6.7: Transient absorption spectra (top) and kinetics (bottom) of BoDiPy 6 in toluene solution. The decay kinetics are fit with exponential and bi-exponential models. The pump region for the spectra at 500 nm (2.5 eV) has been removed. This excitation wavelengths occurs in the $S_0 \rightarrow S_1$ transition peak. Energies of the kinetic slices shown on the lower figure are shown on their respective spectra as vertical grey lines.

state spectrum around ~ 3 eV, we consider that the two negative features may be linked, due to the dip in signal at this energy.

The presence of two isosbestic points around ~ 2.7 eV and ~ 3 eV indicates that the decay of the excited state in solutions of BoDiPy 6 proceeds via a two-step process. The initial

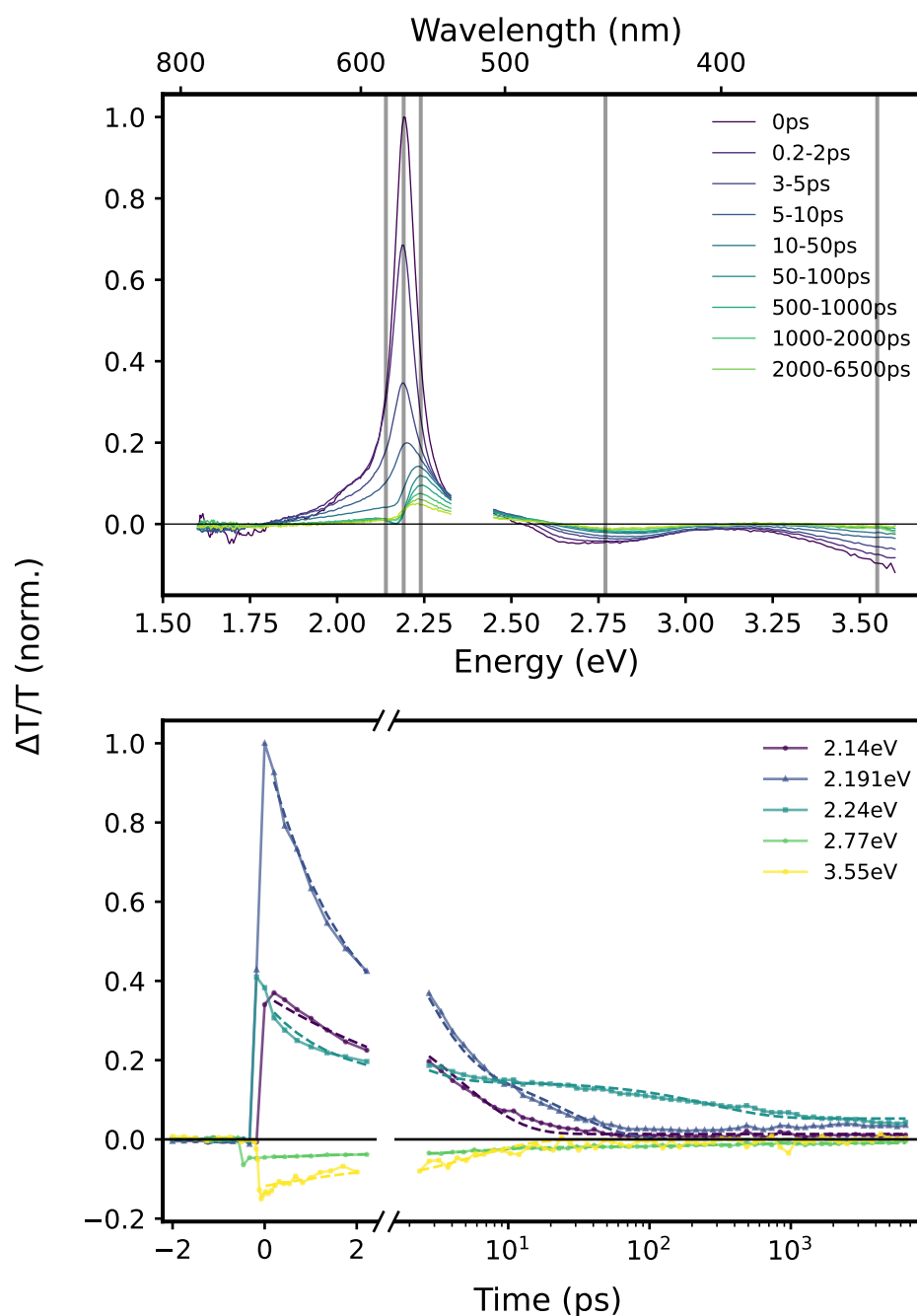


FIGURE 6.8: Transient absorption spectra (top) and kinetics (bottom) of BoDiPy 6 amorphous film. The decay kinetics are fit with exponential and bi-exponential models. The pump region for the spectra at 520 nm (2.4 eV). This excitation wavelengths occurs in the $S_0 \rightarrow S_1$ transition peak. Energies of the kinetic slices shown on the lower figure are shown on their respective spectra as vertical grey lines.

excited state we simply assign to the excited S_1 state, and the excited state absorption at high energy to the $S_1 \rightarrow S_N$ transitions. The decay kinetics of this spectrum (Fig. 6.7, bottom) corroborates this observation, with the lifetimes in Table 6.3 showing the decay of the S_1 state lasting ~ 300 -400 ps, similar to the lifetime observed in the TCSPC (Table 6.2). However, the decay of this state does not recover the ground state, as signal

is observable in the GSB feature at 2.3 eV after the decay of the SE feature, as well as in the ESA feature at 2.64 eV, which changes in shape significantly. This excited state does not decay over the course of the time window of the Helios picosecond transient absorption experiment, but due to the prevalence of ISC in BoDiPy derivatives, as well as the presence of heavy atoms on both BoDiPy 6 and 7, we assign this late-time spectrum to triplet generation via ISC.

The TA spectrum of the amorphous thin film of BoDiPy 6 (Fig. 6.8, top) shows a more intense GSB feature than that of the solution. This may be due to an increase in the SE feature, or to a change in the relative intensities of the dipole moments of the ground and excited state in the amorphous film compared to the solution. While the spectrum at late time is difficult to analyse in this figure, and the late-time spectrum is shown later for easier comparison (Figs. 6.19, 6.15 and 6.16), it can be seen in Fig. 6.3 that the GSB feature remains after the SE feature has decayed fully. The kinetics of the amorphous film (Fig. 6.8, bottom) show that the lifetime of the excited state in the amorphous film is significantly reduced when compared to that of the solution. The fitted decay constants show a lifetime of the S_1 state of the order of picoseconds, with the lifetime varying by an order of magnitude depending on the energy observed. However, there is still some long-lived signal in this sample, with the 2.24 eV kinetic slice, corresponding to the tail of the GSB showing residual signal with a lifetime of ~ 300 ps. This matches the decay of the solution film as well as the TCSPC signal corresponding to the lifetime of the emissive state. This signal is also present in the ESA around 2.7 eV, although much less intense. The decay of the peak of the positive signal, which contains contributions from the SE and the GSB, appears to decay at a much faster rate of 25 ps, although this is likely to result from overlapping decay lifetimes being poorly reproduced by a biexponential decay model.

The TA spectra and kinetics of the crystalline film of BoDiPy 6 with an excitation wavelength of 530 nm (2.3 eV) and a fluence of $1200 \mu W$ (Fig. 6.9) show a more complex spectrum than the other two samples. At short times, the spectrum is composed of a large positive GSB/SE feature between ~ 1.5 and ~ 2.6 eV. This feature has more discernible structure than the other samples, with multiple discernible peaks that have noticeably different lifetimes. This indicates a difference in lifetime between the emissive lifetime and the excited state lifetime, indicating there is some species transfer similar to the amorphous film. The GSB has a flat shoulder feature around 2.54 eV, indicating an overlap with a negative feature, as well as very intense ESA feature at higher energy, indicating a large enhancement of the excited state absorbance in the crystalline film compared to the solution and amorphous film. Similarly to the solution, the ESA features may be a single broad ESA feature overlaid with the $S_0 \rightarrow S_2$ GSB around 3.0 eV.

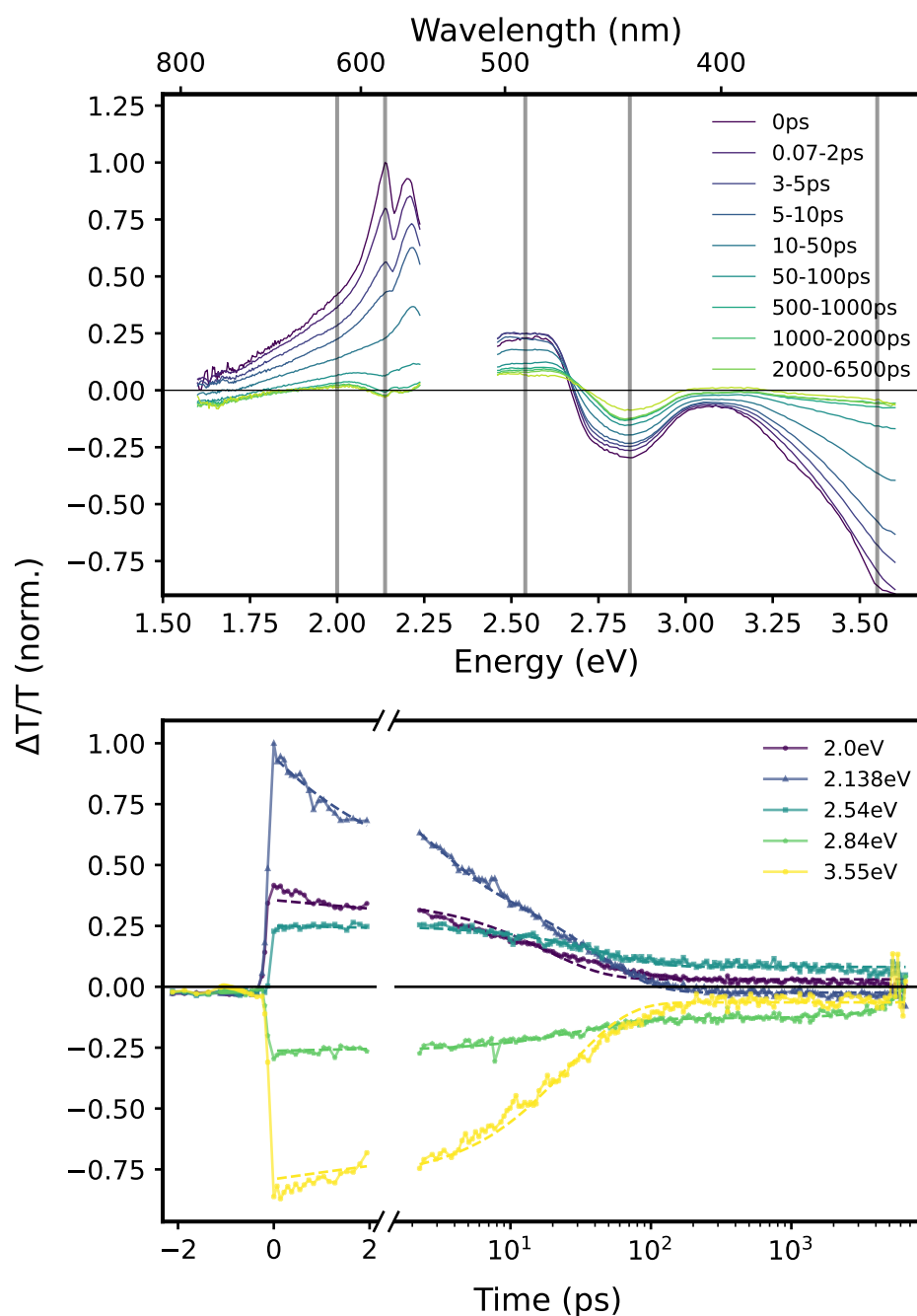


FIGURE 6.9: Transient absorption spectra (top) and kinetics (bottom) of BoDiPy 6 crystalline film. The decay kinetics are fit with exponential and bi-exponential models. The pump region for the spectra at 530 nm (2.3 eV). This excitation wavelength occurs in the $S_0 \rightarrow S_1$ transition peak. Energies of the kinetic slices shown on the lower figure are shown on their respective spectra as vertical grey lines. The crystalline film data used for this graph is the one at $1200 \mu W$ fluence.

The lifetime of the emissive state taken from the kinetic at 2.0 eV is found to be 17.7 ± 0.7 ps. There is a much faster lifetime component that appears in the decay of the GSB feature, however, of ~ 2.5 eV in the peak of the GSB, and of 4.8 ± 0.4 ps. These

lifetimes are comparable to the short lifetime component of the decays of the amorphous films of BoDiPy 6. The long-lifetime component of these decays varies between 25.7 ± 0.8 eV for the 3.55 eV ESA kinetic, and 50 ± 5 ps for the 2.84 eV ESA feature when modelled with a monoexponential decay.

When modelled as a biexponential decay, this feature returned a lifetime for the long-lived excited state species of 2.4 ± 0.4 ps, but due to the large error it was also modelled with a monoexponential decay for comparison.

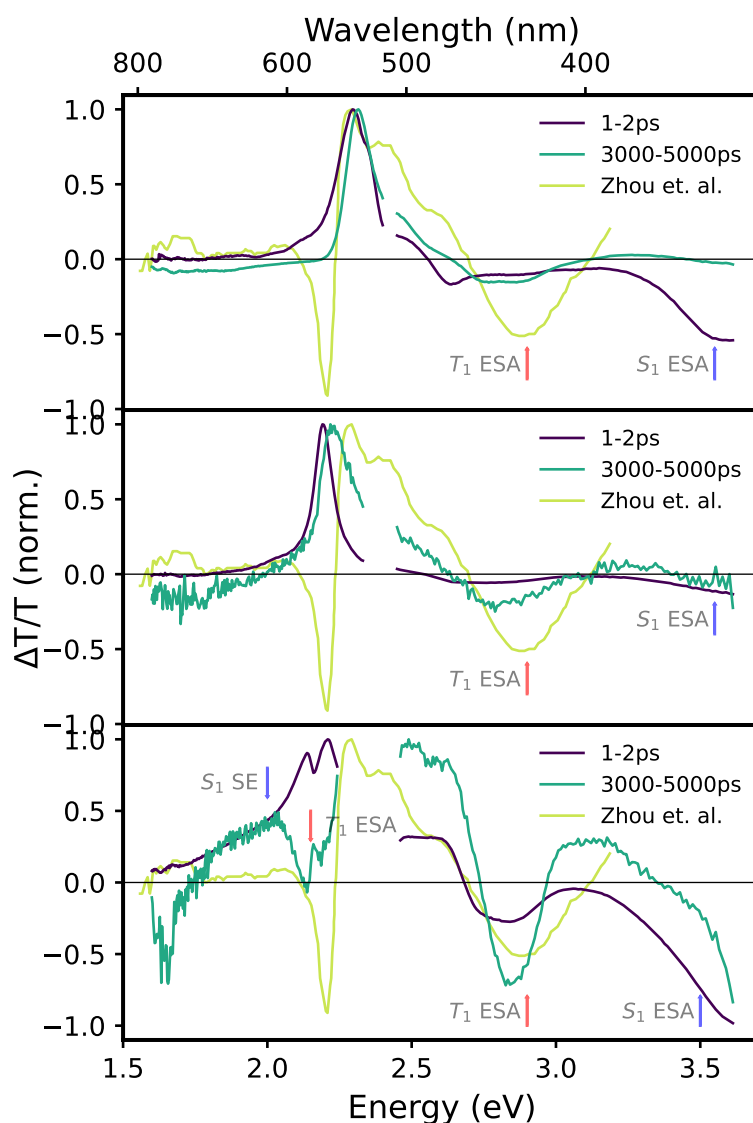


FIGURE 6.10: Comparison of early time (1-2ps) and late time (3000-5000ps) normalised spectra of BoDiPy 6 solution (top), amorphous film (middle) and crystalline film (bottom), to examine the change in spectral features with time. Experimentally determined triplet spectrum obtained from Zhou et al. [125] is shown overlaid with the spectra to illustrate spectral similarities between the late time spectra and the triplet-identified spectrum. Arrows are included on this figure to identify relevant features.

TABLE 6.3: Lifetimes of excited-state decays of BoDiPy 6 from Transient Absorption Spectroscopy decays as shown in Figs. 6.7, 6.8, 6.9, 6.15, 6.16 and 6.19.

Decay energy (eV)	τ_1 (ns)	τ_2 (ns)	$\delta\tau_1$ (ns)	$\delta\tau_2$ (ns)
BoDiPy 6 solution				
2.2	3.4×10^2	-	0.2×10^2	-
2.30 (peak)	4.2×10^2	-	0.2×10^2	-
2.46	1.4×10^2	-	0.1×10^2	-
2.64	3.17×10^2	-	0.09×10^2	-
3.55	3.1×10^2	-	0.1	-
BoDiPy 6 amorphous film				
2.14	4.7	-	0.2	-
2.20 (peak)	1.8	25	0.1	5
2.24	1.4	2.8×10^2	0.1	0.3×10^2
2.77	5.8	3.4×10^2	0.7	0.8×10^2
3.55	10	-	2	-
BoDiPy 6 cryst. film				
Pump wavelength:			400nm	
$500\mu W$				
2.14*	9	47	2	4
2.2*	10	45	2	4
2.5*	38	-	5	-
2.85*	7×10^1	-	2×10^1	-
$1500\mu W$				
2.14*	5.6	38.0	0.3	0.9
2.2*	6.2	35.7	0.4	0.7
2.5*	33	-	1	-
2.85*	44	-	2	-
Pump wavelength:			530nm	
$500\mu W$				
2.14*	2.13	38	0.08	1
2.2*	18	75	2	9
2.5*	58	-	4	-
2.85*	56	-	5	-
$1200\mu W$				
2.0	17.7	-	0.7	-
2.14*	2.4	37	0.1	1
2.14 (peak)	2.6	38	0.1	1
2.2*	4.8	4×10^1	0.4	0.1×10^1
2.54	44	-	2	-
2.5*	44	-	2	-
2.85*	50	-	5	-
2.84	33	2.4×10^3	2	0.4×10^3
3.55	25.7	-	0.8	-

Fig. 6.10 shows the normalised spectra of the BoDiPy 6 TA at early times (1-2 ps) and late times (3000-5000 ps), for samples in solution (top), in amorphous film (middle) and in crystalline film (bottom). In solution, this figure shows that in addition to the decay of the emissive feature around 2 eV, and the ESA feature at 3.55 eV, the spectrum shows a significant difference between 2.5 and 3.0 eV at long TA delays. At early times, this feature is most intense at 2.64 eV, and is broad enough to mix with the 3.55 eV ESA feature, whereas at long times, it is much more even and also more localised. We assign this feature as the signature of the late-time triplet associated spectrum for BoDiPy 6, occurring through ISC in the monomeric solution state.

This allows us to identify similar features in the late time spectra of the amorphous film and crystalline film TA, as both have the same mostly-featureless ESA feature at these wavelengths, suggesting triplet generation occurs in the films also. However, while the triplet-associated spectrum in the amorphous film TA looks very similar to that in solution, albeit less intense as the amorphous film kinetics show a significantly faster decay lifetime, the late-time spectrum in the crystalline film TA is more complex a persistent positive feature between 1.6 eV and 2.1 eV, a very broad GSB feature around 2.5 eV, and the recovery of the proposed $S_0 \rightarrow S_2$ GSB feature between 3.0 eV and 3.3 eV. Furthermore, near the peak of the GSB/SE feature, there appears to be an ESA feature overlapped with the bleach, which may mean that the persistent positive feature between 1.6 eV and 2.1 eV can be identified with the tail of the ground state absorption feature. This ESA feature occurs at a similar energy to the ESA shown in the spectrum from Zhou et al. [125], which is triplet-associated. Thus, we associate both this ESA and the ESA shown in all three samples around 3.0 eV with a triplet species. Finally, there are additional ESA features seen in this spectrum at late times which are not seen in the others, including a persistent ESA at 3.55 eV, as well as a negative feature around ~ 1.6 eV.

Fig. 6.11 shows the TA spectra (top) and kinetics (bottom) of BoDiPy 7 in solution, both of which show similar behaviour to those of the BoDiPy 6 solution. The spectrum shows similar GSB/SE features, and the high ESA feature is similarly overlapped with the region associated with the $S_0 \rightarrow S_2$ transition GSB. In addition, a similar isosbestic point is observed around 2.55 eV, indicating that the decay in this sample also proceeds via a two-step process. The regions associated with the SE feature and the ESA feature at 3.55 eV decay near completely over the course of the experimental time window with lifetimes of 2.1 ± 0.2 ns, and 2.5 ± 0.2 ns, respectively, meaning that the second species involved removes the singlet emission. The shape of the 2.7 eV ESA feature at early and late times are similar to that of the equivalent feature in the BoDiPy 6 spectrum, indicating that the secondary species may also be a triplet generated via ISC. The GSB and 2.7 eV ESA feature do not decay fully over the course of the experiment, and the

time constant of their decay cannot be confidently be determined as such. However, their decays have approximately been fitted with time constants of 2.1 ± 0.2 ns for the peak of the GSB, 3 ± 1 ns for the middle of the GSB peak, and 2.3 ± 0.2 ns for the ESA feature.

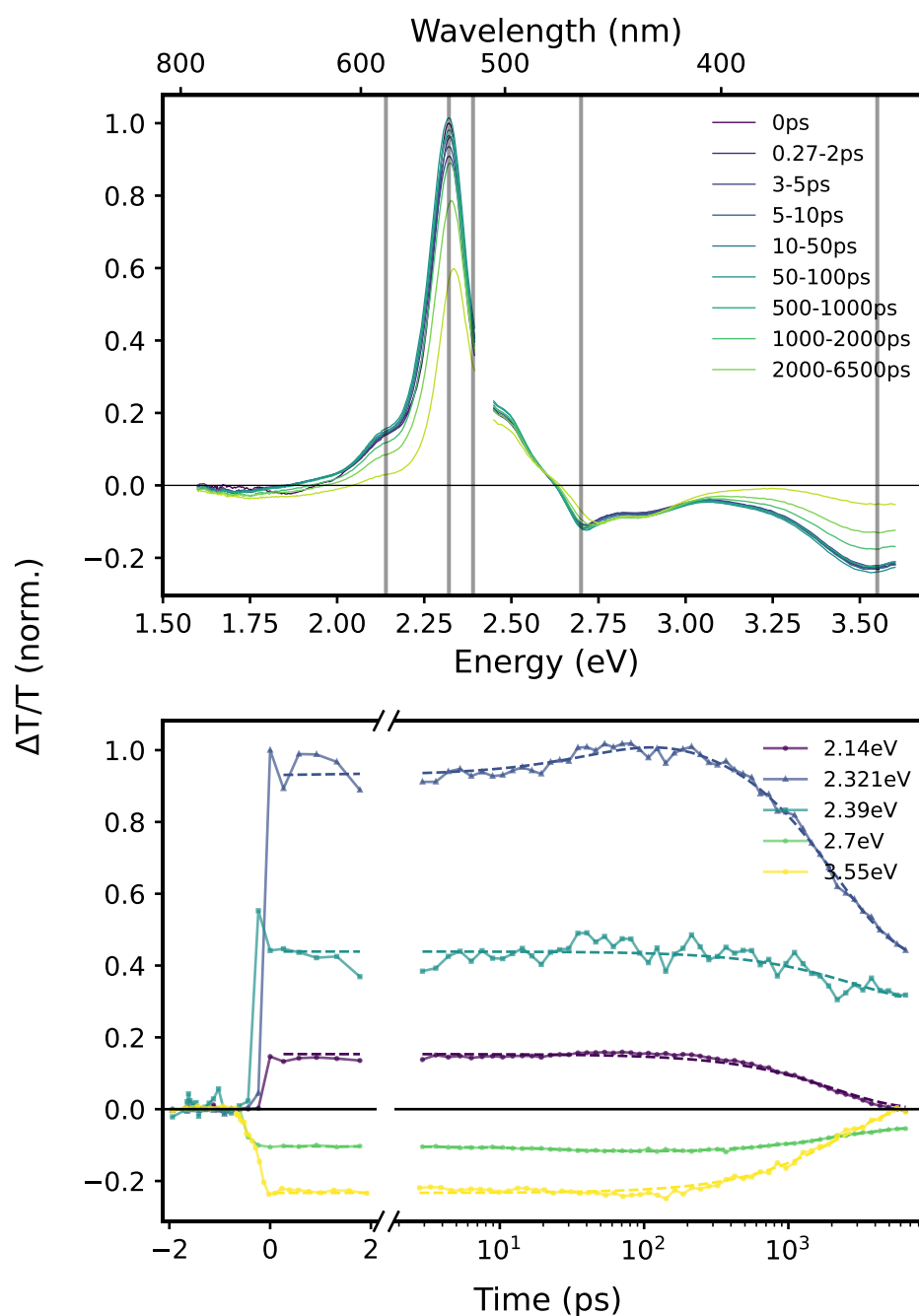


FIGURE 6.11: Transient absorption spectra (top) and kinetics (bottom) of BoDiPy 7 in toluene solution. The decay kinetics are fit with exponential and bi-exponential models. The pump region for the spectra at 500 nm (2.5 eV) has been removed. This excitation wavelengths occurs in the $S_0 \rightarrow S_1$ transition peak. Energies of the kinetic slices shown on the lower figure are shown on their respective spectra as vertical grey lines.

These values are qualitatively very similar to the decay of the S_1 associated features. In addition, the GSB peak (2.32 eV) grows in intensity over a shorter timescale, being 50 ± 10 ps.

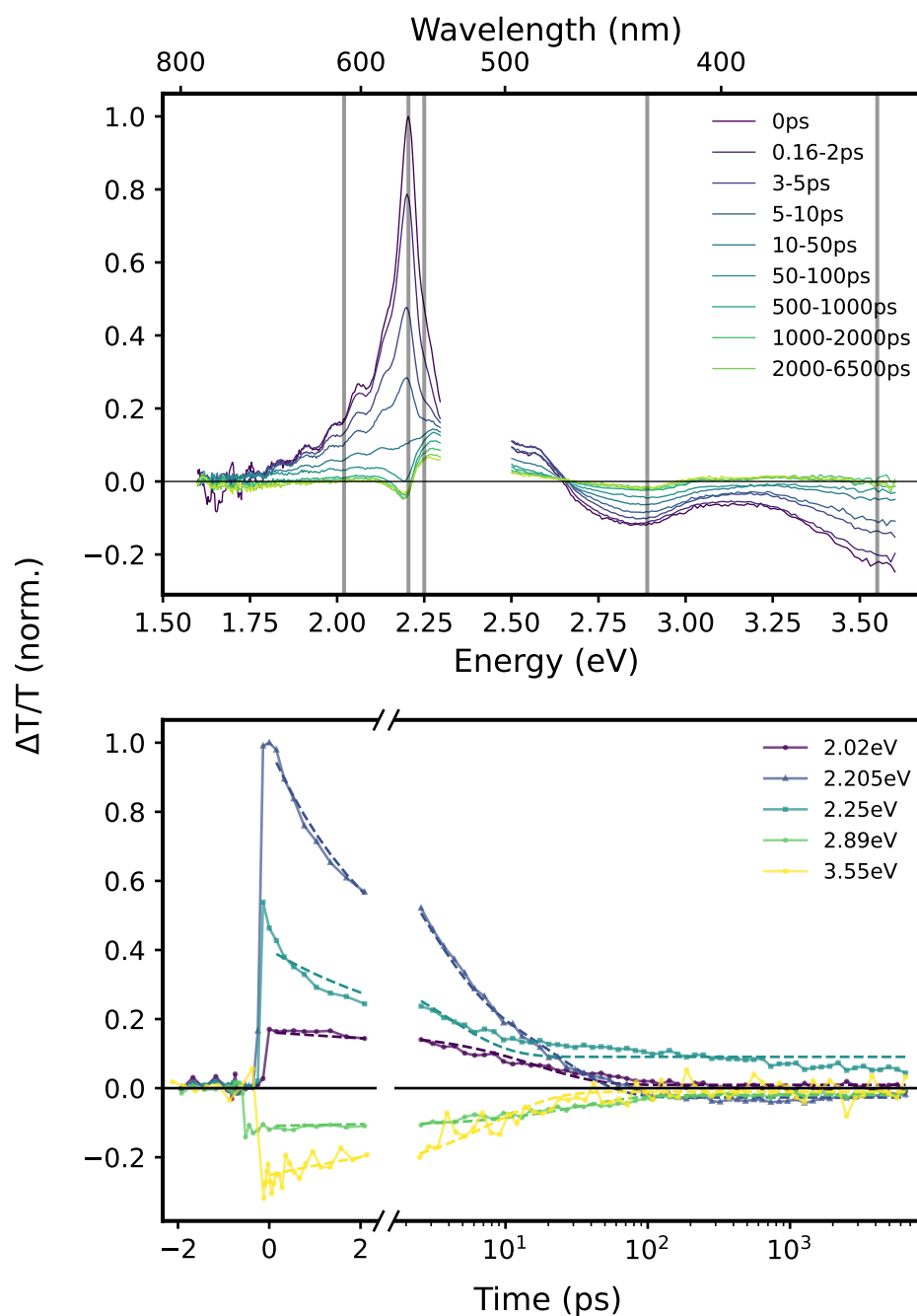


FIGURE 6.12: Transient absorption spectra (top) and kinetics (bottom) of BoDiPy 7 amorphous film. The decay kinetics are fit with exponential and bi-exponential models. The pump region for the spectra at 520 nm (2.4 eV). This excitation wavelengths occurs in the $S_0 \rightarrow S_1$ transition peak. Energies of the kinetic slices shown on the lower figure are shown on their respective spectra as vertical grey lines.

The spectra and kinetics of BoDiPy 7 in amorphous thin film (Fig. 6.12) are also qualitatively similar to those of BoDiPy 6, in that they have a narrow intense GSB/SE feature, a persistent GSB, and a shorter multi-exponential decay than in solution. The primary differences in the amorphous film spectrum are that the high-energy ESA features are more intense in BoDiPy 7 than in BoDiPy 6, and decay over a lifetime of

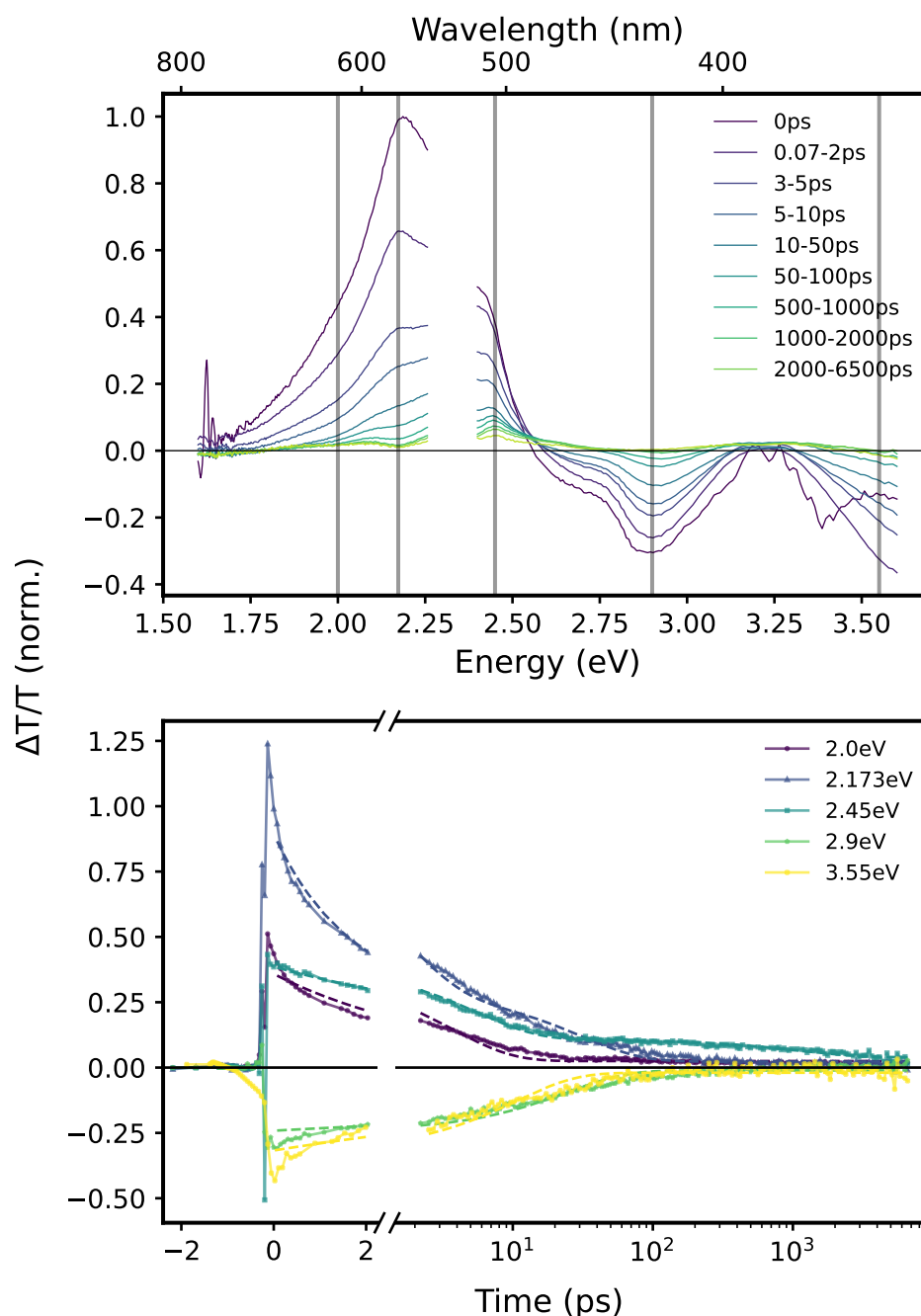


FIGURE 6.13: Transient absorption spectra (top) and kinetics (bottom) of BoDiPy 7 crystalline film. The decay kinetics are fit with exponential and bi-exponential models. The pump region for the spectra at 530 nm (2.3 eV). This excitation wavelengths occurs in the $S_0 \rightarrow S_1$ transition peak. Energies of the kinetic slices shown on the lower figure are shown on their respective spectra as vertical grey lines. The crystalline film data used for this graph is the one at 1200 μW fluence.

33 ± 3 ps and 11 ± 2 ps, respectively, which is similar to the 17 ± 1 ps decay lifetime of the SE feature, and thus can be associated with the decay lifetime of the S_1 state. This is much less than the emissive lifetime of both the lower wavelength emission in the amorphous film as measured with the TCSPC, 358 ± 3 ps. However, while the peak of the GSB decays biexponentially with lifetimes of 2.4 ± 0.1 ps and 23 ± 2 ps, the tail of the GSB decays with a fast lifetime of 3.9 ± 0.4 ps and leaves a residual signal that persists beyond the timescale of the experiment.

The spectrum of the BoDiPy 7 crystalline film TA (Fig. 6.13, top) is qualitatively different from that of BoDiPy 6, with the GSB/SE feature being very broad and lacking many features of the BoDiPy 6 sample, such as the structure of the SE feature, and the difference in the high energy shoulder. It is significant that the lower-energy emissive feature seen in the steady state emission spectrum of BoDiPy 7 does not appear in the TA spectrum of BoDiPy 7. This may be due to the difference in sensitivity between emission spectroscopy and TA. In emission spectroscopy, the intensity of the signal is based on the emissivity of the sample as well as the population of the excited state. In TA, however, the signal is doubly proportional to the population of the excited state due to the nature of the pump-probe setup. As a result, it may be that the lower-energy emissive feature is from a state with a lower population, but high emissivity, and is represented in the emission spectrum disproportionately to its population. The 3.55 eV ESA feature is significantly less intense than that in BoDiPy 6.

The lifetimes of the BoDiPy 7 crystalline thin film TA decays (Fig. 6.13, bottom) vary significantly over the spectrum. The SE feature decays significantly faster than the 358 ± 3 ps decay of the TCSPC signal, with a lifetime of 3.7 ± 0.1 ps. The tail of the GSB feature lasts beyond the time range of the experiment, similar to the amorphous film sample, but in this it decays faster than the amorphous film and has been fit with a multiexponential decay with a short lifetime of 5.6 ± 0.1 ps and a long lifetime of 1.1 ± 0.1 ns. The remaining features decay over a timescale with an order of magnitude of tens of picoseconds. The full details of the lifetime fits to the BoDiPy 7 TA decays can be found in Table 6.4.

Fig. 6.14 compares the spectra of BoDiPy 7 in solution (top) amorphous film (middle) and in crystalline film (bottom, at early (1-2 ps) and late (3000-5000 ps) timescales). In solution, the GSB feature of the spectrum is mostly unchanged, and only a small change is visible in the 2.7 eV ESA feature. This change is less than that observed in the equivalent BoDiPy 6 feature, indicating that either this feature is slower to form, which agrees with the BoDiPy 7 solution kinetics observed, or that the resultant late-time ESA feature differs less from its early-time counterpart in BoDiPy 7. The largest time-dependent differences in the solution spectrum are that the SE feature at low energies

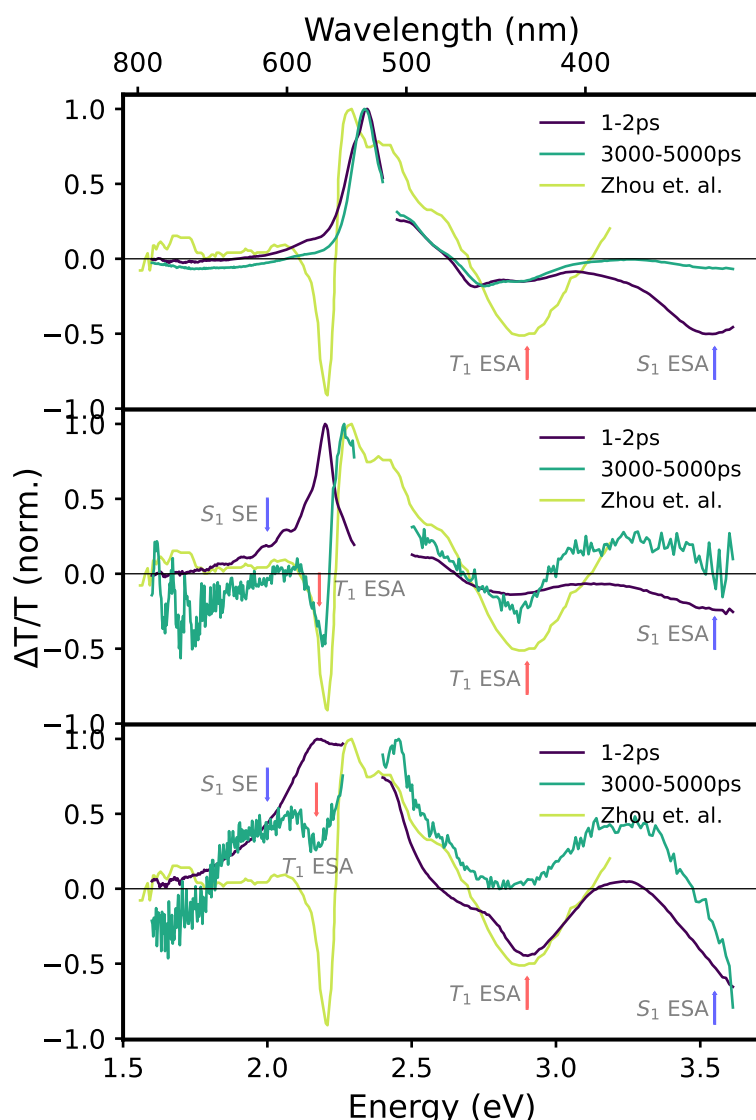


FIGURE 6.14: Comparison of early time (1-2 ps) and late time (3000-5000 ps) normalised spectra of BoDiPy 7 solution (top), amorphous film (middle) and crystalline film (bottom), to examine the change in spectral features with time. Experimentally determined triplet spectrum obtained from Zhou et al. [125] is shown overlaid with the spectra to illustrate spectral similarities between the late time spectra and the triplet-identified spectrum. Arrows are included on this figure to identify relevant features.

has given way to a small ESA feature, and that the high-energy ESA feature has almost disappeared. That the high energy ESA decays with a different timescale to the 2.7 eV indicates that the state corresponding to the 2.7 eV ESA at late time is distinct from the S_1 excited state that is correlated to the 3.55 eV ESA. This supports the idea that BoDiPy 7 also shows ISC from the S_1 state in solution.

The early and late time spectra corresponding to the amorphous film (Fig. 6.14 - middle) show differences similar to those shown by the solution sample, but more intense. The high energy ESA features show a similar trend, wherein the 3.55 eV has decayed

completely by the time of the 3000-5000 ps spectrum, to the point where the S_2 GSB feature has been recovered. The SE feature has also decayed, resulting in a blue shift of the positive GSB/SE feature, as the SE appears more intense than that of the solution spectrum. In addition, an ESA feature has appeared overlapped with the GSB feature, after the decay of the SE feature. This ESA feature can be also seen in the triplet-associated spectrum from Zhou et al. [125]. The presence of this ESA feature suggests that the long-lived species, speculated to be triplets generated from ISC, is also present in amorphous films.

The late time spectrum of the crystalline film of BoDiPy 7 (bottom) is different from those seen in amorphous film and in solution. This is most clearly seen in the 2.7 eV ESA feature, which is not present in the late time spectrum, and the S_2 GSB feature has reappeared. Furthermore, while there is some evidence of the presence of the ESA feature that appeared in the GSB of the amorphous film, which we previously associated with triplet generation, there is also still significant signal in the SE region of the spectrum (~ 2.0 eV). This feature may correspond to the scattering from the ground state absorption feature seen in Fig. 6.5, or may correspond to residual emission spectrum, possibly from a contribution from the longer lived low energy emission seen in Fig. 6.6. Overall, the lack of ESA in the late time spectrum contradicts the hypothesis that triplets are generated in the crystalline film of BoDiPy 7 as suggested by the TCSPC decays in Fig. 6.6. This may suggest a lower triplet yield together with a high degree of reverse-ISC resulting in the delayed fluorescence seen in the TCSPC data, or that the $S_0 \rightarrow S_2$ bleach feature is stronger in the crystalline film and obscures the ESA features.

TABLE 6.4: Lifetimes of excited-state decays of BoDiPy 7 from Transient Absorption Spectroscopy decays as shown in Figures 6.7 to 6.9, 6.17, 6.18 and 6.20.

Decay energy (eV)	τ_1 (ps)	τ_2 (ps)	$\delta\tau_1$ (ps)	$\delta\tau_1$ (ps)
BoDiPy 7 solution				
2.14	2.1×10^3	-	0.2×10^3	-
2.32 (peak)	50	2.1×10^3	10	0.2×10^3
2.39	3×10^3	-	1×10^3	-
2.7	35	2.3×10^3	5	0.2×10^3
3.55	2.5×10^3	-	0.2×10^3	-
BoDiPy 7 amorphous film				
2.02	17	-	1	-
2.2 (peak)	2.4	23	0.1	2
2.25	3.9	-	0.4	-
2.89	33	-	3	-
3.55	11	-	2	-
BoDiPy 7 cryst. film				
Pump wavelength:				400nm
300 μ W				
2.17*	2.10	24	0.07	1
2.23*	4.0	-	0.3	-
2.455*	49	-	7	-
2.9*	49	-	7	-
1000 μ W				
2.14*	1.74	22	0.05	1
2.23*	2.1	-	0.2	-
2.455*	19	-	2	-
2.9*	50	-	2	-
Pump wavelength:				530nm
500 μ W				
2.17*	0.81	21	0.08	1
2.23*	22	2×10^2	6	1×10^2
2.455*	12.2	-	0.3	-
2.9*	61	-	4	-
1200 μ W				
2.0	3.7	-	0.1	-
2.17*	0.72	15.2	0.04	0.9
2.173 (peak)	1.63	31	0.08	2
2.23*	0.75	21	0.04	1
2.45	5.6	1.1×10^3	0.1	0.1×10^2
2.455*	7.4	-	0.4	-
2.9	24	-	1	-
2.9*	23	-	1	-
3.55	11.5	-	0.8	-

6.2.5 Fluence Dependent Transient Absorption Spectroscopy

To examine further the nature of the dynamics in the crystalline films of BoDiPy 6 and 7, the TA was performed at multiple pump powers, between $\sim 500 \mu W$ and $\sim 1200 \mu W$. The pump powers that could be reached on the day of the experiments varied with the capabilities of the laser on that day. In addition, the change in the TA dynamics when excited at 530 nm (2.3 eV) and at 400 nm (3.1 eV) was investigated, as this represents exciting to the S_1 and the S_2 state, respectively, and the fluence dependence of each is presented here.

The fluence dependence of BoDiPy 6 excited at 400 nm (3.1 eV) is shown in Fig. 6.15. The low pump power used for this measurement is $500 \mu W$ and the high pump power used is $1500 \mu W$.

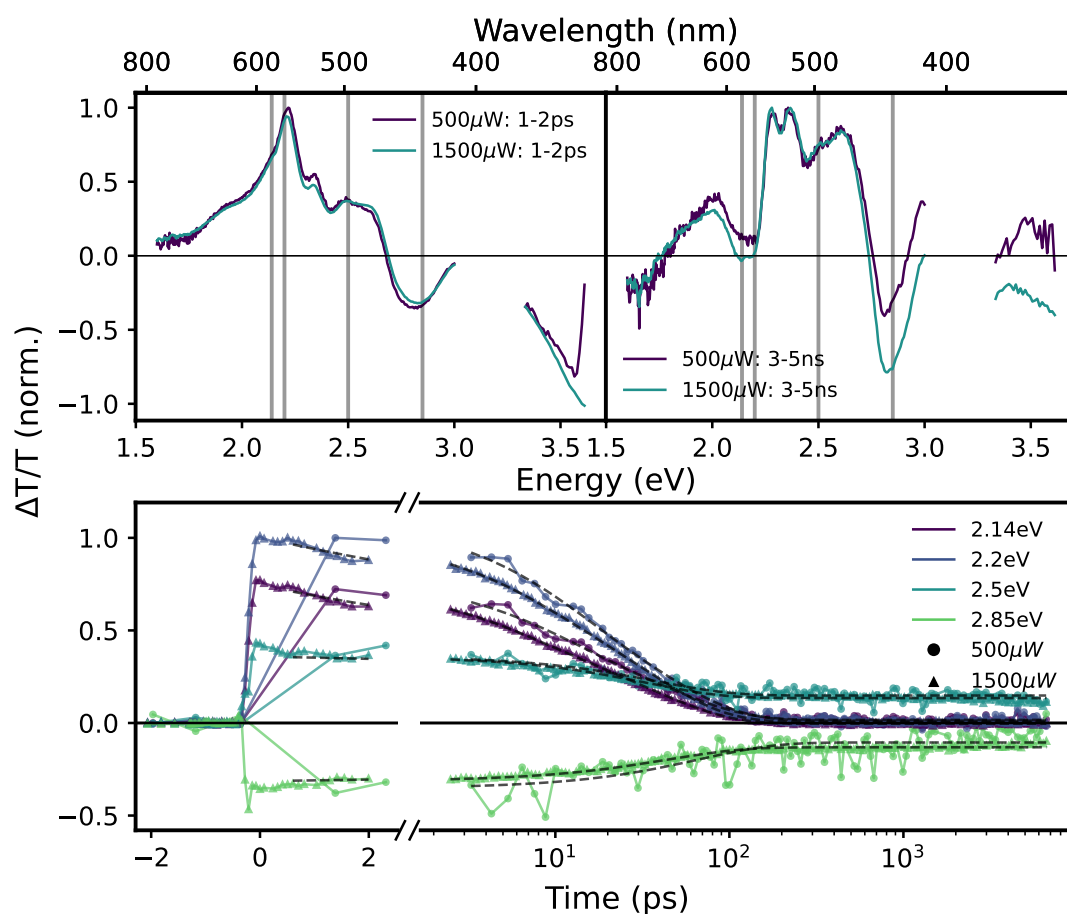


FIGURE 6.15: Fluence dependence of the transient absorption of BoDiPy 6 crystalline thin films at 400 nm (3.1 eV) excitation, showing spectra at early times (1-2 ps, top-left) and late times (3-5 ns, top-right). Comparative kinetic slices between the two spectra are shown on the lower figure, with fits to the data shown as dotted lines. Energies of the kinetic slices shown on the lower figure are shown on their respective spectra as vertical grey lines.

The early time spectra (between 1-2 ps) are shown in the top-left sub-panel, and there does not appear to be any major difference between the two spectra at different fluences. The late time spectra, however, show a more intense 2.85 eV ESA feature when excited at 1500 μW . This could mean a more intense triplet-associated spectral feature and a proportionally larger triplet yield, which may imply that the triplet generating method is bi-molecular. In the kinetics (bottom), the decays are broadly quite similar, save for the features at 2.14 eV and 2.2 eV, which are proportionally more intense than the other two features. This may, however, be due to the lower time resolution in the 500 μW pump power plot, which results in a higher normalisation. The lifetime fits of the kinetics are shown on the plot as a dotted line overlaid with each kinetic. While there is some variation between the two fluences, as shown in Table 6.3, we attribute this mainly to differences in detector signal/noise ratio and normalisation, resulting in universally longer lifetimes in the 500 μW excitation data, as small variations due to noise are exacerbated at lower fluences.

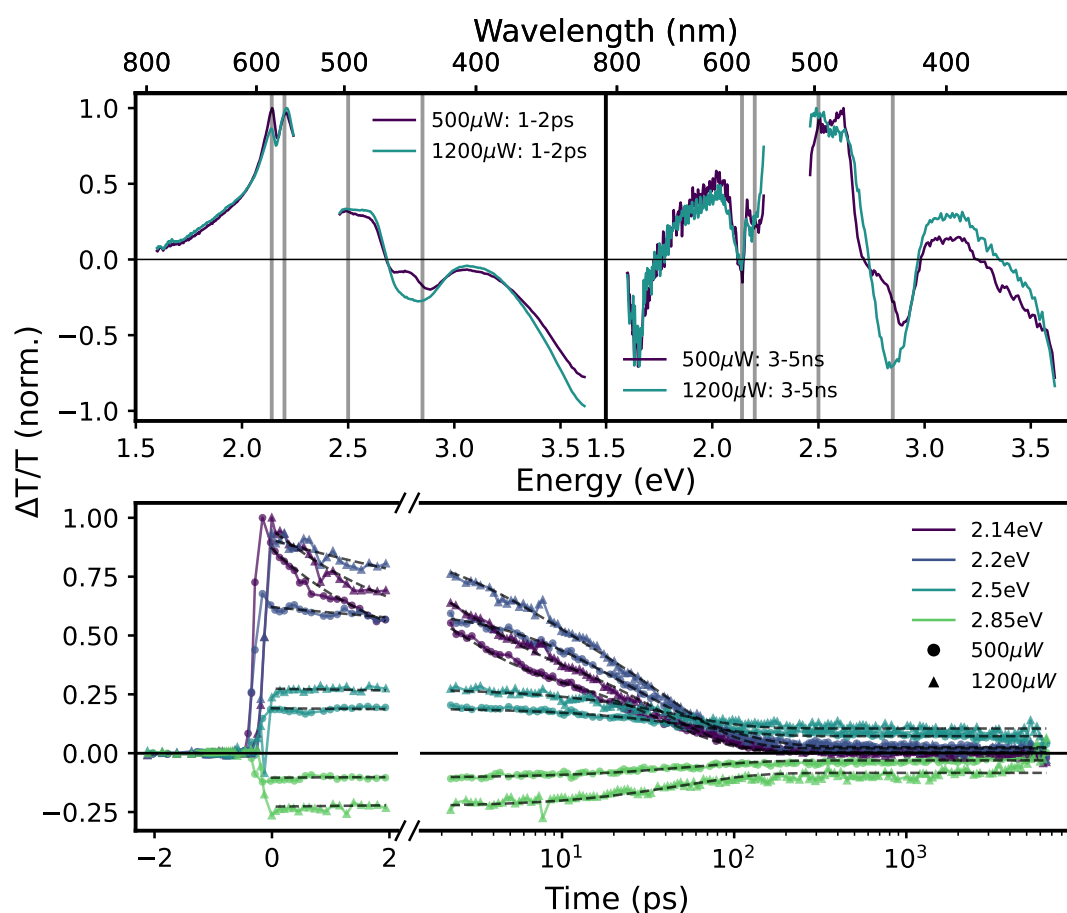


FIGURE 6.16: Fluence dependence of the transient absorption of BoDiPy 6 crystalline thin films at 530 nm (2.3 eV) excitation, showing spectra at early times (1-2 ps, top-left) and late times (3-5 μs , top-right). Comparative kinetic slices between the two spectra are shown on the lower figure, with fits to the data shown as dotted lines. Energies of the kinetic slices shown on the lower figure are shown on their respective spectra as vertical grey lines.

The fluence dependence of BoDiPy 6 excited at 530 nm (2.3 eV) is shown in Fig. 6.16. The powers used for this experiment were $500 \mu W$ for the lower power and $1200 \mu W$ for the high pump power measurement. The most significant differences between the spectra at early times (1-2 ps, top-left) occur at 2.14 eV, in the GSB/SE band, in which the secondary peak is reduced slightly in the higher fluence regime with respect to the lower fluence regime. Other than this, the majority of the GSB/SE band does not vary with an increased fluence. However, the high energy ESA feature changes significantly. The 3.55 eV feature is slightly enhanced with higher fluence, and the shape of the 2.85 eV feature is slightly changed, with more features appearing in the lower fluence plot, and the same feature being broader and more featureless in the $1200 \mu W$ plot.

This indicates that exciting at a higher fluence results in more population being transferred to a the non-emissive state that is associated with the ESA, as the emission is reduced but the ESA is enhanced. This is supported by the fluence-dependent spectra at long times (3000-5000 ps, top-right), as the ESA spectrum at 2.85 eV is similarly enhanced. This in turn supports the assertion drawn from Fig. 6.15, that the triplet generation method is sensitive to the density of excited state species in the sample, meaning that the generation method of the species present at late time is bi-molecular. In addition, the feature from 3.0 eV and above is more positive in the $1200 \mu W$ spectrum, indicating that either the high energy ESA feature has decayed faster, or the GSB has decayed slower, which is supported by the higher excited state population indicated by the increased 2.85 eV ESA feature.

The lifetimes of the excited state kinetics (Fig. 6.16 - bottom) are shown in Table 6.3. The lifetime of the emissive SE feature is very static between the two TA datasets, being composed of a bimolecular decay with a short lifetime component of 2.13 ± 0.08 ps and 38 ± 1 ps in the low-fluence kinetic, and 2.4 ± 0.1 ps and 37 ± 1 ps in the high-fluence kinetic. This indicates that the emissive decay is primarily a monomolecular process. The same is true of the decay of the 3.55 eV ESA, with lifetimes of 56 ± 5 ps and 50 ± 5 ps for the low and high fluence kinetics respectively. This lack of change may suggest that the decay processes do not change with fluence, but the initial population may. However, the lifetimes of the GSB peak and shoulder decay do vary with fluence. The decay of both of these features is significantly faster at higher fluence than at lower fluence. However, this may also be due to higher signal to noise ratio at higher fluence.

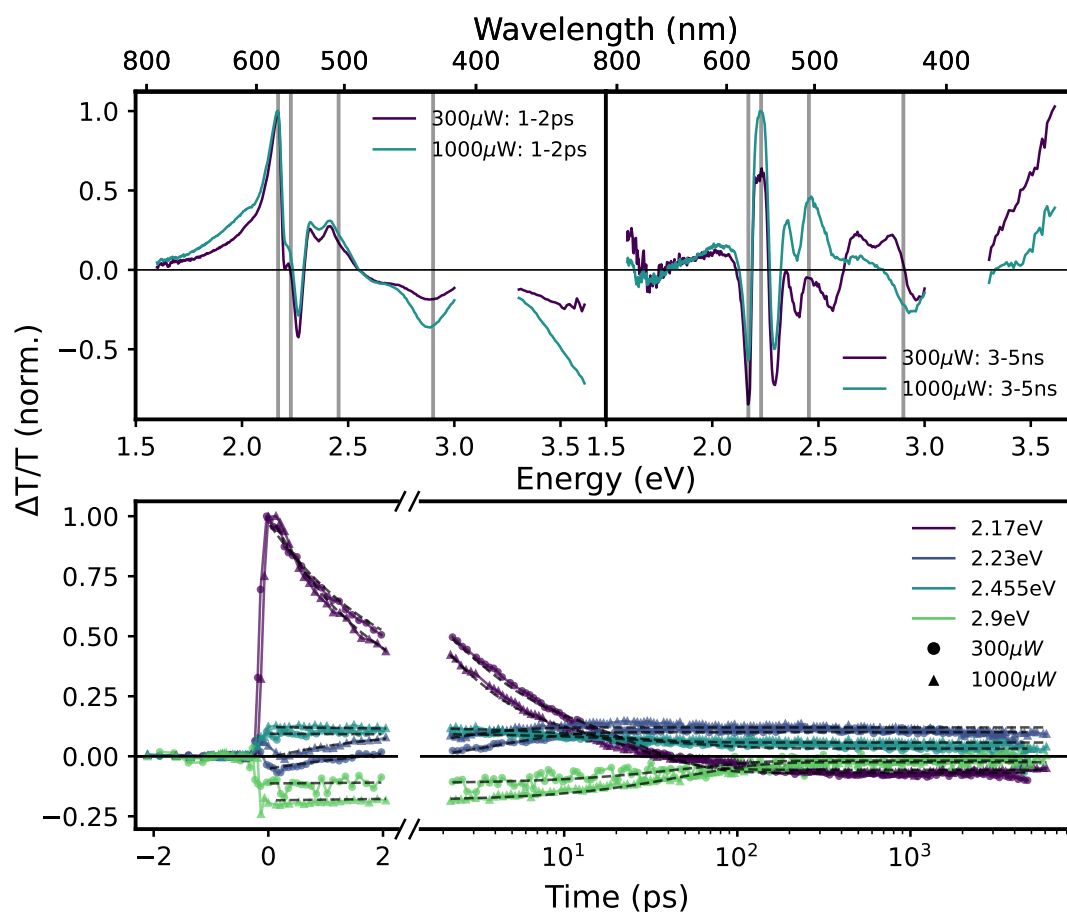


FIGURE 6.17: Fluence dependence of the transient absorption of BoDiPy 7 crystalline thin films at 400 nm (3.1 eV) excitation, showing spectra at early times (1-2 ps, top-left) and late times (3-5 μ s, top-right). Comparative kinetic slices between the two spectra are shown on the lower figure, with fits to the data shown as dotted lines. Energies of the kinetic slices shown on the lower figure are shown on their respective spectra as vertical grey lines.

The fluence dependence of BoDiPy 7 excited at 400 nm (3.1 eV) is shown in Fig. 6.17. The low fluence power used in this comparison is 300 μ W and the high fluence power used is 1000 μ W. At early times (1-2 ps, top-left), the GSB/SE feature differs only slightly, with a slight enhancement to the SE feature at low energies, and a slight broadening to some of the features between 2.0-2.5 eV. In the ESA, however, both ESA features are enhanced with higher fluence.

The long-time spectra, (3000-5000 ps, top-right) of BoDiPy 7 excited at 400 nm (3.1 eV) is complex, and shows similar features to thermally induced artefacts in the TA spectrum. This is supported as the high-energy features of this artefact are more intense in the 1000 μ W pump power measurement.

The fluence dependence of the kinetics of these TA measurements (Fig. 6.17 - bottom) do not show much difference qualitatively. The lifetimes of the fits to these kinetics,

shown on the graph as dotted lines, are shown in Table 6.4. These show that the GSB peak and ESA features are invariant with respect to the fluence, whereas the GSB features at 2.23 eV and 2.455 eV have slightly different lifetimes. The feature at 2.23 eV has a lifetime of 2.1 ± 0.2 ps at $1000 \mu W$ pump power, and has a lifetime of 4.0 ± 0.3 ps at $300 \mu W$ pump power. The feature at 2.455 eV has a lifetime of 20 ± 2 ps at $1000 \mu W$ pump power, and has a lifetime of 49 ± 7 ps at $300 \mu W$ pump power. This is consistent, however, with the trend in the other samples in that the lower fluence measurements have a longer lifetime due to higher noise skewing the fit.

The fluence dependence of BoDiPy 7 excited at 530 nm (2.3 eV) is shown in Fig. 6.18. The powers used in these experiments were $500 \mu W$ for the low pump power measurement and $1200 \mu W$ for the high pump power measurement. The early time measurements (1-2 ps, top-left) show some clear differences. While the GSB/SE feature appears to show an additional peak in the high fluence measurements, this peak is overlaid with

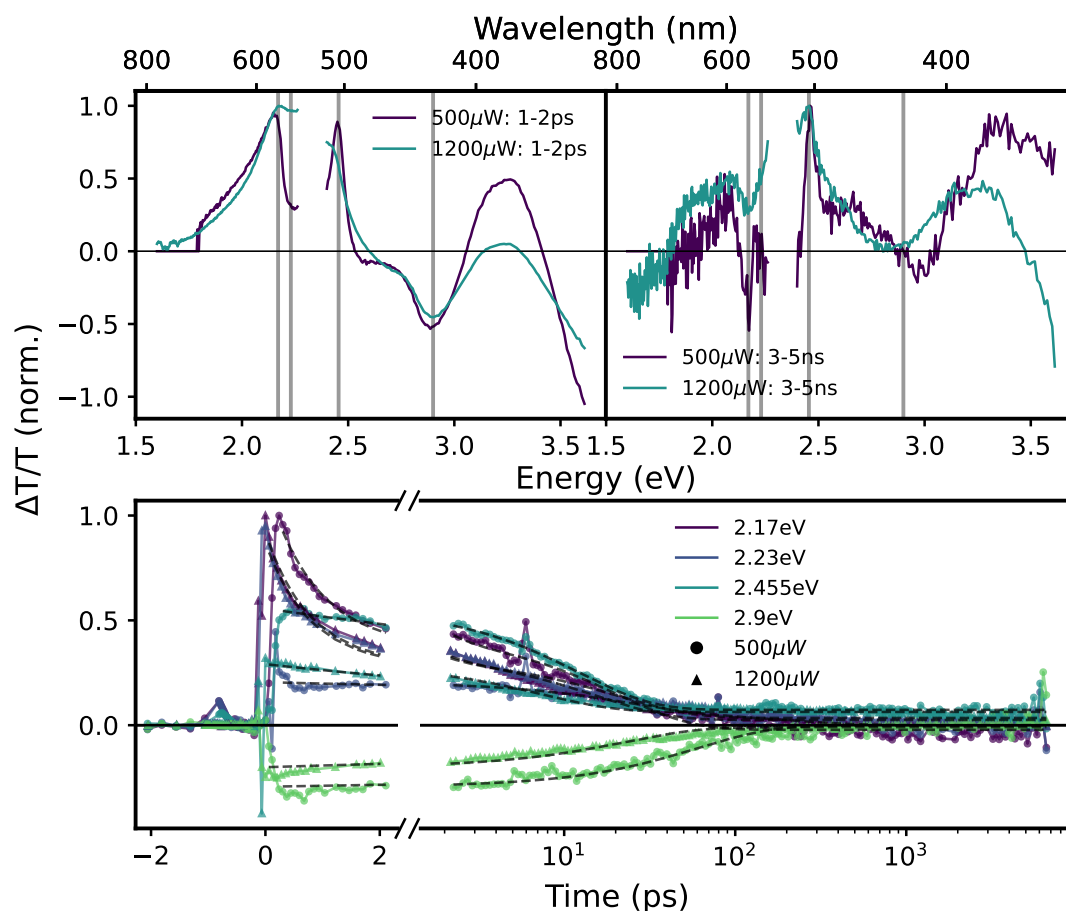


FIGURE 6.18: Fluence dependence of the transient absorption of BoDiPy 7 crystalline thin films at 530 nm (2.3 eV) excitation, showing spectra at early times (1-2 ps, top-left) and late times (3-5 μs , top-right). Comparative kinetic slices between the two spectra are shown on the lower figure, with fits to the data shown as dotted lines. Energies of the kinetic slices shown on the lower figure are shown on their respective spectra as vertical grey lines.

the pump region which has been removed, and thus further conclusions are difficult to draw. However, the appearance of an additional peak at high fluence implies that an additional emissive state is accessed via some intermolecular excited state interaction at short times. Alternatively, this may be due to the increased intensity of the pump affecting the spectrum more than has been accounted for. In addition, at low fluence, the $S_0 \rightarrow S_2$ transition feature of the GSB is significantly higher than at high fluence. This implies that the ESA feature is enhanced by the increased pump power. However, as the ESA around 3.55 eV is also enhanced this may be an artefact in the TA spectrum.

At long times (3000-5000 ps, top-right), the primary difference in the spectrum is at high energies, where the 2.9 eV feature is reduced in the higher fluence measurement, and the feature between 3.0 and 3.5 eV is also reduced in the higher fluence measurement. This is similar to the difference seen at short times, and demonstrates that the ESA in this region is increased with higher pump fluence.

The kinetics vary significantly with fluence in BoDiPy 7 excited at 530 nm (2.3 eV), with the largest difference being in the peak 2.23 eV kinetic, where the low-fluence decay has significantly reduced intensity compared to that of the high-fluence one. In addition, the biexponential decay model used identified a very short < 1 ps component in the high-fluence measurement, potentially due to the higher intensity of the decay overall, whereas a long-lifetime component was identified in the low-fluence measurement, possibly due to the proportionally increased noise in this data. In addition, the decay of the 2.455 eV decay lifetime is reduced from 12.2 ± 0.3 ps in the low-fluence measurement to 7.4 ± 0.4 ps in the high fluence measurement. This is also seen in the spectra, suggesting this difference is not due to noise. The decay lifetime of the 2.9 eV measurement has the greatest proportional change in lifetime, with the 61 ± 4 ps lifetime being reduced to 23 ± 1 ps in the high-fluence data. This all implies that the lifetime of the excited states in crystalline films of BoDiPy 7 are very dependent on excitation fluence, implying a strong dependence on the concentration of excited states in the film.

6.2.6 Pump-Energy Dependent Transient Absorption Spectroscopy

Using the same high-fluence data as presented previously, we present the pump-energy dependence of the TA spectra and kinetics. As exciting at 530 nm (2.3 eV) lies in the $S_0 \rightarrow S_1$ transition, we expect to see differences in the spectrum or kinetics compared to the 400 nm (3.1 eV) excitation spectra or kinetics, as this represents excitation to the S_2 state.

Fig. 6.19 shows the pump energy dependence of the TA spectra and kinetics of BoDiPy 6. The only significant difference between these datasets occurs at 2.14 eV at short

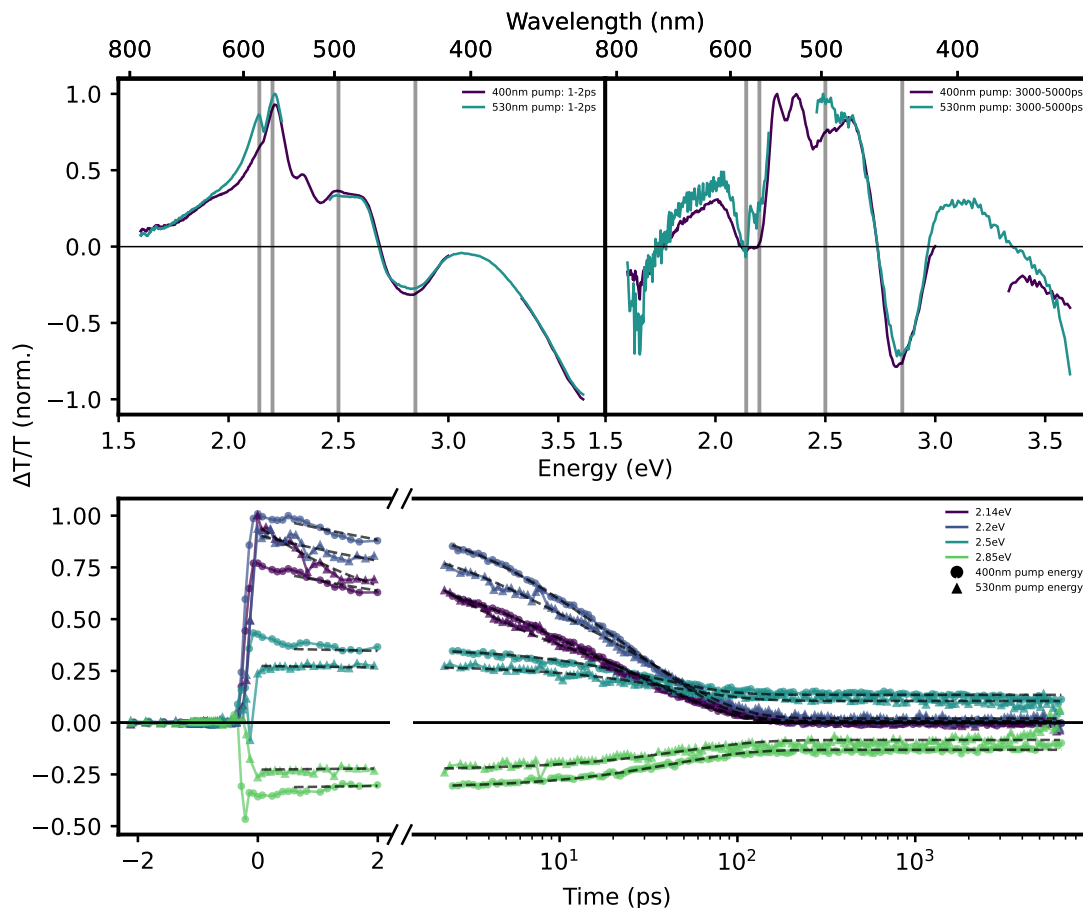


FIGURE 6.19: Pump energy dependent TA and kinetics of crystalline thin films of BoDiPy 6. Samples were excited to the S_1 state, by exciting at 530 nm (2.3 eV), as well as to the S_2 state, by exciting at 400 nm (3.1 eV). The spectra of these two excitation conditions are shown in the top figure, at early times (1-2 ps, top-left) and late times (3-5 μ s, top-right). Comparative kinetic slices between the two spectra are shown on the lower figure, with fits to the data shown as dotted lines. Energies of the kinetic slices shown on the lower figure are shown on their respective spectra as vertical grey lines.

times (1-2 ps, top-left). Here, the peak that is observable in SE feature in the 530 nm (2.3 eV) spectrum is much less present in the 400 nm (3.1 eV) excitation spectrum. This is intuitive, as exciting to the S_2 state should result in significantly less emission from the S_1 excited state; the S_2 state needs to first decay to the S_1 state before emission can occur. The biggest difference between the lifetimes of the different kinetics of these two TA datasets (shown in 6.3) occurs in the 2.14 eV kinetic, in which the short lifetime component is 5.6 ± 0.3 ps for the 400 nm (3.1 eV) excitation, and the long lifetime component is 38.0 ± 0.9 ps, whereas when excited at 530 nm (2.3 eV), the lifetime components are 2.4 ± 0.1 ps and 37 ± 1 ps. As such, the short lifetime component is reduced significantly in 530 nm (2.3 eV) excitation TA data, indicating that exciting to the S_2 state extends the emissive lifetime in the 400 nm (3.1 eV) excitation data. The remaining kinetics shown in fig. 6.19 vary significantly less than this feature.

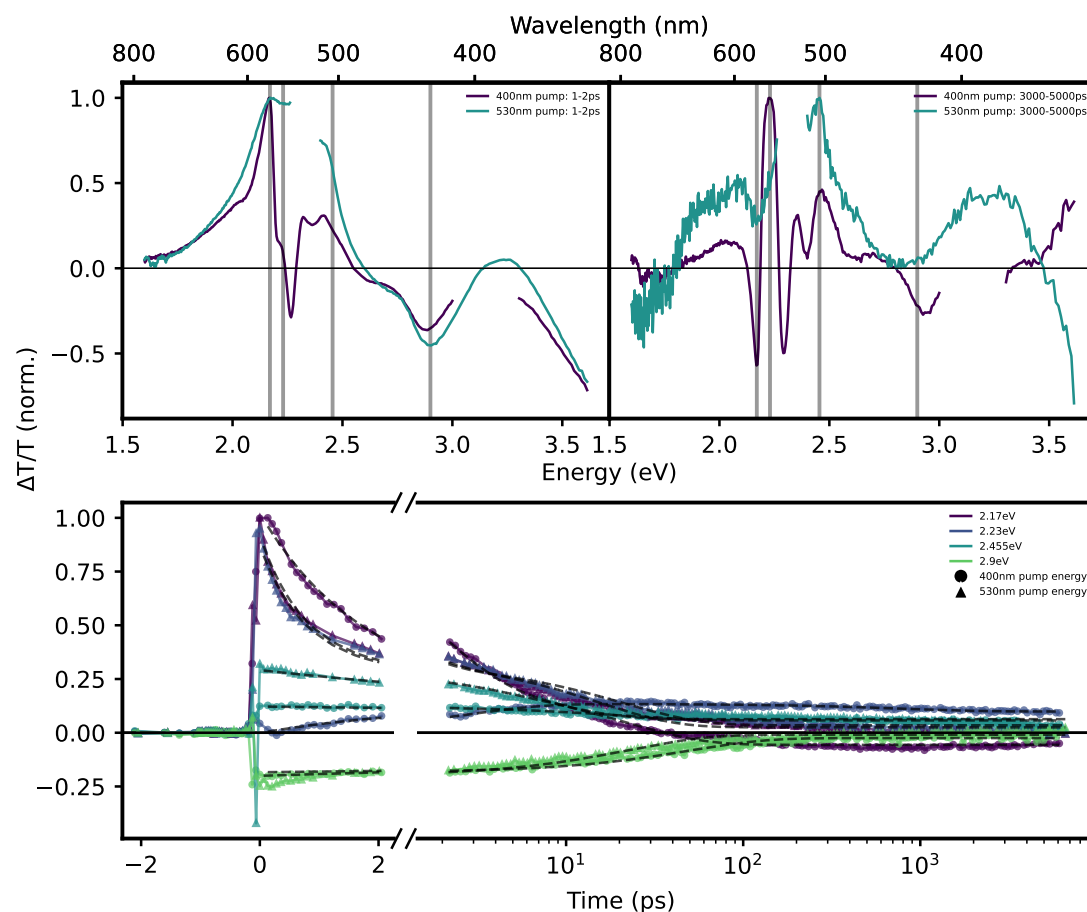


FIGURE 6.20: Pump energy dependent TA and kinetics of crystalline thin films of BoDiPy 7. Samples were excited to the S_1 state, by exciting at 530 nm (2.3 eV), as well as to the S_2 state, by exciting at 400 nm (3.1 eV). The spectra of these two excitation conditions are shown in the top figure, at early times (1-2 ps, top-left) and late times (3-5 μ s, top-right). Comparative kinetic slices between the two spectra are shown on the lower figure, with fits to the data shown as dotted lines. Energies of the kinetic slices shown on the lower figure are shown on their respective spectra as vertical grey lines.

The pump energy dependent TA spectra and kinetics for the BoDiPy 7 crystalline sample are shown in Fig. 6.20. The differences between these spectra are much greater than that for BoDiPy 6. At short times (1-2 ps, top-left), the ESA features at high energies are mostly unchanged. However, the GSB/SE bands in the TA spectrum are much broader in the 530 nm (2.3 eV) compared to the 400 nm (3.1 eV) excitation. While much of the complex structure present in the S_2 excited spectrum is in a region which overlaps with the pump excitation of the S_1 excitation, it is still clear that the feature at 2.455 eV is significantly enhanced in the 530 nm (2.3 eV) pumped spectrum. This, in addition to the negative signal around 2.5 eV in the 400 nm (3.1 eV) pumped spectrum, suggests that when the crystalline film is excited to its S_2 state, an additional ESA feature occurs at this wavelength compared to in its S_1 state. At late times (3000-5000 ps, top-right), the spectrum is significantly different, and difficult to compare quantitatively. We

have identified the nature of the species shown by the late time 530 nm (2.3 eV) pump spectrum as directly associated with the S_1 spectrum, whereas the species shown in the 400 nm (3.1 eV) spectrum is identified with a long-lived, thermal artefact (similar to that shown in chapter 4) resulting from non-radiative decay to the ground state. Underneath this spectrum, there is visible around 2.0 eV and 2.455 eV features similar to those seen in the 530 nm low-energy excited spectrum. This suggests that excitation at higher energy simply results in the generation of excess heat in the sample via vibrational relaxation.

6.2.7 Multivariate Curve Resolution - Alternating Least Squares

To extract the Species-Associated Spectra (SAS) and Concentrations (SAC), global analysis (via the Multivariate Curve Resolution - Alternating Least Squares (MCR-ALS) algorithm, detailed in section 3.11.2) of the TA data from samples of BoDiPy 6 and 7 in solution and amorphous film was performed. The resultant SAS and SAC are shown in Fig. 6.21 and Fig. 6.22, respectively. A similar fitting attempt was made for the crystalline samples, but due to the complexity and non-concurrent decays seen in these samples, the decomposition by MCR-ALS was not successful.

The SAS and SAC for samples of BoDiPy 6 are shown in 6.21. The spectra and concentrations of the solution sample are shown on the left hand side in the figure. The S_1 spectrum shown in the top-left subfigure shows a large GSB feature and a less intense SE feature at lower energy. In addition, there is a broad excited state from ~ 2.5 eV out to higher energies, representing the $S_1 \rightarrow S_2$ excited state absorption. In the late-time spectrum, the SE feature has entirely decayed, and has given way to a low-intensity broad ESA feature. In addition, the shape of the ESA has shifted with a higher energy feature replacing the former, and the region identified with the $S_0 \rightarrow S_2$ absorption has a minor bleach feature present. These observations agree with the hypothesis that the solution undergoes ISC, as this spectrum may represent the decay of the emissive S_1 state and the population of the non-emissive triplet state, with a distinct ESA.

The concentrations, shown in the lower subfigure, are fitted with an exponential decay for the S_1 concentration, and an exponential rise for the concentration of the late time spectrum. These fits are shown on the graphs as dotted lines. The lifetime used for the rise of the late-time concentration is the same as the lifetime of the decay of the S_1 concentration, and only the scale factor and y-axis displacement were allowed to vary.

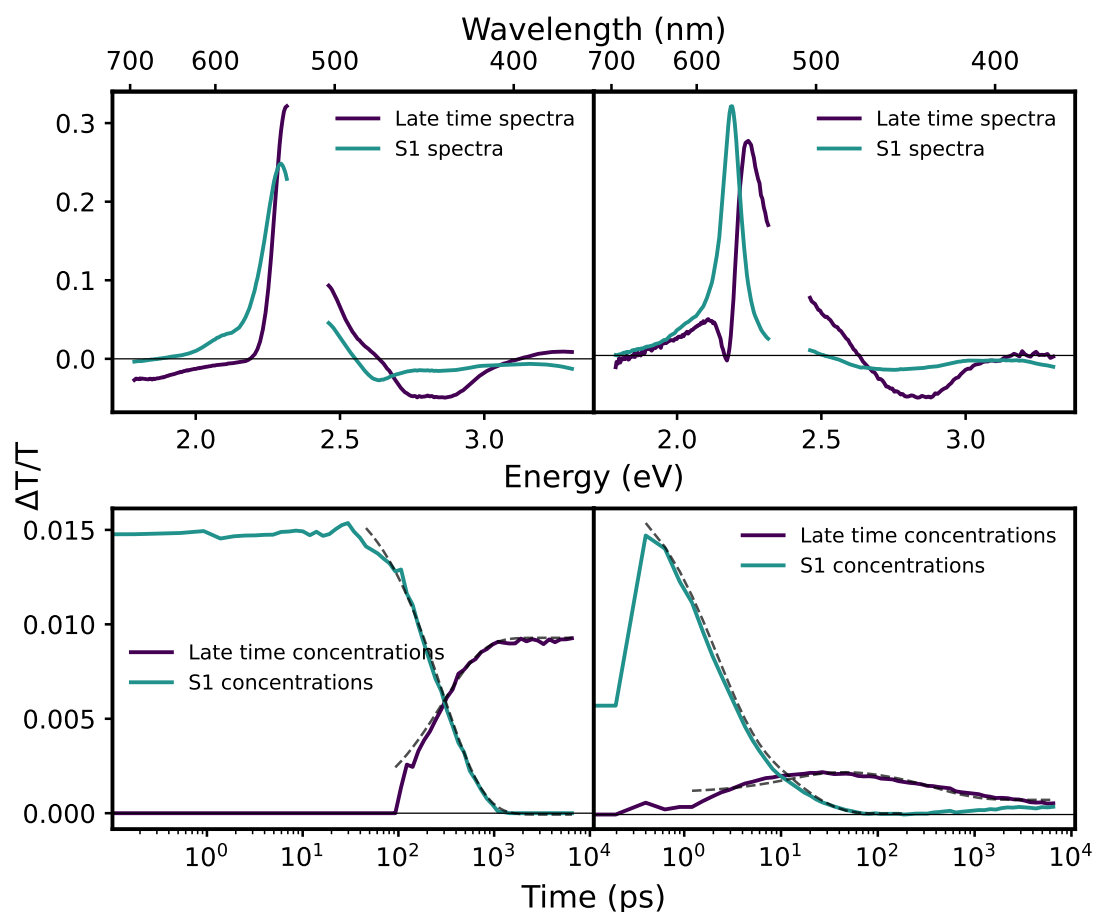


FIGURE 6.21: Species associated spectra (top) and concentrations (bottom) of BoDiPy 6 in solution (left) and in amorphous film (right). The species associated spectra and concentrations were optimised using the MCR-ALS algorithm detailed in section 3.11.2. Fits to the concentration decays were performed using the decay of the S_1 early time spectra to fit the rise of the late time spectra, and in amorphous film, the decay of this feature was fit using a least squares curve-fitting algorithm. The resultant fits to the data are shown on these figures as dashed lines.

The right hand subfigures show the SAS and SAC for the amorphous film of BoDiPy 6. The spectra in the upper figure show similar behaviours to those of the solution, with the depletion of the SE signal resulting in a small blue shift of the GSB/SE band, and a similar change in the late-time ESA shape. However, the S_2 absorption bleach is not recovered as it is in the solution, and there is a residual bleach feature overlaid with a negative ESA feature at lower energy. The bleach feature is likely due to the scattering from the film that is seen in Fig. 6.4. The similarity between the two late-time ESA spectra suggest that the amorphous film does indeed undergo similar ISC to the solution. The concentrations, shown in the lower subfigure, are fitted with an exponential decay for the S_1 concentration, as well as the late-time concentration being fitted with an exponential rise in the same manner as the solution concentrations, as well as a subsequent exponential decay.

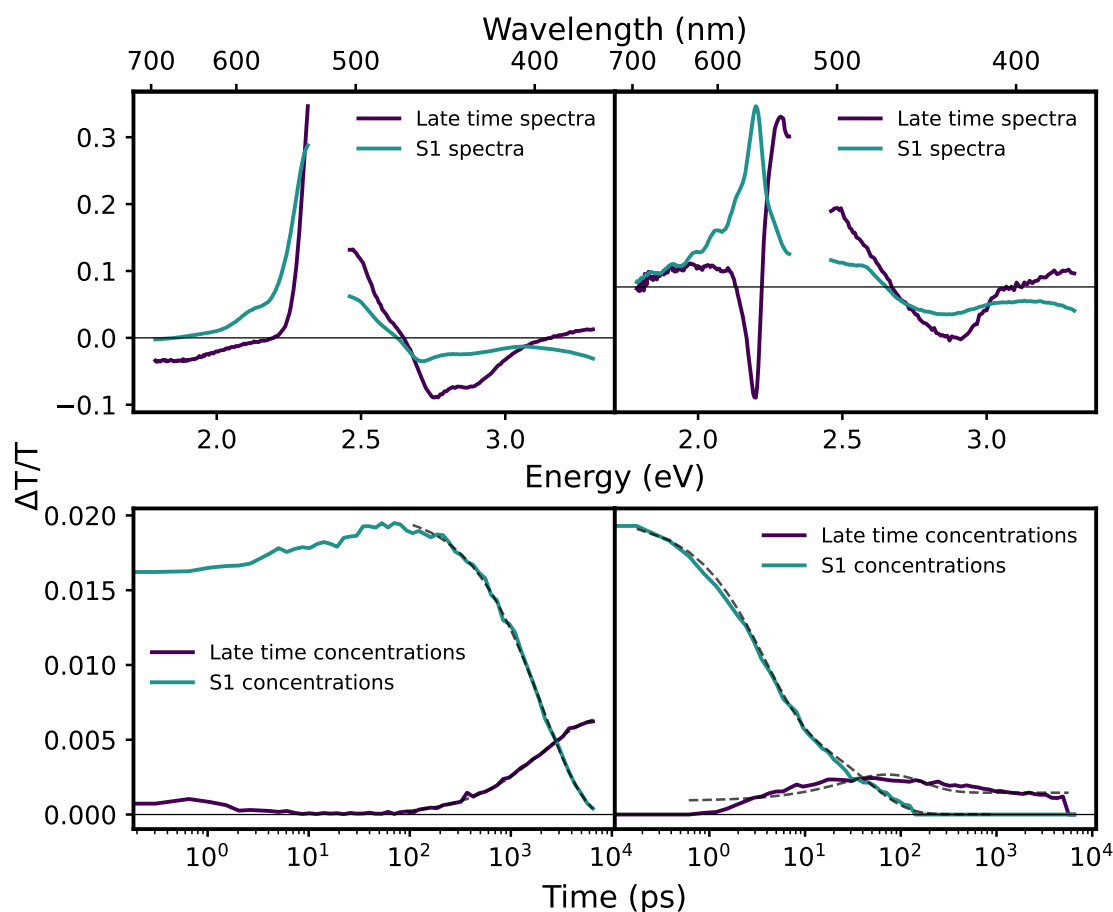


FIGURE 6.22: Species associated spectra (top) and concentrations (bottom) of BoDiPy 7 in solution (left) and in amorphous film (right). The species associated spectra and concentrations were optimised using the MCR-ALS algorithm detailed in section 3.11.2. Fits to the concentration decays were performed using the decay of the S_1 early time spectra to fit the rise of the late time spectra, and in amorphous film, the decay of this feature was fit using a least squares curve-fitting algorithm. The resultant fits to the data are shown on these figures as dashed lines.

The SAS and SAC for samples of BoDiPy 7 are shown in 6.21. The same observations made for the solution samples of BoDiPy 6 are valid for the solution samples of BoDiPy 7 (top-left). The same fitting process was applied to the concentrations of these spectra (bottom-left). The SAS for the amorphous films of BoDiPy 7 (top-right) show similar shapes to those of BoDiPy 6, with an altered ESA at late time, although the S_2 bleach feature is visible here. The residual bleach and scattering feature is also present, though in this SAS the ESA feature overlaid with the GSB scatter is significantly more intense than the one in BoDiPy 6. The SAC for the amorphous films of BoDiPy 7 are shown in the lower-right figure, and are fitted in the same manner as the BoDiPy 6 sample, though the fit in this case is less accurate than in BoDiPy 6.

The full parameters of the exponential fits to these concentrations are for BoDiPy 6 and 7 are shown in 6.5. The fits to the S_1 state concentration decay are done by an

TABLE 6.5: Fitting parameters of exponential and bi-exponential fits to the MCR-ALS concentrations in Fig. 6.21 and 6.22. The (*) indicates that this parameter was taken from the S_1 decay, rather than fit from the late-time concentration data itself.

-	A	Lifetime 1	A_2	Lifetime 2	c
BoDiPy 6 solution					
S_1	0.1780	286	-	-	0
S_1 errors	0.0001	6	-	-	0
Late-time species	-0.0095	286*	-	-	0.00929
LT errors	0.0002	-	-	-	8e-5
BoDiPy 6 amorphous film					
S_1	0.0105	2.00	0.0037	14	0
S_1 errors	0.0002	0.07	0.0002	1	0
Late-time species	-0.0010	14*	0.00134	4.0e+2	0.00061
LT errors	0.0001	-	7e-5	7e+1	5e-5
BoDiPy 7 solution					
S_1	0.0210	2.00e+3	-0.0007	4e+1	0.0005
S_1 errors	0.0002	5e+1	0.0002	3e+1	0.0002
Late-time species	-0.00667	2e+3*	-	-	0.00662
LT errors	6e-5	-	-	-	4.2e-5
BoDiPy 7 amorphous film					
S_1	0.00317	3.6	0.00147	43	0
S_1 errors	6e-5	0.1	5e-5	3	0
Late-time species	-0.0012	43*	0.0010	1e+2	0.00034
LT errors	0.0004	-	0.0004	3e+1	2e-5

exponential or biexponential decay, simplified as necessary where additional components would not improve the fits. The functions used to fit these decays are:

$$f(t) = A * \exp t/\tau + A_2 * \exp t/\tau_2 + c, \quad (6.1)$$

where for the single exponential case, $A_2 = 0$. For the late time data, the same fit is used, except the A parameter is constrained to be negative, to simulate growth of the species, and τ is set to be the longer lifetime of the fit to the S_1 species.

This fit is able to successfully fit the solution data, producing errors on the fit below 10%, but is less capable of fitting the amorphous film data, as the decay of the long-time species is difficult to fit accurately.

6.3 Discussion

We have demonstrated that in the solution samples of BoDiPy 6 and 7 in toluene, that triplet transients are generated on timescales of 100s to 1000s of picoseconds, due to their long lifetime (on the scale of nanoseconds) and their similarity to triplet transient

absorption spectra obtained from literature. In addition, due to the change in the triplet formation rate between BoDiPy 6 and 7, we argue that this triplet generation is mainly due to heavy-atom induced intersystem crossing, as the rate of triplet formation is slower in BoDiPy 7, where the 2-6 substituent halogen molecule is Bromine, which is a lighter molecule compared to Iodine in BoDiPy 6, thus the rate of intersystem crossing in these molecules is proportional to the mass of the 2-6 substituted atoms.

An additional signifier of the triplet state at late times in the solution spectra are shown in Akhuseyin Yildiz et al. [129] where it is shown that in BoDiPy derivatives in solutions of tetrahydrofuran the low-energy Excited State Absorption (ESA) features are associated with triplet generation, and similar features occur at late times in the solution-phase measurements. Due to the scattering observed in the solid state BoDiPy samples, these signals are not seen in the other samples.

In addition, by comparison of the late-time spectrum, the triplet transients visible in the solution spectra of the two BoDiPy molecules can be observed in the late time spectra of the other BoDiPy 6 samples as well as the amorphous film of BoDiPy 7. However, the excited state decay proceeds much faster in the amorphous films than in the solution samples, (with lifetimes of 286 ± 6 ps in BoDiPy 6 solution and 2.00 ± 0.07 ps and 14 ± 1 ps in BoDiPy 6 amorphous film, as well as a primary decay of $\sim 2 \pm 0.05$ ns in BoDiPy 7 solution compared to 43 ± 3 ps in BoDiPy 7 amorphous film). This suggests that either the triplet formation occurs on a much faster timescale, or that in the solid state the radiative decay rate is enhanced, or that a non-radiative decay mechanism is accessible in this state. Given the lower triplet-associated signal in the amorphous film samples, we suggest that the latter two options are more likely, also given the increased stimulated emission (SE) observed in the ground state bleach (GSB)/SE feature.

However, the species associated decays seen in the MCR-ALS plots (Figs. 6.21 and 6.22) suggest that the triplet generation proceeds faster in the amorphous films, as the triplet signal occurs more rapidly in the MCR-ALS concentrations.

It is a possibility that triplet generation is due to intermolecular singlet fission in the solid state. From Zhang et al. [130], we obtain the triplet energy for a BoDiPy 7-like molecule as 1.7 eV, and from Bassan et al. [134] we obtain for a similar BoDiPy 6-like molecule a triplet energy of 1.6 eV. The difference between BoDiPy 6 and 7 and these molecules is the substitution of the *meso*-mesityl group with a phenyl group. It should be noted that while this structural difference is small, twisting of the *meso*-substituted group has been observed to have an impact on intersystem crossing dynamics, and thus might impact the triplet energy [130]. Thus, with singlet energies for these molecules being between 2.0-2.4 eV, singlet fission from the S_1 state is energetically forbidden.

However, singlet fission may be possible from the S_2 state, as the $S_0 \rightarrow S_2$ absorption occurs between 3.0 and ~ 3.5 eV.

Triplet generation is also seen in crystalline films of BoDiPy 6. The presence of triplets in crystalline films of BoDiPy 7 is uncertain, as the characteristic triplet ESA is not present.

In BoDiPy 6, if singlet fission were possible from the S_2 state, then we would expect to see a difference in the pump energy dependent spectra seen in Fig. 6.19. However, the early and late time spectra are near identical, ruling out the possibility of singlet fission from a higher excited state. This may be due to rapid decay to the bottom of the S_2 state potential energy surface putting the S_2 state below $2 \times E(T)$, and thus making singlet fission energetically disfavoured. Instead, intersystem crossing from the S_1 state is a more likely candidate for the triplet generation process, following in the 400 nm (3.1 eV) excitation TA.

In crystalline films of BoDiPy 7, the occurrence of intersystem crossing or singlet fission is ambiguous, as while delayed fluorescence is observed in the fluorescence decay kinetic (Fig. 6.6), the transient absorption spectra do not show conclusive triplet signatures. Thus, we suggest that the lower-energy emissive state which is observed also at long-times in the transient absorption interferes with the triplet generation process as a loss mechanism. The initial emissive decay of this state decays at the same rate as the solution emission as shown in Table 6.2.

While the nature of this state is unknown, we may describe its properties based primarily on the steady state emission, TCSPC, and transient absorption kinetic data. Its emission energy at ~ 1.8 eV is lower than that of the S_1 emission peak. In addition, Pidgeon [2] demonstrates that this emissive feature is positively correlated with the percentage of BoDiPy dye present in a polymer matrix. This suggests the emission is from a state strongly effected by intermolecular interaction, such as an aggregate or excimer state. Furthermore, as it is present in the steady state emission spectrum but not in the transient absorption spectrum, which is doubly sensitive to state population, this state is a highly-emissive, low-population state which serves as a trap state from the primary S_1 state, which may be the cause of the lack of triplet signal observed in the crystalline BoDiPy 7 transient absorption spectrum. Finally, the emission from this low-energy state is shown in the TCSPC decay to have the same lifetime as the BoDiPy 7 excited state in solution, of ~ 2 ns. This could mean either that the intrinsic lifetime of this state is the same as the monomer of BoDiPy 7, which would suggest it arises from an edge state or defect in the BoDiPy 7 crystal, or that it depends on a population with the same lifetime as the monomer to populate it. In conclusion, the low energy emission in the BoDiPy 7 solid films arises due to a low-population, low energy state, implying

a localised exciton-like trap state, which decays at the same rate as the molecule in isolation.

While there is certainly a large amount of heavy-atom effect that mediates the intersystem crossing in BoDiPy derivatives, Martinez-Espinoza et al. [135] presents the solvent dependence of the steady state characteristics of BoDiPy 6 in solution. In this, while they demonstrate some modification to the extinction coefficient of the sample and fluorescence quantum yield, there is very change to the absorption or emission maximum between the solutions of BoDiPy 6 in tetrahydrofuran, dichloromethane, and acetone. This suggests that there is little to no charge transfer character in BoDiPy 6 in solution.

Nevertheless, it is not impossible that, due to the broadness and low-energy tail of the amorphous and crystalline films of BoDiPy 6 and 7, charge transfer states contribute to the dynamics of the solid-state samples of these dyes. This is more difficult to confirm in the solid state, however.

6.3.1 Conclusion

In conclusion, while singlet fission has been predicted to occur in 2,6-di-iodo,4-mesityl BoDiPy and 2,6-di-bromo,4-mesityl BoDiPy (BoDiPy 6 and BoDiPy 7), we have found that both dyes instead undergo triplet generation via intersystem crossing from the S_1 state in both solution of toluene and in amorphous and crystalline thin films. In crystalline films of BoDiPy 7, we suggest that a low-energy monomer-like trap state interferes with the triplet generation process. We also observe delayed fluorescence occurring in the crystalline films of BoDiPy 6 and 7 and in the amorphous film of BoDiPy 6, indicating that following triplet generation, whether by singlet fission or intersystem crossing, the corresponding reverse pathway is present in these samples, either reverse intersystem crossing or triplet-triplet annihilation. We suggest that the process which allows for the necessary spin-orbit coupling in the intersystem crossing process is the heavy atom effect.

Chapter 7

Outlook and Further Work

We have established a model for non-radiative decay in Pigment Red 254 via a proton transfer tautomerisation induced, charge transfer state mediated conical intersection with the ground state, resulting in microsecond-scale long-lived heating artefacts that are visible in both the transient absorption spectra and in the time-resolved infra-red spectra. We suggest that via polymerisation, or as is, Pigment Red 254 could be used for *in-vivo* applications for photothermal therapy, or for solar purification of water via the heat generated by its rapid, efficient non-radiative decay.

We have conducted a detailed transient absorption spectroscopy investigation into two Boron Dipyrromethane (BoDiPy) derivative dyes, referred to as BoDiPy 6 and 7, investigating the different dynamics that result from different sample morphologies; from solution in toluene, as well as in amorphous and crystalline thin films, as well as investigating how the crystalline sample dynamics change when excited to the first and second excited singlet states. We find evidence of rapid heavy-atom mediated inter-system crossing via long-lived triplet associated species that last beyond the nanosecond-scale limit of the transient absorption spectrometer used.

We also find that in the crystalline samples of BoDiPy 6, the energetics permit a delayed fluorescence signal detectable in the emissive decay kinetics of the sample, demonstrating that the triplet generating process can recover the singlet state. We see a lack of triplet generation in the crystalline samples of BoDiPy 7, which may arise from its unique emissive trap state which decays with the same emissive lifetime as the monomer in solution. While we cannot rule out a contribution from singlet fission based on these results, we can only say definitively that triplets are generated by intersystem crossing with a rate that varies based on the mass of the heavy atom substituent.

All three of these molecules have been predicted, by Padula et al. [1] in the case of Pigment Red 254 and by Marco Cavazzini in the case of the BoDiPy derivatives, to have favourable energies for triplet generation by singlet fission. However, we find no evidence for singlet fission in any of these three molecules. We can identify the sources of the decay pathways that out-compete singlet fission in each case. For Pigment Red 254, the inclusion of a non-substituted N-H bond in the molecule has been shown, both in this work and in other literature [23, 25, 106–108] to encourage rapid non-radiative decay to the ground state. The inclusion of heavy atoms in a molecule is a common way to encourage intersystem crossing [21, 33] This work highlights the importance of being aware of common design strategies in organic molecules when attempting to encourage singlet fission in complex polycrystalline thin films. It is unlikely that any molecule with these features will be able to efficiently produced triplets via singlet fission.

However, the results of this work have given inspiration for further work and potential attractive uses for this molecule. In the case of Pigment Red 254, further work could be done to more fully understand the causes of the non-radiative decay process, its dependence on sample morphology, and the nature of the intermediate state, which would assist in the design of diketopyrrolopyrrole based molecules for photothermal applications.

Complete Active Space - Self Consistent Field and Kohn-Sham DFT calculations have been done to determine the energies of charge transfer states in other molecules [136, 137], and thus could be used to help determine the nature of the intermediate state in the non-radiative decay of Pigment Red 254. Other methods that could be used for this include cyclic voltammetry, which can be used to probe many electrochemical properties of a material. In addition, investigating the morphology dependence of this non-radiative decay process may be valuable to optimise this process, as with higher crystallinity, it may be possible to engineer a coherent long range crystalline or polymeric tautomerisation. Furthermore, investigation of the molecules detailed in Mizuguchi and Wooden [94] which have shown similar hydrogen bonding character might show further design possibilities for even more efficient non-radiative decay in the solid state.

Investigation of the *in vivo* hazardous nature of Pigment Red 254 could be done to determine if it is suitable for photothermal cancer therapy. Failing this, chemical alteration, such as polymerisation informed by the in-depth knowledge of the hydrogen bond could be done to improve the safety of the molecule for these applications. Experimenting with device fabrication for solar-driven water purification applications would also be useful further work, as its stability makes it perfect for use in these applications.

For the BoDiPy dye derivatives, further work to determine the nature of triplet generation, such as the magnetic field dependence of the delayed fluorescence of BoDiPy 6, as

well as quantising the triplet yield of these molecules, would be useful to determine their potential for triplet sensitisers. Furthermore, growing single crystal samples of BoDiPy 6 and 7 will permit a greater understanding of their complex morphology dependent dynamics.

Appendix A

Pigment Red 254 UV-Vis Supporting Information

A.1 Franck-Condon Fitting Details

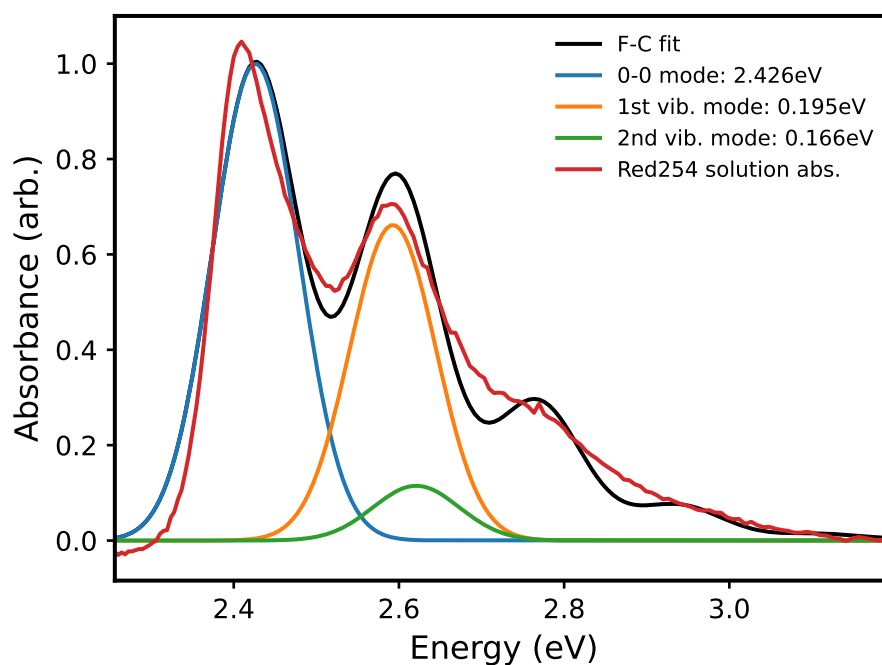


FIGURE A.1: Franck-Condon fit to the Red254 in DMSO solution-phase absorption spectrum, with the vibrational energies obtained from resonance Raman spectroscopy. The vibrational peaks are shown here to better demonstrate the fit.

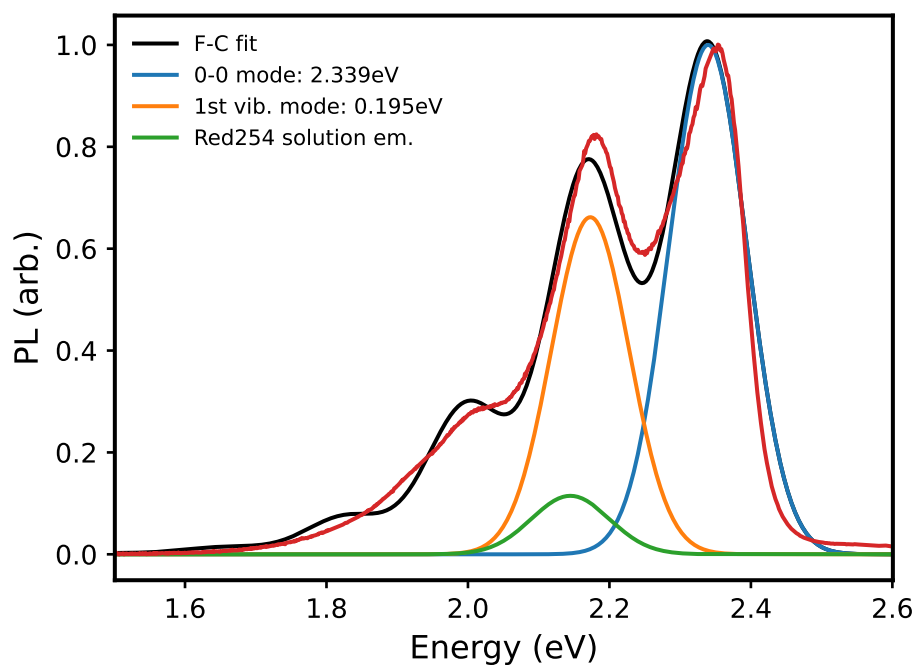


FIGURE A.2: Franck-Condon fit to the Red254 in DMSO solution-phase emission spectrum, with the vibrational energies obtained from resonance Raman spectroscopy, and the Huang-Rhys parameters taken from the absorption spectrum fit. The vibrational peaks are shown here to better demonstrate the fit.

A.2 Grazing Incidence Wide Angle X-ray Scattering (GIWAXS)

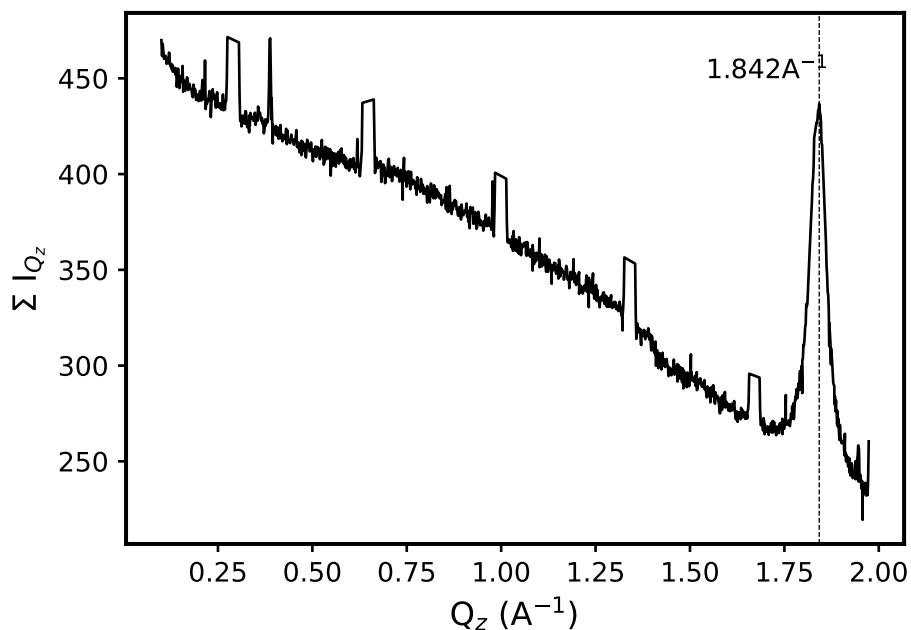


FIGURE A.3: Out-of-plane Grazing Incidence Wide Angle Scattering (GIWAXS) signal of thermally evaporated thin film of Red254 on silicon substrate in atmosphere prepared in the same way as those on quartz. There is one significant peak, indicating that these samples form with the molecules oriented predominantly parallel to the substrate, with intermolecular $\pi - \pi$ spacing of 3.41 Å. However, this is not reliable due to the broad scattering signal and the later measurements. GIWAXS was performed by Daniel T. W. Toolan of the University of Sheffield, both at the University of Sheffield and the Diamond Light Source.

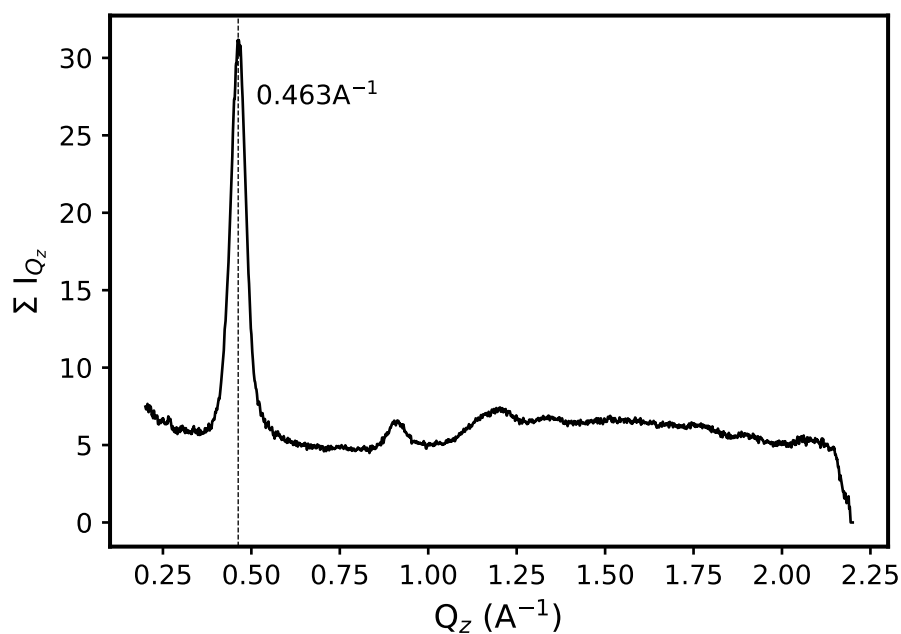


FIGURE A.4: Out-of-plane Grazing Incidence Wide Angle Scattering (GIWAXS) signal of thermally evaporated thin film of Red254 on silicon substrate in vacuum prepared in the same way as those on quartz. There is one significant peak, which is at a different from the previous figure, which may be due to morphology differences or may be due to experimental issues arising from the non vacuum environment. This peak corresponds to a intermolecular crystal spacing of $\sim 13 \text{\AA}$, which may indicate a large $\pi - \pi$ spacing, but more likely represents scattering between more highly spaced crystal planes. In addition, there is a significant scattering background between 1 and 2 \AA , which indicates that the film is highly polycrystalline or amorphous with multiple crystal orientations. GIWAXS was performed by Daniel T. W. Toolan of the University of Sheffield, both at the University of Sheffield and the Diamond Light Source.

A.3 Transient absorption spectra identification

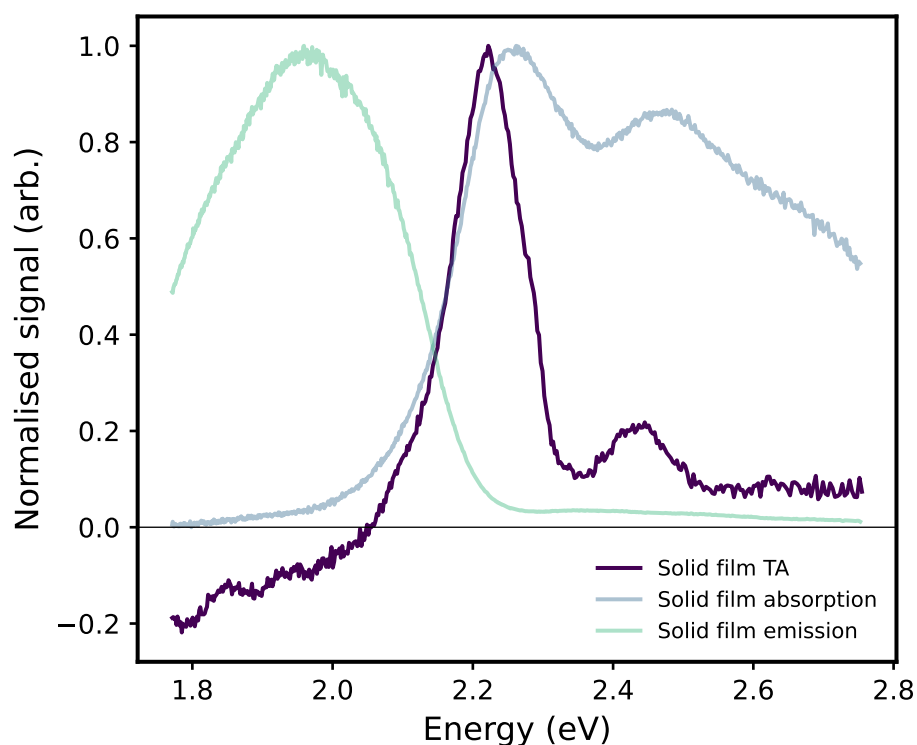


FIGURE A.5: Transient absorption compared with steady state absorption and emission of thin film of Red254, illustrating the motivation behind assigning each region of the TA spectrum to each feature. The large positive signal and secondary positive peak overlap with the steady-state absorption, motivating it's assignment to the ground state bleach feature. The GSB has very different structure compared to the steady state spectrum, with the primary 0-0 peak being proportionally much higher than expected. This combined with no visible stimulated emission suggests there is significant photo-induced absorption overlaid with these features, resulting in the increased absorption below ~ 2.1 eV

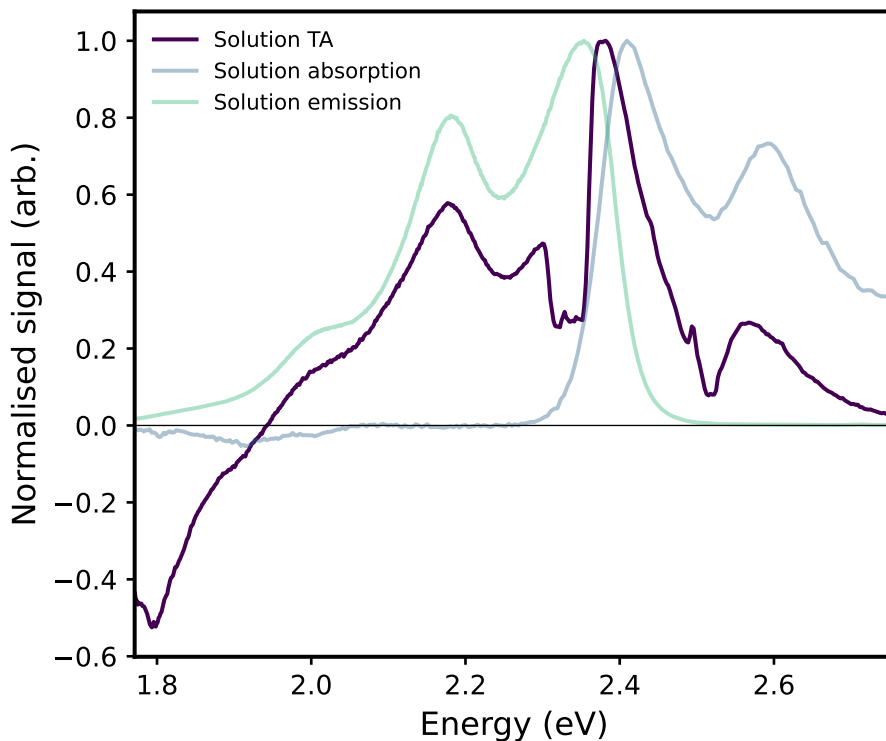


FIGURE A.6: Transient absorption compared with steady state absorption and emission of dilute solution of Red254 in DMSO, illustrating the motivation behind assigning each region of the TA spectrum to each feature. The broad positive feature above ~ 1.9 eV matches well to the structure of the steady state spectra, with the region above ~ 2.4 eV matching the steady state absorption spectrum, and the remainder of the spectrum matching the emission spectrum. The remaining negative signal below ~ 1.9 eV is then naively assigned to photoinduced absorption to higher singlet states.

A.4 Transient absorption lifetime fitting

Table 4.3 shows the fitted lifetime components of the exponential and bi-exponential fits to the excited state absorption (ESA) and ground state bleach (GSB) features of the solid state transient absorption spectra of Red254, respectively. The fits were achieved by simply fitting a single exponential with multiple exponential components, in the form

$$f(x) = A_1 \exp\left(-\frac{x}{\tau_1}\right) + A_2 \exp\left(-\frac{x}{\tau_2}\right) + c \quad (\text{A.1})$$

with τ_i being the reported lifetime. This model is approximate and not physically exact, as this model describes decay from the initially prepared excited state via two distinct decay pathways, whereas what we expect to see is a sequential decay of two species on two separate timescales. This model is, however, sufficient to extract the approximate timescale of the decays.

A.5 Temperature dependent absorption residual plots.

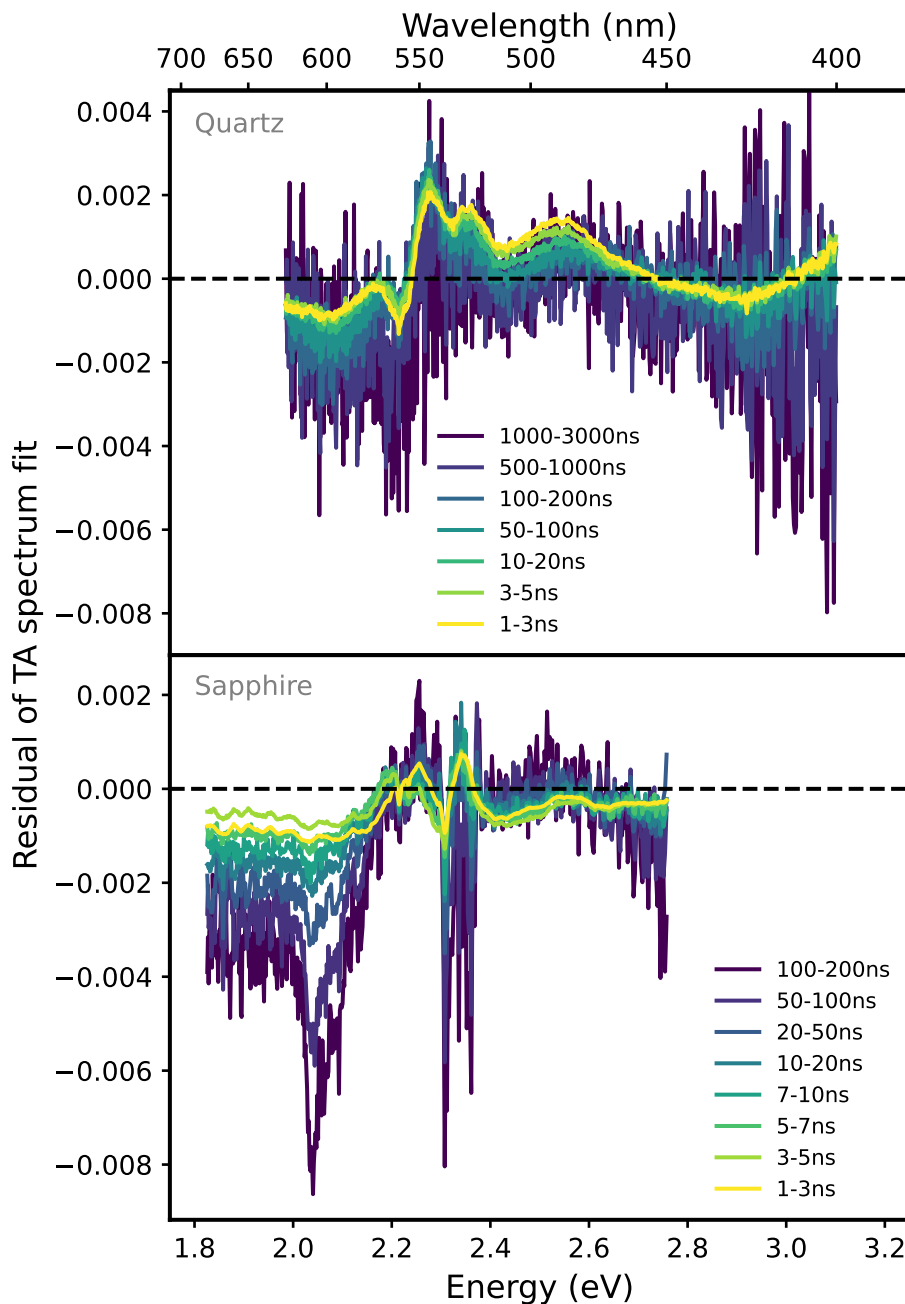


FIGURE A.7: Plot of residuals of a linear fit of the temperature dependent absorption spectra to the long-time TA spectra at various time slices for thin films of Red254 on a quartz substrate (top) and on a sapphire substrate (bottom). This is done to ascertain if there are any time-dependent features obscured by the heat-based artefact that dominates the long-time TA spectrum. However, for the most part, the noise of the resultant residual spectra makes positive identification difficult. The only time dependent feature in the residual spectra is observed at ~ 2.05 eV in the sapphire spectra, which shows a PIA feature increasing in magnitude after ~ 10 ns, potentially indicating the presence of a long-lived species in the solid film of Red254. However, this is not conclusive as a similar feature is not observed in the quartz data. The vertical blue line indicates the pump wavelength for the TA data.

TABLE A.1: Table of sample temperature as set by water bath heater versus measured temperature of substrate back surface.

Set temperature (°C)	Measured temperature (°C)
25	23
35	29.5
45	35
50	38
55	40
65	44

Appendix B

Pigment Red 254 Infra-Red Supporting Information

B.1 Uncorrected TRIR spectra

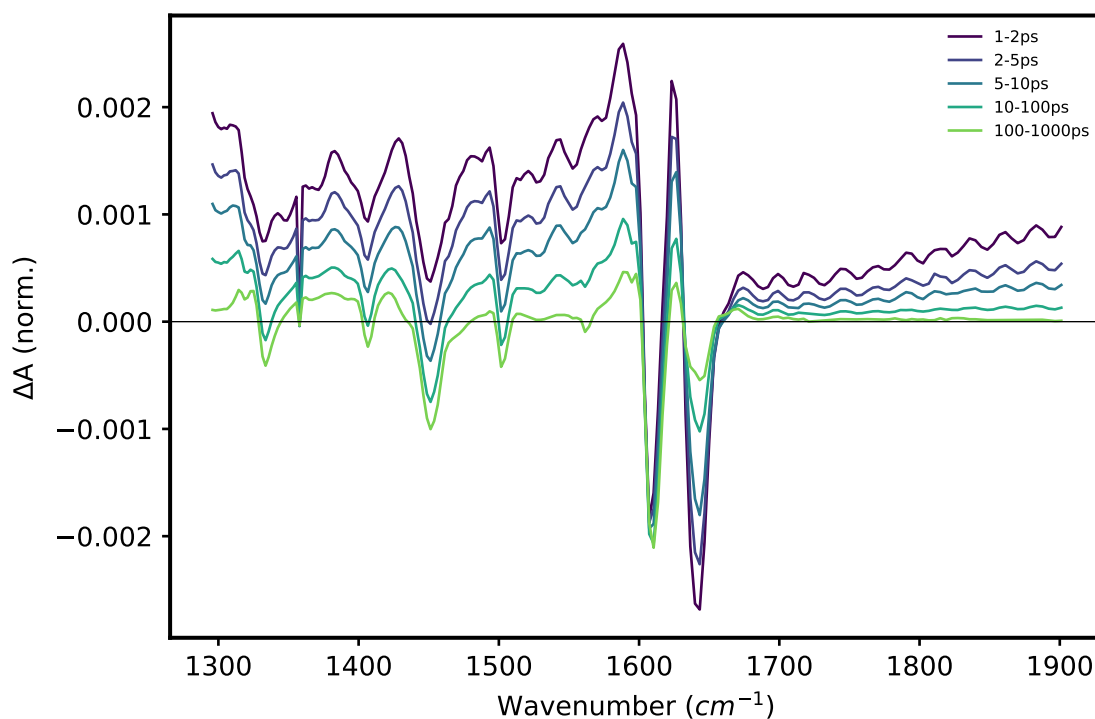


FIGURE B.1: Uncorrected TRIR spectra of Red254 with a pump power of 5mW. These spectra have not been corrected as in the main text using the region between $2000\text{-}2100\text{cm}^{-1}$ as a point of reference for the broad electronic signal that occurs across the spectra.

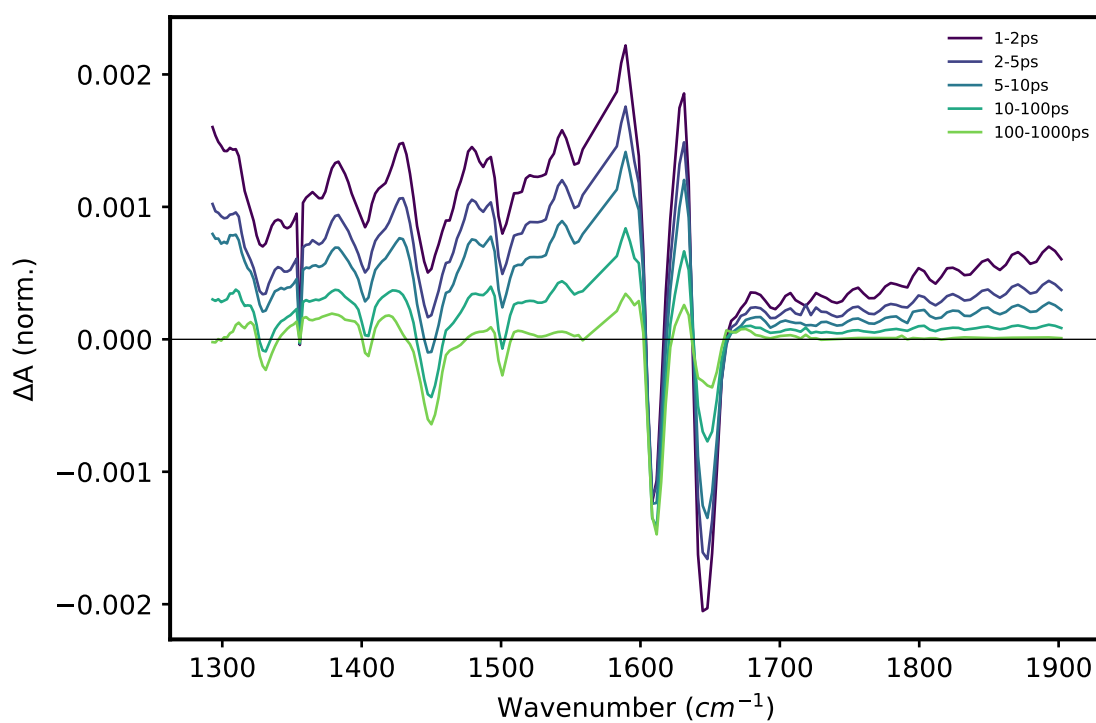


FIGURE B.2: Uncorrected TRIR spectra of Red254 with a pump power of 2.5mW. These spectra have not been corrected as in the main text using the region between 2000-2100 cm^{-1} as a point of reference for the broad electronic signal that occurs across the spectra.

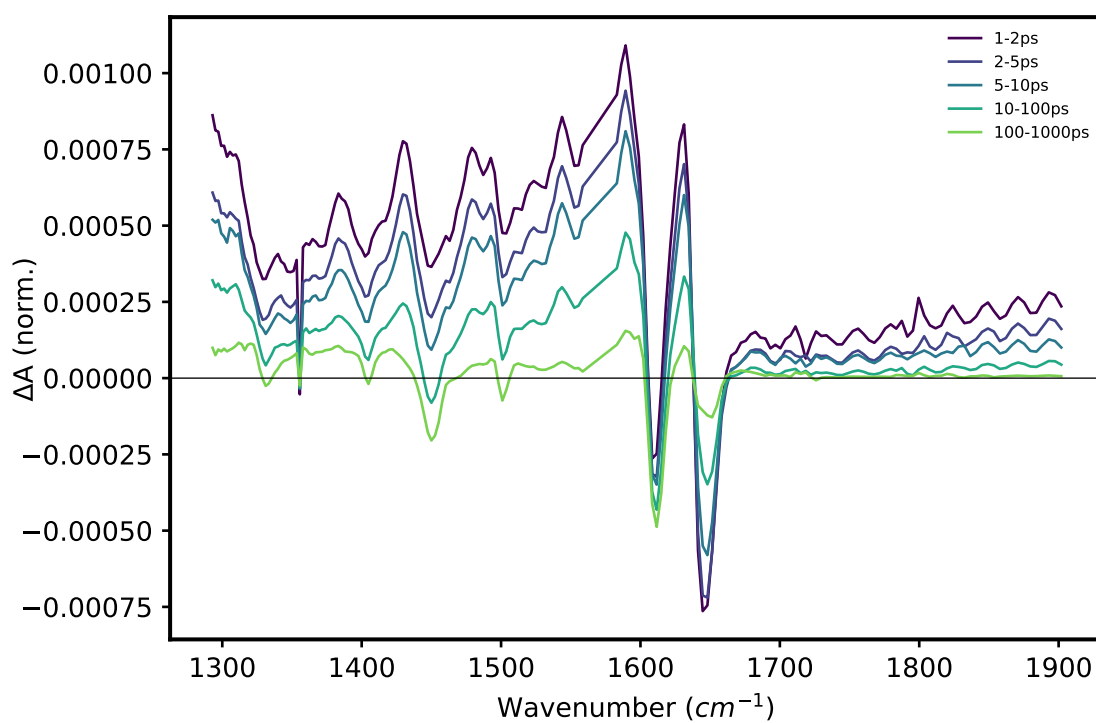


FIGURE B.3: Uncorrected TRIR spectra of Red254 with a pump power of 1mW. These spectra have not been corrected as in the main text using the region between 2000-2100 cm^{-1} as a point of reference for the broad electronic signal that occurs across the spectra.

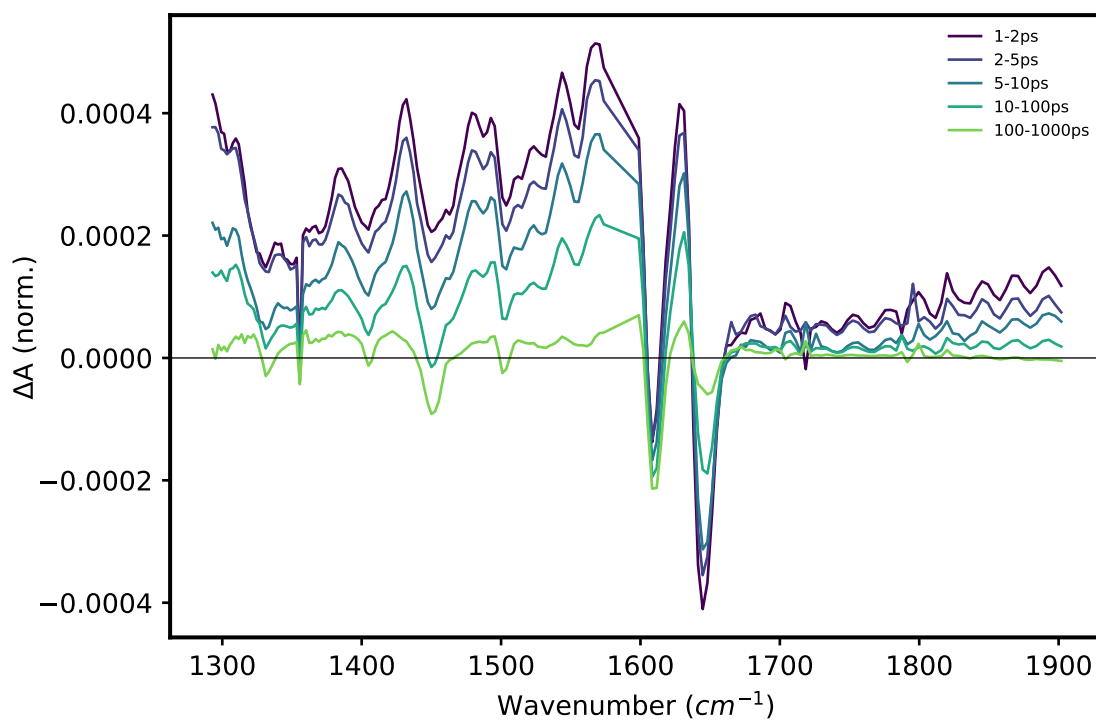


FIGURE B.4: Uncorrected TRIR spectra of Red254 with a pump power of 0.5mW. These spectra have not been corrected as in the main text using the region between 2000-2100 cm^{-1} as a point of reference for the broad electronic signal that occurs across the spectra.

B.2 Fluence dependent TRIR decay lifetimes

TABLE B.1: Lifetimes of excited vibrational decays from Time-Resolved Infra-Red spectroscopy kinetics as shown in Figs. B.5, B.6 and B.7

Wavenumber (cm ⁻¹)	τ_1 (ps)	τ_2 (ps)	$\delta\tau_1$ (ps)	$\delta\tau_2$ (ps)
0.5 mW				
1451	30	-	8.5	-
1589	1.1	78	0.8	24
1610	1.2	-	0.64	-
1627	800	-	530	-
1643	3.4	53	0.95	13.2
1703	3.9	-	1.3	-
1 mW				
1451	14	-	2.1	-
1589	12	160	2.85	39
1610	1.35	-	0.41	-
1627	130	-	26	-
1643	2.9	41	0.45	5.5
1703	3.7	-	0.78	-
2.5 mW				
1451	14.6	-	2.6	-
1589	0.32	33	0.11	3.1
1610	2.1	-	0.49	-
1627	110	-	34	-
1643	2.2	33	0.20	3.4
1703	3.8	-	0.48	-

B.3 Full fluence dependent TRIR spectra and kinetics

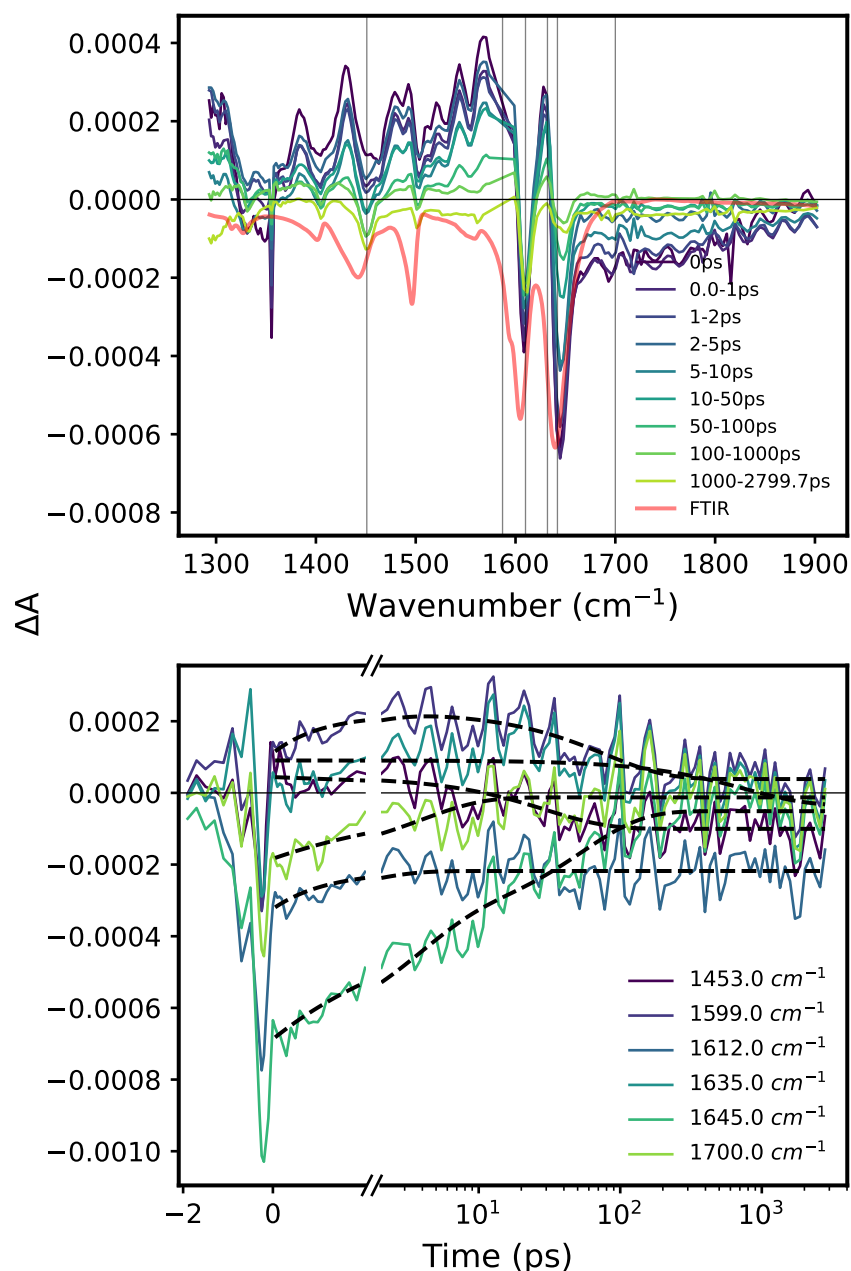


FIGURE B.5: Time Resolved Infra-Red (TRIR) spectra (top) and kinetics (bottom) of thin film of Red254 on calcium fluoride window substrate, using a pump wavelength of 520 nm and power of 0.5 mW. An additional broad electronic signal was seen in all TRIR spectra, and was subtracted from the overall spectrum by subtracting the signal between 2000-2100 cm^{-1} , as the signal appeared the same across the spectrum. The subtracted kinetics are shown in figure 5.7. Overlaid with these spectra is the inverted Fourier Transform Infra-Red (FTIR) obtained from the RAL spectrometer, to assist in identifying the peaks. The locations of the kinetic slices used in TRIR kinetics (bottom) are marked by grey lines on the figure. Exponential and bi-exponential fits to the data are shown on this graph as dotted black lines.

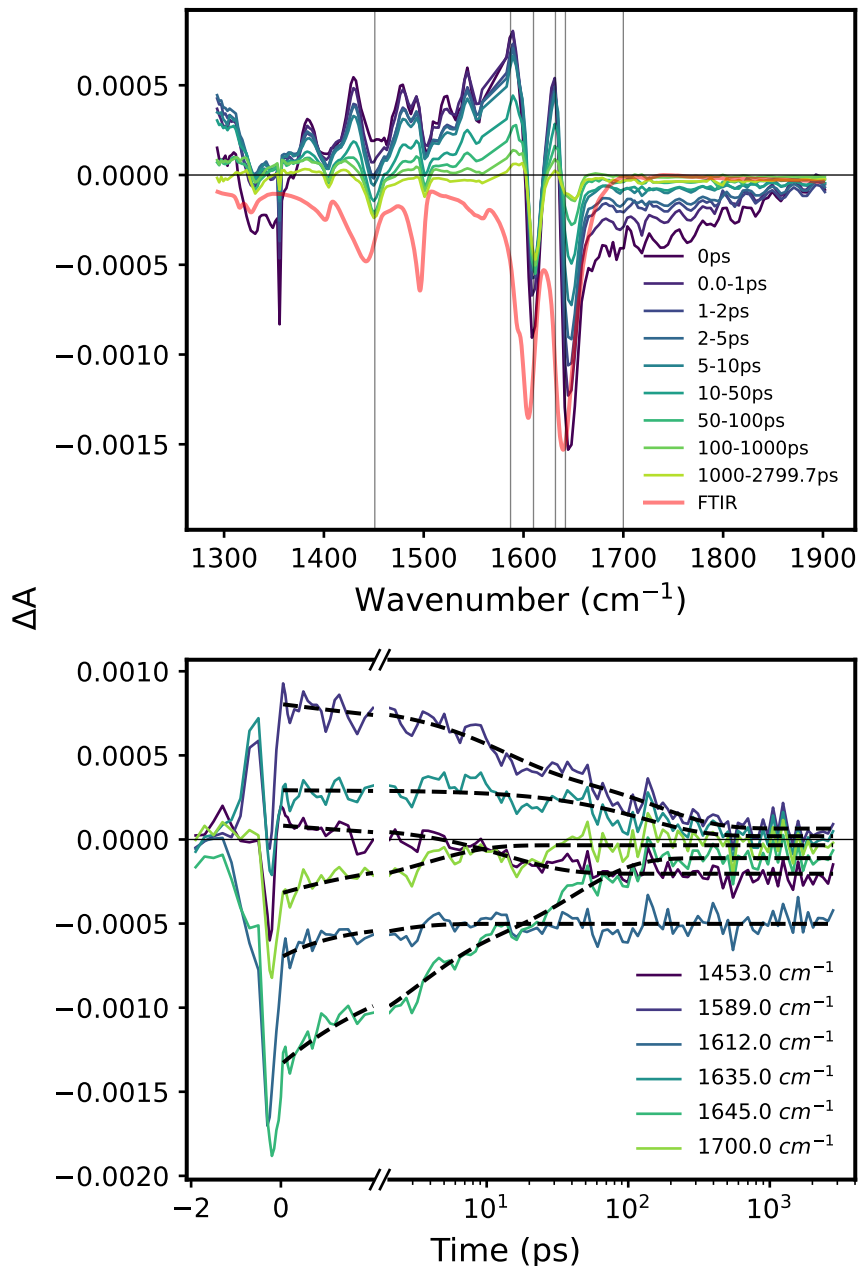


FIGURE B.6: Time Resolved Infra-Red (TRIR) spectra (top) and kinetics (bottom) of thin film of Red254 on calcium fluoride window substrate, using a pump wavelength of 520 nm and power of 1 mW. An additional broad electronic signal was seen in all TRIR spectra, and was subtracted from the overall spectrum by subtracting the signal between 2000-2100 cm^{-1} , as the signal appeared the same across the spectrum. The subtracted kinetics are shown in figure 5.7. Overlaid with these spectra is the inverted Fourier Transform Infra-Red (FTIR) obtained from the RAL spectrometer, to assist in identifying the peaks. The locations of the kinetic slices used in TRIR kinetics (bottom) are marked by grey lines in the figure. Exponential and bi-exponential fits to the data are shown on this graph as dotted black lines.

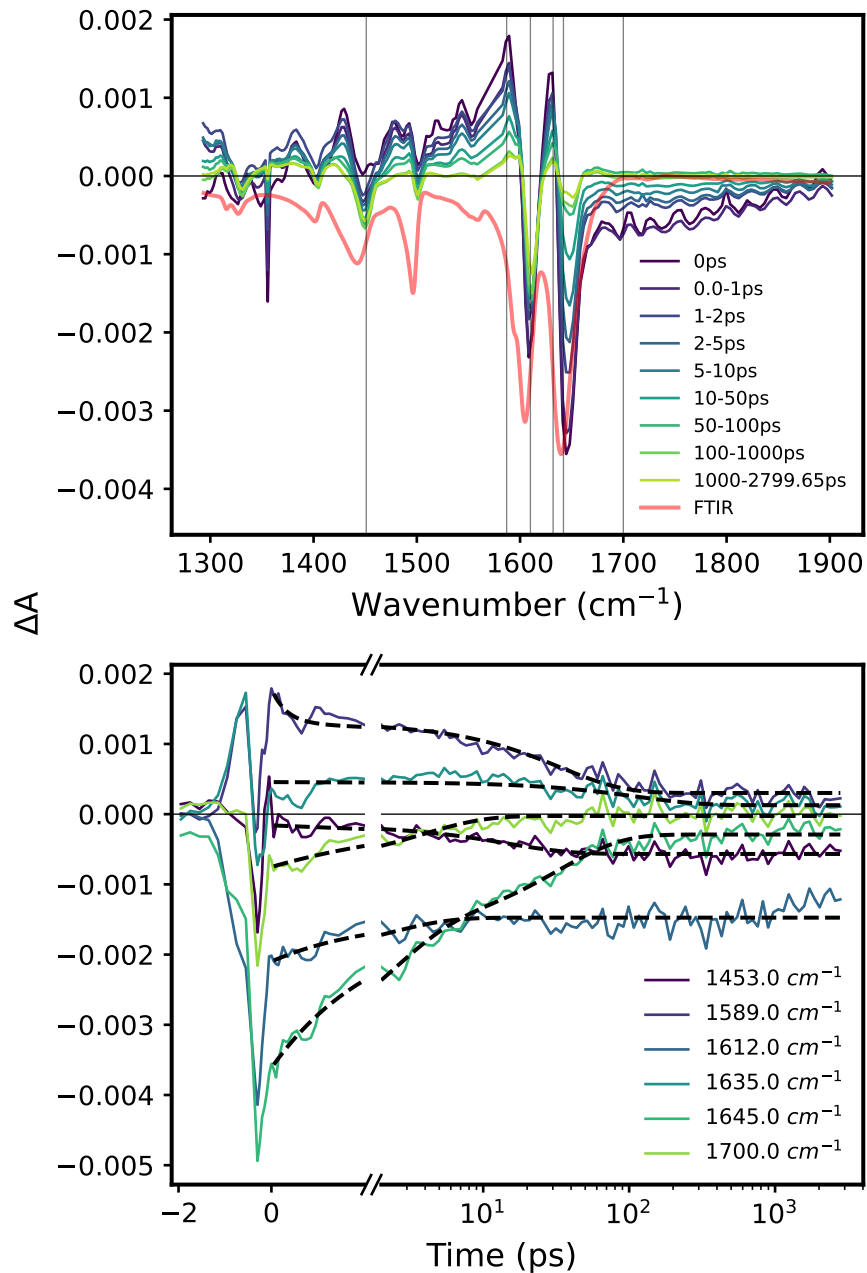


FIGURE B.7: Time Resolved Infra-Red (TRIR) spectra (top) and kinetics (bottom) of thin film of Red254 on calcium fluoride window substrate, using a pump wavelength of 520 nm and power of 2.5 mW. An additional broad electronic signal was seen in all TRIR spectra, and was subtracted from the overall spectrum by subtracting the signal between 2000-2100 cm^{-1} , as the signal appeared the same across the spectrum. The subtracted kinetics are shown in figure 5.7. Overlaid with these spectra is the inverted Fourier Transform Infra-Red (FTIR) obtained from the RAL spectrometer, to assist in identifying the peaks. The locations of the kinetic slices used in TRIR kinetics (bottom) are marked by grey lines in the figure. Exponential and bi-exponential fits to the data are shown on this graph as dotted black lines.

B.4 Comparisons of TRIR kinetics

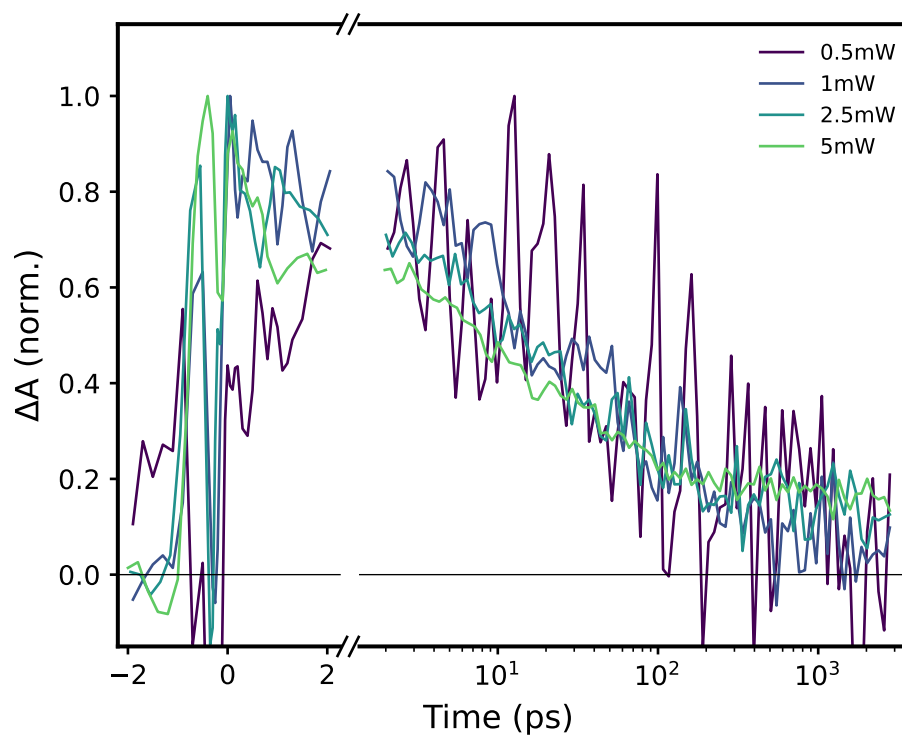


FIGURE B.8: Normalised kinetic decays of the 1589 cm⁻¹ kinetic slice of time-resolved infra-red spectrum of Red254 evaporated thin film on calcium fluoride substrate, using an excitation wavelength of 520 nm at fluences 0.5 mW, 1 mW, 2.5 mW, and 5 mW. Very little variation is visible in the kinetic lineshape, except for the 0.5 mW fluence, which shows higher noise than the others and has a different shape at early times.

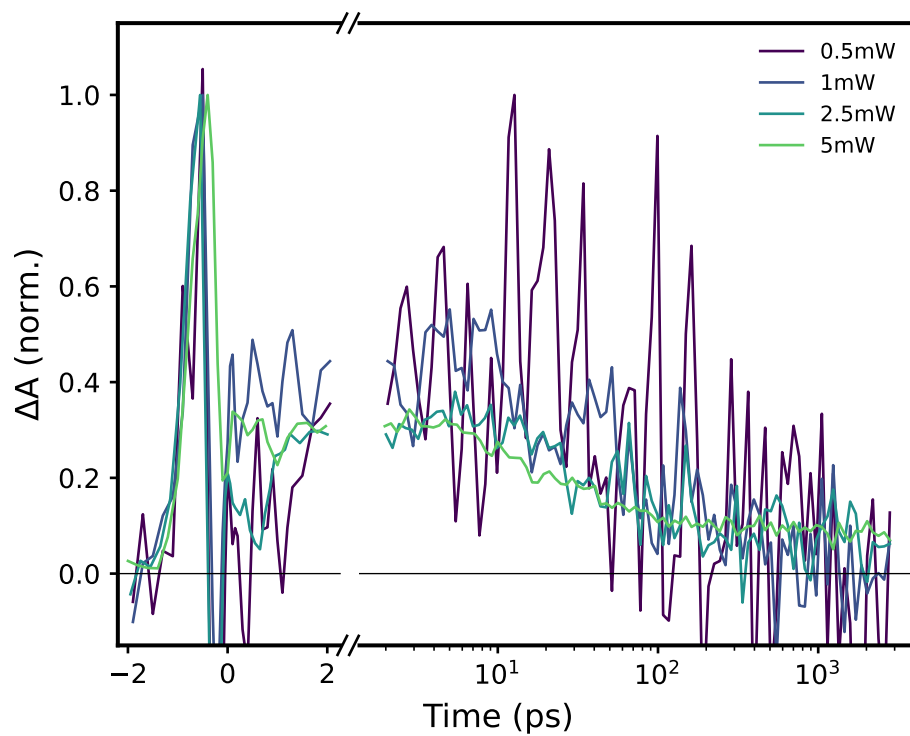


FIGURE B.9: Normalised kinetic decays of the 1627 cm⁻¹ kinetic slice of time-resolved infra-red spectrum of Red254 evaporated thin film on calcium fluoride substrate, using an excitation wavelength of 520 nm at fluences 0.5 mW, 1 mW, 2.5 mW, and 5 mW. While there is little visible variation from this plot, the 0.5 mW kinetic is highly noisy.

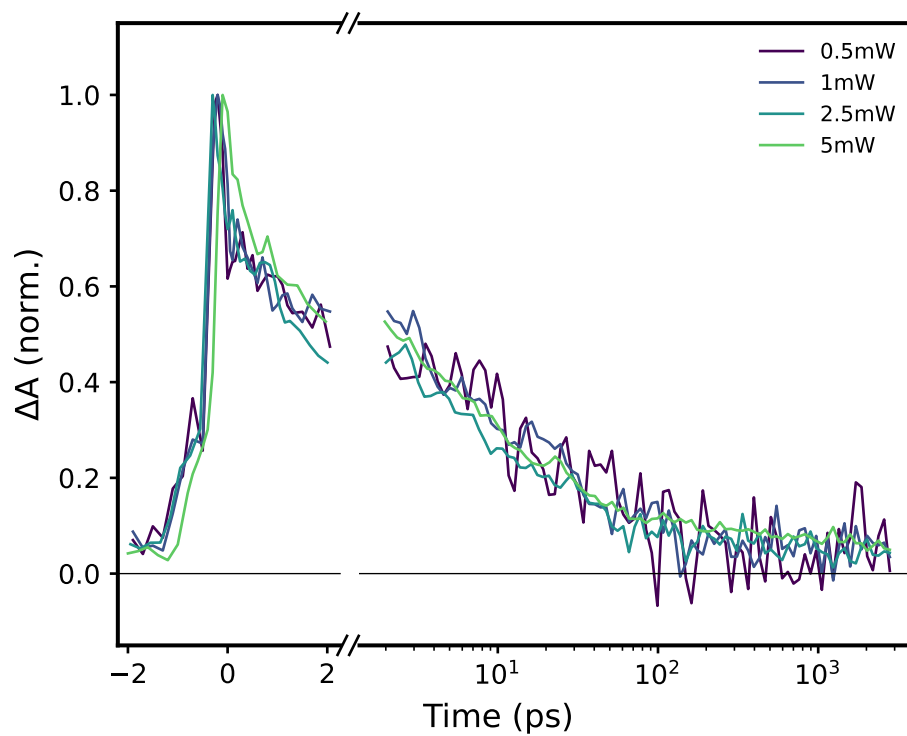


FIGURE B.10: Normalised kinetic decays of the 1643 cm^{-1} kinetic slice of time-resolved infra-red spectrum of Red254 evaporated thin film on calcium fluoride substrate, using an excitation wavelength of 520 nm at fluences 0.5 mW, 1 mW, 2.5 mW, and 5 mW.

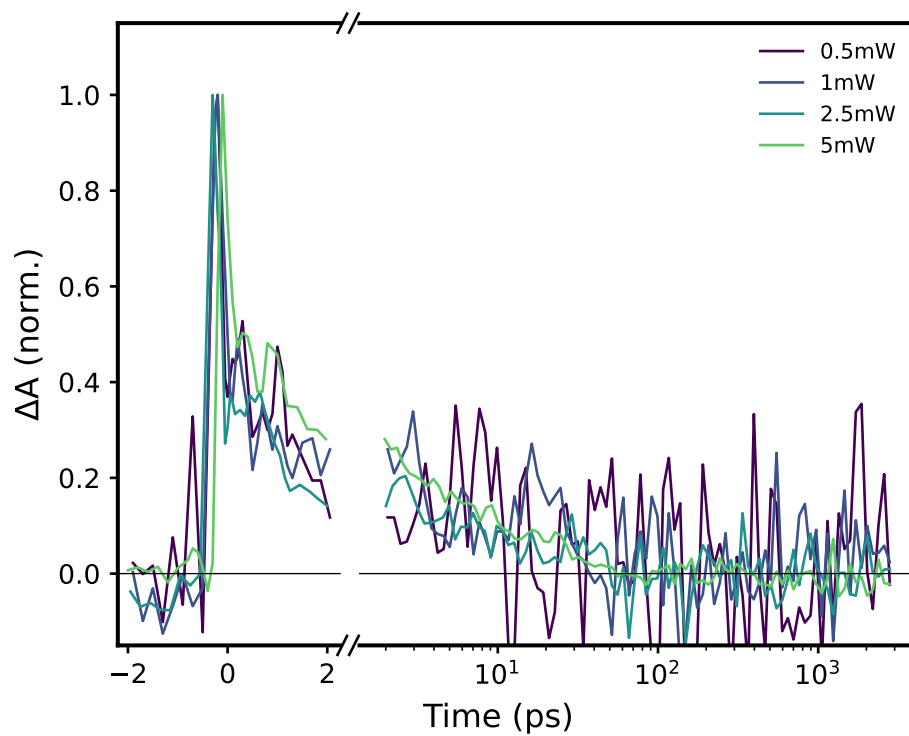


FIGURE B.11: Normalised kinetic decays of the 1703 cm^{-1} kinetic slice of time-resolved infra-red spectrum of Red254 evaporated thin film on calcium fluoride substrate, using an excitation wavelength of 520 nm at fluences 0.5 mW , 1 mW , 2.5 mW , and 5 mW . There is significant noise in the 0.5 mW kinetic.

B.5 Fluence dependent TRIR graphical lifetime comparisons

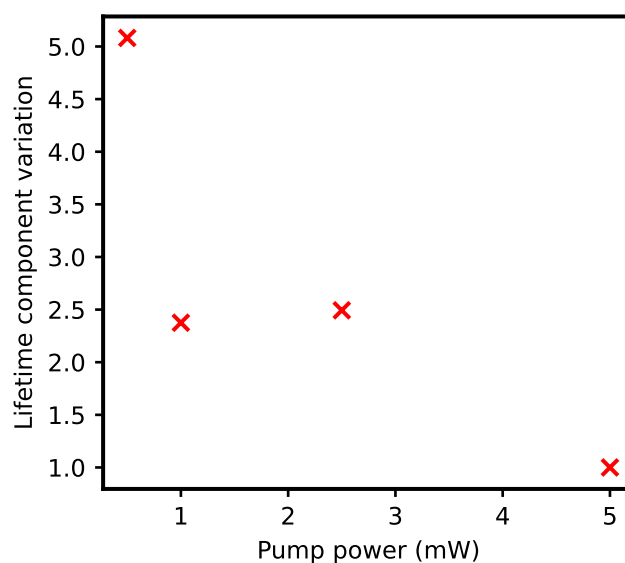


FIGURE B.12: Fluence dependence of fitted exponential lifetimes to the 1451 cm^{-1} kinetic slice of the TRIR spectra of Red254 on calcium fluoride substrate, normalised to the 5 mW kinetic. Lifetimes show large variations, especially at the extremal fluences, with the 0.5 mW kinetic having a lifetime 5 times as long as the 5 mW kinetic. However, this variation can be partially explained due to the large noise to signal ratio visible in this lowest power kinetic.

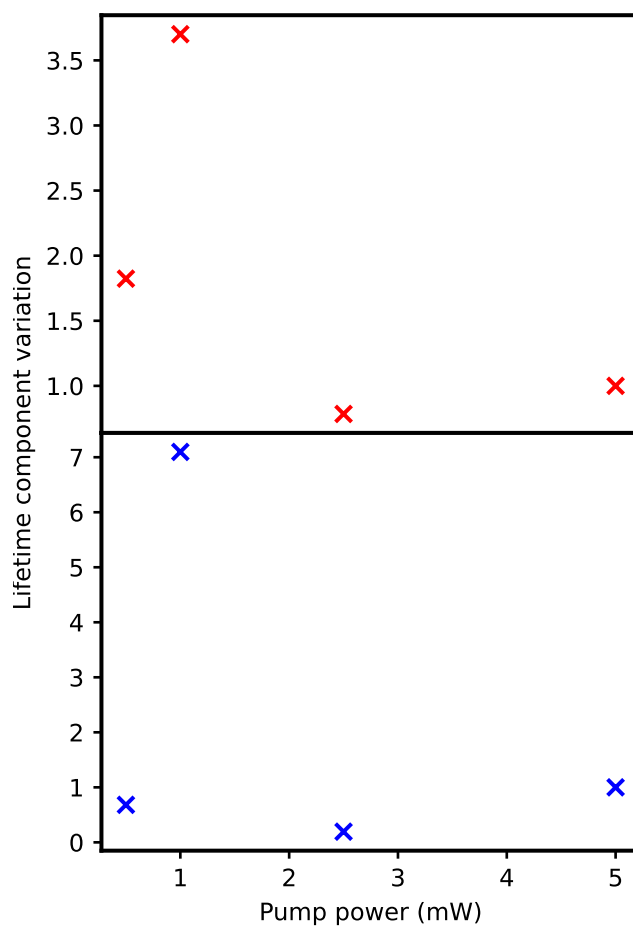


FIGURE B.13: Fluence dependence of fitted exponential lifetimes to the 1589 cm^{-1} kinetic slice of the TRIR spectra of Red254 on calcium fluoride substrate, normalised to the 5 mW kinetic. While there is some variation of lifetime with fluence, there is no monotonic fluence dependence. The 0.5 mW fluence lifetime is a standout from the rest, as the shape of the kinetic is different at this wavenumber, though this may be in part due to the high noise of this fluence kinetic. The lifetime of the 1 mW fluence kinetic is the highest, over 3.5 times that of the 5 mW kinetic, and there is little change between the 2.5 and 5 mW kinetic lifetimes.

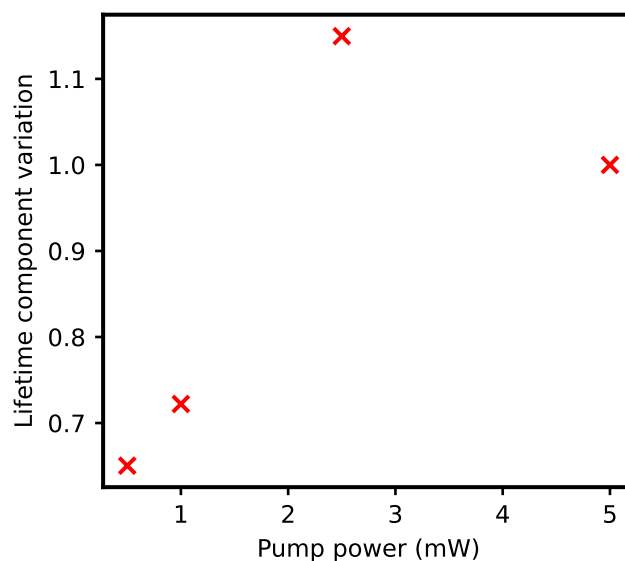


FIGURE B.14: Fluence dependence of fitted exponential lifetimes to the 1610 cm⁻¹ kinetic slice of the TRIR spectra of Red254 on calcium fluoride substrate, normalised to the 5 mW kinetic. This kinetic shows a faster decay at lower fluence, indicating that a higher excitation concentration results in a longer lived population of this vibrational state

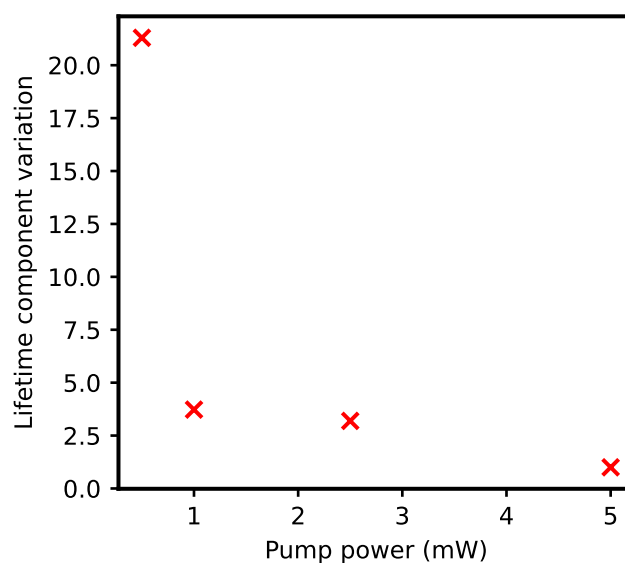


FIGURE B.15: Fluence dependence of fitted exponential lifetimes to the 1627 cm⁻¹ kinetic slice of the TRIR spectra of Red254 on calcium fluoride substrate, normalised to the 5 mW kinetic. The 0.5 mW lifetime has a much longer lifetime than the higher fluence measurements, although we attribute this mostly due to higher noise. The remaining components vary up to 4x greater than the 5 mW kinetic lifetime, indicating a small fluence dependence to the lifetime.

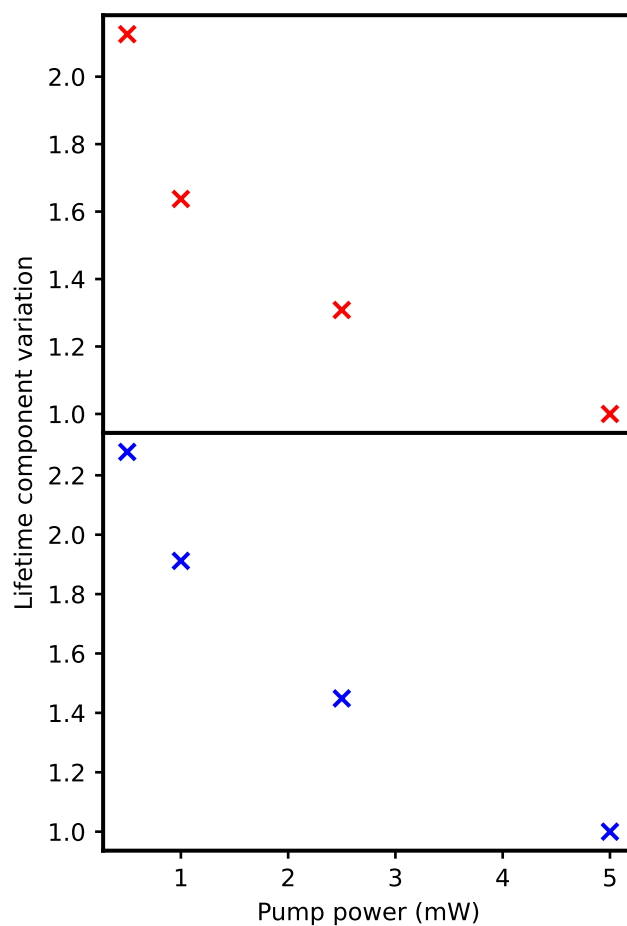


FIGURE B.16: Fluence dependence of the bi-exponential fit lifetimes of the 1643 cm^{-1} kinetic slice of the TRIR spectra of Red254 on calcium fluoride substrate, normalised to the 5 mW kinetic. In both cases, the lifetime components of these kinetics vary by ~ 2 times, with a lower fluence resulting in a longer lifetime. This indicates an intermolecular component to the lifetime of this vibration, in that a higher excitation density results in a faster decay.

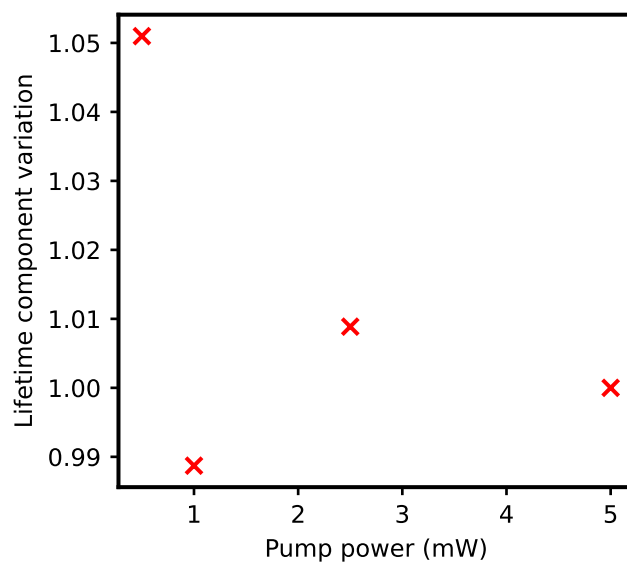


FIGURE B.17: Fluence dependence of fitted exponential lifetimes of the 1703 cm^{-1} kinetic slice of the TRIR spectra of Red254 on calcium fluoride substrate, normalised to the 5 mW kinetic. The lifetime only varies by $\sim 5\%$ overall, indicating little to no fluence dependence of this kinetic.

Appendix C

BoDiPy 6 and 7 Supporting Information

C.1 Beam parameters for BoDiPy Transient Absorption Spectroscopy

TABLE C.1: Beam parameters and excitation density of pump laser used for picosecond transient absorption spectroscopy of BoDiPy 6 samples. Areal excitation density was calculated using absorption spectroscopy of the samples used in TA at the wavelength of the exciting beam.

λ (nm)	Power (μW)	a_{minor} (μm)	a_{major} (μm)	Area ex. dens. (10^{17}m^{-2})
Solution & Amorphous Film				
520	500	861.50	977.04	3.96
Crystal film				
400	500	696.73	723.49	5.08
400	1500			15.25
530	500	565.64	818.66	7.33
530	1200			17.59

TABLE C.2: Beam parameters and excitation density of pump laser used for picosecond transient absorption spectroscopy of BoDiPy 7 samples. Areal excitation density was calculated using absorption spectroscopy of the samples used in TA at the wavelength of the exciting beam.

λ (nm)	Power (μW)	a_{minor} (μm)	a_{major} (μm)	Area ex. dens. (10^{17}m^{-2})
Solution & amorphous film				
520	500	861.50	977.04	3.96
Crystal film				
400	300	696.73	723.49	3.05
400	1000			10.17
530	500	479.40	749.18	9.45
530	1200			22.69

Appendix D

Grant Acknowledgements

DH acknowledges support through Engineering and Physical Sciences Research Council (EPSRC) under grant EP/R/513313/1 and the use of the Lord Porter Laser Facility EP/L022613/1 and EP/R042802/1. JC, SW and RKV acknowledge EP/T012455/1, EP/S002103/1. DJG and AT acknowledge support from European Graphene Flagship Project under grant agreement number 881603 and EPSRC grants EP/S030751/1, EP/V006975/1, and EP/V026496/1. We acknowledge Diamond Light Source for time on I07 under proposal SI23587-1. DTWT acknowledges funding through the EPSRC (UK) via grants EP/V055127/1 and EP/P027814/1. RK acknowledges support from EPSRC for AFM measurements via grant EP/V055127/1 (Manufacturing Organic-Inorganic Nanoparticle Composites with Nanoscale Precision via Directed Self-Assembly)

Bibliography

- [1] Daniele Padula, Ömer H. Omar, Tahereh Nematiaram, and Alessandro Troisi. Singlet fission molecules among known compounds: Finding a few needles in a haystack. *Energy Environ. Sci.*, 12(8):2412–2416, 2019. doi: 10.1039/C9EE01508F. URL <http://dx.doi.org/10.1039/C9EE01508F>.
- [2] James P. Pidgeon. *Time-resolved photophysics of orange carotenoid protein trapped in trehalose-sucrose glass films*. PhD thesis, University of Sheffield, 2023.
- [3] Anna Köhler and Heinz Bässler. *Electronic Processes in Organic Semiconductors; An Introduction*. Wiley-VCH, 2015. ISBN 978-3-527-33292-2.
- [4] Andrzej L. Sobolewski and Wolfgang Domcke. Conical intersections: Efficient excited-state deactivation in organic chromophores and biologically relevant molecules: Role of electron and proton transfer processes. In Wolfgang Domcke, David R Yarkony, and Horst Köppel, editors, *Conical Intersections; Theory Computation and Experiment*, chapter 2, pages 51–82. WORLD SCIENTIFIC, 2011. doi: 10.1142/9789814313452_0002. URL https://www.worldscientific.com/doi/abs/10.1142/9789814313452_0002.
- [5] Robert Englman and Joshua Jortner. The energy gap law for radiationless transitions in large molecules. *Molecular Physics*, 18(2):145–164, 1970. doi: 10.1080/00268977000100171. URL <https://www.tau.ac.il/~jortner/Publications/Pub1-200/129.pdf>.
- [6] Anatoly B. Kolomeisky, Xintian Feng, and Anna I. Krylov. A simple kinetic model for singlet fission: A role of electronic and entropic contributions to macroscopic rates. *The Journal of Physical Chemistry C*, 118(10):5188–5195, 2014. doi: 10.1021/jp4128176. URL <https://doi.org/10.1021/jp4128176>.
- [7] Sana Zafar and Mohd. Imran. Chapter 15 - progress in optoelectronic applications of ionic liquids. In Jamal Akhter Siddique, Shahid Pervez Ansari, Aftab Aslam Parwaz Khan, and Abdullah M. Asiri, editors, *Advanced Applications of Ionic Liquids*, pages 391–413. Elsevier, 2023. ISBN 978-0-323-99921-2.

- doi: <https://doi.org/10.1016/B978-0-323-99921-2.00018-5>. URL <https://www.sciencedirect.com/science/article/pii/B9780323999212000185>.
- [8] M. Terazima, N. Hirota, S. E. Braslavsky, Andreas Mandelis, S. E. Bialkowski, G. J. Diebold, R. J. D. Miller, Danièle Fournier, R. A. Palmer, and A. Tam. Quantities, terminology, and symbols in photothermal and related spectroscopies (iupac recommendations 2004). *Pure and Applied Chemistry*, 76(6):1083–1118, 2004. doi: [doi:10.1351/pac200476061083](https://doi.org/10.1351/pac200476061083). URL <https://doi.org/10.1351/pac200476061083>.
- [9] Tom Markvart and Luis Castañer. Chapter i-1-a - principles of solar cell operation. In Soteris A. Kalogirou, editor, *McEvoy's Handbook of Photovoltaics (Third Edition)*, pages 3–28. Academic Press, third edition edition, 2018. ISBN 978-0-12-809921-6. doi: <https://doi.org/10.1016/B978-0-12-809921-6.00001-X>. URL <https://www.sciencedirect.com/science/article/pii/B978012809921600001X>.
- [10] William Shockley and Hans J. Queisser. Detailed Balance Limit of Efficiency of p-n Junction Solar Cells. *Journal of Applied Physics*, 32(3):510–519, 06 2004. ISSN 0021-8979. doi: [10.1063/1.1736034](https://doi.org/10.1063/1.1736034). URL <https://doi.org/10.1063/1.1736034>.
- [11] M. C. Hanna and A. J. Nozik. Solar conversion efficiency of photovoltaic and photoelectrolysis cells with carrier multiplication absorbers. *Journal of Applied Physics*, 100(7):074510, 10 2006. ISSN 0021-8979. doi: [10.1063/1.2356795](https://doi.org/10.1063/1.2356795). URL <https://doi.org/10.1063/1.2356795>.
- [12] Martin A. Green, Yoshihiro Hishikawa, Ewan D. Dunlop, Dean H. Levi, Jochen Hohl-Ebinger, Masahiro Yoshita, and Anita W.Y. Ho-Baillie. Solar cell efficiency tables (version 53). *Progress in Photovoltaics: Research and Applications*, 27(1):3–12, 2019. doi: <https://doi.org/10.1002/pip.3102>. URL <https://onlinelibrary.wiley.com/doi/abs/10.1002/pip.3102>.
- [13] Jing Zhou, Qian Liu, Wei Feng, Yun Sun, and Fuyou Li. Upconversion luminescent materials: Advances and applications. *Chemical Reviews*, 115(1):395–465, 2015. doi: [10.1021/cr400478f](https://doi.org/10.1021/cr400478f). URL <https://doi.org/10.1021/cr400478f>. PMID: 25492128.
- [14] Jan Christoph Goldschmidt and Stefan Fischer. Upconversion for photovoltaics – a review of materials, devices and concepts for performance enhancement. *Advanced Optical Materials*, 3(4):510–535, 2015. doi: <https://doi.org/10.1002/adom.201500024>. URL <https://onlinelibrary.wiley.com/doi/abs/10.1002/adom.201500024>.

- [15] Murad J. Y. Tayebjee, Dane R. McCamey, and Timothy W. Schmidt. Beyond shockley–queisser: Molecular approaches to high-efficiency photovoltaics. *The Journal of Physical Chemistry Letters*, 6(12):2367–2378, 2015. doi: 10.1021/acs.jpcllett.5b00716. URL <https://doi.org/10.1021/acs.jpcllett.5b00716>. PMID: 26266619.
- [16] Alexander J. Baldacchino, Miles I. Collins, Michael P. Nielsen, Timothy W. Schmidt, Dane R. McCamey, and Murad J. Y. Tayebjee. Singlet fission photovoltaics: Progress and promising pathways. *Chemical Physics Reviews*, 3(2):021304, 05 2022. ISSN 2688-4070. doi: 10.1063/5.0080250. URL <https://doi.org/10.1063/5.0080250>.
- [17] Wenpei Fan, Bryant Yung, Peng Huang, and Xiaoyuan Chen. Nanotechnology for multimodal synergistic cancer therapy. *Chemical Reviews*, 117(22):13566–13638, 2017. doi: 10.1021/acs.chemrev.7b00258. URL <https://doi.org/10.1021/acs.chemrev.7b00258>. PMID: 29048884.
- [18] Qing You, Kaiyue Zhang, Jingyi Liu, Changliang Liu, Huayi Wang, Mengting Wang, Siyuan Ye, Houqian Gao, Letian Lv, Chen Wang, Ling Zhu, and Yanlian Yang. Persistent regulation of tumor hypoxia microenvironment via a bioinspired pt-based oxygen nanogenerator for multimodal imaging-guided synergistic phototherapy. *Advanced Science*, 7(17):1903341, 2020. doi: <https://doi.org/10.1002/adv.201903341>. URL <https://onlinelibrary.wiley.com/doi/abs/10.1002/adv.201903341>.
- [19] Chuanjiang Qin, Toshinori Matsushima, William J. Potscavage, Atula S. D. Sandanayaka, Matthew R. Leyden, Fatima Bencheikh, Kenichi Goushi, Fabrice Mathevet, Benoît Heinrich, Go Yumoto, Yoshihiko Kanemitsu, and Chihaya Adachi. Triplet management for efficient perovskite light-emitting diodes. *Nature Photonics*, 14:70–75, 2020. doi: 10.1038/s41566-019-0545-9. URL <https://doi.org/10.1038/s41566-019-0545-9>.
- [20] Denis Y. Kondakov. Triplet–triplet annihilation in highly efficient fluorescent organic light-emitting diodes: current state and future outlook. *Philosophical Transactions of the Royal Society A: Mathematical, Physical and Engineering Sciences*, 373(2044):20140321, 2015. doi: 10.1098/rsta.2014.0321. URL <https://royalsocietypublishing.org/doi/abs/10.1098/rsta.2014.0321>.
- [21] Anna Köhler and Heinz Bässler. *The Electronic Structure of Organic Semiconductors*. John Wiley & Sons, Ltd, 2015. ISBN 9783527685172. doi: <https://doi.org/10.1002/9783527685172.ch1>.

- [22] Páraic M Keane, Michal Wojdyla, Gerard W. Doorley, John M. Kelly, Anthony W. Parker, Ian P Clark, Gregory M. Greetham, Michael Towrie, Luís M. Magno, and Susan J. Quinn. Long-lived excited states in i-motif dna studied by picosecond time-resolved ir spectroscopy. *Chemical communications*, 50 23:2990–2, 2014. URL <https://api.semanticscholar.org/CorpusID:26181991>.
- [23] Guang-Jiu Zhao and Ke-Li Han. Role of intramolecular and intermolecular hydrogen bonding in both singlet and triplet excited states of aminofluorenones on internal conversion, intersystem crossing, and twisted intramolecular charge transfer. *The Journal of Physical Chemistry A*, 113(52):14329–14335, 2009. doi: 10.1021/jp903200x. URL <https://doi.org/10.1021/jp903200x>.
- [24] László Biczók, Tibor Bérces, and Henry Linschitz. Quenching processes in hydrogen-bonded pairs: Interactions of excited fluorenone with alcohols and phenols. *Journal of the American Chemical Society*, 119(45):11071–11077, 1997. doi: 10.1021/ja972071c. URL <https://doi.org/10.1021/ja972071c>.
- [25] László Biczók, Tibor Bérces, and Haruo Inoue. Effects of molecular structure and hydrogen bonding on the radiationless deactivation of singlet excited fluorenone derivatives. *The Journal of Physical Chemistry A*, 103(20):3837–3842, 1999. doi: 10.1021/jp990208a. URL <https://doi.org/10.1021/jp990208a>.
- [26] Pingping Liang, Qianyun Tang, Yu Cai, Gongyuan Liu, Weili Si, Jinjun Shao, Wei Huang, Qi Zhang, and Xiaochen Dong. Self-quenched ferrocenyl diketopyrrolopyrrole organic nanoparticles with amplifying photothermal effect for cancer therapy. *Chem. Sci.*, 8:7457–7463, 2017. doi: 10.1039/C7SC03351F. URL <http://dx.doi.org/10.1039/C7SC03351F>.
- [27] Lele Sun, Zijian Xiong, Fengyun Shen, Zhanhui Wang, and Zhuang Liu. Biological membrane derived nanomedicines for cancer therapy. *Science China Chemistry*, 64:719–733, 2021. doi: 10.1007/s11426-020-9943-9. URL <https://doi.org/10.1007/s11426-020-9943-9>.
- [28] Xiaojuan Huang, Wenlong Zhang, Guoqiang Guan, Guosheng Song, Rujia Zou, and Junqing Hu. Design and functionalization of the nir-responsive photothermal semiconductor nanomaterials for cancer theranostics. *Accounts of Chemical Research*, 50(10):2529–2538, 2017. doi: 10.1021/acs.accounts.7b00294. URL <https://doi.org/10.1021/acs.accounts.7b00294>. PMID: 28972736.
- [29] Honglei Chen, Shao-Lin Wu, Hua-Li Wang, Qing-Yun Wu, and Hao-Cheng Yang. Photothermal devices for sustainable uses beyond desalination. *Advanced Energy and Sustainability Research*, 2(3):2000056, 2021. doi: <https://doi.org/10.1002/>

- aesr.202000056. URL <https://onlinelibrary.wiley.com/doi/abs/10.1002/aesr.202000056>.
- [30] Wim H. De Jong, Werner I. Hagens, Petra Krystek, Marina C. Burger, Adriënne J.A.M. Sips, and Robert E. Geertsma. Particle size-dependent organ distribution of gold nanoparticles after intravenous administration. *Biomaterials*, 29(12):1912–1919, 2008. ISSN 0142-9612. doi: <https://doi.org/10.1016/j.biomaterials.2007.12.037>. URL <https://www.sciencedirect.com/science/article/pii/S014296120701071X>.
- [31] Manuela Semmler-Behnke, Wolfgang G. Kreyling, Jens Lipka, Stefanie Fertsch, Alexander Wenk, Shinji Takenaka, Günter Schmid, and Wolfgang Brandau. Biodistribution of 1.4- and 18-nm gold particles in rats. *Small*, 4(12):2108–2111, 2008. doi: <https://doi.org/10.1002/smll.200800922>. URL <https://onlinelibrary.wiley.com/doi/abs/10.1002/smll.200800922>.
- [32] Ashkay Rao and Richard H. Friend. Harnessing singlet exciton fission to break the shockley–queisser limit. *Nature Reviews Materials*, 2(17063), 2017. doi: 10.1038/natrevmats.2017.63. URL <https://www.nature.com/articles/natrevmats201763>.
- [33] Peter Atkins and Ronald Friedman. *Molecular Quantum Mechanics*. Oxford University Press, 5 edition, 2011. URL <http://www.nanoer.net/d/img/Molecular%20Quantum%20Mechanics,%205th%20Edition.pdf>.
- [34] Markus Schwoerer and Hans Cristoph Wolf. *Organic Molecular Solids*. Wiley-VCH, 2007. ISBN 978-3-527-40540-4.
- [35] Robert Eisberg. *Quantum Physics of Atoms, Molecules, Solids, Nuclei and Particles*. John Wiley & Sons, 2 edition, 1985. ISBN 0-471-87373-X.
- [36] Francisco Fernández. The born-oppenheimer approximation. 03 2019. doi: 10.13140/RG.2.2.21650.91840.
- [37] Frank L. Pilar. *Elementary Quantum Chemistry*. McGraw-Hill, 1968.
- [38] Attila Szabó and Neil S. Ostlund. *Modern quantum chemistry : introduction to advanced electronic structure theory*. McGraw-Hill, 1996.
- [39] R.G. Woolley. Quantum chemistry beyond the born-oppenheimer approximation. *Journal of Molecular Structure: THEOCHEM*, 230:17–46, 1991. ISSN 0166-1280. doi: [https://doi.org/10.1016/0166-1280\(91\)85170-C](https://doi.org/10.1016/0166-1280(91)85170-C). URL <https://www.sciencedirect.com/science/article/pii/016612809185170C>.

- [40] Heinz Mustroph. Potential-energy surfaces, the born–oppenheimer approximations, and the franck–condon principle: Back to the roots. *ChemPhysChem*, 17(17):2616–2629, 2016. doi: <https://doi.org/10.1002/cphc.201600243>. URL <https://chemistry-europe.onlinelibrary.wiley.com/doi/abs/10.1002/cphc.201600243>.
- [41] Hiroyuki Nohira and Toshiyuki Nohira. Revisiting the von neumann–wigner non-crossing rule and validity of a dynamic correlation diagram method. *Journal of Theoretical and Computational Chemistry*, 18(02):1950013, 2019. doi: 10.1142/S0219633619500135. URL <https://doi.org/10.1142/S0219633619500135>.
- [42] Michael A. Robb. Conical intersections: Conical intersections in organic photochemistry. In Wolfgang Domcke, David R Yarkony, and Horst Köppel, editors, *Conical Intersections; Theory Computation and Experiment*, chapter 1. WORLD SCIENTIFIC, 2011. doi: 10.1142/7803. URL <https://www.worldscientific.com/doi/abs/10.1142/7803>.
- [43] Hugh Christopher Longuet-Higgins. The intersection of potential energy surfaces in polyatomic molecules. *Proceedings of the Royal Society of London. A. Mathematical and Physical Sciences*, 344(1637):147–156, 1975. doi: 10.1098/rspa.1975.0095. URL <https://royalsocietypublishing.org/doi/abs/10.1098/rspa.1975.0095>.
- [44] Philip Bunker and Per Jensen. *Molecular Symmetry and Spectroscopy*. NRC Research Press, 2 edition, 2011. ISBN 0-660-19628-X.
- [45] Spiridoula Matsika. Conical intersections: Three state conical intersections. In Wolfgang Domcke, David R Yarkony, and Horst Köppel, editors, *Conical Intersections; Theory Computation and Experiment*, chapter 3. WORLD SCIENTIFIC, 2011. doi: 10.1142/7803. URL <https://www.worldscientific.com/doi/abs/10.1142/7803>.
- [46] Nina K. Schwalb, Ron Siewertsen, Falk Renth, and Friedrich Temps. Conical intersections: Pump-probe spectroscopy of ultrafast vibronic dynamics in organic chromophores. In Wolfgang Domcke, David R Yarkony, and Horst Köppel, editors, *Conical Intersections; Theory Computation and Experiment*, chapter 17. WORLD SCIENTIFIC, 2011. doi: 10.1142/7803. URL <https://www.worldscientific.com/doi/abs/10.1142/7803>.
- [47] Michael Kasha. Characterization of electronic transitions in complex molecules. *Discuss. Faraday Soc.*, 9:14–19, 1950. doi: 10.1039/DF9500900014. URL <http://dx.doi.org/10.1039/DF9500900014>.

- [48] Alan Corney. *Atomic and Laser Spectroscopy*. Oxford University Press, 1977.
- [49] Joseph R. Lacowicz. *Principles of Fluorescence Spectroscopy*. Springer Science+Business Media, LLC, 3 edition, 2006. doi: 10.1007/978-0-387-46312-4.
- [50] Enrico Fermi, Jay Orear, A. H. Rosenfeld, and R. A. Schluter. *Nuclear Physics: A course given by Enrico Fermi at the University of Chicago*. The University of Chicago Press, 1953.
- [51] W. Siebrand. Radiationless Transitions in Polyatomic Molecules. I. Calculation of Franck—Condon Factors. *The Journal of Chemical Physics*, 46(2):440–447, 05 1967. ISSN 0021-9606. doi: 10.1063/1.1840685. URL <https://doi.org/10.1063/1.1840685>.
- [52] Jack Ly, Kayla Presley, Thomas Cooper, Luke Baldwin, Matthew Dalton, and Tod Grusenmeyer. Impact of iodine loading and substitution position on intersystem crossing efficiency in a series of ten methylated-meso-phenylbodipy dyes. *Physical Chemistry Chemical Physics*, 23(21):12033–12044, 2021. doi: <https://doi.org/10.1039/D0CP05904H>. URL <https://pubs.rsc.org/en/content/articlelanding/2021/cp/d0cp05904h/unauth#!divAbstract>.
- [53] S. Singh, W. J. Jones, W. Siebrand, B. P. Stoicheff, and W. G. Schneider. Laser Generation of Excitons and Fluorescence in Anthracene Crystals. *The Journal of Chemical Physics*, 42(1):330–342, 07 1965. ISSN 0021-9606. doi: 10.1063/1.1695695. URL <https://doi.org/10.1063/1.1695695>.
- [54] Kiyoshi Miyata, Felisa S. Conrad-Burton, Florian L. Geyer, and X.-Y. Zhu. Triplet pair states in singlet fission. *Chemical Reviews*, 119(6):4261–4292, 2019. doi: 10.1021/acs.chemrev.8b00572. URL <https://doi.org/10.1021/acs.chemrev.8b00572>. PMID: 30721032.
- [55] Jonathan J. Burdett and Christopher J. Bardeen. The dynamics of singlet fission in crystalline tetracene and covalent analogs. *Accounts of Chemical Research*, 46(6):1312–1320, 2013. doi: 10.1021/ar300191w. URL <https://doi.org/10.1021/ar300191w>. PMID: 23360099.
- [56] David G. Bossanyi, Yoichi Sasaki, Shuangqing Wang, Dimitri Chekulaev, Nobuo Kimizuka, Nobuhiro Yanai, and Jenny Clark. Spin statistics for triplet–triplet annihilation upconversion: Exchange coupling, intermolecular orientation, and reverse intersystem crossing. *JACS Au*, 1(12):2188–2201, 2021. doi: 10.1021/jacsau.1c00322. URL <https://doi.org/10.1021/jacsau.1c00322>.
- [57] Murad J. Y. Tayebjee, Samuel N Sanders, Elango Kumarasamy, Luis M. Campos, Matthew Y. Sfeir, and Dane R. McCamey. Quintet multiexciton dynamics in

- singlet fission. *Nature Physics*, 13, 2017. doi: 10.1038/nphys3909. URL <https://doi.org/10.1038/nphys3909>.
- [58] Samuel N. Sanders, Andrew B. Pun, Kaia R. Parenti, Elango Kumarasamy, Lauren M. Yablon, Matthew Y. Sfeir, and Luis M. Campos. Understanding the bound triplet-pair state in singlet fission. *Chem*, 5(8):1988–2005, 2019. ISSN 2451-9294. doi: <https://doi.org/10.1016/j.chempr.2019.05.012>. URL <https://www.sciencedirect.com/science/article/pii/S2451929419302220>.
- [59] Sam L. Bayliss, Leah R. Weiss, Akshay Rao, Richard H. Friend, Alexei D. Chepelianskii, and Neil C. Greenham. Spin signatures of exchange-coupled triplet pairs formed by singlet fission. *Phys. Rev. B*, 94:045204, Jul 2016. doi: 10.1103/PhysRevB.94.045204. URL <https://link.aps.org/doi/10.1103/PhysRevB.94.045204>.
- [60] Maria Fumanal and Clémence Corminboeuf. Optimizing the thermodynamics and kinetics of the triplet-pair dissociation in donor–acceptor copolymers for intramolecular singlet fission. *Chemistry of Materials*, 34(9):4115–4121, 2022. doi: 10.1021/acs.chemmater.2c00367. URL <https://doi.org/10.1021/acs.chemmater.2c00367>.
- [61] Shunta Nakamura, Hayato Sakai, Masaaki Fuki, Yasuhiro Kobori, Nikolai V. Tkachenko, and Taku Hasobe. Enthalpy–entropy compensation effect for triplet pair dissociation of intramolecular singlet fission in phenylene spacer-bridged hexacene dimers. *The Journal of Physical Chemistry Letters*, 12(28):6457–6463, 2021. doi: 10.1021/acs.jpcllett.1c01430. URL <https://doi.org/10.1021/acs.jpcllett.1c01430>. PMID: 34236876.
- [62] Sean P. O’Connor, Samantha M. Powell, John M. Rickman, Nathaniel J. Pope, Gary D. Noojin, Marlan O. Scully, Michael L. Denton, and Vladislav V. Yakovlev. Transient absorption spectroscopy to explore cellular pathways to photobiomodulation. *Journal of Photochemistry and Photobiology B: Biology*, 222:112271, 2021. ISSN 1011-1344. doi: <https://doi.org/10.1016/j.jphotobiol.2021.112271>. URL <https://www.sciencedirect.com/science/article/pii/S1011134421001500>.
- [63] Gregory M. Greetham, Pierre Burgos, Qian Cao, Ian P. Clark, Peter S. Codd, Richard C. Farrow, Michael W. George, Moschos Kogimtzis, Pavel Matousek, Anthony W. Parker, Mark R. Pollard, David A. Robinson, Zhi-Jun Xin, and Michael Towrie. Ultra: A unique instrument for time-resolved spectroscopy. *Applied Spectroscopy*, 64(12):1311–1319, 2010. doi: 10.1366/000370210793561673. URL <https://doi.org/10.1366/000370210793561673>. PMID: 21144146.

- [64] David Nečas and Petr Klapetek. Gwyddion: an open-source software for spm data analysis. *Central European Journal of Physics*, 10(1):181–188, 2012. doi: 10.2478/s11534-011-0096-2. URL <https://doi.org/10.2478/s11534-011-0096-2>.
- [65] Z. Jiang. Gixsgui: a matlab toolbox for grazing-incidence x-ray scattering data visualization and reduction, and indexing of buried three-dimensional periodic nanostructured films. *Journal of Applied Crystallography* 2015, 48(3):917–926, 2015. doi: 10.1107/S1600576715004434. URL <https://doi.org/10.1107/S1600576715004434>.
- [66] M. J. Frisch, G. W. Trucks, H. B. Schlegel, G. E. Scuseria, M. A. Robb, J. R. Cheeseman, G. Scalmani, V. Barone, G. A. Petersson, H. Nakatsuji, X. Li, M. Caricato, A. V. Marenich, J. Bloino, B. G. Janesko, R. Gomperts, B. Mennucci, H. P. Hratchian, J. V. Ortiz, A. F. Izmaylov, J. L. Sonnenberg, D. Williams-Young, F. Ding, F. Lipparini, F. Egidi, J. Goings, B. Peng, A. Petrone, T. Henderson, D. Ranasinghe, V. G. Zakrzewski, J. Gao, N. Rega, G. Zheng, W. Liang, M. Hada, M. Ehara, K. Toyota, R. Fukuda, J. Hasegawa, M. Ishida, T. Nakajima, Y. Honda, O. Kitao, H. Nakai, T. Vreven, K. Throssell, J. A. Montgomery, Jr., J. E. Peralta, F. Ogliaro, M. J. Bearpark, J. J. Heyd, E. N. Brothers, K. N. Kudin, V. N. Staroverov, T. A. Keith, R. Kobayashi, J. Normand, K. Raghavachari, A. P. Rendell, J. C. Burant, S. S. Iyengar, J. Tomasi, M. Cossi, J. M. Millam, M. Klene, C. Adamo, R. Cammi, J. W. Ochterski, R. L. Martin, K. Morokuma, O. Farkas, J. B. Foresman, and D. J. Fox. Gaussian~16 Revision C.01, 2016. Gaussian Inc. Wallingford CT.
- [67] Svetlana N. Ivashevskaya. Crystal structure of pigment red 254 from x-ray powder diffraction data. *Acta Crystallographica Section E*, 73(4):507–510, Apr 2017. doi: 10.1107/S2056989017003309. URL <https://doi.org/10.1107/S2056989017003309>.
- [68] Anthony P. Scott and Leo Radom. Harmonic vibrational frequencies: An evaluation of hartree-fock, møller-plesset, quadratic configuration interaction, density functional theory, and semiempirical scale factors. *The Journal of Physical Chemistry*, 100(41):16502–16513, 1996. doi: 10.1021/jp960976r. URL <https://doi.org/10.1021/jp960976r>.
- [69] Khan. Shahid Ali, Sher Bahadar Khan, Latif Ullah Khan, Aliya Farooq, Kalsoom Akhtar, and Abdullah M. Asiri. *Handbook of Materials Characterization*. Springer International Publishing, 2018.
- [70] David Bossanyi. [franckcondon](https://github.com/fast-spectroscopy-sheffield/franckcondon). <https://github.com/fast-spectroscopy-sheffield/franckcondon>, 2020.

- [71] Koichi Momma and Fujio Izumi. *VESTA3* for three-dimensional visualization of crystal, volumetric and morphology data. *Journal of Applied Crystallography*, 44(6):1272–1276, 2011. doi: 10.1107/S0021889811038970. URL <https://doi.org/10.1107/S0021889811038970>.
- [72] Joaquim Jaumot, Anna de Juan, and Romà Tauler. Mcr-als gui 2.0: New features and applications. *Chemometrics and Intelligent Laboratory Systems*, 140:1–12, 2015. ISSN 0169-7439. doi: <https://doi.org/10.1016/j.chemolab.2014.10.003>. URL <https://www.sciencedirect.com/science/article/pii/S0169743914002111>.
- [73] Daniel N. Congreve, Jiye Lee, Nicholas J. Thompson, Eric Hontz, Shane R. Yost, Philip D. Reusswig, Matthias E. Bahlke, Sebastian Reineke, Troy Van Voorhis, and Marc A. Baldo. External quantum efficiency above 100% in a singlet-exciton-fission-based organic photovoltaic cell. *Science*, 340(6130):334–337, 2013. doi: 10.1126/science.1232994. URL <https://www.science.org/doi/abs/10.1126/science.1232994>.
- [74] Sven Rühle. Tabulated values of the shockley–queisser limit for single junction solar cells. *Solar Energy*, 130:139–147, 2016. doi: 10.1016/j.solener.2016.02.015. URL <https://www.sciencedirect.com/science/article/pii/S0038092X16001110>.
- [75] Tobias Ullrich, Dominik Munz, and Dirk M. Guldi. Unconventional singlet fission materials. *Chem. Soc. Rev.*, 50(5):3485–3518, 2021. doi: 10.1039/D0CS01433H. URL <http://dx.doi.org/10.1039/D0CS01433H>.
- [76] Erika Švara Fabjan, Mojca Otoničar, Miran Gaberšček, and Andrijana Severškapin. Surface protection of an organic pigment based on a modification using a mixed-micelle system. *Dyes and Pigments*, 127:100–109, 2016. doi: 10.1016/j.dyepig.2015.12.016. URL <https://www.sciencedirect.com/science/article/pii/S0143720815005033>.
- [77] Marta Anghelone, Valentin Stoytschew, Dubravka Jembrih-Simbürger, and Manfred Schreiner. Spectroscopic methods for the identification and photostability study of red synthetic organic pigments in alkyd and acrylic paints. *Microchemical Journal*, 139:155–163, 2018. ISSN 0026-265X. doi: <https://doi.org/10.1016/j.microc.2018.02.029>. URL <https://www.sciencedirect.com/science/article/pii/S0026265X17309050>.
- [78] Hyun-Young Lee, Ji-Hye Kim, Jae-Sung Yoo, Ji-Hye Bae, Chun Yoon, and Jae-Hong Choi. Synthesis and thermal stability of solvent soluble dyes based on dimerized diketo-pyrrolo-pyrrole pigment. *Bulletin of the Korean Chemical Society*, 35(2):659–662, 02 2014. doi: 10.5012/BKCS.2014.35.2.659. URL <http://koreascience.or.kr/article/JAK0201408439034681.page>.

- [79] Se-Hwa Choi, Oh-Tak Kwon, Na rim Kim, Chun Yoon, Jae-Pil Kim, and Jae-Hong Choi. Preparation of solvent soluble dyes derived from diketo-pyrrolo-pyrrole pigment by introducing an n-alkyl group. *Bulletin of the Korean Chemical Society*, 31(4):1073–1076, 2010. doi: 10.5012/bkcs.2010.31.04.1073. URL <https://www.koreascience.or.kr/article/JAKO201013343110957.pdf>.
- [80] Tae-Heon Kim, Byung-Jun Lee, Sung-Ok An, Joo-Hong Lee, and Jae-Hong Choi. The synthesis of red dyes based on diketo-pyrrolo-pyrrole chromophore to improve heat stability and solubility for colour filter fabrication. *Dyes and Pigments*, 174:108053, 2020. ISSN 0143-7208. doi: <https://doi.org/10.1016/j.dyepig.2019.108053>. URL <https://www.sciencedirect.com/science/article/pii/S0143720819324763>.
- [81] Zhimin Hao and Abul Iqbal. Some aspects of organic pigments. *Chemical Society Reviews*, 26(3):203, 1997. doi: 10.1039/CS9972600203. URL <https://pubs.rsc.org/en/content/articlelanding/1997/cs/cs9972600203>.
- [82] Hyun-Young Lee, Jae-Sung Yoo, Hye-Seon Kwon, Jin-Kyu Oh, and Jae-Hong Choi. Preparation and characterizations of solvent soluble dyes based on dimerized diketo-pyrrolo-pyrrole pigment. *Molecular Crystals and Liquid Crystals*, 617(1):73–81, 2015. doi: 10.1080/15421406.2015.1075831. URL <https://www.sciencedirect.com/science/article/pii/S0040403910001176>.
- [83] Zi-Qiang Wen, Ya-Qing Feng, Xiang-Gao Li, Yu Bai, Xiao-Xu Li, Jing An, and Min Lu. Surface modification of organic pigment particles for microencapsulated electrophoretic displays. *Dyes and Pigments*, 92(1):554–562, 2012. doi: 10.1016/j.dyepig.2011.06.003. URL <https://www.sciencedirect.com/science/article/pii/S0143720811001604>.
- [84] Eric Daniel Głowacki, Halime Coskun, Martin A. Blood-Forsythe, Uwe Monkwius, Lucia Leonat, Marek Grzybowski, Daniel Gryko, Matthew Schuette White, Alán Aspuru-Guzik, and Niyazi Serdar Sariciftci. Hydrogen-bonded diketopyrrolopyrrole (dpp) pigments as organic semiconductors. *Organic Electronics*, 15(12):3521–3528, 2014. doi: 10.1016/j.orgel.2014.09.038. URL <https://www.sciencedirect.com/science/article/pii/S1566119914004303>.
- [85] Wipaporn Kitisriworaphan, Thanyarat Chawanpunyawat, Thanaporn Manyum, Pongsakorn Chasing, Supawadee Namuangruk, Taweesak Sudyoadsuk, and Vinich Promarak. The improvement in hole-transporting and electroluminescent properties of diketopyrrolopyrrole pigment by grafting with carbazole dendrons. *RSC Advances*, 11(21):12710–12719, 2021. doi: 10.1039/d1ra00805f. URL <https://pubs.rsc.org/en/content/articlelanding/2021/ra/d1ra00805f>.

- [86] Akinori Honda, Yoshinori Tamaki, and Kazuo Miyamura. The effects of non-covalent interactions on surface structures formed by diketopyrrolopyrrole pigment and its alkyl-derivatives on hopg substrate. *Bulletin of the Chemical Society of Japan*, 88(7):969–975, 2015. doi: 10.1246/bcsj.20150049. URL <https://doi.org/10.1246/bcsj.20150049>.
- [87] Patrick E. Hartnett, Eric A. Margulies, Catherine M. Mauck, Stephen A. Miller, Yilei Wu, Yi-Lin Wu, Tobin J. Marks, and Michael R. Wasielewski. Effects of crystal morphology on singlet exciton fission in diketopyrrolopyrrole thin films. *The Journal of Physical Chemistry B*, 120(7):1357–1366, 2016. doi: 10.1021/acs.jpcc.5b10565. URL <https://pubs.acs.org/doi/10.1021/acs.jpcc.5b10565>.
- [88] Catherine M. Mauck, Patrick E. Hartnett, Eric A. Margulies, Lin Ma, Claire E. Miller, George C. Schatz, Tobin J. Marks, and Michael R. Wasielewski. Singlet fission via an excimer-like intermediate in 3,6-bis(thiophen-2-yl)diketopyrrolopyrrole derivatives. *Journal of the American Chemical Society*, 138(36):11749–11761, 2016. doi: 10.1021/jacs.6b05627. URL <https://pubs.acs.org/doi/10.1021/jacs.6b05627>.
- [89] Claire E. Miller, Michael R. Wasielewski, and George C. Schatz. Modeling singlet fission in rylene and diketopyrrolopyrrole derivatives: The role of the charge transfer state in superexchange and excimer formation. *The Journal of Physical Chemistry C*, 121(19):10345–10350, 2017. doi: 10.1021/acs.jpcc.7b02697. URL <https://pubs.acs.org/doi/10.1021/acs.jpcc.7b02697>.
- [90] Frank C. Spano, Jenny Clark, Carlos Silva, and Richard H. Friend. Determining exciton coherence from the photoluminescence spectral line shape in poly(3-hexylthiophene) thin films. *The Journal of Chemical Physics*, 130(7):074904, 2009. doi: 10.1063/1.3076079. URL <https://doi.org/10.1063/1.3076079>.
- [91] David C. Young, Mariusz Tasiar, Adèle D. Laurent, Łukasz Dobrzycki, Michał K. Cyrański, Nikolai Tkachenko, Denis Jacquemin, and Daniel T. Gryko. Photostable orange-red fluorescent unsymmetrical diketopyrrolopyrrole–bf₂ hybrids. *J. Mater. Chem. C*, 8:7708–7717, 2020. doi: 10.1039/D0TC01202E. URL <http://dx.doi.org/10.1039/D0TC01202E>.
- [92] J. Mizuguchi, A. Grubenmann, and G. Rihs. Structures of 3,6-bis(3-chlorophenyl)pyrrolo[3,4-*c*]pyrrole-1,4-dione and 3,6-bis(4-chlorophenyl)pyrrolo[3,4-*c*]pyrrole-1,4-dione. *Acta Crystallographica Section B*, 49(6):1056–1060, 1993. doi: 10.1107/S0108768193007645. URL <https://doi.org/10.1107/S0108768193007645>.

- [93] Xian-Kai Chen, Veaceslav Coropceanu, and Jean-Luc Brédas. Assessing the nature of the charge-transfer electronic states in organic solar cells. *Nature Communications*, 9:5295, 2018. doi: 10.1038/s41467-018-07707-8. URL <https://doi.org/10.1038/s41467-018-07707-8>.
- [94] Jin Mizuguchi and Gary Wooden. A large bathochromic shift from the solution to the solid state in 1,4-diketo-3,6-diphenyl-pyrrolo-[3,4-c]-pyrrole. *Berichte der Bunsengesellschaft für physikalische Chemie*, 95(10):1264–1274, 1991. doi: 10.1002/bbpc.19910951016. URL <https://onlinelibrary.wiley.com/doi/abs/10.1002/bbpc.19910951016>.
- [95] Akshay Rao, Mark W. B. Wilson, Sebastian Albert-Seifried, Riccardo Di Pietro, and Richard H. Friend. Photophysics of pentacene thin films: The role of exciton fission and heating effects. *Physical Review B*, 84(19):195411, 2011. doi: 10.1103/PhysRevB.84.195411. URL <https://journals.aps.org/prb/pdf/10.1103/PhysRevB.84.195411>.
- [96] Sebastian Albert-Seifried and Richard H. Friend. Measurement of thermal modulation of optical absorption in pump-probe spectroscopy of semiconducting polymers. *Applied Physics Letters*, 98(22):223304, 2011. doi: 10.1063/1.3595340. URL <https://doi.org/10.1063/1.3595340>.
- [97] Gwantaek Kim, Donghyuk Kim, Sukkyung Kang, Jaisuk Yoo, and Hyunjung Kim. Research on measuring thermal conductivity of quartz and sapphire glass using rear-side photothermal deflection method. *Applied Sciences*, 11(4), 2021. doi: 10.3390/app11041535. URL <https://www.mdpi.com/2076-3417/11/4/1535>.
- [98] Wenbo Hu, Xiaofei Miao, Haojie Tao, Alexander Baev, Can Ren, Quli Fan, Tingchao He, Wei Huang, and Paras N. Prasad. Manipulating nonradiative decay channel by intermolecular charge transfer for exceptionally improved photothermal conversion. *ACS Nano*, 13(10):12006–12014, 2019. doi: 10.1021/acsnano.9b06208. URL <https://doi.org/10.1021/acsnano.9b06208>. PMID: 31518102.
- [99] A. Manian, R. A. Shaw, I. Lyskov, W. Wong, and S. P. Russo. Modeling radiative and pathways at both the franck–condon and herzberg–teller approximation level. *The Journal of Chemical Physics*, 155(5):054108, 2021. doi: 10.1063/5.0058643. URL <https://doi.org/10.1063/5.0058643>.
- [100] Md. M. Alam, F. Bolze, C. Daniel, L. Flamigni, C. Gourlaouen, V. Heitz, S. Jenni, J. Schmitt, A. Sour, and B. Ventura. π -extended diketopyrrolopyrrole–porphyrin arrays: one- and two-photon photophysical investigations and theoretical studies. *Phys. Chem. Chem. Phys.*, 18:21954–21965, 2016. doi: 10.1039/C6CP01844K. URL <http://dx.doi.org/10.1039/C6CP01844K>.

- [101] Gabriela Wiosna-Salyga, Monika Gora, Malgorzata Zagorska, Petr Toman, Beata Luszczynska, Jiri Pflieger, Ireneusz Glowacki, Jacek Ulanski, Jozef Mieczkowski, and Adam Pron. Diketopyrrolopyrroles disubstituted with alkylated thiophenes: effect of the donor unit size and solubilizing substituents on their redox, photo- and electroluminescence properties. *RSC Adv.*, 5:59616–59629, 2015. doi: 10.1039/C5RA06811H. URL <http://dx.doi.org/10.1039/C5RA06811H>.
- [102] Catherine M. Mauck, Youn Jue Bae, Michelle Chen, Natalia Powers-Riggs, Yi-Lin Wu, and Michael R. Wasielewski. Charge-transfer character in a covalent diketopyrrolopyrrole dimer: Implications for singlet fission. *ChemPhotoChem*, 2(3):223–233, 2018. doi: 10.1002/cptc.201700135. URL <https://chemistry-europe.onlinelibrary.wiley.com/doi/abs/10.1002/cptc.201700135>.
- [103] Yi Qu, Jianli Hua, and He Tian. Colorimetric and ratiometric red fluorescent chemosensor for fluoride ion based on diketopyrrolopyrrole. *Organic Letters*, 12(15):3320–3323, 2010. doi: 10.1021/ol101081m. URL <https://doi.org/10.1021/ol101081m>. PMID: 20590106.
- [104] Jin Mizuguchi. Correlation between crystal and electronic structures in diketopyrrolopyrrole pigments as viewed from exciton coupling effects. *The Journal of Physical Chemistry A*, 104(9):1817–1821, 2000. doi: 10.1021/jp992302x. URL <https://doi.org/10.1021/jp992302x>.
- [105] Yuki Suna, Jun-ichi Nishida, Yoshihide Fujisaki, and Yoshiro Yamashita. Ambipolar behavior of hydrogen-bonded diketopyrrolopyrrole–thiophene co-oligomers formed from their soluble precursors. *Organic Letters*, 14(13):3356–3359, 2012. doi: 10.1021/ol3013364. URL <https://doi.org/10.1021/ol3013364>. PMID: 22716905.
- [106] Simone De Camillis, Jordan Miles, Grace Alexander, Omair Ghafur, Ian D. Williams, Dave Townsend, and Jason B. Greenwood. Ultrafast non-radiative decay of gas-phase nucleosides. *Phys. Chem. Chem. Phys.*, 17:23643–23650, 2015. doi: 10.1039/C5CP03806E. URL <http://dx.doi.org/10.1039/C5CP03806E>.
- [107] Yuyuan Zhang, Kimberly de La Harpe, Ashley A. Beckstead, Roberto Improta, and Bern Kohler. Uv-induced proton transfer between dna strands. *Journal of the American Chemical Society*, 137(22):7059–7062, 2015. doi: 10.1021/jacs.5b03914. URL <https://doi.org/10.1021/jacs.5b03914>. PMID: 26005794.
- [108] Guang-Jiu Zhao and Ke-Li Han. Hydrogen bonding in the electronic excited state. *Accounts of Chemical Research*, 45(3):404–413, 2012. doi: 10.1021/ar200135h. URL <https://doi.org/10.1021/ar200135h>.

- [109] Bartolome Soberats, Markus Hecht, and Frank Würthner. Diketopyrrolopyrrole columnar liquid-crystalline assembly directed by quadruple hydrogen bonds. *Angewandte Chemie International Edition*, 56(36):10771–10774, 2017. doi: <https://doi.org/10.1002/anie.201705137>. URL <https://onlinelibrary.wiley.com/doi/abs/10.1002/anie.201705137>.
- [110] Long Yang, Yuyan Yu, Yulong Gong, Jiarong Li, Feijie Ge, Long Jiang, Fang Gao, and Yi Dan. Systematic investigation of the synthesis and light-absorption broadening of a novel diketopyrrolopyrrole conjugated polymer of low and high molecular weight with thermo-labile groups. *Polym. Chem.*, 6:7005–7014, 2015. doi: 10.1039/C5PY01086A. URL <http://dx.doi.org/10.1039/C5PY01086A>.
- [111] Nhung Thanh Thi Truong, Loc Tan Nguyen, Huyen Le Thi Mai, Bao Kim Doan, Dat Hung Tran, Khuong Tung Truong, Viet Quoc Nguyen, Le-Thu T. Nguyen, Mai Ha Hoang, Toai Van Pham, Vuong Mau Nguyen, Tien Minh Huynh, Tin Chanh Duc Doan, and Ha Tran Nguyen. Phenothiazine derivatives, diketopyrrolopyrrole-based conjugated polymers: synthesis, optical and organic field effect transistor properties. *Journal of Polymer Research*, 27, 2020. doi: 10.1007/s10965-020-02199-x. URL <https://doi.org/10.1007/s10965-020-02199-x>.
- [112] Amparo Ruiz-Carretero, Nelson Ricardo Ávila Rovelo, Swann Militzer, and Philippe J. Mésini. Hydrogen-bonded diketopyrrolopyrrole derivatives for energy-related applications. *J. Mater. Chem. A*, 7:23451–23475, 2019. doi: 10.1039/C9TA05236D. URL <http://dx.doi.org/10.1039/C9TA05236D>.
- [113] Alfred Treibs and Franz-Heinrich Kreuzer. Difluoroboryl-komplexe von di- und tripyrrylmethenen. *Justus Liebigs Annalen der Chemie*, 718(1):208–223, 1968. doi: <https://doi.org/10.1002/jlac.19687180119>. URL <https://chemistry-europe.onlinelibrary.wiley.com/doi/abs/10.1002/jlac.19687180119>.
- [114] Aurore Loudet and Kevin Burgess. Bodipy dyes and their derivatives: Syntheses and spectroscopic properties. *Chemical Reviews*, 107(11):4891–4932, 2007. doi: 10.1021/cr078381n. URL <https://doi.org/10.1021/cr078381n>. PMID: 17924696.
- [115] Gilles Ulrich, Raymond Ziessel, and Anthony Harriman. The chemistry of fluorescent bodipy dyes: Versatility unsurpassed. *Angewandte Chemie International Edition*, 47(7):1184–1201, 2008. doi: <https://doi.org/10.1002/anie.200702070>. URL <https://onlinelibrary.wiley.com/doi/abs/10.1002/anie.200702070>.
- [116] Kishor G. Thorat, Priyadarshani Kamble, Ramnath Mallah, Alok K. Ray, and Nagaiyan Sekar. Congeners of pyromethene-567 dye: Perspectives from synthesis,

- photophysics, photostability, laser, and td-dft theory. *The Journal of Organic Chemistry*, 80(12):6152–6164, 2015. doi: 10.1021/acs.joc.5b00654. URL <https://doi.org/10.1021/acs.joc.5b00654>. PMID: 26001098.
- [117] Jorge Bañuelos. Bodipy dye, the most versatile fluorophore ever? *The Chemical Record*, 16(1):335–348, 2016. doi: <https://doi.org/10.1002/tcr.201500238>. URL <https://onlinelibrary.wiley.com/doi/abs/10.1002/tcr.201500238>.
- [118] Selin Duman, Yusuf Cakmak, Safacan Kolemen, Engin U. Akkaya, and Yavuz Dede. Heavy atom free singlet oxygen generation: Doubly substituted configurations dominate s1 states of bis-bodipys. *The Journal of Organic Chemistry*, 77(10):4516–4527, 2012. doi: 10.1021/jo300051v. URL <https://doi.org/10.1021/jo300051v>. PMID: 22530939.
- [119] Raúl Montero, Virginia Martínez-Martínez, Asier Longarte, Nerea Epelde-Elezcano, Eduardo Palao, Iker Lamas, Hegoi Manzano, Antonia R. Agarrabeitia, Iñigo López Arbeloa, Maria J. Ortiz, and Inmaculada Garcia-Moreno. Singlet fission mediated photophysics of bodipy dimers. *The Journal of Physical Chemistry Letters*, 9(3):641–646, 2018. doi: 10.1021/acs.jpcllett.7b03074. URL <https://doi.org/10.1021/acs.jpcllett.7b03074>. PMID: 29337574.
- [120] Jin Wen, Bowen Han, Zdeněk Havlas, and Josef Michl. An ms-caspt2 calculation of the excited electronic states of an axial difluoroborondipyrromethene (bodipy) dimer. *Journal of chemical theory and computation*, 14(8):4291–4297, 2014. doi: 10.1021/acs.jctc.8b00136. URL <https://pubmed.ncbi.nlm.nih.gov/29874458/>. PMID: 29874458.
- [121] Yuri E. Kandrashkin, Zhijia Wang, Andrei A. Sukhanov, Yuqi Hou, Xue Zhang, Ya Liu, Violeta K. Voronkova, and Jianzhang Zhao. Balance between triplet states in photoexcited orthogonal bodipy dimers. *The Journal of Physical Chemistry Letters*, 10(15):4157–4163, 2019. doi: 10.1021/acs.jpcllett.9b01741. URL <https://doi.org/10.1021/acs.jpcllett.9b01741>. PMID: 31283880.
- [122] Raúl Montero, Virginia Martínez-Martínez, Asier Longarte, Nerea Epelde-Elezcano, Iker Lamas, and Iñigo López Arbeloa. Viewpoint regarding “singlet fission mediated photophysics of bodipy dimers”. *The Journal of Physical Chemistry Letters*, 12(31):7439–7441, 2021. doi: 10.1021/acs.jpcllett.1c01941. URL <https://doi.org/10.1021/acs.jpcllett.1c01941>. PMID: 34338533.
- [123] Takao Tsuneda and Tetsuya Taketsugu. Singlet fission initiating triplet generations of bodipy derivatives through π -stacking: a theoretical study. *Scientific Reports*, 12(1):19714, 2022. doi: 10.1038/s41598-022-23370-y. URL <https://www.nature.com/articles/s41598-022-23370-y>.

- [124] Lijuan Xue, Xinyu Song, Yiwei Feng, Shibo Cheng, Gang Lu, and Yuxiang Bu. General dual-switched dynamic singlet fission channels in solvents governed jointly by chromophore structural dynamics and solvent impact: Singlet prefission energetics analyses. *Journal of the American Chemical Society*, 142(41):17469–17479, 2020. doi: 10.1021/jacs.0c06919. URL <https://doi.org/10.1021/jacs.0c06919>. PMID: 32927954.
- [125] Yichen Zhou, Wenjun Ni, Lin Ma, Licheng Sun, Jianzhang Zhao, and Gagik G. Gurzadyan. Singlet fission from upper excited states of bodipy crystalline film and single crystal. *The Journal of Physical Chemistry C*, 126(40):17212–17222, 2022. doi: 10.1021/acs.jpcc.2c05665. URL <https://doi.org/10.1021/acs.jpcc.2c05665>.
- [126] Jianhua Zou, Zhihui Yin, Kaikai Ding, Qianyun Tang, Jiewei Li, Weili Si, Jinjun Shao, Qi Zhang, Wei Huang, and Xiaochen Dong. Bodipy derivatives for photodynamic therapy: Influence of configuration versus heavy atom effect. *ACS Applied Materials & Interfaces*, 9(38):32475–32481, 2017. doi: 10.1021/acsami.7b07569. URL <https://doi.org/10.1021/acsami.7b07569>. PMID: 28875695.
- [127] Xiaofei Miao, Wenbo Hu, Tingchao He, Haojie Tao, Qi Wang, Runfeng Chen, Lu Jin, Hui Zhao, Xiaomei Lu, Quli Fan, and Wei Huang. Deciphering the intersystem crossing in near-infrared bodipy photosensitizers for highly efficient photodynamic therapy. *Chem. Sci.*, 10:3096–3102, 2019. doi: 10.1039/C8SC04840A. URL <http://dx.doi.org/10.1039/C8SC04840A>.
- [128] Miao Liu, Chengjun Wang, and Ying Qian. Novel indole-bodipy photosensitizers based on iodine promoted intersystem crossing enhancement for lysosome-targeted imaging and photodynamic therapy. *New J. Chem.*, 45:18082–18089, 2021. doi: 10.1039/D1NJ03628A. URL <http://dx.doi.org/10.1039/D1NJ03628A>.
- [129] Elif Akhuseyin Yildiz, Ebru Yabaş, Fazlı Sözmen, Yasemin Bozkurt, Ahmet Karatay, Bahadır Boyacıoğlu, Hüseyin Ünver, and Ayhan Elmali. Effects of heavy iodine atoms and π -expanded conjugation on charge transfer dynamics in carboxylic acid bodipy derivatives as triplet photosensitizers. *ChemPhysChem*, 24(5):e202200735, 2023. doi: <https://doi.org/10.1002/cphc.202200735>. URL <https://chemistry-europe.onlinelibrary.wiley.com/doi/abs/10.1002/cphc.202200735>.
- [130] Xian-Fu Zhang, Xudong Yang, Kui Niu, and Hao Geng. Phosphorescence of bodipy dyes. *Journal of Photochemistry and Photobiology A: Chemistry*, 285:16–20, 2014. ISSN 1010-6030. doi: <https://doi.org/10.1016/j.jphotochem.2014.04.009>. URL <https://www.sciencedirect.com/science/article/pii/S1010603014001324>.

- [131] Raymond Ziessel, Ben Allen, Dorota Rewinska, and Anthony Harriman. Selective triplet-state formation during charge recombination in a fullerene/bodipy molecular dyad (bodipy=borondipyrromethene). *Chemistry*, 15:7382–93, 2009. doi: 10.1002/chem.200900440. URL <https://pubmed.ncbi.nlm.nih.gov/19551782/>.
- [132] Kepeng Chen, Yu Dong, Xiaoyu Zhao, Muhammad Imran, Geliang Tang, Jianzhang Zhao, and Qingyun Liu. Bodipy derivatives as triplet photosensitizers and the related intersystem crossing mechanisms. *Frontiers in Chemistry*, 7, 2019. ISSN 2296-2646. doi: 10.3389/fchem.2019.00821. URL <https://www.frontiersin.org/articles/10.3389/fchem.2019.00821>.
- [133] Christina Kaiser, Oskar Sandberg, Nasim Zarrabi, Wei Li, Paul Meredith, and Ardalan Armin. A universal urbach rule for disordered organic semiconductors. *Nature Communications*, 12:3988, 2021. doi: 10.1038/s41467-021-24202-9. URL <https://www.nature.com/articles/s41467-021-24202-9>.
- [134] Elena Bassan, Yasi Dai, Daniele Fazzi, Adnrea Gualandi, Pier Giorgio Cozzi, Fabrizia Negri, and Paola Ceroni. Effect of the iodine atom position on the phosphorescence of bodipy derivatives: a combined computational and experimental study. *Photochemical & Photobiological Sciences*, 21:777–786, 2022. doi: 10.1007/s43630-021-00152-5. URL <https://link.springer.com/article/10.1007/s43630-021-00152-5>.
- [135] Maria I. Martinez-Espinoza, Lorenzo Sori, Andrea Pizzi, Giancarlo Ter-raneo, Ivana Moggio, Eduardo Arias, Gianluca Pozzi, Simonetta Orlandi, Valentina Dichiarante, Pierangelo Metrangolo, Marco Cavazzini, and Francesca Baldelli-Bombelli. Bodipy dyes bearing multibranching fluorinated chains: Synthesis, structural, and spectroscopic studies. *Chemistry – A European Journal*, 25(38):9078–9087, 2019. doi: <https://doi.org/10.1002/chem.201901259>. URL <https://chemistry-europe.onlinelibrary.wiley.com/doi/abs/10.1002/chem.201901259>.
- [136] Andrew T. B. Gilbert, Nicholas A. Besley, and Peter M. W. Gill. Self-consistent field calculations of excited states using the maximum overlap method (mom). *The Journal of Physical Chemistry A*, 112(50):13164–13171, 2008. doi: 10.1021/jp801738f. URL <https://doi.org/10.1021/jp801738f>. PMID: 18729344.
- [137] Diptarka Hait and Martin Head-Gordon. Excited state orbital optimization via minimizing the square of the gradient: General approach and application to singly and doubly excited states via density functional theory. *Journal of Chemical Theory and Computation*, 16(3):1699–1710, 2020. doi: 10.1021/acs.jctc.9b01127. URL <https://doi.org/10.1021/acs.jctc.9b01127>. PMID: 32017554.